Simulations of the circum-galactic medium - a comparative study of subgrid models for star formation and their feedback

Maxime Rey


Numéro National de Thèse : 2022ENSL0040

THESE

en vue de l'obtention du grade de Docteur, délivré par

l'ECOLE NORMALE SUPERIEURE DE LYON

Ecole Doctorale N° 52
École Doctorale de Physique et Astrophysique

Discipline : Physique
Discipline : Astrophysique

Soutenue publiquement le 18/10/2022, par :

Maxime REY

Simulations du milieu circum-galactique - étude comparative de modèles sous-grille pour la formation d'étoiles et leur rétroaction.

Devant le jury composé de :

DEVRIENDT	Julien	Professeur	Oxford University	Rapporteur
PEROUX	Céline	Chargée de recherche	ESO (Garching)	Rapporteure
BOURNAUD	Frédéric	Chercheur	CEA (Paris)	Examinateur
LAIGLE	Clotilde	Astronome adjoint	IAP (Paris)	Examinatrice
GUIDERDONI	Bruno	Directeur de recherche	CRAL (Lyon)	Examinateur
BLAIZOT	Jérémy	Professeur	CRAL (Lyon)	Directeur de thèse

Dang it, Jim ! I'm an astronomer, not a doctor !
I mean, I am a doctor, but I'm not that kind of doctor.
I have a doctorate, it's not the same thing.
You can't help people with a doctorate. You just sit there and you're useless !

– Dr. Delbert Doppler

Résumé

Au cours des dernières décennies, les simulations numériques se sont révélées être un des instruments majeurs de l'astrophysique. Elles ont permis des avancées notables, de l'échelle planétaire à la structure du gaz et de la matière noire dans l'univers, la toile cosmique. Par le biais de supercalculateurs, ces simulations permettent aux théoriciens d'accéder à une puissance de calcul formidable et de simuler l'évolution de systèmes complexes. En effet, l'astrophysique implique l'étude de phénomènes multiéchelles, allant de l'unité astronomique au mégaparsec, mais aussi de nombreux processus physiques tels que la gravité, le rayonnement et les champs magnétiques. De par des simulations de plus en plus poussées et une puissance de calcul croissante, les simulations de formation de galaxies permettent dorénavant d'atteindre une résolution de l'ordre de la dizaine de parsecs tout en modélisant l'impact de la toile cosmique sur celles-ci. Cependant, de telles résolutions ne permettent pas de modéliser tous les processus physiques impliqués dans la formation des galaxies.

Deux phénomènes ayant lieu à des échelles inférieures à celles résolues, mais ayant néanmoins un impact majeur à l'échelle galactique, sont la formation d'étoiles et les divers processus de rétroaction stellaire. Ces processus peuvent diminuer la formation stellaire en chauffant les nuages moléculaires (lieux au sein desquels se créent les étoiles), en entravant l'accrétion de gaz par les filaments cosmiques, mais également en éjectant du gaz hors des galaxies. Sources de cette rétroaction, les processus de formation d'étoiles et de rétroaction stellaire sont fortement intriqués.

Un challenge majeur vis-à-vis des phénomènes stellaires est qu'ils surviennent à des échelles largement inférieures à la résolution maximale des simulations actuelles. L'approche pour les modéliser est alors d'utiliser des modèles dit *sous-grilles*. Ces modèles permettent de modéliser l'impact de phénomènes non résolus à l'échelle de résolution des simulations numériques. En suivant différentes considérations physiques, de multiples modèles peuvent être développés, aussi bien pour la formation des étoiles que pour leur rétroaction sur le gaz. Il est alors commun de calibrer ces différents modèles à l'aide d'observables. Un exemple de courbe de calibration fréquemment utilisée est la relation entre la masse stellaire des galaxies et la masse de leur halo de matière noire. Ceci entraîne donc la création de modèles sous-grilles décrivant un même phénomène à travers des considérations physiques distinctes, mais capables de donner lieu à la formation de galaxies ayant une masse similaires. L'objectif de ma thèse est ainsi de trouver une autre observable permettant de les discriminer.

Un milieu très sensible aux processus de rétroaction stellaire est le milieu dit *circum-galactique* (CGM). Le CGM est défini comme l'environnement proche entourant la galaxie, et qui s'étend typiquement jusqu'au rayon typique de stabilité gravitationnelle du halo galactique, appelé le rayon du Viriel. Ce lieu est sujet à de nombreuses interactions ayant pour origine la galaxie et la toile cosmique. En effet, lors de phénomènes de rétroaction stellaire, une partie du gaz de la galaxie peut-être éjectée hors de la galaxie, dans le CGM. Ce gaz chauffe alors le CGM en interagissant avec le gaz froid accrété par les filaments cosmiques. Présentant une forte sensibilité à l'éjection de gaz hors des galaxies tout en étant le lieu d'interaction de différentes phases thermiques, le CGM est un milieu extrêmement complexe à simuler. Cette complexité en fait ainsi un endroit propice à la contrainte de différents modèles sous-grilles pour la formation galactique.

N'émettant pas spontanément de lumière et étant relativement peu dense, le CGM est cependant difficile à observer. Pour inférer son contenu, les observations reposent sur l'émission lumineuse des quasars, les objets astronomiques les plus brillants de l'univers. Ceux-ci sont généralement situés à de grandes distances, ce qui leur permet d'illuminer l'arrière de nuages de gaz plus proches. Si le gaz est suffisamment dense, il absorbera une partie de la lumière émise par le quasar. En analysant la quantité de lumière absorbée, il est alors possible de calculer la quantité de gaz que la lumière a traversé.

Mon objectif est de trouver une observable complémentaire aux relations déjà existantes permettant de lever la dégénérescence qui existe entre différents modèles sous-grilles. Pour ce faire, en partant des mêmes conditions initiales, je simule l'évolution d'une galaxie par différents modèles sous-grilles. Après les avoir calibrées en masse, je mesure les densités de colonne de différents ions dans le CGM et les compare à des observations. Par ce biais, je réponds à la problématique de mon travail en montrant que les densités de colonne d'ions situés dans le CGM représente effectivement une nouvelle contrainte permettant de lever, au moins en partie, la dégénérescence des modèles sous-grilles.

Je poursuis ensuite l'étude des lignes d'absorption simulées et montre que l'évolution de la densité de colonne des ions simulés en fonction du paramètre d'impact sont décrites de manière satisfaisante par un profil exponentiel combiné à une valeur plateau. Les densités de colonne présentent également toutes une soudaine chute aux abords du disque galactique. La taille de cette chute est corrélée à l'énergie d'ionisation de l'ion en question.

Je montre aussi que toutes les simulations présentent des densités de colonnes largement inférieures à celles observées pour presque tous les ions. Ce désaccord semble être principalement dû à deux effets. Le premier est que les phénomènes de rétroaction galactique n'éjectent pas assez de gaz enrichi dans le CGM. Le second est que les fractions d'ionisations des ions simulés sont potentiellement incorrectes (ce qui peut être dû à une modélisation inexacte de l'état thermique du CGM).

J'explore également d'autres axes d'approche propriétés de la galaxie liées aux modèles sous-grilles ou aux observations. J'étudie les processus qui entraînent la formation d'étoiles (par compression turbulente ou par instabilité gravitationnelle), la morphologie du disque gazeux des galaxies, et enfin, l'évolution temporelle des densités de colonnes simulées.

Abstract

Over the last decades, numerical simulations have proven to be one of the major tools of astrophysics, enabling significant advances from the planetary scale to the structure of gas and dark matter in the universe, the cosmic web. Through supercomputers, these simulations allow theorists to access formidable computing power and thus simulate the evolution of complex systems. Indeed, astrophysics involves the study of multiscale phenomena, ranging from the astronomical unit to the megaparsec, but also of many physical processes such as gravity, radiation and magnetic fields. Thanks to more and more advanced models and growing computational power, simulations of galaxy formation can now resolve about a dozen parsecs while modelling the impact of the cosmic web on them. However, such resolutions do not allow the modelling of all the physical processes involved in the formation of galaxies.

Two processes occurring at scales lower than those resolved in such simulations, but which nevertheless have a major impact on the galactic scale, are star formation and various stellar feedback processes. These feedback processes can impact star formation by heating molecular clouds (where stars are created), hindering gas accretion from cosmic filaments, but also by ejecting gas from galaxies. Being the source of this feedback, star formation and stellar feedback are strongly intertwined.

A major challenge regarding these phenomena is that they occur at scales well below the maximum resolution of current numerical simulations. The approach to model them is therefore to rely on so-called *subgrid models*. These models describe the effects of these unresolved phenomena at the resolution of numerical simulation. By following different physical considerations, multiple methods can be developed to simulate these mechanisms. It is then common to calibrate these different models using observable quantities. An example of a frequently used calibration curve is the relation between the stellar mass of a galaxy and the mass of its host halo. This calibration results in the creation of subgrid models describing the same phenomenon through distinct physical considerations, but all producing galaxies with the same stellar mass. The objective of my thesis is therefore to find another complementary observable to discriminate such models.

A medium highly sensitive to feedback processes is the circumgalactic medium (CGM). The CGM is the medium surrounding the galaxy and is typically defined up to the virial radius, which describes the size of a gravitationally bound halo. The CGM hosts many interactions, as well as from the galaxy from cosmic filaments. In-

deed, feedback processes usually eject a significant fraction of gas out of the galaxy, in the CGM. This gas then heats the CGM by interacting with the cold gas accreted by cosmic filaments. The CGM is an extremely complex medium to simulate, possibly showing a high sensitivity to the ejection of gas from galaxies, as well as being the site of interaction of different thermal phases. This complexity makes it a suitable medium to produce new constraints to the various subgrid models for galaxy formation.

However, since the CGM does not emit light spontaneously and is at relatively low densities, this medium is hard to observe. To infer its content, observations rely on the emission of light from quasars, the brightest astronomical objects of the universe. Being mostly located in the early universe (at great distances), they act as background sources, lighting up gas clouds from behind. If the gas is dense enough, it will absorb part of the light emitted by the quasar. By analysing this light and how much of it was absorbed, it is then possible to compute how much gas this light went through.

My goal is to find a constraint complementary to those already existing, to raise the degeneracy that exists between different subgrid models. To this aim, I study the CGM of galaxies simulated with different subgrid models and calibrated in mass (thus respecting the first constraint). I then simulate the observation of the CGM and the measure of column densities and compare results from observations. This way, I show that quasar absorption lines do indeed represent a new constraint that allows lifting, at least in part, the degeneracy found between different subgrid models.

I then continue the study of these simulated absorption lines and show that the column density of all ions as a function of impact parameters is well-described by an exponential profile combined with a plateau and that they present a sudden drop at the edge of the galactic disc. The size of this drop is correlated with the ionisation energy of the ion in question.

I also show that almost all the simulations have column densities that are much lower than observed for all ions. This disagreement seems to be mainly due to two effects. The first is that galactic feedback does not eject enough enriched gas into the CGM. The second is that the ionisation fractions of the simulated ions are likely incorrect (which may be due to inaccurate modelling of the thermal state of the CGM).

I then explore other properties of the galaxy and subgrid models. I study the processes that lead to star formation (by turbulent compression or gravitational instability), the morphology of the gaseous disc of the galaxy, and finally, the evolution in time of column densities.

Contents

List of Figures

List of Tables

Chapter 1

Introduction to the universe

In this first chapter, I introduce the scientific knowledge necessary to navigate my thesis. In the first part, we depict our current understanding of the history of the universe and then detail quickly the current standard model of cosmology, the λCDM model, describing the universe as a combination of dark energy, dark matter and ordinary matter. We then explain how stars formed and shaped into the galaxies we observe today, alongside some of their key properties for this work. Finally, we detail how, as astrophysicists bound to Earth's vicinity and unable to put a galaxy on a weighing scale, we learn about them.

1.1 From the big bang to the reionisation

In this section, we present briefly the Big Bang Theory, as illustrated in Fig. 1.1. We describe how the universe expanded from its initial state up to the reionisation era when the first stars and galaxies formed.

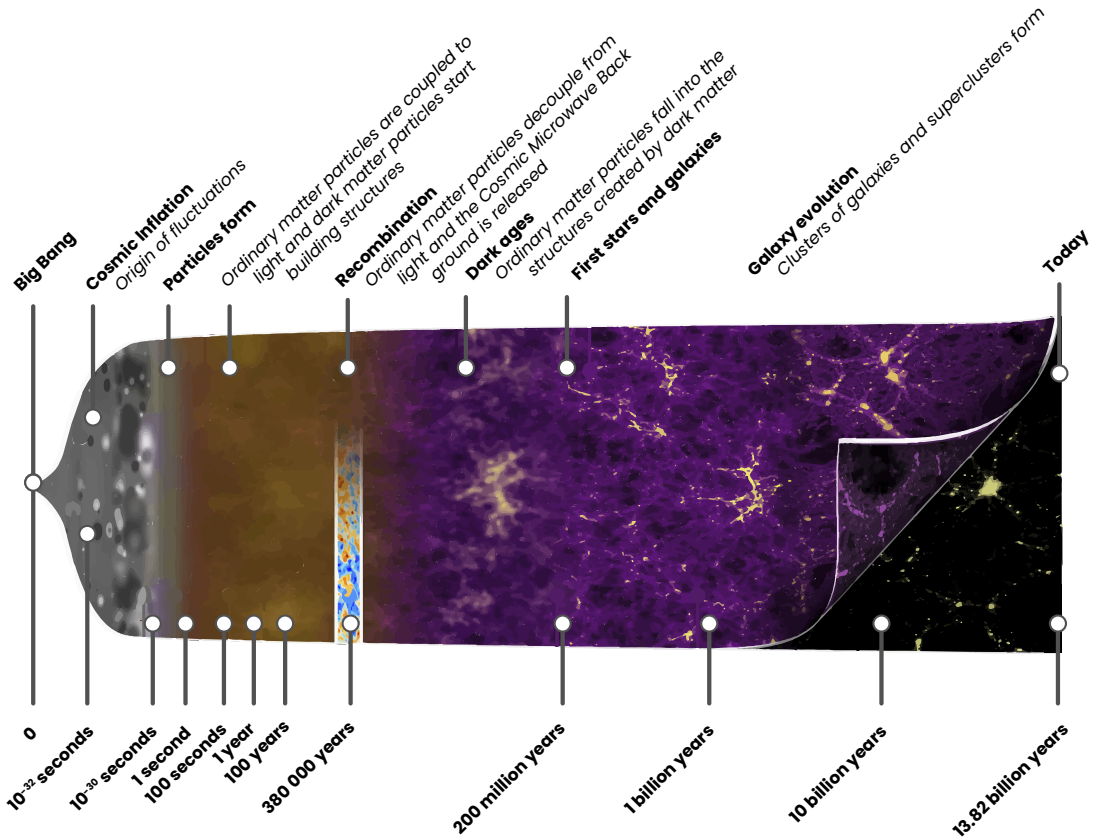

Figure 1.1 – Illustration of the evolution of the universe from its early stages to today. The top row details major events, while the bottom row indicates the timeline of these events. Illustration inspired by ESA.

1.1.1 The first seconds of the universe

Current physics cannot describe what would correspond to a time $t = 0$, the beginning of our universe. The four fundamental interactions (electromagnetism, weak and strong nuclear forces, and gravitation) are unified and cannot be described by current models (they can only describe phenomena in which these forces are applied separately). We refer to this era as the Planck epoch, and we define the time $t = 0$ by extrapolating backwards cosmic expansion equations relying on general relativity and neglecting the three other forces. This results in a universe with an age of 13.82 Gyr. The first unknown stages of the universe are delimited by considering the time a photon takes to cover Planck's length, the length below which a theory of quantum gravity is necessary, i.e. the time below which our theories crumble, $t = 10^{-44}$ s.

At this point, the universe has a length of 10 μm, a temperature of 10^{32} K and a density of 10^{96} g cm^{-3}. Gravity is then separated from the three other forces (electromagnetism, weak and strong nuclear forces, still unified, and after 10^{-35} s, inflation occurs, and the universe undergoes an extremely fast exponential expansion, with an increase in length of a factor possibly as high as $10^{26} - 10^{50}$ in $10^{-32} - 10^{-36}$ s. This expansion cools the universe down to 10^{15} K and a density of 10^{33} g cm^{-3}.

The four fundamental forces are decoupled from 10^{-9} s, but the universe is still described as a *hot soup*. Its main ingredients are quarks, a fundamental constituent of matter, and gluons, which are the strong force carriers between quarks. This high temperature restrains these elementary particles from combining into hadrons such as protons or neutrons.

Protons and neutrons are formed during the hadronic era at 10^{-6} s, which is followed by the leptonic era, at 10^{-4} s, where the universe is still dominated by light, electrons, and neutrinos. After a second, most electrons are annihilated with their counterparts the positrons, and leave the universe mostly composed of light with a small fraction of electrons, neutrons, and protons. Lastly, after 10^2 s, primordial nucleosynthesis occurs and the first nucleus of isotopes of hydrogen, helium, and lithium are formed (deuterium, tritium, etc.). The universe then has a characteristic length of 10^{18} m, a density of 4 g cm^{-3} (a thousand times less dense than air on earth) and a temperature of $10^7 - 10^9$ K.

1.1.2 Recombination

After $\sim$ 377 700 yr (Planck Collaboration et al., 2016), the universe cools down to $\sim$ 3000 K, and finally enables the combination of nuclei and electrons into atoms[1]. Before that temperature was reached, the universe was opaque to electromagnetic radiation. Photons could not travel freely as they were absorbed by electrons almost instantaneously after being emitted. When electrons combined with nuclei to form the first hydrogen atoms, the universe became *transparent* and allowed light to travel freely. This radiation is known as the cosmic microwave background (CMB).

Its observation is a key discovery that was made accidentally. In 1964, Arno Penzias and Robert Woodrow Wilson were trying to re-affect an observation antenna for the Echo satellite by using it as a radio telescope. They had to characterise precisely the noise of their observations (such as emission from their wires and other sources), but could not explain a component that was isotropically and uniformly distributed, with no daily nor seasonal variation. They later found that this was the CMB, the first image of the universe, which we show in Fig. 1.2. This radiation corresponds to a black-body spectrum[3], with a characteristic temperature of $\sim$ 2.7 K (the universe cools down as it expands), and variations of the order of 18 μK. This map exhibits how, on large scales, the universe is homogeneous and isotropic but not on small scales. The variations we observe trace primordial quantum fluctuations, which expanded with the universe. As these fluctuations are Gaussian, the CMB

[1]The *recombination* is effectively the first combination of electrons and nuclei.

[2]The Mollweide projection, also called homalographic or homolographic projection, represents the full sky and favours the conservation of surfaces instead of angles.

[3]A black body is a body in thermal equilibrium that absorbs electromagnetic radiation at all frequencies and angles of incidence. It has a characteristic temperature which emits *black-body* radiation and is described by Planck's law.

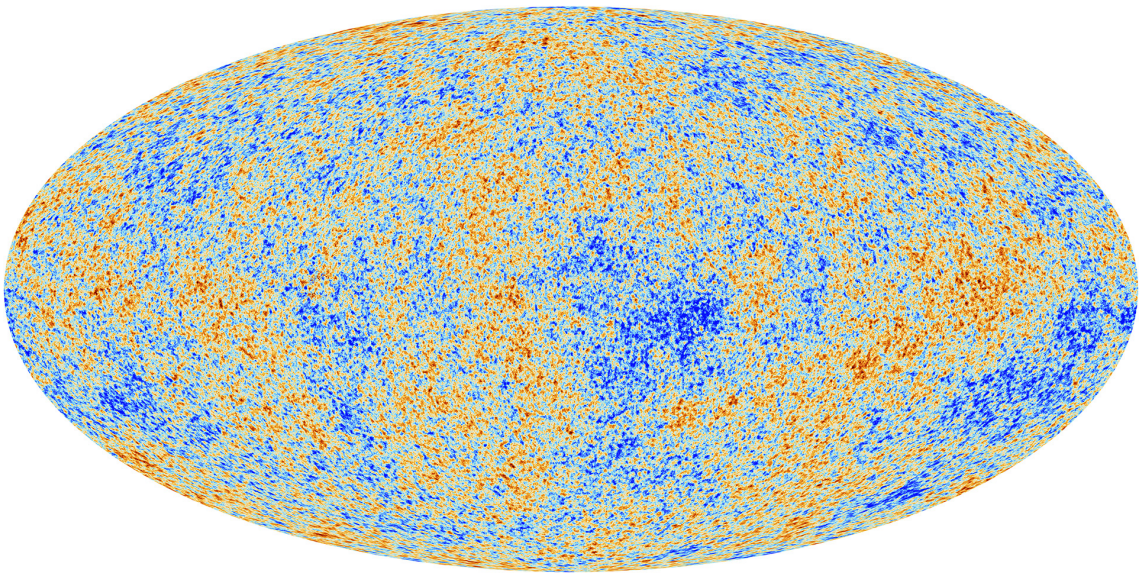

Figure 1.2 – The cosmic microwave background under a Mollweide projection[2]. This relic radiation corresponds to the *first light* of the universe. It corresponds to the emission of a black body and is isotropic throughout the sky with variations of the order 10^{-5}. It strengthened the hypothesis of the Big Bang and enabled the computation of the proportion of dark energy, dark matter, and baryonic matter in the universe. Image from Planck/ESA.

can be described by its power spectrum, a unique spectral fingerprint from which cosmological parameters can be constrained.

1.1.3 Dark ages and the reionisation

Three million years after the CMB radiation was emitted, there was almost no new source that could produce light (except rare 21 cm emission from hydrogen atoms), and the CMB peak wavelength shifted to non-visible wavelengths, leaving the universe in the dark. Thus, this period is referred to as the *Dark ages*. With time, gas collapsed to form the first stars and galaxies. These emitted photons are energetic enough to ionise the neutral hydrogen in the universe. This process is called reionisation (it is the second phase transition of the universe, the first being recombination). It started between $250-500$ Myr after the big bang and lasted until the universe was fully ionised at ~ 1 Gyr. This period is at the limit of what we can observe and is of great interest, as the sources of ionising radiation are still under debate, and simulating it is a challenge for numerical models. To illustrate that, we define the escape fraction, which is the fraction of photons able to escape their host galaxy. While analytical models often require an escape fraction of $\sim 20\%$ to reionise the universe, observations of galaxies in the local universe find escape fractions of $\sim 1-3\%$. Learning more about the processes involved in galaxy formation is thus critical to understanding this discrepancy.

1.2 The ΛCDM model

Having now a broad picture of how the universe expanded, we halt our description of the formation of structures to describe the content of the universe at this point. We do so by presenting the concordance cosmological model, the ΛCDM model, which describes its content and its evolution.

1.2.1 An expanding universe

In 1927, Georges Lemaître predicted and observationally confirmed (Lemaître, 1927, 1931) that the further the observed galaxies were from us, the more their spectrum was shifted towards redder wavelengths due to the Doppler effect, i.e. the faster they were moving from us. The growing separation of galaxies observed does not come from their proper motion, but rather from space itself extending. Similarly to a cookie dough expanding in the oven and pushing each chocolate chip further from one another, the universe is expanding and pushing galaxies further and further apart from one another. This expansion accelerates with time and stems from energy which we refer to as the *dark energy*. The dark energy can be described as a scalar field such as quintessence (Ratra & Peebles, 1988; Wetterich, 1988) or as a constant, as used in the ΛCDM model and noted with the variable Λ.

As the universe expands, a given physical distance expands with time. Thus, we can write the physical coordinates $\mathbf{r} = a(t)\mathbf{x}$. $a(t)$ is the *expansion factor* and $\mathbf{x}$ are the comoving coordinates, i.e. the coordinates in which the object is at rest with respect to the expansion. If we then consider the corresponding speed, we obtain $\mathbf{v} = d\mathbf{r}/dt = \dot{a}/a\mathbf{r} + a\dot{\mathbf{x}}$. In honour of Hubble who observed this result in 1929, we refer to the flow that describes the expansion of the universe, $\dot{a}/a$, as the Hubble flow, noted $H(t)$. $\mathbf{u} = a\dot{\mathbf{x}}$ corresponds to the peculiar speed of the object considered. We use the subscript 0 to denote current values. For example, the Hubble constant H_0 is the current expansion rate of the universe.

1.2.2 Dark matter

Another key component to describe the universe is the presence of non-visible matter permeating the universe. Its presence was initially hypothesised by William Thomson in 1884 (Kelvin, 1904), using the velocity dispersion of stars in the Milky Way. Unlike stars, this matter cannot be observed directly and is thus called *dark matter* (from Henri Poincaré describing it as a *matière obscure*). Strong evidence for the existence of dark matter is provided by galaxy rotation curves. If computed through a Keplerian approach, the expected galaxy rotation curve should exhibit a decline when going far from the galaxy (see orange curve in Fig. 1.3) as the amount of visible matter rapidly drops to zero. However, the value observed in galaxies plateaus from a certain distance to the centre (in green). The most straightforward explanation is to question one of the main ingredients of the modelling, which is the mass profile of matter in the galaxy. By adding another mass component (corresponding to the red curve), the analytical computation can derive results matching observations.

This explanation is the most commonly accepted and has been confirmed through many other means, one of the strongest constraints being gravitational lensing.

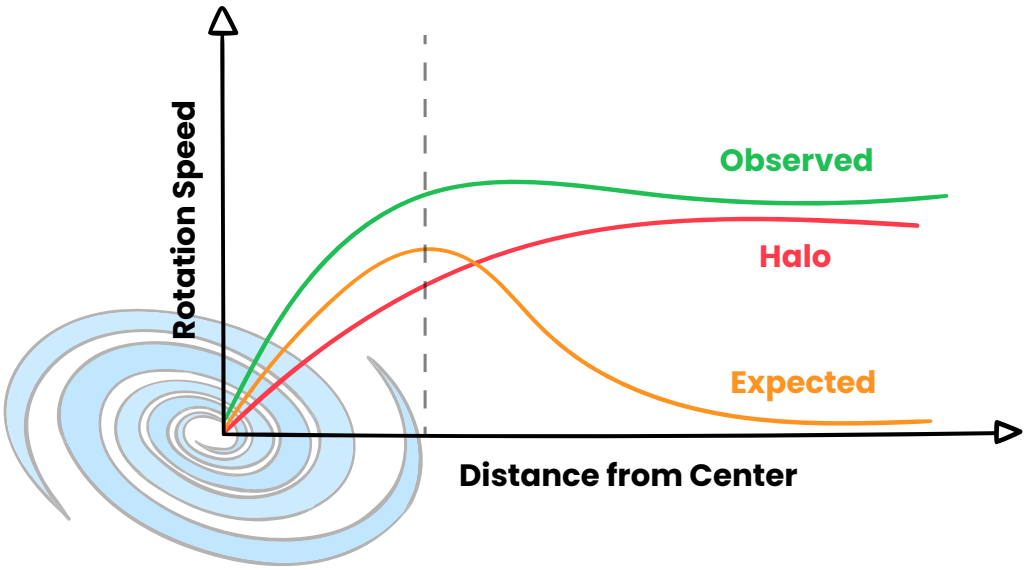

Figure 1.3 – Illustration of a galaxy rotation curve as a function of the distance to the centre of the galaxy. We superpose the image of a galaxy behind it to illustrate how we expected the rotation speed to decrease from the galaxy's edge (in orange). There is a discrepancy between this prediction only considering the gravitational potential of luminous matter and observations (in green). By adding a complementary mass component (in red) and dark matter, mathematical predictions can match observations.

Gravitational lensing is a phenomenon in which massive systems curve spacetime and bend the originally straight trajectory of light. Through gravitational lensing modelling, the mass distribution of clusters can be inferred precisely. Then, by comparing it to the mass of visible matter, the location of dark matter can be found and was confirmed in many cases.

Some alternative models try to answer the discrepancy found between galaxy rotation curves observed and computed without dark matter by instead modifying physical laws, such as the Modified Newtonian dynamics (MOND) (Milgrom, 1983). There, Newton's second law of dynamics is modified by adding an interpolating function. However, this approach is challenged by gravitational lensing. A very powerful constraint comes from collisions of galaxy clusters, such as the bullet cluster. If MOND was correct, observations made with lensing would find that all of the mass is where the gas is. However, such observations find that most of the mass is in a distinct region from the gas. Also, the second region of mass (the dark matter) passes by the gas without being impacted by it other than through gravitational interactions. This exhibits a second property of dark matter which is that it interacts at most weakly through collisions. Models consider different flavours of dark matter, describing it as either cold or warm (Peebles, 1982; Bond et al., 1982; Blumenthal et al., 1982) depending on how massive the particles constituting it are and how fast they propagate (Silk, 2000; Paduroiu, 2022). There are also different hypothetical definitions for the constituents of this matter, such as weakly interacting massive particles (WIMPs). Currently, the accepted model is that of cold dark matter (CDM), i.e. massive particles.

1.2.3 The cosmic web

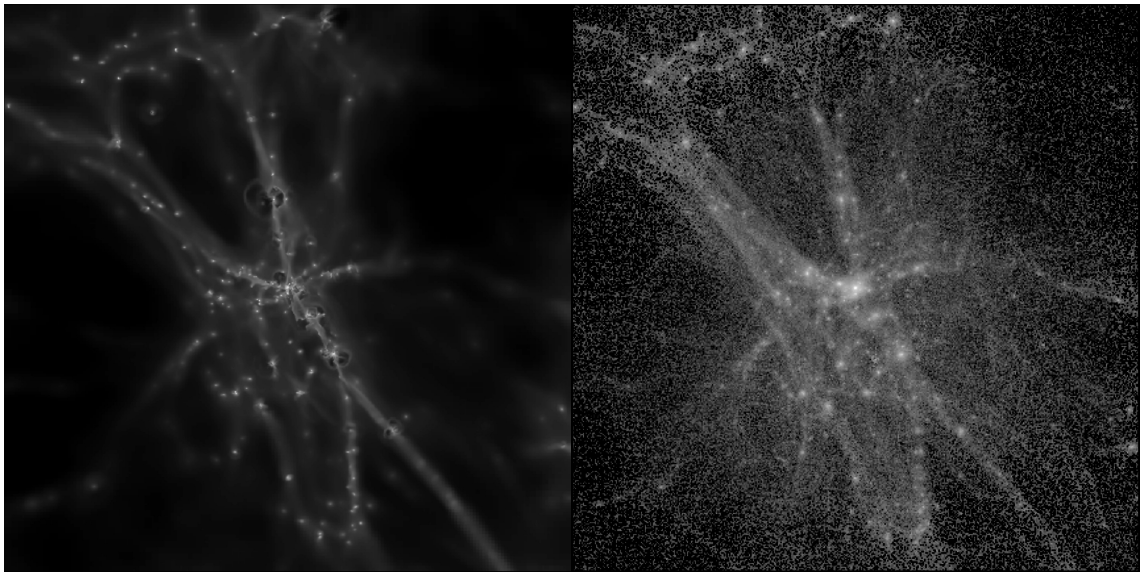

Figure 1.4 – Density-weighted projection of the gas density (left panel) and surface density of dark matter (right panel). Both of these images are taken at redshift $z \sim 3.7$ from the simulation KI_HR in Sec. 5.2. This shows the filamentary structure of both gas and dark matter. Galaxies are in the brighter clumps of both maps. They are located in the filamentary structure and fall towards the node at the centre of this structure. This node is where the most massive galaxy of the simulation is located. The maps are different due to the different nature of the gas and dark matter in simulations (see Sec. 2.2). In the left panel, the gas is traced through cells. In the right panel, dark matter is traced through particles. The lower density of points at the edges of the image (see the top right of the right panel) is due to the simulation being a zoom (see Sec. 2.1). These particles are *low resolution* particles and trace more mass than those in the inner regions. Less low-resolution particles are needed to trace the same mass as high-resolution particles.

The primordial density fluctuations inferred from the CMB describe both baryonic matter and dark matter. After the recombination, the matter is thus not distributed homogeneously at small scales and is only subject to gravitation. Regions with a slightly higher density also have a higher gravitational potential. With time, matter falls into these gravitational potential wells, leading to even deeper gravitational potential wells. This induces the accretion of more matter and so forth. In this manner, the distribution of matter in the universe gets structured into filaments and nodes. This structure is the cosmic web. It describes both the distribution of gas and dark matter on large scales. We show it for gas and dark matter in Fig. 1.4. In filaments, the gas cools down to form galaxies. Small galaxies then fall towards the nodes of the structure, which often host a more massive galaxy. All of these galaxies are embedded in a dark matter halo which is significantly more massive than they are.

1.2.4 Composition and curvature

Dark energy (Λ) and cold dark matter (CDM) fashion together the current formalism describing the universe, the ΛCDM model. It can be described by six free and independent parameters chosen to be the baryon energy density[4], the dark matter energy density, the age of the universe, the scalar spectral index n_s (describing the primordial density fluctuation spectrum), the curvature fluctuation amplitude, and the reionisation optical depth for electron scattering. Other cosmological parameters are either fixed, constrained by non-cosmological observations or derived from these six parameters and could have been chosen as fundamental parameters instead. Assuming the cosmological principle (a spatially homogeneous and isotropic universe) and using the Friedmann–Lemaître–Robertson–Walker metric, it can be shown that there is a relation between the different energy density components of the universe, given by

$$\frac{H^2}{H_0^2} = \Omega_{0,\mathrm{R}} a^{-4} + \left(\Omega_{0,\mathrm{b}} + \Omega_{0,\mathrm{DM}}\right) a^{-3} + \Omega_{0,\mathrm{k}} a^{-2} + \Omega_{0,\Lambda}. \tag{1.1}$$

$\Omega_{0,\mathrm{X}} = \rho_{\mathrm{x}}(t)/\rho_{\mathrm{c}}$ is the energy density parameter of X, with $\rho_{\mathrm{c}} = 3H^2/8\pi G$ the critical energy density of the universe (the average energy density of an exactly flat universe). $\Omega_{0,\mathrm{R}}$ corresponds to the radiation density parameter, which is of the order $\Omega_{0,\mathrm{R}} \sim 10^{-4}$. $\Omega_{0,\mathrm{DM}}$ and $\Omega_{0,\mathrm{b}}$ respectively describe the content of the universe in dark matter and in *baryonic* matter. $\Omega_{0,\Lambda}$ is the density parameter of dark energy (assumed to be a constant here) and lastly, $\Omega_{0,\mathrm{k}}$ describes the curvature of the universe. k has a value of -1 for hyperbolic, 0 for flat and $+1$ for spherical and $\Omega_{0,\mathrm{k}}$ can take any value (1 corresponding to a flat curvature). The latest values obtained from the Planck collaboration (Planck Collaboration et al., 2020) give $H_0 = (67.4 \pm 0.5)\ \mathrm{km\,s^{-1}\,Mpc^{-1}}$, and

$$\Omega_{0,\mathrm{DM}} = 0.26 \quad \Omega_{0,\mathrm{b}} = 0.049 \quad \Omega_{0,\mathrm{k}} = 0.001 \pm 0.002 \quad \Omega_{0,\Lambda} = 0.6847 \pm 0.0073.$$

From these observations, the content of the universe is flat, infinite (non-positive curvature) and mainly composed of dark energy ($\sim 68.8\%$), dark matter ($\sim 26.1\%$) and baryonic matter ($\sim 4.9\%$).

1.3 What is a galaxy ?

We have now presented key elements of the cosmological model. A fundamental assumption is the cosmological principle, as we assume the universe to be homogeneous and isotropic. The main energy constituents of this universe are dark energy, dark matter and baryonic matter. Dark energy causes the universe to expand, and dark matter is a non-visible component permeating it, interacting mainly gravitationally. Baryonic matter follows the gravitational potential of dark matter to form the cosmic web but is able to lose its energy by cooling down. Gas can then form smaller structures such as galaxies. In this section, we describe what are the constituents of galaxies and some of their properties.

[4]In astrophysics, *baryonic matter* is a language misuse and also includes electrons even though they are fermions. This term encompasses all the ordinary matter.

1.3.1 A gravitationally bound system

We have seen that galaxies, congregations of stars, are embedded in a dark matter halo. We often describe the mass or radius of haloes by considering the matter gravitationally bound to them. To do so, we rely on the virial theorem, which equates the kinetic energy of a system to its potential energy neglecting surface terms. It is simply written as $\overline{T} = -\overline{U}/2$, with $\overline{T}$ and $\overline{U}$ the average kinetic energy and the average potential energy of the system. From this, if we consider the halo as a uniform sphere, a relation between the mass of the system and its radius can be obtained as

$$\frac{3}{5}\frac{GM}{R} = \frac{3}{2}\frac{k_{\rm B}T}{m_{\rm p}}, \tag{1.2}$$

with G the gravitational constant, M a mass contained within a radius R, $k_{\rm B}$ the Boltzmann constant, T the temperature, and $m_{\rm p}$ the mass of a proton. We then define the virial radius $R_{\rm vir}$ (and the virial mass $M_{\rm vir}$) of this system by computing the radius (or the mass) within which the virial theorem holds. I have found that during the early stages of galaxy formation in simulations, this radius varies significantly and could differ depending on the underlying models used. Instead, I characterise haloes by $\rm R_{200}$, which is the radius within which the total density of the medium (including dark matter) is $200\rho_c$. This value comes from the typical characterisation of collapsed dark matter haloes through their overdensity compared to the background density which is approximately 200 using a spherical top-hat model (Peebles, 1980). $\rm M_{200}$ is the corresponding mass.

1.3.2 Gas

Gas in galaxies is located between stars, and we thus refer to this medium as the interstellar medium (ISM). The ISM plays a crucial role in galaxy evolution as it contains the gas fuelling star formation, ultimately dictating the evolution of the galaxy. However, the edges of a galaxy are diffuse and not trivial to define. In this work, we define the ISM as all the gas comprised within 0.1 $\rm R_{200}$ (Mo et al., 1998).

As it hosts a vast range of physics, the ISM hosts extreme temperatures and densities ranging respectively over more than six and ten orders of magnitude. Depending on these two quantities, the ISM can be separated into different components, which we detail in table 1.1.

Complementary to the ISM, a very important place to understand galaxy evolution is the CGM, the close surroundings of the galaxy. We define it as gas within $0.1 - 1$ $\rm R_{200}$. This is a medium relatively devoid of stars (compared to the galaxy), composed of hot gas ejected by supernovae and cold gas accreted by cosmic filaments, leading to a complex multiphase state.

1.3.3 Stars

Having characterised the gas content of galaxies, we now describe how gas can turn into stars. We then describe briefly stellar evolution and the last stages which stars go through, as they are crucial for galaxy evolution.

Table 1.1 – The different ISM phases and their density, temperature, volume fraction and the most common techniques through which they can be observed. Molecular clouds are mostly made up of H_2 and are the birthplace of stars. They are typically observed through CO, as the ratio between CO and H_2 is thought to be constant and H_2 is difficult to observe directly. Stars can ionise their surrounding medium, which was initially cold, to temperatures around 10^4 K. After their last evolutionary stages, they can even heat this medium to temperatures higher than 10^6 K. We detail these processes in the next paragraphs.

Phases	Density [cm^{-3}]	Temperature [K]	Volume [%]	Observations
Molecular clouds	$10^2 - 10^6$	10^1	~ 1	CO line
H II regions	$10^2 - 10^4$	10^4	< 1	Hα
Cold neutral medium	$10^0 - 10^3$	$10^1 - 10^2$	$1 - 5$	H I (21 cm)
Warm neutral medium	$10^{-1} - 10^1$	$10^3 - 10^4$	$30 - 60$	H I (21 cm)
Warm ionised medium	10^{-1}	$10^3 - 10^4$	~ 20	Hα
Hot ionised medium	$10^{-4} - 10^{-2}$	$10^5 - 10^7$	$20 - 50$	X-ray/UV lines

A star is born

As gas falls under the effect of gravity, it shapes into cool clouds. Under these conditions, hydrogen atoms can combine and form molecular hydrogen, H_2. We refer to these clouds as molecular clouds. Due to their low temperature ($T \sim 10 - 20$ K) and high density ($n_H > 100$ cm^{-3}), they present ideal conditions for star formation (Kennicutt & Evans, 2012; Girichidis et al., 2020). Indeed, star formation is dictated by a competition between gravitation and internal pressure pushing gas outward. Additional pressure supports such as turbulence or magnetisation (Elmegreen & Scalo, 2004; Scalo & Elmegreen, 2004) can also play a role in this competition. When the pressure support becomes insufficient, molecular clouds undergo gravitational collapse (Prialnik, 2000). For each protostellar cloud formed (smaller clouds that will form each star), the pressure will first disassociate H_2 in its inner regions. With time, the pressure in the inner regions of the cloud will increase and reach values so high that nuclear fusion will begin and form elements heavier than hydrogen and helium. As molecular clouds typically collapse at masses of $10^2 - 10^3$ $M_\odot$, they form many stars at the same time. We refer to a group or cluster of stars that formed together as a Single Stellar Population (SSP).

Depending on the state of the molecular cloud and the time at which the SSP formed, stars can be more or less massive and have different metallicities[5]. The distribution of stellar masses formed in an SSP is described by an Initial Mass Function (IMF). We show in the left panel of Fig. 1.5 examples of different IMFs inferred from observation. This shows the number of stars in a given mass range, and that there are significantly more low-mass stars than there are massive stars. This distribution is very important to model the later stages of stellar evolution in simulations, as only more massive stars turn into type II supernovae.

[5]In astrophysics, since most of the universe is made of hydrogen and helium, we define as metals all elements heavier than helium.

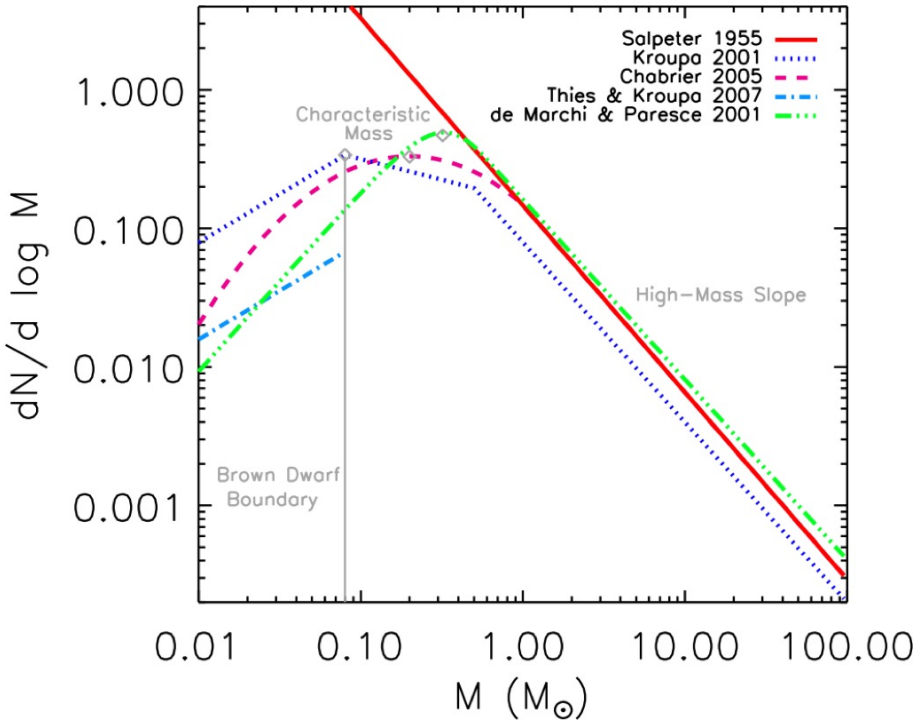

Figure 1.5 – Initial mass functions, representing the distribution of the number of stars in a single stellar population as a function of their masses. We show here that most stars are slightly less massive than the sun, with a large fraction of them being at the low mass end. Stars that will undergo a supernova have a mass typically higher than ~ 10 $M_\odot$, and only represent a small fraction of the stellar population. Most stars will expand into red giants, and expel their outer layers without exploding. Graph extracted from Offner et al. (2014).

Stellar life

Stellar evolution consists of the formation of heavier and heavier elements from hydrogen and helium. This process is called stellar nucleosynthesis. We illustrate it in Fig. 1.6. This example does not describe all stars, but only the most massive ones. Less massive stars will not be able to form elements as heavy as massive stars (which typically form elements up to iron) but are nonetheless important to form elements such as carbon.

Young blue stars (O and B stars) emit very energetic radiation which can ionise the neutral hydrogen surrounding them. This radiation heats the gas and generates an outward pressure, acting as pre-supernova feedback (see Sec. 1.3.4). Such processes can hinder star formation and greatly impact the evolution of the galaxy. These regions, called H II regions, are modelled as Strömgren spheres, with a typical radius

$$R_{\rm st} = \left(\frac{3 N_{\rm ph,sn}}{4\pi \ 2.6 \times 10^{-13} \, n_{\rm H}^2} \right)^{1/3}, \tag{1.3}$$

with $N_{\rm ph,sn}$ the rate of ionising photons in the cell.

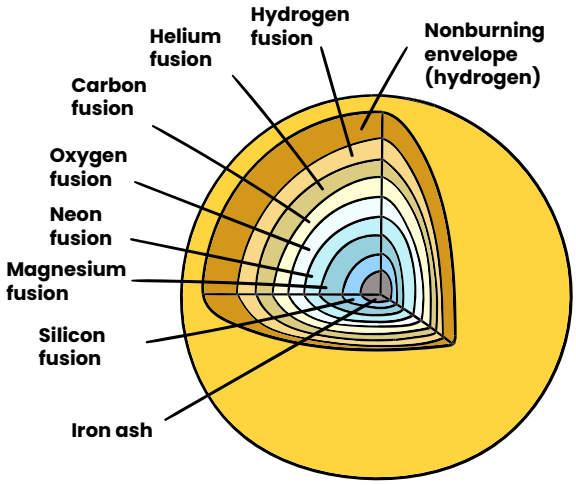

Figure 1.6 – Illustration of the composition of a massive star and stellar nucleosynthesis. During their life, stars produce heavier and heavier elements at their core, up to iron for the most massive stars. This leads to an onion structure with heavier elements in the centre and lighter elements in the outer parts up to the hydrogen envelope.

Death stars

The lifetime of a star depends on its initial mass and its metallicity. The heavier a star, the faster it will burn its fuel and the faster it will die. Although massive stars explode after a few million years, very low-mass stars such as red dwarfs would take trillions of years to cease their hydrogen fusion. However, there is no observation of red dwarves in their advanced stages, as the universe is too young for them to have reached this stage (Adams et al., 2004). In this section, we concentrate on low-mass stars (up to ~ 10 $M_\odot$) and massive stars (from ~ 10 $M_\odot$).

Once low-mass stars are in their latest stages, they expand into red giants and expel their outer layers (forming *planetary nebulae*). The inner part of the stars cools down, leaving an extremely dense core, a white dwarf, with a size similar to the Earth but a mass comparable to that of the Sun.

Massive stars and specific binary systems can finish their evolution through events significantly more extreme than their single low-mass counterparts: supernovae. They are split into two types depending on their origin. The first are Type Ia supernovae (SNIa). They typically happen in binary systems of $3 - 16$ $M_\odot$ (Raiteri et al., 1996). In such systems, the more massive star evolves faster than the other one and eventually leaves a white dwarf. White dwarfs are held together by electron degeneracy pressure[6] and the maximum mass for which they can sustain themselves is approximately the Chandrasekhar mass, 1.44 $M_\odot$ (Lieb & Yau, 1987). A hypothesis for the cause of the supernova is that by accreting gas from its companion, the white dwarf will exceed this mass and collapse on itself, exploding into a supernova and

[6]From Pauli exclusion principle, fermions cannot be in the same quantum state. This creates a pressure resisting against the compression of matter.

leaving a neutron star[7]. This process is referred to as a thermonuclear supernova. SNIa are often neglected in galaxy formation numerical simulations, as they are believed to only represent a small fraction of all supernovae. Direct measurements of SNIa from star formation rate (Dahlen et al., 2004; Scannapieco & Bildsten, 2005; Sullivan et al., 2006) find that SNIa occur in $8-18\%$ of stars within $3-8$ $M_\odot$, and numerical predictions lead to SNIa fraction of $5-9\%$ (Few et al., 2014). However, estimations based on abundance ratios find larger fractions of $11-40\%$ (de Plaa et al., 2007; Maoz, 2008).

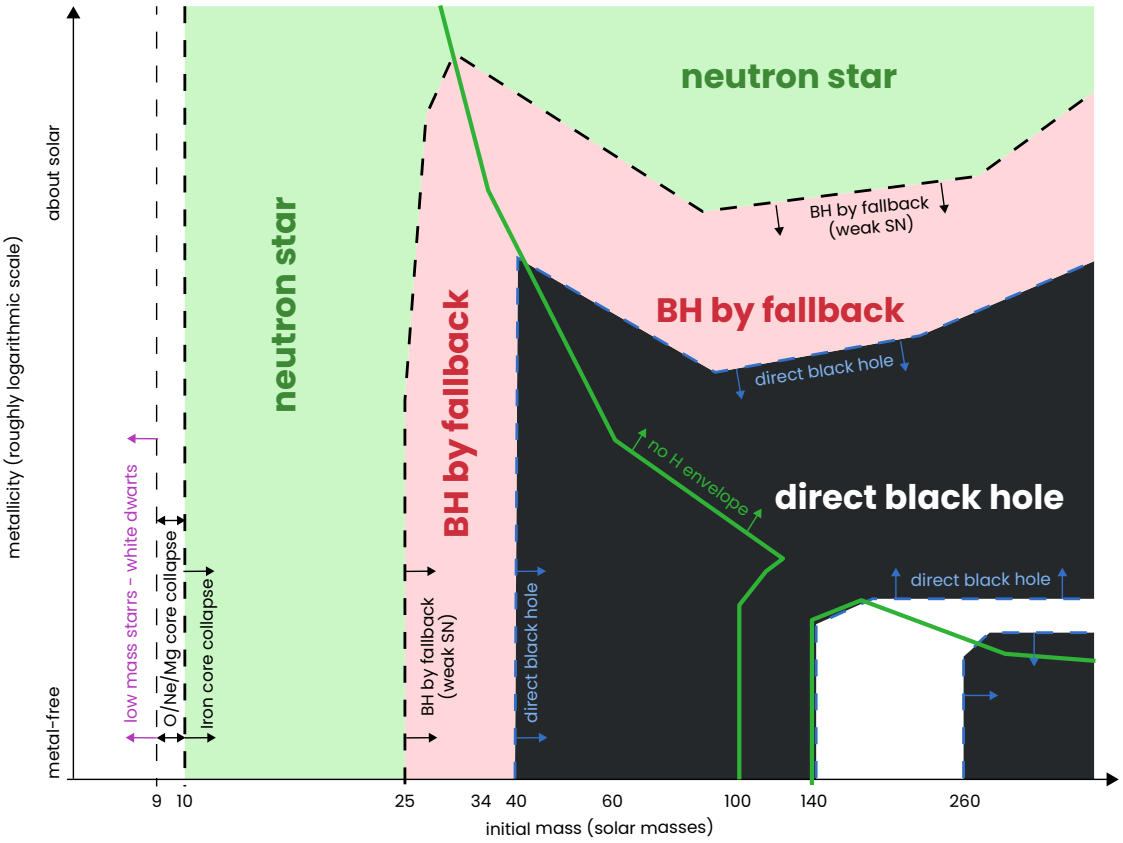

Figure 1.7 – Final state of the supernova progenitors, depending on their initial mass and metallicity. All stars with masses lower than ~ 10 $M_\odot$ end up as white dwarfs independently of their metallicity. More massive stars end up either as neutron stars or black holes, depending on both their initial mass and their metallicity. Figure adapted from Heger et al. (2003).

The main type of supernovae are Type II supernovae (SNII). This process can be ignited as early as after 3 Myr for the most massive stars, while 8 $M_\odot$ stars can sustain nuclear fusion for more than 40 Myr. As iron is the element with the highest binding energy, stars cannot form heavier elements through fusion. Once massive stars synthesise it, they will form an iron core that will grow with time. The only process preventing the core from collapsing is the electron degeneracy pressure.

[7]This view is challenged by recent models which hypothesise that the Chandrasekhar mass is almost reached but that before that, the rise in temperature of the core favours a deflagration caused by carbon fusion

When the core reaches the Chandrasekhar mass, it is disrupted and collapses on itself, turning iron into neutrons and neutrinos[8]. The neutrinos are not interacting strongly with matter and can thus escape freely from the collapsing core. By doing so, they reduce the energy in the core, accelerating the collapse. The core is hence separated from the layers of the star, which lose their inner pressure support and also collapses. As they cannot collapse further than the dense core created, they bounce back on it and form an expanding shockwave. These supernovae are referred to as core-collapse supernovae. For masses lower than ~ 20 $M_\odot$, the core forms a neutron star, while for more massive stars, it typically becomes a black hole (depending on its metallicity), as shown in Fig. 1.7. For stars more massive than 50 $M_\odot$, the remnant is however subject to more uncertainty.

Supernovae eject a few solar masses of material[9] at velocities of a few percent of the light speed and heat the medium surrounding them. This greatly impacts galaxy evolution by hindering star formation and removing gas that could form stars. The typical energy of supernovae is 10^{51} erg (Kasen & Woosley, 2009; Pejcha & Prieto, 2015). These events are so powerful that their luminosity can shortly match that of their host galaxy.

The four stages of a supernova

When a star turns into a supernova, a blastwave is formed and expands in the surrounding media, we refer to it as a supernova remnant (SNR). Its evolution can be described in four phases (Reynolds, 2008), which we describe in the next paragraphs and in Fig. 1.8.

- Free expansion
  The first phase is the free expansion of a supersonic blastwave. We illustrate it through the 3 panels of Fig. 1.9. As the ISM pressure is far lower than that of the pressure from the ejecta, the ejecta expands freely and forms a shockwave[10] (panel 1). This shock-wave compresses the ambient medium, accumulating gas behind itself (but in front of the ejecta). This gas is separated from the shockwave by a contact discontinuity[11] (panel 2). By shocking the ambient medium, a reverse shockwave also develops and heats the ejecta to high temperatures while slowing it down. As more gas accumulates behind the wavefront, the gas swept up eventually gets comparable to that of the shocked ejecta and a reverse shockwave forms (panel 3).

- Adiabatic phase
  The reverse shockwave heats the gas in the inner regions to temperatures high enough so that radiative losses are negligible. Thus, this phase can be considered an energy-conserving, pressure-driven blastwave. It can be described by the self-similar solution to the problem of an adiabatic explosion in a medium with negligible pressure, found by both Taylor (1950) and Sedov (1959).

[8] Particles interacting only via the weak nuclear force and gravitation.

[9] Remnants of the star as well as more massive elements synthesised during the supernova.

[10] A shockwave is a pressure front moving faster than the sound speed. This makes the surrounding medium unable to react and causes a sharp pressure discontinuity called the shock front.

[11] A contact discontinuity corresponds to a discontinuity between two phases with the same pressure and velocity but a different density

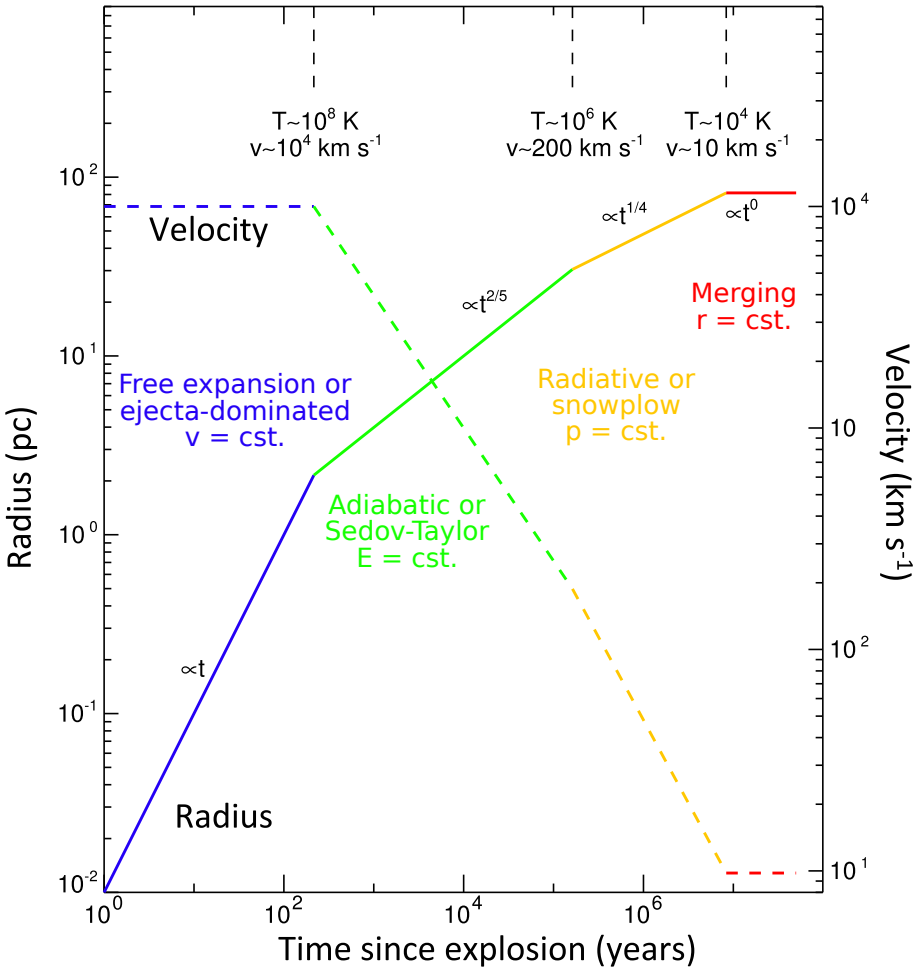

Figure 1.8 – Radius (full lines) and velocity (dotted lines) of a supernova as a function of the elapsed time after the explosion. The four colours describe the four phases of the supernova evolution: the free expansion phase (blue), the adiabatic phase (green), the radiative phase (yellow), and the merging phase (red). Figure adapted from Micelotta et al. (2018).

- Radiative phase
  By expanding, the SNR cools adiabatically (i.e. only due to its expansion) until it reaches a critical temperature at which ionised atoms can recombine with free electrons. This process allows atoms to lose energy through radiation, making radiative losses significant. As the SNR cools, gas accumulates into a thin, dense shell, surrounding a hotter interior where radiative loss remains negligible. If this interior does not cool, it provides pressure support, allowing the supernova to continue its expansion. Once the hot interior cools, the shell continues its expansion in a momentum-conserving way (what is lost in speed is gained in mass). Therefore, this phase is also called the snowplow phase.

- Merging phase
  Finally, as the velocity of the SNR decreases, it reaches the turbulent velocity of the ISM and fragments. These hot fragments then likely merge with the cold ISM through Rayleigh–Taylor instabilities. The final remains of the kinetic and thermal energy from the SNR fuel turbulence in the ISM.

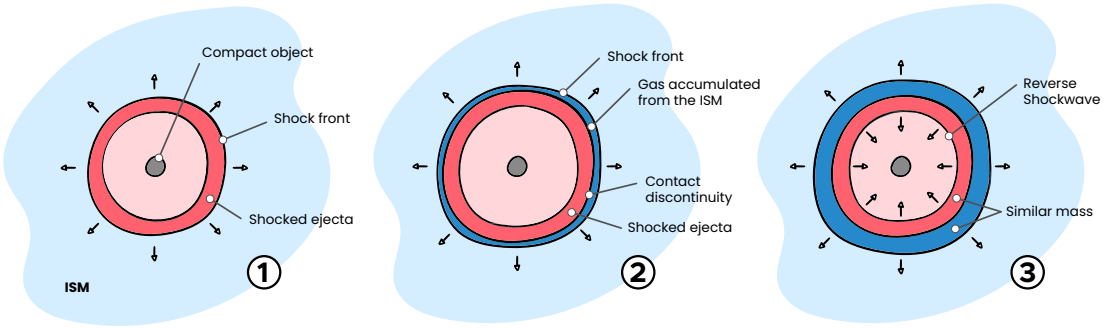

Figure 1.9 – Illustration of the expansion of a supernova during the first ejecta-dominated phase up to the transition to the adiabatic phase. The first panel shows the earliest stages of the supernova, where no mass has been swept up yet from the ISM. The second panel illustrates how gas accumulates behind the shock front but in front of the shocked ejecta, forming a contact discontinuity. The last panel shows that while expanding, the supernova shell accumulates more and more mass from the ISM until it eventually reaches a mass comparable to that of the ejecta. At this moment, a reverse shock wave forms and heats the inner region of the supernova remnant.

Active galactic nuclei and quasars

We have seen how stellar black holes are formed, but some black holes have masses higher than 10^6 $M_\odot$. These supermassive black holes (SMBH) are typically found in most massive galaxies (Merritt, 2013) and play a very important role in their evolution. They have also recently been found to populate galaxies of lower masses and might impact their evolution as well (Miller et al., 2015; Mezcua et al., 2016; Lemons et al., 2015). Their origin is still debated, possibly being early stellar black holes which have grown through time by accreting gas and merging with other stellar black holes. A small fraction of SMBHs present an accretion disc around them, and, when accreting matter, generate powerful jets. As for their formation, the origin of this jet is still debated. An explanation is that while twirling around the galaxy, charged particles within the gas produce an extremely strong magnetic field. By being dragged by the rotating SMBH, this magnetic field shapes into a tight cone perpendicular to the accretion disc. This cone can then accelerate particles to relativistic speeds (Okamoto, 2006). Another one is that the rotation of the SMBH can extract energy from infalling matter while ejecting part of it at a higher speed (Penrose, 2002). These jets produce strong emissions at the centre of the galaxies and are referred to as active galactic nuclei (AGN). The brightest objects in the universe are extremely luminous AGNs. They are generally located at high redshift and called quasars or QSO (respectively quasi-stellar radio sources and quasi-stellar objects).

1.3.4 Properties

We have seen that a galaxy is a gravitationally bound system comprised of gas, dust, stars and their by-products, and is generally embedded in a dark matter halo. They all interact together to shape what we see when observing galaxies. Cosmic dust can have important repercussions on different astrophysical phenomena and favours star formation (Zhukovska et al., 2016). As it represents only a small mass fraction of the galaxy, it is often ignored in galaxy formation simulations, as we do here. We now focus on two properties of observed galaxies, namely their morphologies and their masses.

Morphology

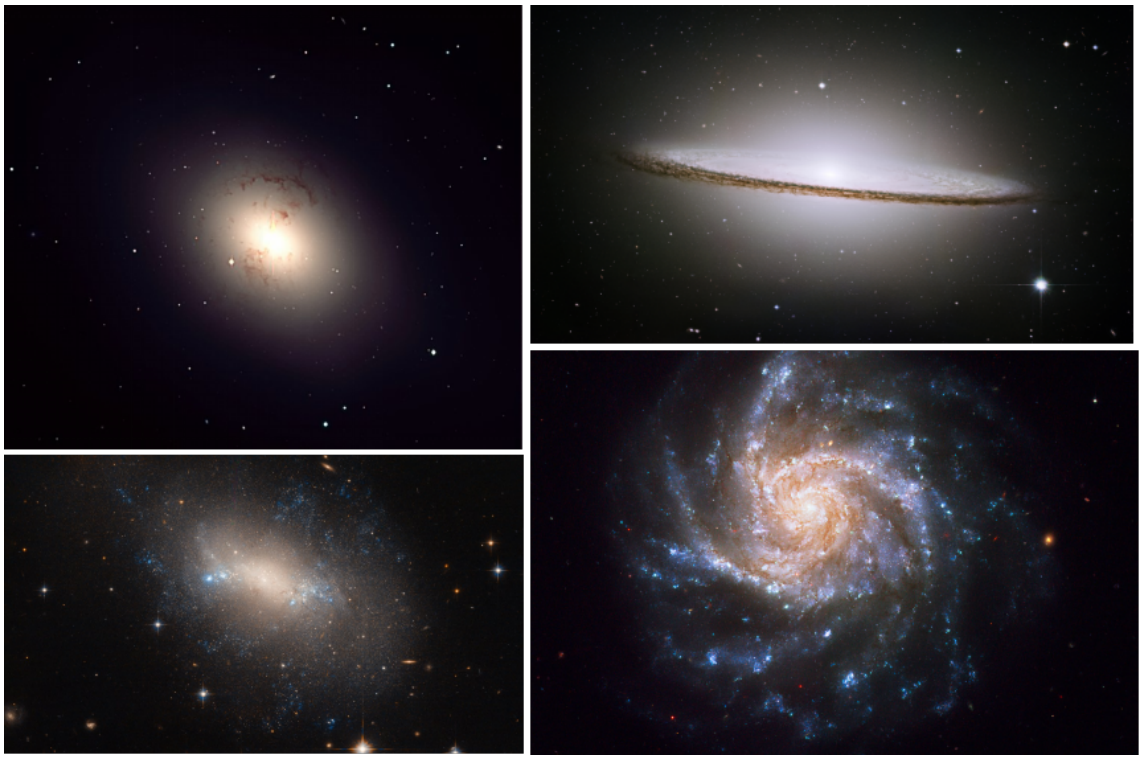

Figure 1.10 – Images of different morphology of galaxies. We show here an elliptical galaxy (NGC 1316, top left), a lenticular galaxy (M104 or the sombrero galaxy, top right), an irregular galaxy (NGC 2337, lower left), and a spiral galaxy (NGC 1376, lower right). The images are respectively extracted from ESO, NASA, ESA and ESA.

Galaxies exhibit various shapes, which can be separated into subcategories. We illustrate the variety of structures found in Fig. 1.10. The most famous classification is the Hubble sequence, developed by Edwin Hubble in 1926 and extended by Gérard de Vaucouleurs and Allan Sandage later on. They are split into four main classes.

- Elliptical galaxies: E
  These galaxies are smooth massive galaxies, generally in the form of an ellipsoid, and do not present any notable other structure (upper left panel). The

interstellar medium is relatively empty in cold gas and dust, leading to a low star formation rate. The stars are generally old stellar populations exhibiting a radial motion. Due to their spectrum, these galaxies are called *red galaxies*.

- Spiral galaxies: S
  Spiral galaxies are generally composed of a bulge of relatively old stars at their centre, surrounded by a disc. The disc is often actively forming stars, with a consequent cold gaseous content, and forms arms rotating around the bulge (bottom right panel). Almost half of spiral galaxies, such as the Milky Way, also exhibit a bar in their bulge and are called barred spirals.

- Lenticular galaxies: S0
  Between elliptical and spiral galaxies are lenticular galaxies (upper right panel). They represent a transition between these two types of galaxies and exhibit a bulge surrounded by a disc (as spiral galaxies) but no spiral arms (as elliptical galaxies). They are, however, closer to elliptical galaxies, as they present an old stellar population and a low star formation.

- Irregular galaxies: Irr
  The last major class of galaxies is the one comprising galaxies which initially did not fit in elliptical, spiral or lenticular categories (bottom left panel). They are generally star-forming dwarf galaxies rich in gas and young stars. The origin of their irregularity can be multiple. When two galaxies merge, gravitational interactions can give rise to peculiar shapes. Also, strong feedback or tidal interactions from more massive galaxies can rip gas off of smaller galaxies, making them irregular.

All of these shapes should be retrieved when doing simulations of galaxy formation. However, simulations have struggled for a long time in reproducing the whole range of morphologies found in the universe, notably the disc component of massive spiral galaxies. We briefly investigate in this work how subgrid models for star formation and feedback can impact greatly the formation of a disc in simulations.

The stellar mass to halo mass relation

The distribution of galaxies in the universe is not the same for all masses, as illustrated by Fig. 1.11. This figure shows that most galaxies are low-mass galaxies and that high-mass galaxies are more scarce in the universe. Also, elliptical galaxies (or spheroids, in red) generally dominate the most massive part of the galaxy mass function, while spiral disc-dominated galaxies (in blue) mainly contribute to the lower mass end. For comparison, the Milky Way is a barred spiral galaxy with a stellar mass of $\sim 10^{11}$ $M_\odot$ (Posti & Helmi, 2019).

In the current view of structure formation and from the primordial density fluctuations, dark matter is distributed in a web-like structure as it collapsed under its gravitational potential. In this manner, haloes and sub-haloes were formed, with gas following their gravitational potential and galaxies formed in their centre. Following this picture, there should be a strong correlation between the halo mass and the galaxy mass function presented in the previous paragraph. This is what was found in dark matter simulation, in which the distribution of halo masses in the universe

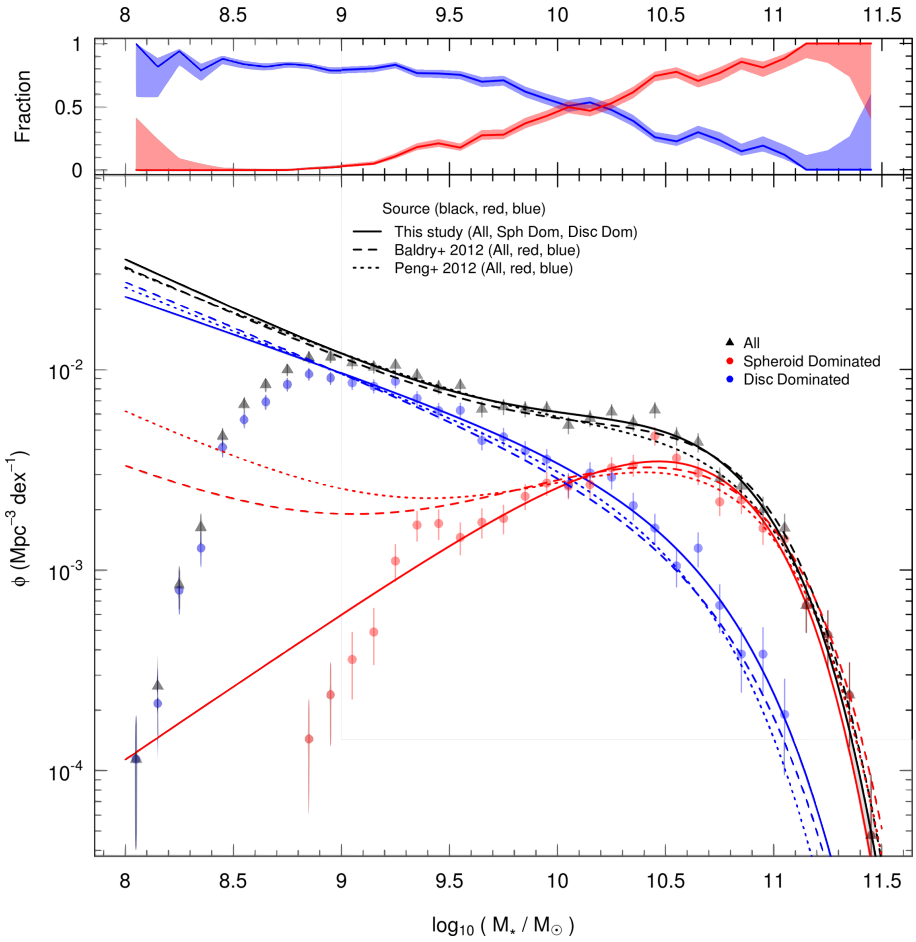

Figure 1.11 – Galaxy stellar mass function. It also shows the galaxy stellar mass function split between elliptical (red) and spiral (blue) galaxies. Figure adapted from Kelvin et al. (2014).

closely followed that of galaxies masses that we showed in Fig. 1.11. The *abundance matching technique* was thus developed, based on the correlation between these two quantities. This led to the establishment of the stellar mass to halo mass (SMHM) relation. This relation is shown in Fig. 1.12 and shows, the distribution of the stellar mass of galaxies against the mass of their host halo.

The SMHM relation is an extremely powerful tool to constrain cosmological simulations of galaxy formation. Indeed, if simulations were to only include gravitation, we would expect gas to fall alongside dark matter. Then, the mass of visible matter in galaxies divided by the dark matter mass would correspond to the universal baryon fraction (in red). However, we find that there is a discrepancy between this hypothesis and the observationally inferred curves. Observations peak at $M_*/M_h \sim 0.03$, which corresponds to $\sim 20\%$ of the baryonic mass expected with the approach including only gravitation. This underlines why more ingredients are necessary to explain the formation of galaxies, as their content is not solely driven by gravitation.

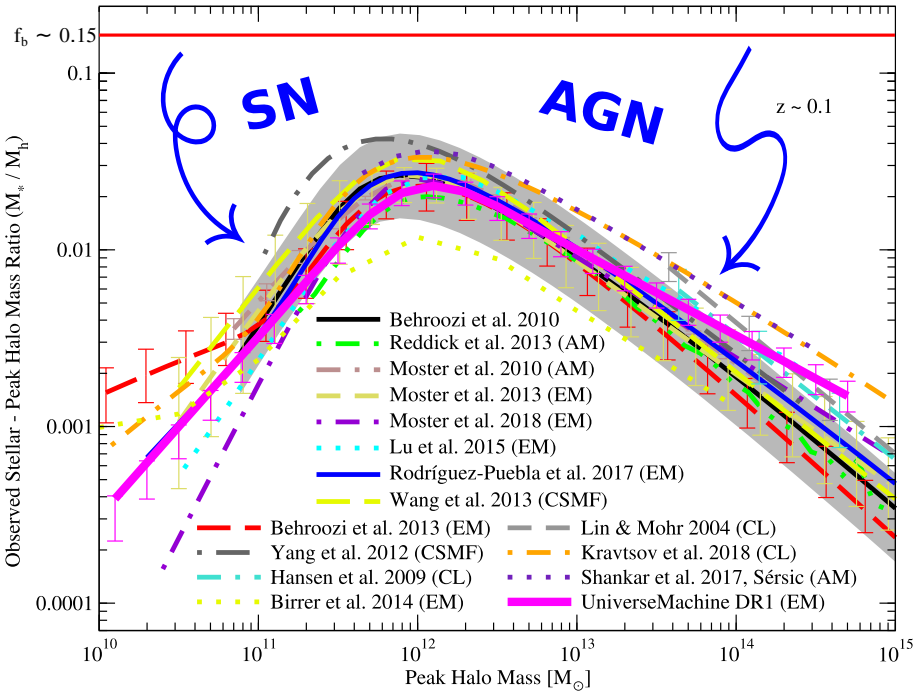

Figure 1.12 – Stellar mass to halo mass relation at redshift $z \sim 0.1$. M_* is the stellar mass and M_h is the corresponding halo mass. The dark matter mass associated with the baryonic mass is computed from a dark matter-only simulation using abundance matching. The different curves illustrate results from different studies. We indicate the universal baryon fraction by a red horizontal line. We also show the main processes invoked to explain the difference between the universal baryon fraction and the mass of baryons found in galaxies. For low-mass galaxies, the driving mechanism is SN feedback, while AGN feedback is the dominant one for high-mass galaxies. Image adapted from Behroozi et al. (2019).

Feedback processes

Processes that can explain this discrepancy are phenomena that can hinder star formation and are referred to as feedback processes[12]. Feedback can prevent filamentary accretion and/or eject gas out of the galaxy, thus removing the fuel for star formation. It can also heat or disrupt molecular clouds, inhibiting star formation at their birth sites. Feedback can be produced through different means. The most powerful are SNe and AGNs. Indeed, producing an expanding shockwave can considerably alter the local interstellar medium (ISM) and show an impact on galactic scales (Krumholz et al., 2014; Keller et al., 2020; Keller & Kruijssen, 2020). These processes transfer a considerable amount of energy in the ISM and induce turbulence (McKee & Ostriker, 1977; Mac Low & Klessen, 2004; Klessen & Glover, 2016) whilst sweeping gas away through powerful outflows. Stellar radiation in the form of either H II ionising regions (Matzner, 2002; Walch et al., 2012) or radiation pressure (Murray et al., 2005; Krumholz & Matzner, 2009), as well as stellar winds from massive stars (Dale et al., 2014) are also forms of feedback, often referred to as pre-SN feedback. These early processes can create low-density channels in the molecular

[12]Feedback refers to phenomena retroactively affecting processes which created them. In astrophysics, this typically refers to stellar processes that hinder gas collapse and star formation.

clouds in which stars are formed before they explode in a supernova. This allows the supernovae to expand more freely, sweeping less gas and consequently retaining a higher fraction of their energy for a longer time, thus increasing their impact at the galactic scale (Lucas et al., 2020).

AGNs typically reside in massive galaxies (Naab & Ostriker, 2017). Although recent observations have started to uncover AGNs in dwarf galaxies (Mezcua et al., 2016), they are expected to have less impact in low-mass galaxies, SNe being the main process that reduces the baryonic content of low-mass galaxies (Dekel & Silk, 1986; Oppenheimer & Davé, 2006). In higher mass galaxies, the gravitational potential is stronger than for low mass galaxies, and SNe are then unable to eject and unbind a significant fraction of their gas. However, it is common for galaxies of such masses to host AGNs. These AGNs are the main channel through which massive galaxies lower their baryon fraction (Silk & Rees, 1998; Benson et al., 2003). These two regimes are represented in Fig. 1.12, with the discrepancy between the red line and the observation being explained by SNe for low-mass galaxies and by AGNs for high-mass galaxies. The transition between these two regimes occurs coincidentally at the mass of the Milky Way.

1.4 How do we learn about galaxies ?

To finish this introduction, we now describe how we use light to learn more about the universe and how we combine it with theories to build our current understanding of the universe. We introduce the concepts of redshift, emission and absorption lines, and why theory relies today on numerical simulations.

1.4.1 Through light...

Until the observation of gravitational waves in 2015 (Abbott et al., 2016; Castelvecchi & Witze, 2016), the only way to look at objects as distant as stars or galaxies was through the light they emit. By simply *looking*, we learned most of what we know today about the properties of the universe. Here, we detail how light carries information and how we gain access to it.

Bringing galaxies to light

Light is an electromagnetic wave carrying energy which can be quantified and thus can be described as a particle through photons. This energy can be transmitted to electrons or atoms[13] through four main processes that will heat or cool the corresponding medium.

- bound–bound: In this process, photons are either emitted or absorbed by atoms, making them increase or decrease their energy level. This corresponds to a change of orbital for one of the electrons of the atom. The photon involved in this interaction has an energy corresponding exactly to the difference

[13] Atoms are the combination of a nucleus and electrons and can have different energies depending on the position of its electrons, defined by orbitals. Atoms connected by chemical bonds are referred to as molecules. We will only mention atoms here, since most of the gas in the universe is not in molecular form

between the two energy levels of the atom, i.e. $|\mathrm{E} = \mathrm{E}_i - \mathrm{E}_j|$, with E_i its initial state and E_j its final state. This is called bound–bound, as the electron remains attached to an atom.

- bound–free: Also called ionisation, this is a process through which an atom or a molecule can gain or lose an electron. We detail the three main processes causing it in the next paragraph.

- free–free: Also called Bremsstrahlung, this corresponds to a deceleration of a charged particle caused by a particle of opposite charge, which leads to a loss of kinetic energy through the emission of a photon. The charged particle is both free before and after the emission of radiation, and the transition is thus referred to as a free–free transition.

- Compton/Inverse Compton: Photons can scatter after interacting with a stationary charged particle. This leads to a change of energy for the photon. The inverse Compton scattering corresponds to the case where the particle gives some of its energy to the photon.

Amongst these different phenomena, we focus on ionisation, which is a key process in regulating the temperature of the universe and allowing us to observe it. When an atom loses an electron, its electric charge increases and the resulting ion is usually noted with a $^+$ for each ionisation (e.g. H^+ for hydrogen ionised once). In astrophysics, the writing convention is different, and the ionisation state of atoms is written through Roman numerals. Neutral hydrogen is written as H I, and ionised hydrogen is written as H II(which can lead to confusion with molecular hydrogen H_2 in oral communications). There are three main processes which can change the ionisation state of an atom. If a photon is absorbed by an atom, it can release one of its electrons through **photoionisation**. The atom can also lose an electron by colliding with another particle; this is **collisional ionisation**. Lastly, electrons can recombine with ions through **recombination** and thus emit a photon. Both photoionisation and recombination involve the emission or absorption of a photon. The energy of this photon corresponds exactly to the binding energy of the electron, which is characteristic of each atom. For hydrogen, this energy is 13.6 eV. For Helium, the ionisation energies are 24.59 eV and 54.42 eV (as it has two electrons, it can be ionised twice). This energy can be transcribed into a wavelength through $E = h\nu = hc/\lambda$, with h the Planck constant and λ the wavelength of the photon. We thus see that each transition corresponds to a single wavelength. By this correspondence, we can infer what gas is observed by measuring its wavelength. As an example, O I and O VI can be observed at wavelengths within $900 \lesssim \lambda \lesssim 2000$ Å while O II to O V lie within $400 \lesssim \lambda \lesssim 800$ Å and O VII and O VIII are typically at ~ 20 Å (Tumlinson et al., 2017).

Redshift

The wavelength of the photons emitted in the universe can be shifted, making some of them harder to observe. The two main processes through which this happens are the cosmological expansion and the Doppler effect (which are in essence the same). If the source of a photon with an initial wavelength λ_0 is moving away or toward us

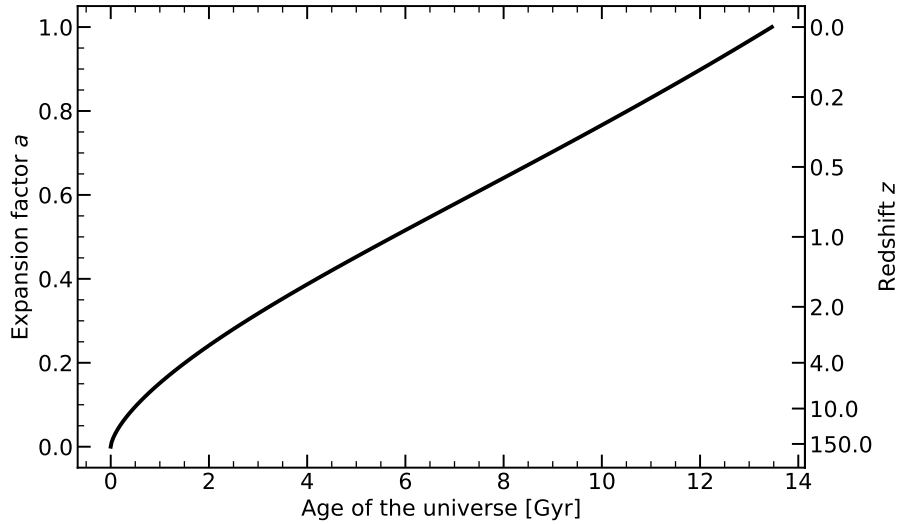

Figure 1.13 – Z against Gyr.

with a speed v, its wavelength will be shifted by $\Delta\lambda = \lambda_0 v/c$. If the source is moving closer to the observer, the photon will be *blue shifted* (toward smaller wavelengths), while if it is moving away, the photon will be *redshifted* (toward larger wavelengths). As space itself expands with time, a similar phenomenon occurs for all observations in the universe. This shifts all observed wavelengths towards higher wavelengths. The further the source is, the more the wavelength is going to be redshifted. This is what leads to the measure used to describe a given period in time in astrophysics, the *cosmological redshift*. It is defined through the variable z as

$$\frac{\lambda_{\text{obs}}}{\lambda_{\text{rest}}} = \frac{1}{a} = 1 + z. \tag{1.4}$$

λ_{rest} is the rest-frame wavelength, which was redshifted to λ_{obs} while the universe expanded of a factor a (see 1.2.4). As the rest of the thesis will use the redshift instead of the age of the universe, we show in Fig. 1.13 the correspondence between the redshift and the age of the universe.

Overall, as summarised by Fig. 1.14, different ions will trace different gas components and the wavelengths at which we observe them changes with time as the universe expands.

Emission and absorption lines

When a line is emitted, different effects can affect it so that photons will not be emitted at a single wavelength. This is called line broadening. This can be caused by several phenomena, such as natural broadening (the uncertainty of the energy of a photon from Heisenberg's uncertainty principle leads to a spread in emitted wavelengths), Doppler broadening (due to the random motion of particles at a given temperature) or even due to the instrumental noise associated with their detection.

If numerous lines are emitted, they can reach a point where they are not distinguishable and form a continuum spread across wavelengths, a spectrum (left plot in Fig. 1.15). We can access the spectrum of a light ray by dispersing the light, for example with a prism. Before reaching our telescopes, part of this light emitted

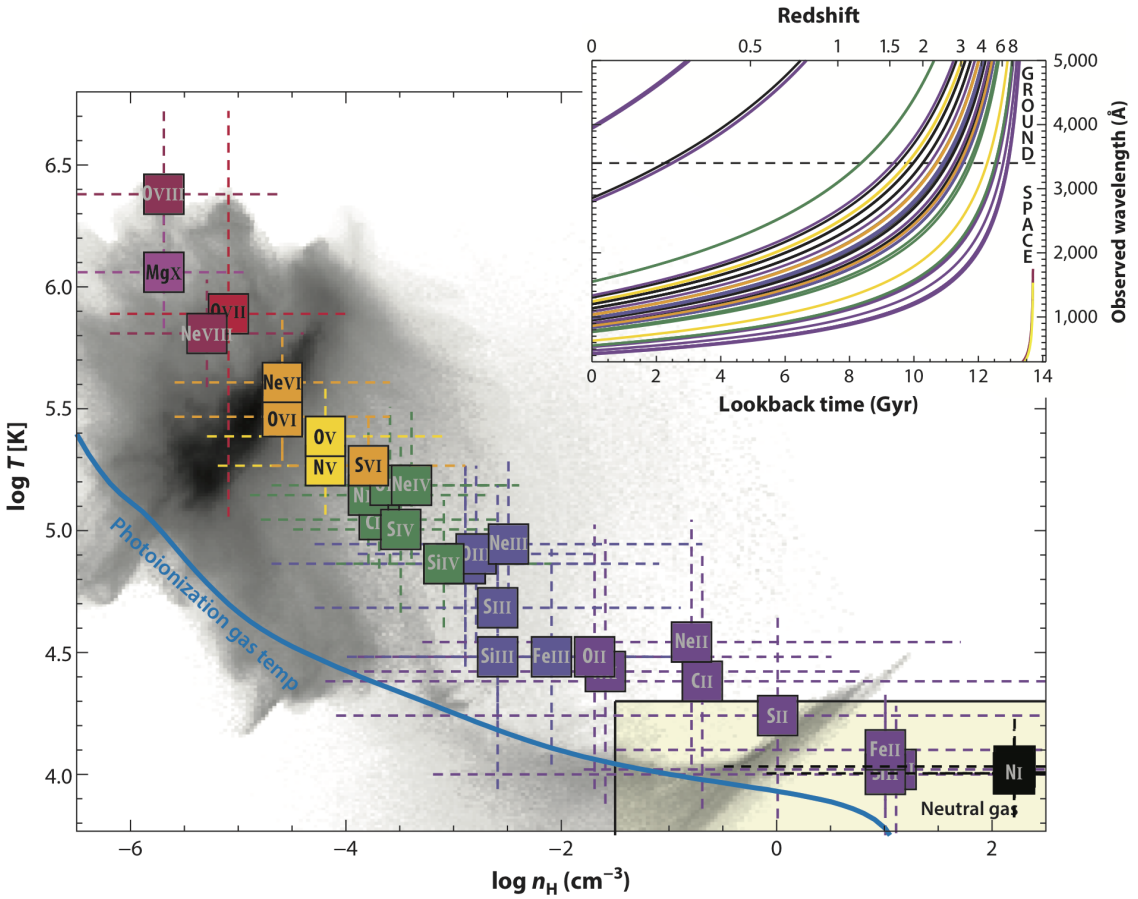

Figure 1.14 – Properties of the medium traced by different ions. Each ion is shown with a coloured square, and the temperatures and densities it traces are shown with dashed lines. The upper-right plot shows the observed wavelength of these ions depending on the redshift at which they were emitted. The rest frame corresponds to the intersection of the curves with the y-axis at $z = 0$. These data are taken from the EAGLE simulation (Oppenheimer et al., 2016), and are indicative, as they are model dependent. Image extracted from Tumlinson et al. (2017).

by a source can be absorbed by other astronomical objects, which will change the spectrum observed by producing absorption lines (right plot in Fig. 1.15). These absorptions will also eventually be reemitted as emission lines (middle plot in Fig. 1.15).

Absorptions can be described by parameters such as their equivalent width. This is a measure of the surface of an absorption feature and can be linked to the column density[14] which caused the absorption. For example, for an optically thin regime (i.e. a medium relatively transparent), the column density is linked to the equivalent width by

$$N_{\text{ion}} = 1.136 \times 10^{14} \frac{W_{ion}}{f_{12}\lambda_{1000}^2}. \tag{1.5}$$

N_{ion} is the column density, W_{ion} the equivalent width and f_{12} the oscillator strength

[14]The column density corresponds to a mass par area instead of the usual density in mass per volume. This is often used in astrophysics as the sky is in two dimensions because measures are integrated along the line of sight

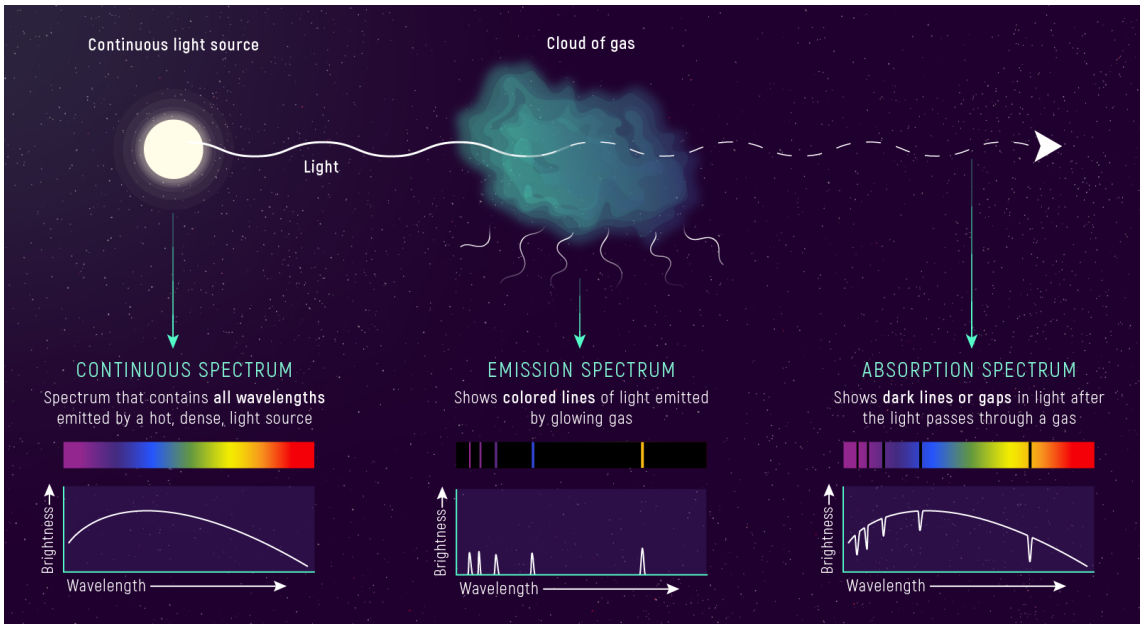

Figure 1.15 – Origin of spectra and their emission and absorption lines. We show in the lower part of this panel the dispersed light observed and its projection on a figure tracing its brightness as a function of wavelength. When looking at an object such as a star, a continuous spectrum will be observed. If its radiation propagates through a gas cloud, some of it will be absorbed and re-emitted in a different direction. If we look at this cloud from the side, we will only see what it re-emitted as an emission spectrum. If we look at it in the direction of the star, we will see the spectra of the stars with absorptions corresponding to what the gas re-emitted in a different direction. The emission and absorption lines trace the content of the gas cloud. Image from the NASA.

of the ion considered.

The gas can sometimes absorb all the photons at a given wavelength. This is called a saturated line and is generally treated as a lower limit of the column density. Conversely, the absorption is sometimes too small to be detected (for instance, if there is too much noise or if the column density is very small) and leads to an upper limit on the column density.

Quasar absorption sightlines

We have seen how to determine the composition of observed astronomical objects by dispersing the light they emit or absorb, and that their composition traces different phases of the gas. We can thus theoretically indirectly access the density and temperature of every object observed. However, observing diffuse regions not emitting light themselves such as the CGM is difficult, as a background light source is needed to learn their composition. To this aim, we rely on quasar absorption spectra. As mentioned in Sec. 1.3.3, quasars are the most luminous objects of the galaxy and are at high redshift. They are thus the perfect means to have access to absorption

[15]The impact parameters corresponds to the distance from the centre of the galaxy in the two-dimensional plane of the observer.

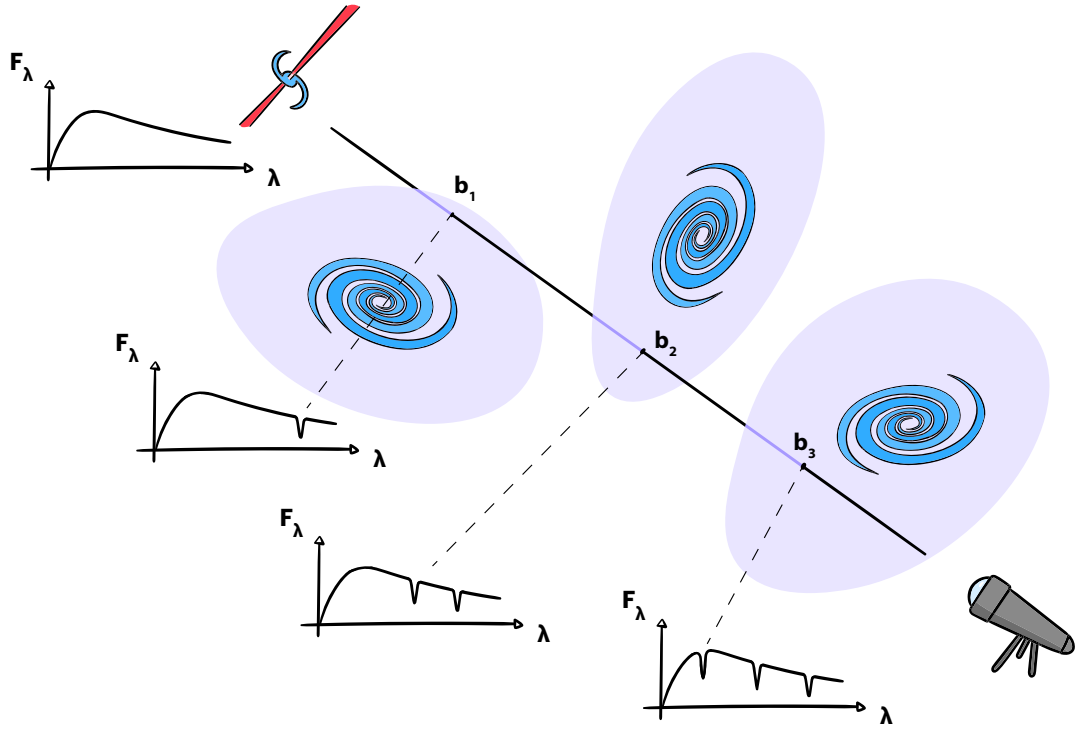

Figure 1.16 – Illustration of how quasar absorption sightlines are created in the CGM. A distant quasar (top left object) emits strong lights with a known spectrum. This light can go through different media which will absorb part of its light. On the illustration, the quasar crosses the CGM of three galaxies at impact parameters[15] b_1, b_2 and b_3. Each of these leads to absorptions in the observed spectrum. Thanks to the expansion of the universe, even if the gas crossed is the same in all three galaxies and should be absorbed with the same wavelength, the absorptions from different galaxies will not be superposed. Indeed, while propagating, the quasar spectrum is shifted towards higher wavelengths before reaching new galaxies. This allows observations to detect CGM absorptions from galaxies at different redshifts for a single quasar spectrum.

features from diffuse media such as the CGM. We illustrate in Fig. 1.16 how we learn from the CGM using quasar absorption spectra. As seen in the last section, quasars act as background sources which radiate light through the universe. This light can come across the CGM of galaxies, which will absorb a fraction of the light from the quasar spectra. By observing the quasar spectra, we can thus find the absorption lines of different ions and infer their column densities. This method is a key process for my work and the study of the CGM.

1.4.2 ... and theories !

In science, models and observations work in a coordinated manner. Observations allow us to witness the physics that permeates the world, and we interpret them with models. Through said models, we can describe these physics and make predictions, which can in turn be accepted or refuted through observations and become part of

the theory that describes them.

In astrophysics, more specifically, building a theory describing the evolution of the universe is extremely complex due to multiple factors. The first aspect is that a lot of domains in physics are involved. Fluid mechanics dictates the transfer of mass, momentum, and energy through space and time, gravitation describes how gas accretes and collapses to form stars, radiation determines the thermal state of the galaxies and leads to the production of observables, and so forth. In the Milky Way, it was found that there is energy equipartition when considering the gravitational, kinetic, thermal, radiative, magnetic, and cosmic ray energies of 1 eV cm^{-3} (Boulares & Cox, 1990), meaning that all of these components probably play a role in galaxy formation. Furthermore, these physics imply the consideration of an extensive range of scales. In galaxy formation, it is necessary to represent accurately structures surrounding the galaxy studied through the cosmological context, with scales larger than the megaparsec. It is also necessary to model relatively small scales, such as those dictating the evolution of stars, which are typically at the order of the size of the sun $\sim 10^{-8}$ pc. Lastly, the timescales that need to be considered in the evolution of the universe down to the present day are also humongous, covering $\sim 14 Gyr$ for its extent with events happening on scales smaller than a day, such as the first stages of a supernova (the core of a star takes less than a second to collapse !).

To answer this complexity and with the development of computing resources, astrophysics theory largely turned to numerical simulations. Simulations can be seen as abstract boxes filled with numbers representing a chosen subspace and its properties at a given time. In a way, they are multidimensional experiments evolving through time. We obtain the initial state of the experiments from our knowledge of the early universe and compute their evolution in time through equations describing the laws of physics. By pausing the experiment, we obtain snapshots of the universe — the universe of our simulation —, which can be compared to observations of our universe. The more physics there is and the longer the timescale we simulate, the longer the production.

Summary

We have seen that the universe is composed of several components, including dark matter and ordinary or baryonic matter. Under the effect of gravitation, small overdensities became denser and denser until cold gas clouds eventually collapsed and form the first stars. With time, these stars clumped together to form galaxies, which then increased in mass through accretion and interactions with other galaxies. The formation of galaxies involves many processes and many scales. As shown in Fig. 1.17, galaxy evolution involves the modelling of the cosmic web which generates gas inflow and fuels the galaxy in gas, but also stellar physics as they lead to processes regulating the evolution of the galaxy. These different components typically interact in the CGM, resulting in a multiphase medium extremely complex to model, but also an excellent place to study the effects of feedback. To model such complex systems, theorists hence turned to numerical simulations.

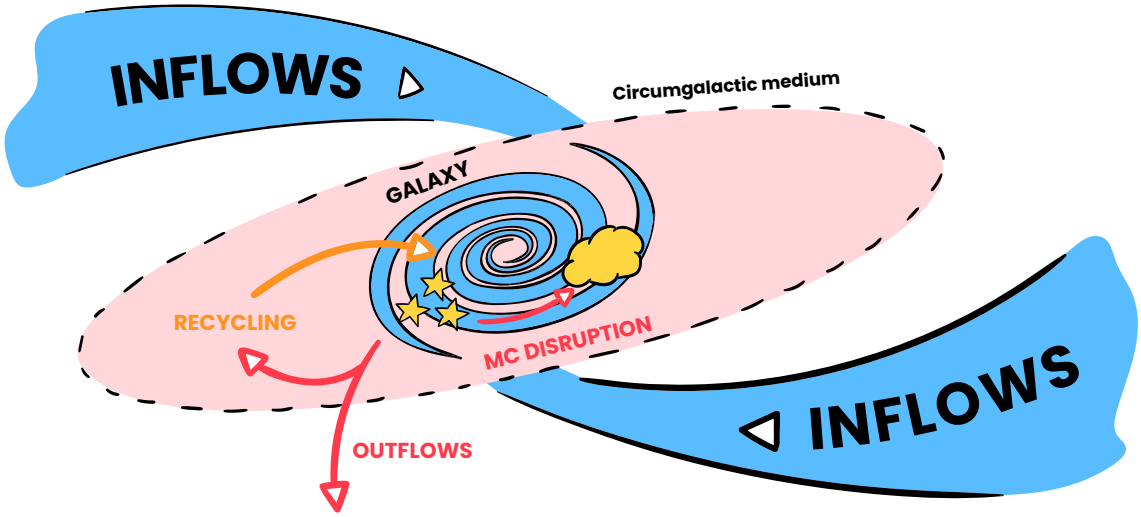

Figure 1.17 – Illustration showing the complexity of galaxy formation processes. Gas accretion brings gas into the ISM and fuels galaxy growth (blue). This gas fragments and condenses in molecular clouds, which, in turn, will fragment and collapse into stars (yellow). The massive stars formed generate different forms of feedback, such as photoionisation, radiation pressure, or supernovae explosions (red). Together, these processes can disrupt the molecular clouds and trigger galaxy-scale outflows, which can remove gas from the galaxy. Part of the ejected gas is heated up to high temperatures and ejected outside the dark matter halo, escaping from the gravitational potential of the galaxy, but a fraction of the ejected gas is pushed away less strongly and may fall back to fuel future generations of stars (orange).

Chapter 2

Numerical simulations

My work relies heavily on the code RAMSES, which is a code initially developed by Teyssier (2002) to study large-scale structures and galaxy formation and written in Fortran 90 with considerable use of the MPI library. RAMSES models grid-based hydrodynamics coupled with adaptive mesh refinement for the gas and N-body for stars and dark matter. Its fundamental parts are the AMR module (dealing with

the refinement, parallel computing and timesteps), the hydrodynamic solver, the particles module and the Poisson solver. New modules are frequently developed to implement additional physics such as radiative transfer (Aubert & Teyssier, 2008; Commerçon et al., 2011; Rosdahl et al., 2013) or magneto-hydrodynamics (Fromang et al., 2006; Dubois & Teyssier, 2008a), as well as new processes such as active galactic nuclei (Dubois et al., 2010), cosmic rays (Dubois & Commerçon, 2016). A recent version, RAMSES-RTZ (Katz, 2022), even couples the ionization states of individual metals (including C, N, O, Mg, Si, S, Fe, and Ne) to the radiation implemented in Rosdahl et al. (2013). With the extensive range of physics implemented, RAMSES is now used to model a wide variety of processes over a broad range, from protoplanetary discs (Hennebelle et al., 2016, 2020), protostellar core collapse (Commerçon et al., 2008) or Lyα emission from giant molecular clouds (Kimm et al., 2022) at a sub-parsec resolution to cosmological simulation (Lee et al., 2021) reaching gigaparsecs.

In this chapter, we first introduce different approaches to simulations of galaxy formation in section 2.1. We detail how such simulations are structured in section 2.2 and delve into the implementation of the equations dictating their evolution in section 2.3. We then describe how particles are modelled through N-body dynamics in section 2.4. Finally, we present how radiation and cooling are modelled in section 2.5.

2.1 The classes of galaxy formation simulations

Numerical simulations are an extremely powerful tool which has a wide range of applications, from weather forecasts to motions in a mosh pit (Silverberg et al., 2013). In astrophysics, they are used for scales ranging from planet formation and stellar physics to large scale structure simulations. In this work, we focus on galaxy formation simulations.

We refer to our simulation volume as a *box*, which is mainly characterised by its physical size and its resolution. In these two considerations lies a subtle balance that has to be set, as the computational cost is largely dependent on these quantities. We illustrate this with Fig 2.1. This figure plots existing galaxy formation simulations, showing their mass resolution in baryons as a function of the volume of the simulation. A similar plot could be done with the spatial resolution instead of the mass resolution. We see that simulations in galaxy formation tend to be limited and either choose a large box or a high resolution. Both have their advantages and limits. A large box leads to better statistics, as there will be more numerous — but unresolved — galaxies. A high resolution will lead to a better resolution of physics, but the results will be limited to a single galaxy. Different approaches can thus be made to model galaxy formation, and we focus here on two of them, *idealised simulations* and *zoom-in cosmological simulations*. We present both of these in the next sections.

Furthermore, the full figure has more dimensions as a simulation has indeed a given size and resolution, but it also models a certain timeframe. The longer this timeframe is (or the higher the time resolution is), the longer the simulation will take. Lastly, more computing power is needed as more precise physics such as radiative transfer or magnetic fields are implemented. In our simulations, the variables we

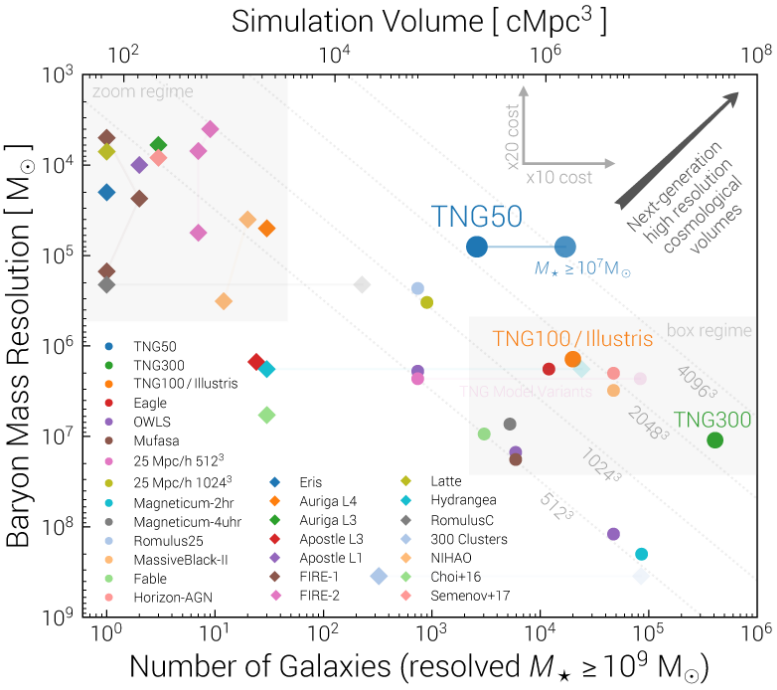

Figure 2.1 – Map of different simulation suites depending on their resolution in mass and the simulated volume. With increasing simulated volumes and increasing resolutions, the computational cost increases greatly, setting an artificial limit to these quantities. Courtesy of the TNG project.

track for the gas are its density ρ, its velocity $\mathbf{u} = (u_x, u_y, u_z)$, its energy density ε and its metallicity Z. By including radiative transfer, we increase by fifteen the number of variables tracked (see section2.5).

2.1.1 Idealised simulations

In idealised simulations, the idea is to ignore the cosmological context and solely model an isolated galaxy at the centre of a DM halo. This peculiarity leads to significantly faster simulations, which allow simulators to test the impact of different effects on galaxy formation. For example, the effect of different feedback schemes can be tested (Rosdahl et al., 2018). In this example, while conclusions can be reached on the propensity of these schemes to launch powerful outflows or hinder star formation locally, no conclusion can be reached on their effect on gas inflows which play a major role in galaxy formation by fuelling galaxies.

Idealised simulations often rely on initial conditions (ICs) describing a *pre-formed* galaxy. The initial setup is often a combination of gas and stars rotationally supported and forming the disc of a galaxy, which is set up in a dark matter halo. The main parameters of these initial conditions are the stellar mass of the disc, the mass of the DM halo, and the temperature and metallicity of both the CGM and the ISM. Very important parameters are also the profile of the stellar, gaseous and dark matter profiles, the gas fraction of the galaxy, and its circular velocity. It is also common to find the galaxy described through both a bulge and a disc component. The size of the box simulated then depends on the size of the galaxy, as it should be

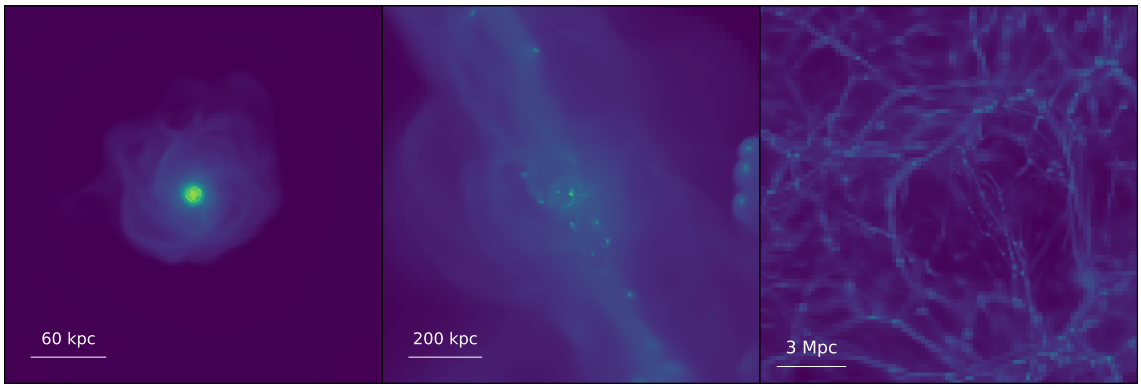

Figure 2.2 – Density-weighted maps of the density in simulations. On the leftmost panel, we show the example of an idealised simulation, while the middle and rightmost panels are a zoom-in simulation. As the zoom-in simulation covers almost six orders of magnitude in length, we show the same image at different scales.

made big enough so that boundary conditions are not limiting regarding outflows and the recycling of gas (see Sec. 2.2.3). Also, the temperature and metallicity of both the disc and the CGM have to be set.

We illustrate what an idealised simulation is in the left panel of Fig. 2.2 in which we show a density-weighted map of the gas density in an idealised simulation. This simulation is presented in Chap. 4 (see Ki9), and uses initial conditions made by Rosdahl et al. (2015) with MakeDisc (Springel et al., 2005; Kim et al., 2014).

2.1.2 Cosmological zoom-in simulations

In idealised simulations, we ignore the cosmological context, which is a key component of galaxy formation and evolution. In cosmological simulations, we model the cosmological context following the ΛCDM model. This means that we model dark matter and baryonic physics as in idealised simulations, but that we additionally include dark energy and the expansion of the universe. Furthermore, cosmological simulations start from ICs derived from the CMB power spectrum and develop *naturally* (as opposed to idealised simulations where ICs are *artificially* constructed). The cosmic web can thus form, and other galaxies can also be simulated and interact together. Such simulations can be also used to test alternative dark matter or gravitational models, but we only use here the standard ΛCDM, with energy density parameters $\Omega_\Lambda = 0.6825, \Omega_\mathrm{m} = 0.3175, \Omega_\mathrm{b} = 0.049$.

Zoom-in simulations

As mentioned a few paragraphs earlier, cosmological simulations are very costly. Indeed, unlike idealised simulations, they include the cosmological context which directly affects the number of computations that are done for a given timestep. Furthermore, these simulations are larger (going from hundreds of kiloparsecs to at least a few megaparsecs) and adding the cosmological context leads to the formation of other galaxies. These galaxies are dense regions where the resolution needs to be higher and thus more costly in computational power. To circumvent this problem,

a solution is to make an approach in-between idealised simulations and full cosmological simulations: zoom-in simulations. With this design, a whole cosmological volume is simulated (30 Mpc in our case) but the resolution is limited everywhere except in a given region. In this region ($\sim$ 3 R_{vir} at $z = 1$ in our simulations), the resolution of the simulation is increased and reaches tens of parsec, which is state-of-the-art. Such simulations focusing on one halo can thus model the cosmological context while resolving galaxies at extremely high resolution, at the cost of statistics.

We show such a zoom-in simulation in the second and third panels of Fig. 2.2 with a density-weighted map of the gas density. They are both from the same simulation but at different scales. In the middle panel, the whole map is in the zoom region, and we can see the galaxy embedded in a filament and surrounded by small satellites. In the rightmost panel, we zoom out and show the low-resolution region which covers most of the simulation box. The zoom region corresponds to the region with smaller filaments. As the resolution is increased, filaments contract further and become thinner and denser than at lower resolution.

MUSIC and the initial conditions

To produce IC for zoom-in cosmological simulations, use the MUSIC software (MUlti-Scale Initial Conditions, Hahn & Abel, 2011). The CMB can be described by a random Gaussian field, so the first step is to generate a white noise field through a normalised Gaussian distribution with a mean of zero and a variance of unity. It is then convolved with a transfer function $T(\mathbf{r})$ so that the amplitude of the field at different scales follows that of the CMB power spectrum. The power spectrum used in our ICs follows $H_0 = 67.11$, a normalisation $\sigma_8 = 0.83$, and a spectral index $n_s = 0.962$. This convolution leads to an initial spatially correlated overdensity field $\delta(\mathbf{r})$. The density field thus generated reproduces the two-point autocorrelation function, which describes the correlation between overdensities separated by a given distance. As the fluctuations are small and would induce large errors by simulating gravitation, they are evolved further in time — down to redshift $z = 150$ in our simulations — relying on the first-order Lagrangian perturbation theory and using the Zel'dovich approximation. This approximation describes analytically the growth of large-scale structures, assuming that on sufficiently large scales, thermal pressure can be neglected, and only gravitation will play a role, resulting in pancakes, filaments, and clumps of matter (Shandarin & Zeldovich, 1989).

From this set of ICs at $z = 150$, a first N-body simulation is run down to $z = 0$, only including dark matter. In this simulation, we then select a dark matter halo and trace the position of all dark matter particles in a given radius back to their position in the ICs. With these positions, we re-generate ICs and increase the resolution in the region of the selected particles so that there are no *low-resolution* particles within the chosen radius at any redshift. In this way, we obtain *zoom-in* ICs. We include baryons as a fraction of dark matter, following the same distribution in space. Finally, we run the simulation wanted with said ICs and including radiative hydrodynamics.

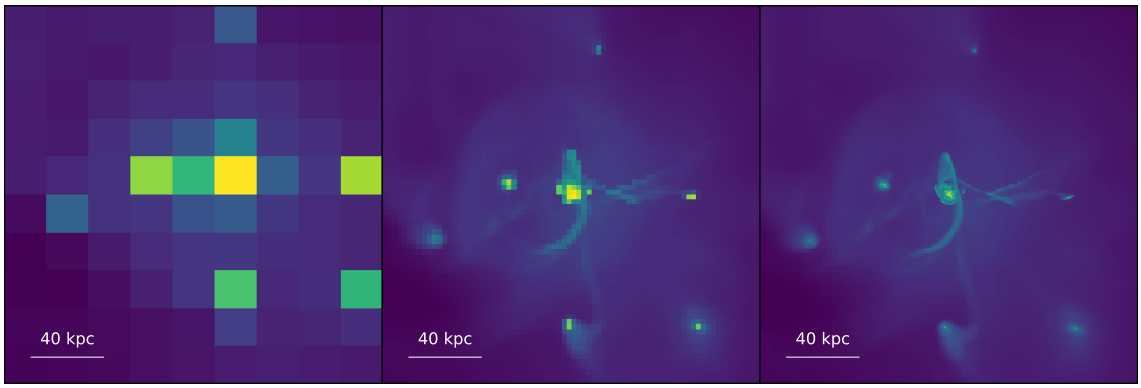

Figure 2.3 – Density-weighted maps of the density in simulations. We show maps with a very low (left panel), low (middle panel) and very high (right panel) resolution to illustrate the difference between continuous and discrete spaces.

2.2 The structure of simulations

Astrophysical simulations aim to model the evolution of gas to study various large scale processes. It is however not possible to model each particle constituting the gas individually on such scales as it would require an unrealistic amount of computation time. The solution is thus to model the gas as a fluid, through an average description of its properties. We now present how gas is modelled and structured in simulations.

2.2.1 Spatial discretisation

On macroscopic or larger scales, gas flow can be described as a fluid through a *continuous*, *measurable* variable (showing no discontinuity in its variation). Simulations are unable to model continuous data such as the flow of air and discrete, *countable* variables must be used. We illustrate discretisation in Fig. 2.3. If we look at the leftmost panel, an image with poor resolution, we can easily distinguish each pixel. Each of these pixels is associated with a single value shown with its colour, this is a discrete space. Going to the rightmost figure, which *seems* continuous, as it has a resolution high enough so that we cannot distinguish each pixel by eye. In simulations, space must thus ideally be discretised with a resolution high enough to resolve the smallest partitions of space. There are two major approaches to the discretisation of space in numerical simulations: Adaptive Mesh Refinement (AMR) and Smoothed Particles Hydrodynamics (SPH).

AMR and the Eulerian approach

The Adaptive Mesh Refinement is commonly used in numerical simulations of galaxy formation. It is for example used in ART (Kravtsov et al., 1997), FLASH (Fryxell et al., 2000), RAMSES (Teyssier, 2002), ATHENA (Stone et al., 2008) or ENZO (Bryan et al., 2014). With this scheme, space is discretised into cells. Each of these cells is then associated with our set of variables, as done in pictures (but in 3D for my simulations !). Such simulations generally trace 3 variables by default, which are the density ρ, the speed $\mathbf{u}$ (a vector, so it has three dimensions), and the internal energy density ε. To optimise the computing time, not all cells have the same size.

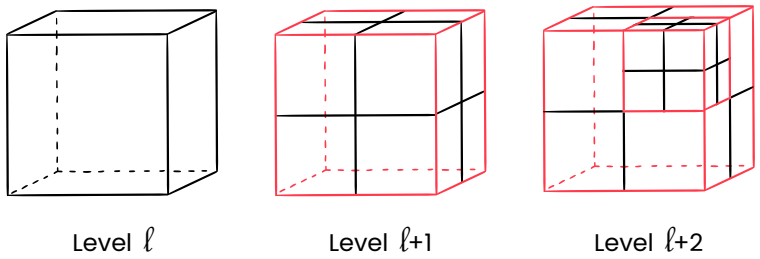

Figure 2.4 – AMR structure in RAMSES. From left to right, the resolution level increases and cells become parent cells as they form children cells. We show parent cells in red and children cells in black. At level $\ell + 2$, there are parent cells at both levels ℓ and $\ell + 1$.

They are organised by level which describes their scale, following Khokhlov (1998). The cell size is defined by $\Delta x = L_{\rm box}/2^{\ell}$, where $L_{\rm box}$ is the size of the simulated volume. The first cell is our box, which corresponds to the level $\ell = 0$. Then, each time the resolution in a cell is increased, the *parent cell* is divided into 8 *children cells* with a length half that of the parent cell. We refer to this structure as an *oct*. We illustrate this structure in Fig. 2.4. Also, two neighbour cells cannot have a level difference of more than one. We refer to cells with no children as *leaf cells*. Each cell is linked to its parent cell, its six neighbours, and its eight children cells if it is not a leaf cell.

SPH and the Lagrangian approach

The second main approach to numerical simulations is the Lagrangian approach. It is typically used in SPH, which was initially developed simultaneously by Lucy (1977) and Gingold & Monaghan (1977) for stellar astrophysics. In SPH, gas is followed through particles instead of cells. A given quantity is then obtained by weighting the number of neighbours of a given particle by a smoothing function, a kernel. One of the characteristics of this kernel is its typical thickness, the smoothing length h, which is analogous to the resolution in grid simulations. One of the strengths of SPH is that, by allowing the smoothing length to vary through time and defining it depending on the number of neighbours, it scales naturally and produces a higher resolution in regions with many particles. This is particularly convenient in astrophysical simulations, which typically cover a large dynamical range in density. However, this approach struggles to model shocks, shear such as the Kelvin–Helmholtz instability and large temperature gradients typically found in astrophysical conditions (Agertz et al., 2007; Springel, 2010a). Nonetheless, several SPH codes are actively in use and methods to avoid spurious features in discontinuous situations have been implemented in e.g. GASOLINE2 (Wadsley et al., 2017), GADGET-4 (Springel et al., 2021, 2022) (and their previous versions). SPH is also used to model special effects in movies and was used to simulate the fall of Gollum into the lava of Mount Doom in the last opus of *The Lord of the Rings*.

Other variations

There also exist other variations of these approaches, attempting to compensate for the limits of the previous schemes. For example, AREPO (Springel, 2010b) relies on the Moving Mesh Finite Volume approach, in which the mesh is unstructured and can move following Voronoi tessellation points. Based on a given set of seeds (i.e. points in space), the cells are structured so that they contain all the points closest to that seed. In GIZMO (Hopkins, 2015), the Meshless Finite Volume/Mass is presented. This variation can be seen as a generalisation of the Voronoi tessellation as it is based on a similar approach but combines it with a kernel smoothing its edges, as in SPH. The result can be illustrated as a Voronoi diagram, but with the edges of the Thiessen polygons more or less diffuse, depending on the steepness of the kernel function.

2.2.2 Refinement

We have seen that we use AMR in our simulations and have explained how there is a hierarchy of cells with parents and children cells, but have not explained further the criteria which lead to refining or de-refining a cell. We detail the ones we use in this section.

A very common criterion for refinement is to refine the simulations on density. The higher the density in a given region, the higher the resolution. This is the refinement criterion most used in such simulations, as dense regions are typically where more complex physics and smaller scale physics will take place. There is no interest in modelling cosmic voids with high precision for galaxy formation, but modelling the inter-stellar medium is essential. This density condition depends on both dark matter and baryons and can be transcribed as $m_{\text{DM, cell}} + f_{\text{b}}^{-1} m_{\text{b, cell}} \geq 8 m_{\text{DM, part}}$, with $m_{\text{DM, cell}}$ is the dark matter mass in the cell, $f_{\text{b}} = \Omega_{\text{b}}/\Omega_{\text{m}}$ the universal baryon fraction, $m_{\text{b, cell}}$ the baryonic mass in a cell (gas + stellar mass) and $m_{\text{DM, part}}$ the mass of a single dark matter particle.

Our second criterion for refinement depends on the thermal Jeans length,

$$\lambda_{\text{J,ref}} = \sqrt{\frac{\pi c_{\text{s}}^2}{\rho G}}, \tag{2.1}$$

which is required to be of at least four cells width at every point in the simulation (Truelove et al., 1997). c_{s} is the sound speed, defined by $\gamma P = c_{\text{s}}^2 \rho$ (we take the isothermal case $\gamma = 1$ here), with P the pressure and G the gravitational constant. This length is a characteristic stability criterion, weighting the internal pressure of the gas to its self-induced gravitational potential. If the Jeans length in a cell is small compared to the resolution of the cell, then the gas in the cell is likely to collapse on itself and the resolution needs to be increased to allow for the collapse to develop. In our simulations, this criterion typically has an impact on cells at the highest resolution levels in the ISM (the densest media).

As mentioned earlier, some of our simulations are zoom-in simulations. This is a refinement criterion in which AMR is not allowed outside the zoom region. We show in Fig. 2.5 resolution maps of an idealised simulation and a zoom simulation at two different scales.

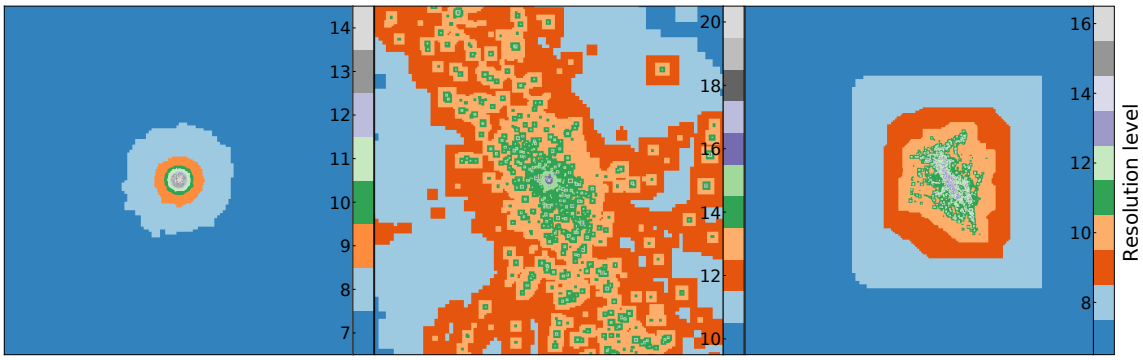

Figure 2.5 – Level maps of the simulations. These three maps are the same as in Fig. 2.2. On the leftmost panel, we show an idealised simulation, while the middle and rightmost panels are zoom-in simulations at different scales.

In our cosmological simulations, an additional criterion is used so that the physical resolution remains constant. Higher resolution levels are unlocked with decreasing redshift as the box size gets larger in physical units. In idealised simulations, the box size is constant, so there is no need to use such a criterion.

Lastly, simulations can increase arbitrarily resolution by forcing a fixed uniform resolution on specific subregions that can move over time. This is a method that was, for example, used to model the CGM with more resolution (Peeples et al., 2019; Hummels et al., 2019). Indeed, the CGM is a region with low gas density and thus at a low resolution when applying the quasi-Lagrangian and the Jeans refinement criterion. It is nonetheless a very complex medium due to its multiphase nature and a resolution too low might induce spurious effects such as thermal mixing. One can thus use additional refinement criteria which, for example, refine depending on the cooling time.

2.2.3 Boundary conditions

We have explained how simulations are structured as a box in the previous section, but an important consideration is the modelling of the cells and particles at the boundaries of the box. Indeed, to model the evolution of a cell, one has to consider all the surrounding cells. However, if the cell is at the boundaries of the computational domain, it has no neighbour on at least one of its sides. To overcome this limitation, we define ghost zones outside the computational domain. These ghost zones are defined to mimic one of four behaviour: periodic, reflexive, outflow, or inflow boundaries. In our idealised simulations, we use outflow boundaries. With this approach, the ghost zones are made so that there is no gradient at the boundaries and the gas can leave freely but cannot fall back (the box is however big enough so that no gas or almost none reaches its boundaries). Depending on the study, it is thus important to choose a box large enough so that gas is allowed to fall back onto the galaxy and form a new generation of stars.

In our zoom simulations, we use periodic boundaries. There, if gas reaches one side of the box, it is reinjected on the other side of the box. This is the default mode used in cosmological simulations as it represents well the homogeneity of the universe for large-enough volumes. We illustrate these two approaches in Fig. 2.6.

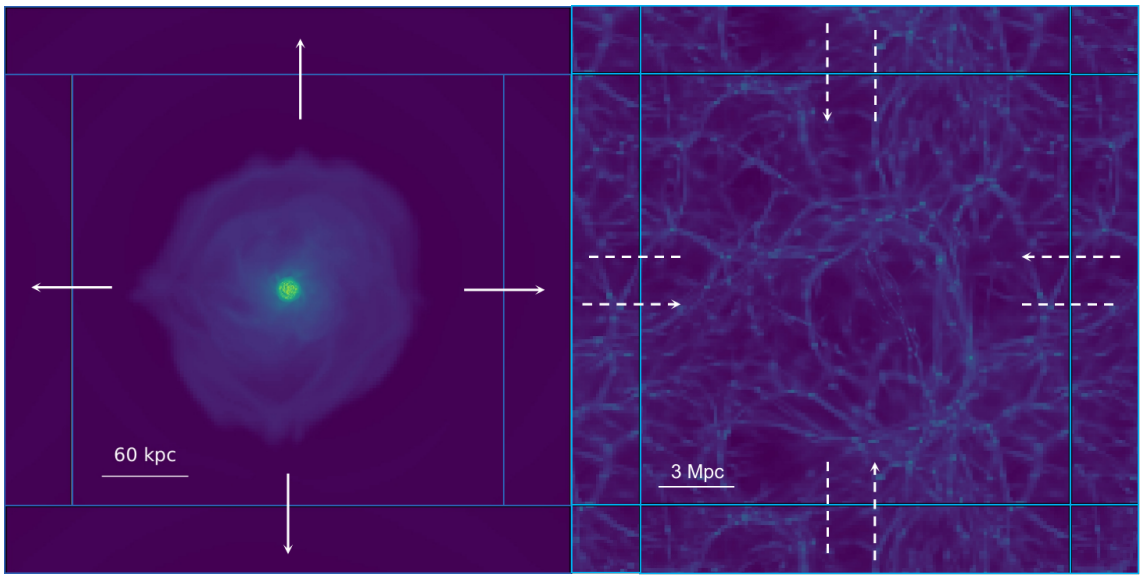

Figure 2.6 – Representation of the ghost zone of the simulation of an isolated galaxy (left panel) and a cosmological zoom-in simulation (right panel). The central figure is the simulation, and the blue-contoured images correspond to the ghost zones. The white arrows represent the trajectory of outflowing gas at the edges of the simulations. In the left panel, the ghost zones are made so that there is no pressure gradient at the boundaries and the gas can leave the simulation freely. In the cosmological simulation, the gas that would leave on either side of the plot is reinjected on the other side.

Boundaries must also be considered for the gravitational potential. For the Poisson equation, the boundaries are set to be periodic if ghost regions are periodic or with a null gravitational potential in case of outflowing boundaries.

2.2.4 Time discretisation

We have seen that space is discretised, but time is also discretised. To avoid instability in the simulation, we follow the Courant–Friedrichs–Lewy (CFL) condition, which ensures that information does not travel more than one cell in a single timestep. The timestep Δt must thus be lower than the maximum speed attainable in the simulation and is defined as $\Delta t = C\Delta x / c_{\max}$, with $C < 1$. $c_{\max}$ corresponds to the sound speed added to the bulk gas speed, and $C = 0.8$ is the Courant factor (Teyssier, 2002; Rosdahl et al., 2013).

The timestep is often determined at the highest resolution level, where Δx is the smallest. As parents cells are twice wider, ($\Delta x_{\ell+1} = 0.5\Delta x_\ell$), a cell at the level $l+1$ generally goes through two timesteps before the cell at the level l advances by one timestep ($\Delta t_{\ell+1} = 0.5\Delta t_\ell$). This subcycling is not necessarily constant and can be set up so that two levels have the same timestep (while respecting the CFL condition, i.e. Δt_ℓ can be made shorter but $\Delta t_{\ell+1}$ cannot be made longer). This fine-tuning can lead to faster simulations in some cases. In several of my simulations, I noticed that with an increasing number of resolution levels, setting an equal timestep for more levels (i.e. a subcycling of one for the levels with the lowest resolution and

two for the others) indeed made simulations faster. I thus changed the subcycling of the first levels throughout several zoom-in cosmological simulations presented here. This is discussed in section 5.2.

2.3 Ruling equations

We have described how gas is structured in our simulations, and we now present how it evolves through time through the AMR grid.

2.3.1 Euler's conservation equations

In hydrodynamical simulations, the gas is treated as a fluid. We thus rely on the Navier–Stokes equations, which describe the flow of Newtonian fluids. We more precisely consider a special case of these equations in which the gas is considered ideal, i.e. without viscosity nor thermal conductivity. This corresponds to the three Euler equations, which describe respectively the conservation of mass, momentum, and energy. Here, we also use sink and source terms with the gravitational potential Φ and the cooling function $\Lambda(\rho, \varepsilon)$ which we detail in Sec. 2.4.1 and Sec. 2.5.4. The equations are then given by

$$\begin{aligned} \frac{\partial \rho}{\partial t} + \nabla \cdot (\rho \mathbf{u}) &= 0, \\ \frac{\partial}{\partial t}(\rho \mathbf{u}) + \nabla \cdot (\rho \mathbf{u} \otimes \mathbf{u}) + \nabla P &= -\rho \nabla \Phi, \\ \frac{\partial}{\partial t}(\mathcal{E}) + \nabla \cdot [(\mathcal{E} + P)\mathbf{u}] &= -\rho \mathbf{u} \cdot \nabla \Phi + \Lambda(\rho, \varepsilon), \end{aligned} \tag{2.2}$$

where $\mathcal{E}$ is the total energy density, split between kinetic and thermal energy density as $\mathcal{E} = \rho \mathbf{u}^2/2 + \varepsilon$. As there are four variables in the conservative form of the equations (ρ, $\mathbf{u}$, P and ε), a fourth equation is needed to close the system. This is the role of the equation of state,

$$P = (\gamma - 1)\varepsilon, \tag{2.3}$$

where γ is the adiabatic index or Laplace coefficient of the medium. It is defined as the ratio of the heat capacity of the medium at constant pressure to its heat capacity at constant volume $\gamma = \frac{C_P}{C_V}$. Its value is usually set to $\gamma = 5/3$ in RAMSES, as we consider the gas to be in monatomic form.

2.3.2 Equations discretisation

To discretise the continuous equations considered above, we can first rewrite the Euler conservation equations as flux equations, under the form:

$$\frac{\partial \mathbf{U}}{\partial t} + \nabla \cdot \mathbf{F}(\mathbf{U}) = \mathbf{S}(\mathbf{U}), \tag{2.4}$$

with $\mathbf{U} = (\rho, \rho\mathbf{u}, \rho\varepsilon)$, $\mathbf{S_x}$ the source term such as gravitation or cooling, and $\mathbf{x}$ the position vector. Through the finite volume method, it can be rewritten as

$$\mathbf{U}^{n+1} = \mathbf{U}^n - \frac{\Delta t}{\Delta \mathbf{x}} \left(\sum_{(\mathbf{x},\mathbf{i})} \mathbf{F_x}(\mathbf{U})_{\mathbf{i}+\frac{1}{2}} - \mathbf{F_x}(\mathbf{U})_{\mathbf{i}-\frac{1}{2}} \right), \tag{2.5}$$

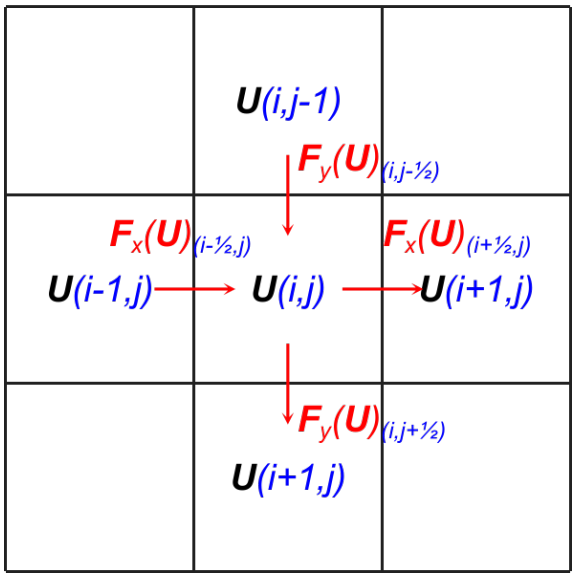

Figure 2.7 – Representation of the grid structure and the inter-cell fluxes. We note the content of the cell with the vector $\mathbf{U}$, its position along the x-axis with i, and along the y-axis with j. We note the inter-cell fluxes with the vector F.

with $\frac{\partial \mathbf{U}}{\partial t} \sim \frac{\mathbf{U}^{n+1}-\mathbf{U}^{n}}{\Delta t}$ and $\frac{\partial \mathbf{F_x}(\mathbf{U})}{\partial \mathbf{x}} \sim \frac{1}{\Delta \mathbf{x}} \left(\mathbf{F_x}(\mathbf{U})_{\mathbf{i}+\frac{1}{2}} - \mathbf{F_x}(\mathbf{U})_{\mathbf{i}-\frac{1}{2}} \right)$. Here, we have split space into cells, which we refer to through their index along the ndim axes $\mathbf{i}$. The subtle part is then the expression of the fluxes at the cells' interfaces $\mathbf{F_x}(\mathbf{U})_{\mathbf{i}\pm\frac{1}{2}}$. A first naïve method is to take the average flux of the two cells, but it yields unstable results. The method implemented in RAMSES thus relies on a second-order Godunov method (or Piecewise Linear Method) (Toro, 1999) and is based on Colella (1990) and Saltzman (1994).

2.4 The content of simulations

We have seen how gas is structured in simulations, AMR being the method used to discretise the simulation volume in RAMSES. Complementary to the baryonic gas, we also model the evolution of dark matter and stars. We describe their implementation in this section.

2.4.1 Dark matter and stellar particles

We do not treat here the formation, life (winds and similar phenomenon) and death of stars in this section as chapter 3 is dedicated to it. In our simulations, stars are not modelled individually, but through particles describing a population of stars. For example, in several of our simulations, the stellar particles represent a population of at least 3200 $M_\odot$. The population traced by stellar particles is characterised by their position, velocity, initial mass, current mass, age, and metallicity.

Dark matter is also modelled through particles representing a given mass of dark matter. Both the dark matter particles and the stellar particles are represented as collisionless particles. This collisionless aspect follows the current image of dark matter in the ΛCDM model, but the fact that we consider dark matter through

particles is a numerical choice. These particles are modelled through a parallel N-body simulation (a Lagrangian approach) and the coupling between their position and the gravitational field is described by a Vlasov-Poisson system of equations. The first equation is simply derived from Newton's second law of motion as

$$\frac{\mathrm{d}^2\mathbf{x}}{dt^2} = -\nabla\Phi, \tag{2.6}$$

and the gravitational potential Φ is defined through $\Delta\Phi = 4\pi G\rho_{\mathrm{tot}}$, with the Laplacian $\Delta = \nabla^2$ and G the gravitational constant. The density ρ_{tot} here includes dark matter as well as all the baryonic matter in the simulation. The gravitational potential in each cell is computed using a *Cloud-in-Cell* (CIC) interpolation, which links particles to host cells proportionally to the amount of volume of the cell they cover. With this method, particles are considered as clouds which cover different cells and the corresponding fraction of mass is then attributed to each cell. The acceleration in cells is then computed through a finite-difference approximation and is computed for each particle using a reverse CIC interpolation. Then, the velocity and new position of the particles are updated.

2.4.2 Metals

Up to this point, we described gas as a unique quantity, but astrophysical gases are composed of many elements from the periodic table. In astrophysics, most of the gas is in the form of hydrogen and helium, and we refer to all the other elements as metals. We describe them through the equation $X + Y + Z = 1$, the respective mass fraction of hydrogen, helium, and metals. In our simulations, we trace the gaseous content of hydrogen and helium assuming $X = 0.76$ and $Y = 0.24$. It is also important to track metals as they are essential to model cooling properly. We show this with the cooling rates plotted in Fig. 2.8 as a function of temperature. In both plots, we see there is a notable contribution from metals to the cooling curve. However, we cannot track each element individually as it would lead to too many variables. We thus track metals through a single independent variable, which behaves as a passive scalar advected with the gas, though many modern codes track several species individually. The relative abundance of metals is assumed to be Solar, and the metal content of a cell only increases when the medium is enriched through supernovae. In one of the models we test (Agertz et al., 2013), the metal prescription is changed and instead of tracking all metals through solely one variable, both Fe and O are tracked. The total metallicity is then defined by the combination of Z_{Fe} and Z_{O} as $Z = 1.06Z_{\mathrm{Fe}} + 2.09Z_{\mathrm{O}}$ (Asplund et al., 2009). Stars also have a metallicity for which the latter equation can be applied, but with limits in metallicity of 0.0004 and 0.05 (Raiteri et al., 1996). For the following chapters, we define $Z' = max(Z/Z_{\odot}, 0.01)$ for all models. Z' is a metallicity floor which models the effect of primordial cooling for a pristine gas.

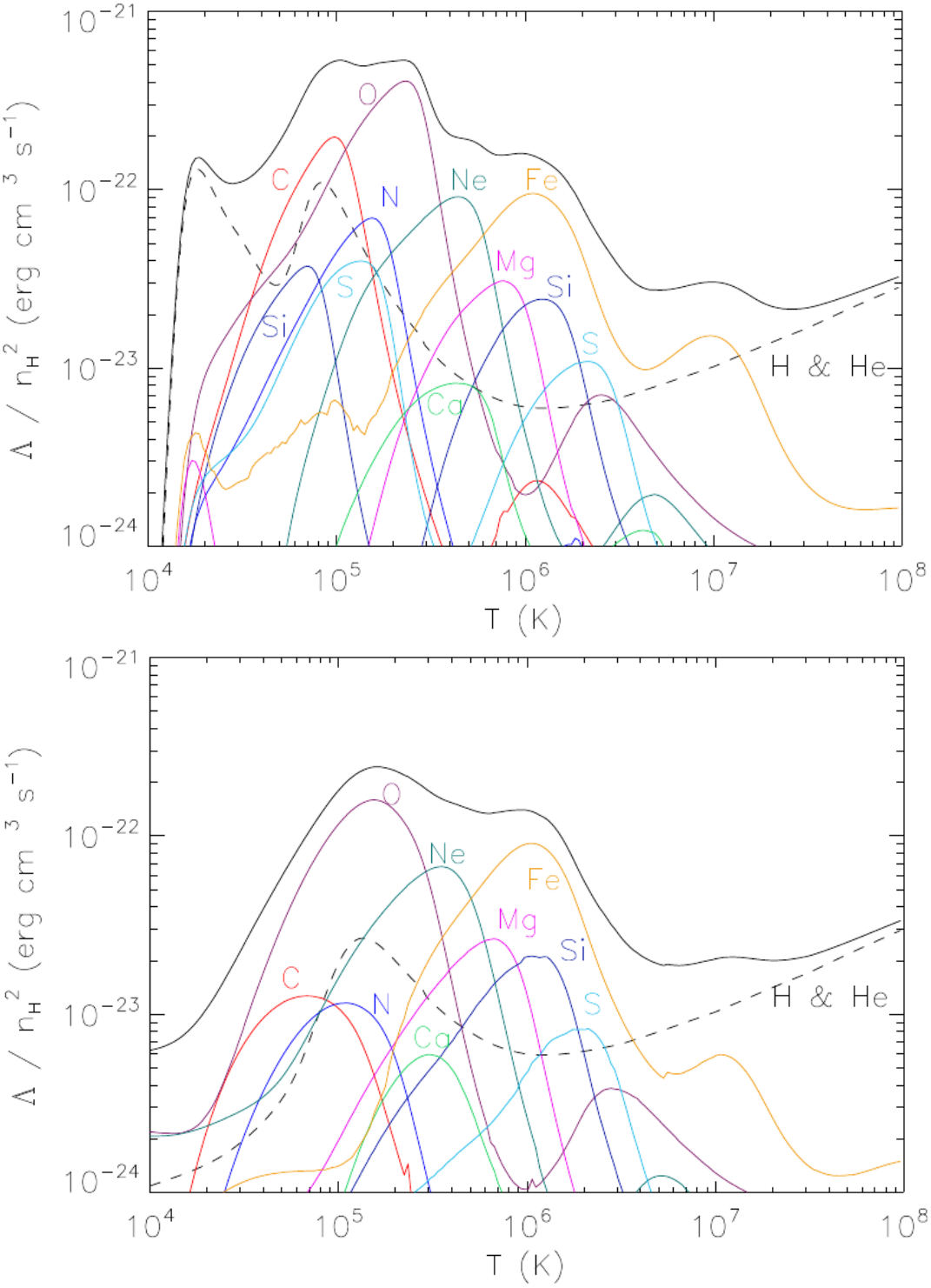

Figure 2.8 – Cooling rates of as a function of temperature, assuming collisional ionisation (top panel) and photoionisation (bottom panel, with $n_{\rm H} = 10^{-4}$ cm^{-3}) equilibrium. The cooling curve in photoionisation equilibrium is dependent on the density considered, but not under the hypothesis of collisional ionisation. The coloured, solid curves show the contributions from individual elements. The black, solid curve indicates the total cooling rate and the black, dashed curve shows the contribution from H and He. These figures are extracted from Wiersma et al. (2009).

2.5 Radiative transfer and non-equilibrium chemistry

As mentioned in Sec. 1.4.1, atoms can gain or lose energy by emitting or receiving radiation. On a larger scale, this means that when a gas cloud interacts with radiation, its thermal state changes. Light is thus an essential component in galaxy formation simulations. Furthermore, stellar radiation is thought to be an important source of feedback. As stars heat the surrounding media by forming expanding warm HII regions, they can both boost other feedback sources and hinder star formation. This radiation can also be an additional source of feedback through radiation pressure.

Each atom has a given probability to absorb a photon and get ionised or to emit one after recombination with an electron. This regulates radiation through a broad range of wavelengths. To model radiation, one thus ideally needs to model (almost) the whole periodic table and all the ionisation states of each atom. For obvious reasons, it is not feasible in current numerical simulation and approximations have to be made. A first solution is to assume that, depending on the local density and temperature field, there is a given distribution for each element with a given ionisation state in equilibrium. Then, values of the radiation field can be tabulated and included in cooling and heating equations. However, this is a strong approximation, which also ignores stellar ionisation as a source of feedback. We thus turn to a second method used in the RT module from Rosdahl et al. (2013); Rosdahl & Teyssier (2015). This consists in tracking the ionisation state of the two elements making most of the universe: hydrogen and helium. In practice, this adds three new variables treated as passive scalars (i.e. advected with the gas), which are the ionisation fraction of H and He, as

$$x_{\mathrm{HII}} = \frac{n_{\mathrm{HII}}}{n_{\mathrm{H}}} \quad , x_{\mathrm{HeII}} = \frac{n_{\mathrm{HeII}}}{n_{\mathrm{He}}} \quad , x_{\mathrm{HeIII}} = \frac{n_{\mathrm{HeIII}}}{n_{\mathrm{He}}}. \tag{2.7}$$

The evolution of ionising photons in space and time is described by the radiative transfer equation which can be written as (Rosdahl, 2012)

$$\frac{1}{c}\frac{\partial I_\nu}{\partial t} + \frac{\mathbf{n}}{a}\cdot\nabla I_\nu - \frac{H}{c}\left(\nu\frac{\partial I_\nu}{\partial \nu} - 3I_\nu\right) = -\kappa_\nu I_\nu + \eta_\nu. \tag{2.8}$$

Here, ν corresponds to the frequency, I_ν the radiation-specific intensity and $\mathbf{n}$ the unit vector in its direction of propagation. a and H are respectively the expansion factor and the Hubble expansion rate and describe its evolution with redshift (lengths are diluted as a^{-1} and the radiation energy density is diluted as a^{-4}). On the left-hand side, the first term describes its evolution with time, the second its propagation in space and the third the impact of the cosmological dilution. The cosmological terms are only partially included in the current implementation of RT (see Sec. 3.3 in Rosdahl, 2012) and are not used in the idealised simulations. On the right-hand side, the first term describes the absorption (κ_ν being the absorption coefficient) and the second one describes its emission (η_ν being the source term).

2.5.1 The moment method

A first difficulty faced with Eq.2.8 is that it involves a total of seven dimensions (three spatial, two angular, one temporal and one spectral), making it very costly numer-

ically. To go around this issue, the RT module relies on the *moment* method. It broadly consists in removing the angular dimensions by taking the angular moments of the radiative transfer equation. The n^{th} moment of a function $f(x)$ corresponds to the f-weighted average of x^n and is defined as $\int x^n f(x)dx$. In our case, f is the radiative transfer equation and x is the radiation-specific intensity I_ν. Taking the n^{th} moment replaces the direction of each photon at a given point with an average direction. This leads to a loss of directionality of the photons, which makes radiation more diffusive in the case of the optically-thin limit (i.e. when a medium has a low opacity) and coarse shadows. However, this leads to equations in the form of conservation laws which can be coupled with Euler conservation equations and solved with the same techniques. A second complication regarding the number of dimensions is that the full spectrum of observable frequencies is continuous, and a virtually infinite number of variables would be needed to trace it fully. To further diminish the number of dimensions involved, we discretise radiation on a certain number of bins. For all simulations presented here, there are three bins with boundaries defined by the hydrogen and helium ionisation energies, as

$$]13.6, 24.59], \quad]24.59, 54.42], \quad]54.42, \infty[\quad \text{eV}. \tag{2.9}$$

The number of photons populating these three radiation bins is each associated with a three-dimensional flux (the number of photon per unit area, time, and frequency). In the end, including RT in our simulations adds fifteen variables: the three ionisation fractions of H and He (x_{HII} , x_{HeII} and x_{HeIII}) as well as the flux vector (3 axes for each photon group) plus the number of photons it contains for each photon group.

2.5.2 A reduced speed of light

The second main obstacle is that light is... *too fast*. We have seen in a previous section that the Courant condition sets a maximal timestep as $\Delta t = 0.8\frac{\Delta x}{c_{\text{max}}}$, with c_{max} the maximal speed attainable within the simulation. In the simulations presented here, outflows typically peak near 1500 $\text{km}\,\text{s}^{-1}$. If we now compare it to the speed of light $c \sim 3 \times 10^5$ $\text{km}\,\text{s}^{-1}$, we see that there is a ratio of 200. This means that there must *at least* be a ratio of 200 between the RT timestep and the hydrodynamical timestep. Doing this would increase considerably the computational time of simulations, and a solution is to consider instead a reduced speed of light approximation (RSLA, Gnedin & Abel, 2001). In this approximation, the simulated speed of light is simply taken to be a fraction of the real speed of light. It is based on the assumption that the decisive quantity in radiation propagation is not the speed of light, but the speed of the ionisation fronts. This approximation is thus valid as long as the photon speed is greater than the fastest ionisation front. The speed of the ionisation front can be approximately computed in an idealised setup (Strömgren, 1939) to verify in which regimes it is valid, but it is not so trivial in more complex simulations. We used a fraction of 5×10^{-3} for all our simulations, which is expected to be a valid approximation for galaxy formation simulations (Rosdahl, 2012). Indeed, ionisation fronts will mainly play a role in H II regions, relatively dense media where the fastest ionisation front will be slower than the photon speed.

2.5.3 The photon sources

In our simulations, the main sources of photons are stars. To accurately model how stellar particles radiate their energy in our simulations, we model their stellar spectral energy distributions with the Binary Population and Spectral Synthesis code (v2.2.1, Stanway & Eldridge, 2018) depending on their IMF, obtained through their age and metallicity. Then, by integrating the SED of each stellar particle over each spectral bin, the number of injected photons per bin is computed.

However, this only takes into account radiation from stars in the main galaxy of our simulations. If the simulation is a zoom-in or an isolated galaxy simulation, the light from other galaxies must also be included to compute a correct radiative flux. In our simulations, following Faucher-Giguère et al. (2009), we include a uniform redshift-dependant UV background of ionising radiation which models the combined emission from unresolved or non-simulated galaxies. In zoom-in simulations, we activate it from $z = 8.5$. It is combined with self-shielding (optically thick gas protecting itself from external radiation), which is modelled by an exponential damping factor above densities of 10^{-2} cm^{-3}.

2.5.4 Cooling and ionisation state

With the photon flux for each stellar bin computed through the SED of the main galaxy and the UV background, the new number of ionising photons in each cell can then be obtained. From that point, thermochemistry can be solved in the simulation. This is the only step in which radiative transfer is coupled to hydrodynamics, and it dictates the change in the different ionisation fractions as well as the temperature evolution of the gas. From the ideal gas law $Pm_{\rm H} = \rho k_{\rm B} T_\mu$ and the equation of state Eq. 2.3, the temperature in a cell is given by

$$T_\mu = \varepsilon \frac{(\gamma - 1) m_H}{\rho k_{\rm B}}. \tag{2.10}$$

$T_\mu = T/\mu$, with μ the average mass per particle in units of the proton mass m_H, ϵ is the thermal energy density and $k_{\rm B}$ is the Boltzmann constant. In time, it evolves following

$$\frac{\partial T_\mu}{\partial t} = \frac{(\gamma - 1) m_{\rm H}}{\rho k_{\rm B}} \Lambda, \tag{2.11}$$

with

$$\Lambda \equiv \dot{\varepsilon} = (\mathcal{H} + \mathcal{L} + Z\mathcal{L}_Z)\, n_{\rm H}^2, \tag{2.12}$$

which describes the cooling and heating rate. For H and He, these rates are computed out of equilibrium on the fly. The heating component is described by $\mathcal{H}(T_\mu, n_{\rm H}, N_i, x_{{\rm X}i})$[1], with N_i the numerical density of photons, and comes from the photoheating, the UVB heating and the photoelectric heating. The cooling component $\mathcal{L}(T_\mu, n_{\rm H}, N_i, x_{{\rm X}i})$ depends on collisional ionisation and excitation, recombination, Bremsstrahlung, Compton scattering and dielectronic recombination. The metal cooling component $\mathcal{L}_{\rm Z}(T_\mu, n_{\rm H})$ is tabulated at equilibrium, and decoupled from the radiation flux. It is split into two temperature regimes. Above 10^4 K, it

[1]We write $x_{{\rm X}i}$ instead of $x_{\rm HII}$, $x_{\rm HeII}$ and $x_{\rm HeIII}$ for conciseness.

is modelled following CLOUDY tables (Ferland et al., 1998, version 6.02) assuming photoionisation equilibrium with a redshift independent UV background from Haardt & Madau (1996). Below 10^4 K, fine structure metal cooling rates from Rosen & Bregman (1995) are used down to 10 K.

2.6 Post-processing

As it is costly to model a large number of physical processes during a simulation, *on-the-fly*, it is common to *post-process* some of them, i.e. compute quantities solely on the chosen timesteps after the simulations are done. Such an example is RT, which is quite costly and was first done through post-processing in RAMSES (Aubert & Teyssier, 2008). In our case, we post-process simulations with two aims. The first goal is to compute the ionisation state of several elements in the simulation (we only model $x_{\rm HII}$, $x_{\rm HeII}$ and $x_{\rm HeIII}$ on-the-fly). The second goal is to model line-of-sights in simulations to compute column density.

2.6.1 KROME

To compute the ionisation fraction of chosen elements, we first need to extract the mass fraction of each element. To do so, we simply weigh the metallicity by the Solar abundance of the chosen element. Here, we consider magnesium, carbon and oxygen, which have respective Solar abundances of $A_{\rm Mg,\odot} = 3.98 \times 10^{-5}$, $A_{\rm C,\odot} = 2.69 \times 10^{-4}$ and $A_{\rm O,\odot} = 4.9 \times 10^{-4}$ (Grevesse et al., 2010). The number density of the ionisation state i of an element is ruled by a set of ordinary differential equations of the form (Grassi et al., 2014)

$$\frac{{\rm d}n_i}{{\rm d}t} = \sum_{j \in F_i} \left(k_j \prod_{r \in R_j} n_{r(j)} \right) - \sum_{j \in D_i} \left(k_j \prod_{r \in R_j} n_{r(j)} \right) , \tag{2.13}$$

where the first sum describes the ionisation states *ending* in the ith state (set F_i), and the second sum describes *leaving* the ith state (set D_i). Each reactant (set R_j) has a number density of $n_{r(j)}$, with a reaction rate coefficient k_j. We use the chemistry package KROME (Grassi et al., 2014) to solve these rate equations, relying on the cell's metallicity, density, temperature and ionising radiation flux. Then, we iterate the process and evolve the ionisation balance to equilibrium following the method from Mauerhofer et al. (2021). We thus obtain Mg II, C IV and O VI. We choose to track these three ions as they outline complementary gas phases (see Sec. 5.3), and they are accessible through CGM observations.

2.6.2 RASCAS

Having the ionisation state of each cell, we can now compute corresponding column densities. A first method is to take a given volume from the simulation surrounding the galaxy and project it on a two-dimensional (2D) plane. To do this, we split low-resolution cells equally in size until they reach the size of high-resolution cells. By doing so, we assume that the physical quantities are split equally between the

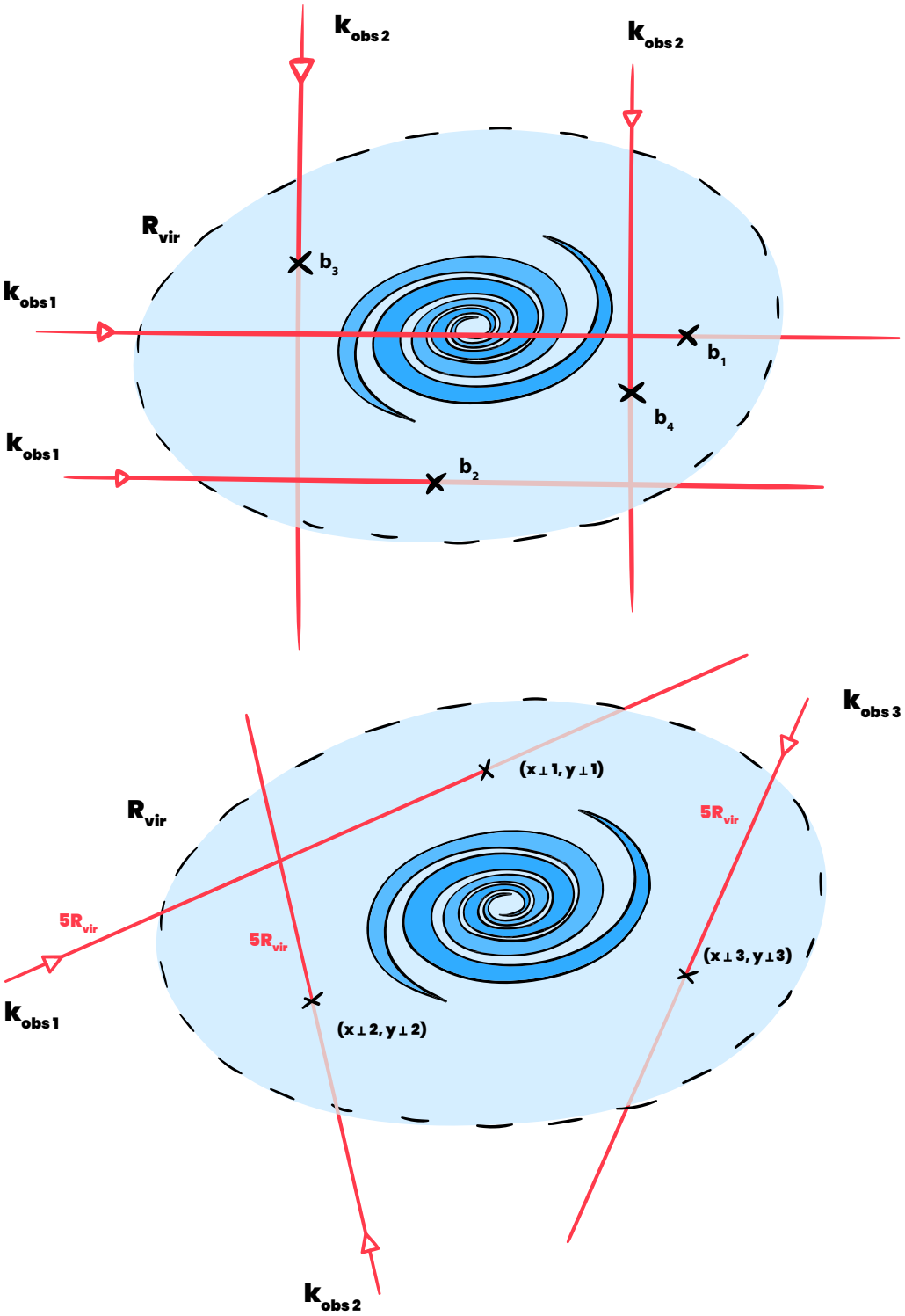

Figure 2.9 – Illustrations of the computation of column densities with and without RASCAS. The upper panel shows the method relying on the uniformisation of the grid and its projection on a 2D plane. This is done along three different axes (we only show two for clarity). The lower panel shows the method relying on ray tracing from RASCAS, with rays crossing the CGM from random directions.

children cells (this is illustrated by going from the middle panel of Fig. 3.1 to the right panel). All cells are then at the same level and can be projected in a 2D plane. This method however presents several limitations. Projecting an array of cubic cells at a random angle is complex. We thus only used the three axes naturally present in the simulation and do not trace a random angle to the galaxy plane. Also, these operations are costly and increase drastically with increasing computation domain. We illustrate this method on the upper panel of Fig. 2.9.

For all the results presented here, we thus rely on RASCAS (Michel-Dansac et al., 2020a,b) for more precise computation of the column densities. We first initialise rays. The two ingredients to initialise rays are a random direction $\mathbf{k}_{\rm obs}$ and a random position defined by $x_\perp$ and $y_\perp$ on the plane perpendicular to $\mathbf{k}_{\rm obs}$ which contains the centre of the galaxy. Then, from these two quantities, the starting position of the ray can be determined by following $-\mathbf{k}_{\rm obs}$ over a distance of half the integration length Δz (we want the integration length to be centred on the plane containing the galaxy centre). With RASCAS, we then propagate the ray and integrate densities of the cells crossed from its starting point, following $\mathbf{k}_{\rm obs}$ over Δz. We do this for 10^5 rays, chose a maximal impact parameter of 2 $\mathrm{R_{vir}}$ and an integration length of $\Delta z = 5$ $\mathrm{R_{vir}}$. We illustrate this process in the lower panel of Fig. 2.9.

Chapter 3

Subgrid physics

As simulations are limited in resolution, the effect of small-scale phenomena on large scales has to be modelled explicitly through *subgrid models*. A perfect example is the modelling of stellar physics in galaxy formation simulations. While stars have a typical scale of $10^{-11} - 10^{-8}$ pc, they can have an impact reaching the galactic scale and beyond. However, the typical resolution of state-of-the-art galaxy formation simulations reaches at best $\sim 10^{1}$ pc. It is thus necessary to be able to model their unresolved formation as realistically as possible, along with the processes they induce (stellar winds, SNe, ...). In this section, we present different published models and their implementation in the RAMSES simulations. We introduce star formation subgrid models with a *standard* approach based on the Schmidt law and a density threshold. It is used in most cosmological simulations and we will follow the model from Agertz et al. (2013). We then detail the multi-freefall star formation model and its implementation by Kimm et al. (2017) and Kretschmer & Teyssier (2020). After briefly explaining what runaway stars are and their implementation, we describe different approaches to supernova modelling. To this aim, we define what overcooling is and the different methods used to compensate for it. More specifically, we introduce the delayed cooling from Teyssier et al. (2013), and the mechanical feedback used in Agertz et al. (2013), Kretschmer & Teyssier (2020), and Kimm et al. (2015). We then present two other sources of feedback, radiative feedback and stellar winds, before concluding this chapter.

3.1 Star formation

Since current mass resolution in galaxy formation simulations cannot realistically resolve stars individually, they are modelled as *stellar particles*. These objects effectively represent single stellar populations, in other words, a group or cluster of stars that formed together and thus have identical ages and metallicities. They are characterised by their mass, metallicity, age, position, and velocity.

Their formation is modelled in three steps. The first is to determine whether the current cell can be star-forming, typically depending on its density. For example, star formation is generally not considered at densities lower than 0.1 cm^{-3} in Kretschmer & Teyssier (2020) to avoid useless computational expenses. The mass of gas that will turn into a population of stars is computed through a *star formation efficiency* (SFE) parameter ϵ_{ff}. These two steps are those differing the most with different models. We describe these steps for the three subgrid models we adopt in our simulation in Sec. 3.1.1 and Sec. 3.1.2. The third step is common to many models and consists of Poisson-sampling the computed star forming mass (with a roof value of 90% of the cell gas mass), and expressing it in units of $m_{*,\mathrm{min}}$.

$m_{*,\mathrm{min}}$ is the minimal mass of a stellar particle and is set to match the resolution of the rest of the simulation while limiting its computational cost and avoiding having to sample the IMF. We use a value of $\sim 1600 - 3200$ $\mathrm{M}_\odot$ in most of our simulations, except when testing the effect of this mass on the simulations. A smaller value reflects modelling closer to reality (we ideally want to model stars individually) but also an increased computational cost. Also, we model these stellar particles as single stellar populations described by an averaged Kroupa IMF (Kroupa, 2001). If the stellar particles' masses are smaller than ~ 500 $\mathrm{M}_\odot$, explicitly sampled IMF would be needed (Smith, 2021).

3.1.1 Schmidt law

The basis to star formation in simulations is to consider how much of the gas in a given cell will collapse and form a star. If we consider a spherical body with a density ρ and no pressure support, it can be shown that the typical time it would take to collapse on itself due to its gravity is the free-fall time

$$t_{\mathrm{ff}} = \left(\frac{3\pi}{32\rho G}\right)^{1/2}. \tag{3.1}$$

From this, a first straightforward approach to the physics governing the gravitational collapse of a molecular cloud can be derived. If we consider an isolated spherically symmetric gas cloud, as it is only bound by its gravity, one can argue that the rate of star formation will scale linearly with density and be inversely proportional to t_{ff}, so that

$$\dot{\rho} = \epsilon_{\mathrm{ff}} \frac{\rho}{t_{\mathrm{ff}}} \propto \rho^{1.5}, \tag{3.2}$$

where ϵ_{ff} is a global efficiency parameter. This hypothesis closely resembles the Kennicutt-Schmidt relation, which correlates empirically the gas surface density to the stellar surface density with a power-law index of ~ 1.4 (Schmidt, 1959; Kennicutt, 1998; Agertz et al., 2011). The efficiency depends on several parameters such

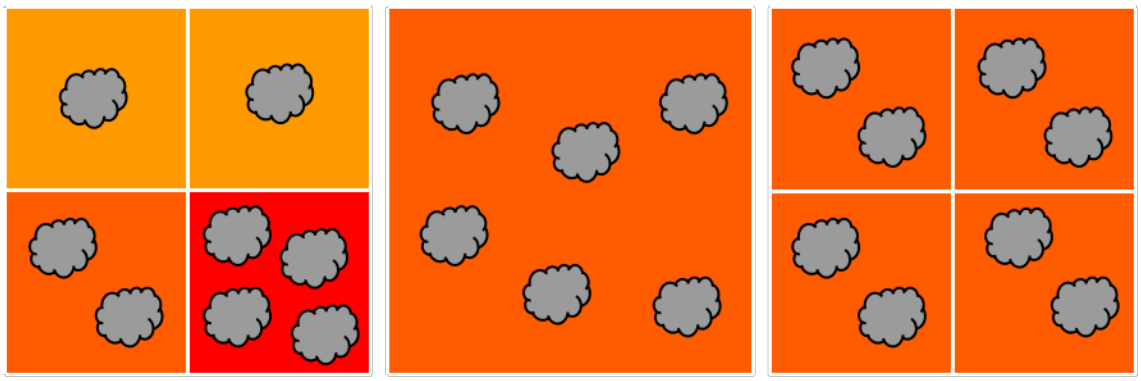

Figure 3.1 – Example of star formation at low and high resolution. We represent the gaseous mass with clouds and the density with colours (redder colours correspond to higher densities). These three grids all have the same mass, but different resolutions. In the left panel, the densest cell is denser than in the lower-resolution cell. With a density threshold criterion, this difference can lead the left grid to form a stellar particle, while the right one does not.

as the local star formation efficiency (protostellar jets, winds), the turbulence of the medium, and the structure of the molecular cloud, and is often calibrated by hand.

This is the model followed in (Agertz et al., 2013) and is used alongside a density threshold n_* and a temperature threshold T_*. The temperature criterion depends on the polytropic equation of state (Dubois & Teyssier, 2008b)

$$T_{\rm poly} = T_0 \left(\frac{n_{\rm H}}{n_*}\right)^{g_*-1}, \tag{3.3}$$

with $T_0 = 0.01$ and $g_* = 2$. The temperature threshold for star formation is then given by $T_* = (2 \times 10^4 + T_{\rm poly})$ K. The role of this additional pressure criterion is to prevent artificial fragmentation and gas collapse in regions where the molecular clouds are unresolved. However, since $T_0 = 0.01$ and the density in most cells is typically lower than $n_* = 10^3$ cm^{-3}, the polytropic temperature is far lower than 2×10^4 K and should play a negligible role. We use a density threshold of $n_* = 25$ cm^{-3} unless stated otherwise. If the density of the cell is below n_* or if the local temperature T is higher than the temperature threshold T_*, star formation is not allowed (if the gas is too hot or not dense enough, pressure will counter the gravitational force). Otherwise, star formation can take place with a star formation efficiency $\epsilon_{\rm ff}$. In the following simulations, we fix most of these parameters, except for the density threshold and the global star formation efficiency.

In the scope of numerical simulations with fixed parameters, the result of this star formation scheme depends on the resolution of the simulation. As illustrated by Fig. 3.1, if one considers a group of pixels in a high-resolution simulation with a dense pixel surrounded by lower density pixels (left panel), the equivalent lower resolution pixel would have a lower density (middle panel). Except for resolution, the lower resolution pixel is equivalent to the grid shown in the right panel. The difference between the rightmost and leftmost panels shows how density structures are impacted by resolution. Additionally, depending on the density threshold chosen, say 3 clouds/cell in this illustration, the high-resolution simulation (left panel) forms

stars while the low-resolution one (middle panel) does not. The seemingly simple density threshold model thus requires precise knowledge of star formation and its calibration to be used properly.

3.1.2 Multi-freefall

A major limit to the model presented in Sec. 3.1.1 is that it was found that the star formation efficiency parameter depends on its environment (Murray, 2011; Padoan et al., 2012). Molecular clouds are seldom spherical and sufficiently isolated to safely ignore their surroundings. They are typically found in the ISM and host powerful events such as SN which induce turbulence as well as their dispersal. This leads to different global efficiencies in star formation. We present here an alternative model that takes the variation of the global star formation efficiency into consideration.

General principle

Krumholz & McKee (2005) improved the model relying on a density threshold and a constant star formation efficiency by defining a variable star formation efficiency. This new definition depends on both the density and the turbulent state of the gas and removes the need for a density threshold. Indeed, the star formation efficiency in regions with densities too low to form stars is naturally small, leading to no star formation. The model with a variable star formation efficiency was then further improved by Hennebelle & Chabrier (2011) by implementing a multi-freefall version of this model.

The two main assumptions of the multi-freefall models are that star formation occurs in a supersonic turbulent medium and that a log-normal probability density function describes its density. This corresponds to a normal distribution in $s \equiv \ln(\rho/\rho_0)$ described by

$$p_s(s) = \frac{1}{\sqrt{2\pi\sigma_s^2}} \exp\left(-\frac{\left(s+\frac{1}{2}\sigma_s^2\right)^2}{2\sigma_s^2}\right), \tag{3.4}$$

with ρ_0 being the mean density and $\sigma_s^2 = \ln(1+b^2\mathcal{M}^2)$ the standard deviation of the density due to its dependence to turbulence. b is the turbulent parameter and describes if the turbulence is in a purely solenoidal mode (divergence-free) or a compressive mode (curl-free) (Federrath et al., 2008). We use $b = 0.4$, which describes a mix of the two regimes (Federrath et al., 2010). $\mathcal{M} = \sigma_{1D}/c_s$ is the Mach number and depends on the thermal state of the gas through the sound speed c_s, and the turbulent state of the gas through the velocity dispersion σ_{1D}. We can then combine Eq. 3.1 and Eq. 3.4 to obtain the distribution of the local star formation rate density $\frac{\rho}{t_{ff}(\rho)} p_s(s)$. By normalising and then integrating this expression over all densities above a critical threshold s_{crit} (see Eq. 3.10 and Eq. 3.15 depending on the model), the dimensionless star formation rate is

$$\epsilon'_{ff} = \frac{\epsilon}{\phi_t} \int_{s_{crit}}^{\infty} \frac{t_{ff}(\rho_0)}{t_{ff}(\rho)} \frac{\rho}{\rho_0} p_s(s) ds \tag{3.5}$$

$$= \frac{\epsilon}{2\phi_t} \exp\left(\frac{3}{8}\sigma_s^2\right) \left[1 + \mathrm{erf}\left(\frac{\sigma_s^2 - s_{crit}}{\sqrt{2\sigma_s^2}}\right)\right], \tag{3.6}$$

where erf is the Gauss error function. Not all the gas falls onto the stars during a cloud collapse, as some of it is ejected through protostellar jets and winds. The *local* star formation efficiency ϵ is a constant used to account for these unresolved physics and ϕ_t accounts for the estimated error on the typical timescale over which the gas becomes unstable (Krumholz & McKee, 2005, hereafter KM05). The strength of this law is to be self-regulating, depending on the local conditions of the considered cell and its environment.

In the following sections, we present two implementations of the multi-freefall model from (Kimm et al., 2017) and (Kretschmer & Teyssier, 2020). Overall, they differ in their selection of star-forming cells and for three free parameters: the definition of the minimal density s_crit, the 1D turbulent gas velocity dispersion σ_1D and the value of ϵ/ϕ_t. We present them in the next sections.

Model from Kimm et al. (2017)

Local turbulence approximation

In the model based on Kimm et al. (2017), the first criterion to allow star formation is that the cell must have a hydrogen number density higher than 10 cm^{-3} and represent a local maximum over the six neighbouring cells. This avoids unnecessary computations and should not impact results. Then, it is verified that the flow is locally converging by computing $\nabla(\rho\mathbf{u})$. It is also checked that the turbulent Jeans length $\lambda_\mathrm{J,turb}$ is not resolved by at least 4 cells (i.e. that the gas is Jeans unstable), with

$$\lambda_\mathrm{J,turb}(\rho) = \frac{\pi\sigma_\mathrm{1D}^2 \pm \sqrt{36\pi c_\mathrm{s}^2 G\Delta x^2\rho + \pi^2\sigma_\mathrm{1D}^4}}{6G\Delta x\rho}, \tag{3.7}$$

As this is applied in the unresolved ISM which is considered isothermal ($\gamma = 1$), c_s is the isothermal sound speed, with $P = c_\mathrm{s}^2\rho$. The turbulent Jeans length is obtained by adding a turbulent pressure in the thermal Jeans length from Eq. 2.1 (Chandrasekhar, 1951; Bonazzola et al., 1987). The gas velocity dispersion σ_1D is obtained by first removing the average velocity of each cell and then estimating the norm of the gradient of the velocity field in the central cell such that $\sigma_\mathrm{1D} = \|A\|^2 = \mathrm{Tr}\left(AA^T\right)$, with the tensor

$$\mathbf{A} = \nabla(\rho\mathbf{u}) = \begin{pmatrix} \partial u_x/\partial x & \partial u_y/\partial x & \partial u_z/\partial x \\ \partial u_x/\partial y & \partial u_y/\partial y & \partial u_z/\partial y \\ \partial u_x/\partial z & \partial u_y/\partial z & \partial u_z/\partial z \end{pmatrix}. \tag{3.8}$$

Partial derivatives are obtained by interpolating the velocities from the neighbouring cells.

A stellar efficiency criterion of $\epsilon = 0.5$ is adopted, and the estimated error on the typical timescale over which the gas becomes unstable $\phi_\mathrm{t} = 0.57$ follows the best fit of an update of the results from Federrath & Klessen (2012) (*private communication with Taysun Kimm*).

Finally, following the multi-freefall extension of the model from Padoan & Nordlund (2011, hereafter PN11) and with the virial parameter

$$\alpha_\mathrm{vir} = \frac{5}{\pi\rho G}\frac{\sigma_\mathrm{1D}^2 + c_\mathrm{s}^2}{\Delta x^2}, \tag{3.9}$$

the threshold considered for the density above which star formation is allowed is given by

$$s_{\rm crit} = \ln\left[0.62\alpha_{\rm vir}\mathcal{M}^2\right]. \tag{3.10}$$

Fig. 3.2 shows the main variables to determine how star formation is set in the current implementation of the code for the model from Agertz et al. (2013) and Kimm et al. (2015). This illustrates the significant number of free parameters in such simulations.

Model from Kretschmer & Teyssier (2020)
Subgrid turbulence model, the implicit Large Eddy Simulation

In the model following Kretschmer & Teyssier (2020), the only criterion allowing for potential star formation is that the cell density should be higher than 0.1 cm^{-3}.

As presented earlier, the stability of a cloud depends mainly on its gravitational boundness (described by the virial parameter) and its collapse efficiency (depending on the local critical density and the density distribution of the gas). Both of these depend largely on the turbulent state of the gas (through $\sigma_{\rm 1D}$ and $\mathcal{M}$), making turbulence a major criterion in star formation. Turbulence modelling is one of the main differences between the star formation modelling of Kimm et al. (2017) and Kretschmer & Teyssier (2020). While Kimm et al. (2017) uses a local approximation of the turbulent state of the gas, Kretschmer & Teyssier (2020) uses a subgrid model for supersonic turbulent flows. This model relies on numerical diffusion from the large eddy simulation model instead of adding supplementary diffusion (Schmidt et al., 2006).

Writing the velocity field as $v = \tilde{v} + v''$, with $\tilde{v} = \overline{\rho V}/\bar{\rho}$ the mass-weighted average velocity and v'' the fluctuations relative to the mean, the turbulent kinetic energy can be written as

$$K_T = \frac{1}{2}\overline{\rho v''^2} = \frac{1}{2}\bar{\rho}\left(\sqrt{3}\sigma_{\rm 1D}\right)^2, \tag{3.11}$$

introducing the term $\sigma_{\rm 1D}$, which plays the same role as in the previous model presented from Kimm et al. (2017). The subgrid model does not modify the Euler conservation equations but instead considers an additional equation describing the turbulent kinetic energy of the gas as (Schmidt, 2014; Semenov et al., 2016)

$$\frac{\partial}{\partial t}K_{\rm T} + \frac{\partial}{\partial x_j}\left(K_{\rm T}\widetilde{v_j}\right) + \frac{2}{3}K_{\rm T}\frac{\partial \tilde{v}_j}{\partial x_j} = C_{\rm T} - D_{\rm T}. \tag{3.12}$$

$C_{\rm T}$ is a creation term:

$$C_{\rm T} = 2\mu_{\rm T}\sum_{ij}\left[\frac{1}{2}\left(\frac{\partial \widetilde{v_i}}{\partial x_j} + \frac{\partial \widetilde{v_j}}{\partial x_i}\right) - \frac{1}{3}(\nabla\cdot\widehat{\mathbf{v}})\delta_{ij}\right]^2 = \frac{\bar{\rho}\Delta x}{2}\sigma_{\rm 1D}\left|\bar{S}_{ij}\right|^2, \tag{3.13}$$

expressed in the mixing length theory, which describes momentum transfer at the boundaries of a Newtonian fluid through eddy viscosity. The destruction term $D_{\rm T}$ describes the dissipation through a turbulent cascade on a crossing time

$$D_{\rm T} = \frac{K_{\rm T}}{\tau_{\rm diss}} = \sigma_{\rm 1D}\frac{K_{\rm T}}{\Delta x}. \tag{3.14}$$

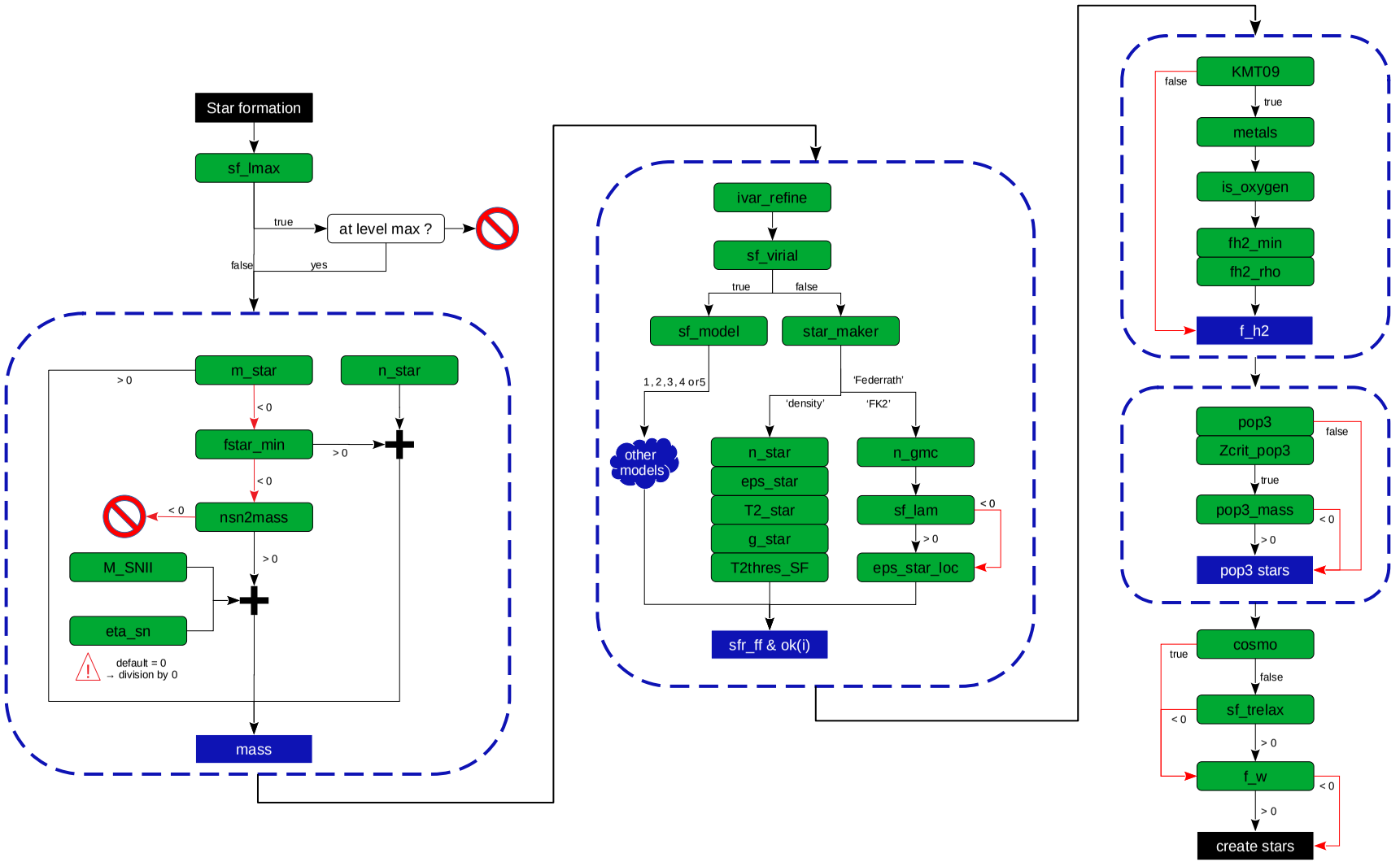

Figure 3.2 – Principle scheme for star formation in *ramses_cral*. The filled green boxes are the variables set by the user, and the blue ones show the computed quantity. *sfr_ff* corresponds to the star formation efficiency $\epsilon'_{\rm ff}$, and *ok(i)* is a flag that enables or not star formation in the cell i. The model from Kimm et al. (2015) and Agertz et al. (2013) are respectively following 'FK2' and 'density' with the *star_maker* variable.

With the turbulence σ_{1D} impacting $\mathcal{M}$ and α_{vir} (see Eq. 3.9), Kretschmer & Teyssier (2020) then write the critical density as (Krumholz & McKee, 2005)

$$s_{crit} = \ln\left[\alpha_{vir}\left(1 + \frac{2\mathcal{M}^4}{1+\mathcal{M}^2}\right)\right]. \tag{3.15}$$

This model also assumes that $\phi_t = 1$ and that all the gas fall into the star on a local scale $\epsilon = 1$ (compared to $\frac{\epsilon}{\phi_t} \sim 0.88$ in the previous model).

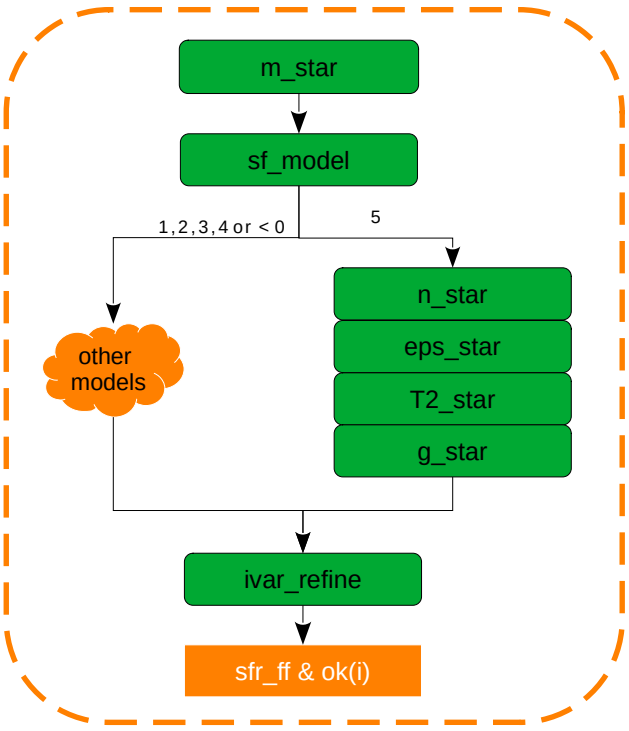

Figure 3.3 – Principle scheme for star formation in *ramses_cral*. The filled green boxes are the variables set by the user. *sfr_ff* is the global star formation efficiency and *ok(i)* is a flag that enables or not star formation in the cell *i*. This model is in a patch independent of the two previously shown, and case 5 for *sf_model* corresponds to Kretschmer & Teyssier (2020).

As for the previous models, Fig. 3.3 shows the variable controlling star formation when we follow Kretschmer & Teyssier (2020) in *ramses_cral*.

3.2 Runaway stars

For decades, stars have been observed with discrepant velocities above that of their surroundings (Blaauw & Morgan, 1954; Blaauw, 1956, 1961). One of the explanations lies in gravitational interactions when close encounters between stars and binaries occur and can lead to the ejection of stars out of their birth clouds (Schoettler et al., 2022). The velocities of these *runaway stars* are such that they can travel to lower-density regions before undergoing supernovae. By having less material to

push on the path of the generated shockwave, they retain more energy while producing stronger outflows and reaching bigger scales than when trapped in their dense local cloud. This can lead to more numerous supernovae explosions in low-density media, an order of magnitude higher mass loading factors and a more extended multiphase CGM alongside a population of cold dense clouds in the halo Andersson et al. (2020). Such an effect is unresolved and often ignored in simulations. We introduce a variation of the model following Kimm et al. (2017) by also testing this effect. Usually, when stars are formed, they are given the velocity properties of their host cell. Here, we model runaway stars by giving their initial velocity an additional random kick. Andersson et al. (2020) used a power law model with velocities ranging from 3 km s^{-1} to 385 km s^{-1} with 14% of the stars moving faster than 30 km s^{-1}, in good agreement with observations from Maíz Apellániz et al. (2018). Here, in the hope to increase the impact of runaway stars and obtain a more drastic change in the simulations, we choose to give a uniform kick within $0 - 50$ km s^{-1} to each stellar particle. At 50 km s^{-1}, a stellar particle can thus travel ~ 150 pc (a few cells at our resolutions) before producing the first supernovae (~ 3 Myr). In this model, energy is injected as momentum is not conserved when giving the kick.

3.3 SNe feedback

It is widely believed that the most important form of feedback for galaxies with masses typically lower than the Milky Way is SN-induced feedback. When massive stars die, they typically inject 10^{51} erg into their environment. This energy can disrupt molecular clouds and heat them, hence hindering star formation, as well as ejecting gas out of the galaxy, thus removing the very fuel needed for star formation. Most SNe are in the form of SNII (Sec. 1.3.3) so some models chose to ignore SNIa.

We can broadly summarise the principle of supernova modelling in three steps. The first step is to determine whether the stellar particle will host supernovae, and, if it does, their number. The second step is to compute the corresponding energy thermal energy. The third is, depending on the model, either to inject this thermal energy into the host cell or to convert this thermal energy into kinetic energy and inject it into the neighbouring cells. Each of those steps can differ between models, and we present different approaches in the following sections, namely the thermal feedback, the delayed cooling feedback and the mechanical feedback.

3.3.1 Thermal feedback

The first approach to model SN feedback is to model what happens physically by injecting the energy of the supernova as thermal energy.

When the stellar particle reaches a given age (50 Myr in our simulations), the supernova event occurs for all stars within the population it represents, and thermal energy is injected into the supernova host cell. The mass of the ejecta is described by $M_{\rm ej} = \eta_{\rm SN} M_{\rm star}$, with $M_{\rm star}$ the mass of the stellar particle and $\eta_{\rm SN}$ the fraction of the stellar particle's mass undergoing supernovae. The metallicity of the ejecta is $Z_{\rm ej} = \eta_Z + (1d0 - \eta_Z)Z$, with $\eta_Z = 0.075$.

A major problem this model quickly faced is *overcooling* as radiative losses were too efficient, preventing the SN energy from developing into a shockwave. Indeed,

SNe typically occur in dense hot (due to the SN) media in which radiative cooling is particularly efficient (Sec. 2.4.2) and leads to a very short cooling time. Besides, the dynamical time of the supernova is directly related to the resolution in simulations (if a simulation is at a lower resolution, the supernova will take more time to expand). Thus, in a *low resolution* simulation, the characteristic time for the supernova expansion will be far greater than the cooling time and lead to over-efficient cooling (Katz, 1992; Cho & Kang, 2008; Ceverino & Klypin, 2009; Chaikin et al., 2022). All the energy of the SN is hence radiated away before it can develop into a shockwave and impact its surrounding medium. Even increasing the thermal energy is not sufficient, as the cooling time in such regions is very small (Springel & Hernquist, 2003). With the main obstacle to star formation removed, the gas collapses and cools in an unhindered fashion, leading to an excessive star formation rate. This model thus produces unrealistic results in galaxy formation simulations, with a stellar mass in galaxies significantly above the expected halo mass to stellar mass relation (Sec. 1.3.4) (Agertz et al., 2013; Rosdahl et al., 2017). However, note that smaller-scale simulations with high enough resolution can resolve the Sedov-Taylor phase and avoid overcooling (Rey et al., 2022). The primary drive for subgrid models developed henceforth was hence to overcome this *overcooling* problem by different means.

3.3.2 Delayed cooling

The first solution we present is to turn cooling off for a certain amount of time around SN regions. With the cooling turned off, the SN energy can expand naturally and form a shockwave (Gerritsen & de Blok, 1999; Stinson et al., 2006; Governato et al., 2010; Teyssier et al., 2013; Rieder & Teyssier, 2016). In this work, we use the implementation of Teyssier et al. (2013), with the use of a tracer variable $\epsilon_{\rm DC}$. The core principle of this approach is to consider how the cooling switch $\epsilon_{\rm DC}/\rho$ compares to a given threshold. If the cooling switch is strictly above the chosen threshold, cooling is turned off and the thermal energy loss is ignored. Once the cooling switch gets below the threshold, cooling is re-activated. Other than this, the prescription is the same as for thermal feedback.

The first step to model this approach is to inject the SN energy as thermal energy. Then for each SN, the variable $\epsilon_{\rm DC}$ is increased by a value corresponding to the SN mass loss $\dot{M}_{\rm loss}$. For each timestep, $\epsilon_{\rm DC}$ is then exponentially dampened over a dissipation timescale $t_{\rm diss}$. The evolution of $\epsilon_{\rm DC}$ can thus be described by

$$\frac{{\rm D}\epsilon_{\rm DC}}{{\rm D}t} = \frac{\dot{M}_{\rm loss}}{\Delta x^3} - \frac{\epsilon_{\rm DC}}{t_{\rm diss}}. \tag{3.16}$$

$\epsilon_{\rm DC}$ is treated as a passive scalar advected with the gas. We use a threshold of 10^{-3} (Teyssier et al., 2013; Rosdahl et al., 2017, it can also be interpreted as a speed) and a typical molecular cloud lifetime of 10 Myr for our dissipation timescale (Williams & McKee, 1997; Teyssier et al., 2013).

Though widely used, critics are that it leads to over-predictions of thermal energy and momentum in SN remnants (Martizzi et al., 2015). As we are ignoring here a physical process that hinders the expansion of SN, the energy it transfers to its ambient medium might be over-estimated. However, it can be argued that it is fair

compensation for the non-simulated non-thermal phenomenon that would store the SN energy and induce a significantly longer dissipation timescale. Such processes would be the turbulence and magnetisation of SN remnants (seen to be strong in X-ray) (Teyssier et al., 2013). As they are relativistic, there could also be an impact from cosmic rays by affecting the dynamics of the propagating shockwave (Ellison et al., 2004; Ferrand & Marcowith, 2010). This model can lead to unrealistic values in the temperature-density phase diagram, as shown in Sec. 5.3, but these only represent a small fraction of the gas, which is furthermore concentrated in the ISM.

3.3.3 Mechanical feedback

As explained in Sec. 1.3.3, an SN can be described through two main phases at our scales, which are both described analytically. A second solution to the overcooling problem, the *kinetic feedback*, is thus to wholly ignore the first phase and inject directly the energy of the blast wave in kinetic form (Navarro & White, 1993; Dubois & Teyssier, 2008a). Given the high Mach number, a shock immediately develops and converts this energy into thermal energy which is once more dissipated through overcooling if the resolution is not sufficient. An improved version dubbed *Mechanical feedback* was then developed in Kimm & Cen (2014) and Hopkins et al. (2014) to inject the correct momentum in the snowplow phase. In this prescription, a chosen quantity (the resolution of the SN host cell or the ejected mass, depending on the model) is evaluated and compared to an analytical value to determine in which regime the SN is expected to be. Then, depending on the result, different momentum injections are considered. In the following sections, we describe models from Agertz et al. (2013); Kimm et al. (2015); Kretschmer & Teyssier (2020).

Model from Agertz et al. (2013)
Cooling radius and momentum injection

In this model, both SNIa and SNII are modelled, assuming that they both release the same energy and that they are injected in the same fashion. In both cases, the first step is to compute the mass of stars that exit the main sequence at a given timestep, depending on the age of the stellar population and its metallicity. This is applied for all stellar particles and at every timestep following Raiteri et al. (1996). By considering the age of the stellar population before and after the timestep, a maximal mass M_+ and a minimal mass M_- can be obtained (massive stars explode earlier). Depending on these masses, processes for either SNIa or SNII are treated. For both SNIa and SNII, the expected number of supernovae is then computed by integrating a normalised Chabrier IMF Chabrier (2003) between the minimal and the maximal mass of the stars (M_- and M_+). We describe in the next paragraphs how they are computed in more detail and the resulting mass of the ejecta.

SNII

If both M_- and M_+ are within $8 - 80$ $\mathrm{M}_\odot$, the stellar particle will host SNII, and

$$N_{\mathrm{SNII}} = -M_{\mathrm{init}} \frac{0.31491}{1.3} \left(M_+^{-1.3} - M_-^{-1.3} \right), \tag{3.17}$$

where M_{init} is the initial mass of the stellar particle.

To compute the mass ejected, we define the average mass of the supernovae $M_{\rm mean} = (M_+ + M_-)/2$. The mass ejecta then follows $M_{\rm ej} = 0.7682 N_{\rm SN} M_{\rm mean}^{18/17}$ (Woosley & Weaver, 1995; Raiteri et al., 1996), with an upper limit which is the current mass of the particle minus 10% of its initial mass. With $M'_{\rm mean} = \min(M_{\rm mean}, 40\ {\rm M}_\odot)$, the mass loss in Fe and O is given by (Woosley & Heger, 2007)

$$M_{\rm loss,Fe} = \frac{0.375}{\Delta x^3} N_{\rm SN} e^{-17.94/M'_{\rm mean}}\ {\rm M}_\odot, \tag{3.18}$$

$$M_{\rm loss,O} = \frac{27.66}{\Delta x^3} N_{\rm SN} e^{-51.81/M'_{\rm mean}}\ {\rm M}_\odot. \tag{3.19}$$

SNIa

If both M_- and M_+ are within $1.5 - 8\ {\rm M}_\odot$, the stellar particle will host SNIa. For this case, the IMF of the secondary star also has to be considered (Greggio & Renzini, 1983; Raiteri et al., 1996). In the same fashion, the number of SNIa is given by

$$N_{\rm SNIa} = M_{\rm init}(M_+ - M_-)\frac{N_{-,\rm SN} + N_{+,\rm SN}}{2}. \tag{3.20}$$

Here, $N_{\pm,\rm SN} = -0.31491 f_{\rm SNIa} M_\pm^{2/3.3}\left((2M_\pm)^{-3.3} - (M_\pm + 8)^{-3.3}\right)$ and $f_{\rm SNIa} = 0.16$ is the fraction of SNIa, based on the SN rate in Milky Way-like galaxies van den Bergh & McClure (1994). Each SNIa is assumed to be at the Chandrasekhar limit ($M_{\rm ch} = 1.4\ {\rm M}_\odot$). The mass ejected in that case is assumed to be $M_{\rm ej} = N_{\rm SN} M_{\rm ch}$ with the same upper threshold as for SNII. The metals injected are then given by $M_{\rm loss,Fe} = 0.63 N_{\rm SNIa}/\Delta x^3$ and $M_{\rm loss,O} = 0.13 N_{\rm SNIa}/\Delta x^3$ (Thielemann et al., 1986).

We then estimate the radius at which the cooling time is equal to the age of the SN remnant. Agertz et al. (2013) follows Blondin et al. (1998); Hopkins et al. (2013); Cioffi et al. (1988) to write

$$R_{\rm cool} = 30 N_{\rm SN}^{5/17} n_{\rm H}^{-0.43} (Z' + 0.01)^{3/17}\ {\rm pc}. \tag{3.21}$$

This radius is then compared to the maximal cell resolution Δx. If the cooling radius is resolved by at least 3 cells (Kim & Ostriker, 2017), the Sedov-Taylor phase is considered and the momentum injected is given by

$$p_{\rm ad,Ag} = 3.6 \times 10^4 N_{\rm SN}\ {\rm M}_\odot\,{\rm km\,s^{-1}}, \tag{3.22}$$

which corresponds to 12 $\rm M_\odot$ at 3000 $\rm km\,s^{-1}$ per SN event, calibrated on the STARBURST99 code (Leitherer et al., 1999, SB99). This equation is also the one used in the case of very diffuse gas with densities of 10^{-4} $\rm cm^{-2}$. Otherwise, the snowplow phase is considered, and the momentum injected is initialised following (Thornton et al., 1998; Blondin et al., 1998; Kim & Ostriker, 2015; Hopkins et al., 2018)

$$p_{\rm rad,Ag} = 4.0 \times 10^5 N_{\rm SN}^{16/17} n_{\rm H}^{-2/17} Z'^{-0.2}\ {\rm M}_\odot\,{\rm km\,s^{-1}}. \tag{3.23}$$

This momentum corresponds to the momentum of the adiabatic phase at the transition from the energy-conserving phase to the momentum-conserving phase. The mass and momentum are then injected in the seven neighbouring cells included in the corresponding oct equally, considering that the SN occurred at its centre and ignoring densities anisotropy.

Model Kretschmer & Teyssier (2020)
Cooling radius, thermal energy and momentum injection

In this model, type II supernovae explode only from $t_0 = 3$ Myr to $t_{\rm end} = 20$ Myr, and the average number of events per stellar particle is given by

$$\overline{\mathrm{d}N_{\rm SN}} = \eta_{SN} \frac{M_{init}}{M_{SN}} \frac{\mathrm{d}t}{t_{\rm end} - t0}. \tag{3.24}$$

M_{init} is the initial mass of the stellar particle and $\mathrm{d}t$ is the local timestep. The factor $\mathrm{d}t/(t_{\rm end} - t0)$ henceforth describes a uniform sampling of supernovae through time. They use a value of $M_{SN} = 10$ M$_\odot$ as the mass of the average SNII. This number of supernovae is then Poisson-sampled and the ejecta mass is given by $M_{\rm ej} = N_{\rm SN} M_{SN}$.

In all cases, the supernova energy is deposited as thermal energy, as presented in Sec. 3.3.1. If the cell has a resolution high enough to resolve the Sedov-Taylor phase, the correct amount of energy is injected, and a shockwave will be able to form. Otherwise, this energy will be radiated away through spurious cooling. In this case, the snowplow phase is modelled directly and the expected energy is additionally included as kinetic energy.

The transition at which the radiative losses become important is defined through a cooling radius, as done with Agertz et al. (2013) and is given by (Martizzi et al., 2015)

$$R_{\rm cool,Kr} = 6.3 \left(\frac{n_{\rm H}}{100}\right)^{-0.42} Z'^{-0.05} \text{ pc}. \tag{3.25}$$

If the cooling radius is not resolved by at least four cells, the momentum considered is

$$p_{\rm rad,Kr} = 1.11 \times 10^5 \eta_R N_{\rm SN} Z'^{-0.114} \left(\frac{n_{\rm H}}{100}\right)^{-0.19} \text{ M}_\odot \,\text{km}\,\text{s}^{-1}, \tag{3.26}$$

with $\eta_R = \min\left(1, \left(\frac{\Delta x_{\rm min}}{R_{\rm cool}}\right)^{3/2}\right)$.

Unlike previous models, this momentum is not solely injected in the form of momentum in the neighbouring cells but also converted to a supernovae dynamical pressure $P_* = p_{\rm rad,Kr2}/\Delta x^2 \Delta t$ and added to the momentum equation (inspired by another model from Agertz et al. 2013 and by Hopkins et al. 2014)

$$\frac{\partial}{\partial t}(\rho \mathbf{u}) + \nabla \cdot (\rho \mathbf{u} \otimes \mathbf{u}) + \nabla (P + P_\star) = -\rho \nabla \Phi. \tag{3.27}$$

Its work is furthermore removed from the energy equation, to obtain

$$\frac{\partial}{\partial t}(\mathcal{E}) + \nabla \cdot [(\mathcal{E} + P + P_\star)\mathbf{u}] = P_\star \nabla \cdot \mathbf{u} - \rho \mathbf{u} \cdot \nabla \Phi + \Lambda(\rho, \varepsilon). \tag{3.28}$$

The location of each explosion is chosen at random amongst the eight cells comprised in the oct hosting the supernova to try to avoid gird alignment effects (due to the structure of the grid, propagation along the closest neighbours is favored). It furthermore injects 10% of its mass into the medium as metals. There is both a weak and a strong version of this model where the exponents used differ (Kretschmer et al., 2020; Kretschmer & Teyssier, 2020) but we did not find a significant difference between both and used the weak version.

Model from Kimm et al. (2015)
Ejected mass ratio and momentum injection

The first condition for a supernova to occur in this model is that the stellar particle must be older than

$$t_0 = \frac{0.08612668 + 0.1698731 \log Z" - 0.1867337 \log Z"^2}{0.04208666 + 0.02152643 \log Z" + 0.07893866 \log Z"^2}, \tag{3.29}$$

with $Z" = \max(\min(Z, 0.05), 0.008)$. This translates into an age that ranges within $0 - 2.29$ Myr and younger than 50 Myr. In this model, the total number of SNe that could occur for a given stellar particle is given by $N_{\rm SN} = \eta_{\rm SN} M_{\rm part}/M_{\rm SNII}$ with $M_{\rm part}$ the mass of the stellar particle, $M_{\rm SNII} = 20$ M$_\odot$ the mean mass of SNII (following the Kroupa IMF) and $\eta_{\rm SN} = 0.2$ (Few et al., 2012) the mass fraction of a stellar population that will turn into SNe. Then, based on the total number of SNe, $N_{\rm SN}$, that might occur, the lifetime of each of these massive stars is sampled randomly over time, relying on a polynomial fit to the integrated SNII rate. This computed rate is obtained through the population synthesis code SB99 (Leitherer et al., 1999) and depends both on the age of the stellar population (and thus of the star considered) and on its metallicity. This is illustrated in Fig. 2 of Kimm et al. (2015) and enables the modelling of multiple explosions in time instead of a single one per stellar particle.

We now define χ, the ratio of the mass initially ejected by the supernova, $M_{\rm ej} = M_{\rm SNII} N_{\rm SN}$, to the mass of the supernova wind, $M_{\rm W}$. The wind mass is composed of the mass swept up by the supernova, both from the host cell ($M_{\rm host}$) and the neighbouring cells (M_{nei}), as well as the ejected gas. The ratio of both these quantities is then given by

$$\chi \equiv \frac{{\rm d}M_{\rm W}}{{\rm d}M_{\rm ej}} = \frac{M_{\rm nei} + \frac{1}{N_{\rm c}}\left(M_{\rm host} + M_{\rm ej}\right)}{\frac{1}{N_{\rm c}} M_{\rm ej}}, \tag{3.30}$$

where $N_{\rm c} = 52$ is the number of cells over which mass is spread (48 neighbouring cells[1] plus 4 host cells[2]).

The momentum of the adiabatic phase in Kimm et al. (2015) is then given by

$$p_{\rm ad,KI} = \sqrt{2 \chi M_{\rm ej} f_{\rm e} E_{\rm SN}}, \tag{3.31}$$

with $E_{\rm SN} = 10^{51}$ erg the SN energy, and $f_{\rm e} = 1 - (1 - f_{\rm tr})(\chi - 1)/(\chi_{\rm tr} - 1)$ a factor ensuring a smooth transition between the momentum of the adiabatic phase and the momentum of the radiative phase. $f_{\rm tr} = 0.676$ is the fraction of the supernova energy in kinetic form (Blondin et al., 1998). The momentum of the radiative phase

[1] In case the neighbouring cells have a different resolution than the central cell, all cells involved in the computation are considered to be one level higher than the host cell. Then, the number of neighbour cells sharing at least two vertices is $N_{\rm nei} = 48$ (6 neighbours share exactly 4 vertices and 12 neighbours share only 2).

[2] As we consider cells one level higher than the host cell, one would expect $N_{\rm cen} = 8$. However, by doing so, the central cell has more weight (8 higher-resolution cells) than its immediate neighbours (4 higher-resolution cells for each of the neighbours sharing 4 vertices). Thus, to distribute mass more evenly between the central cell and the immediate neighbours, it was decided that $N_{\rm cen} = 4$.

is given by (Blondin et al., 1998; Thornton et al., 1998; Kim & Ostriker, 2015; Martizzi et al., 2015)

$$p_{\rm rad,KI} = 2.5 \times 10^5 N_{\rm SN}^{16/17} n_{\rm H}^{-2/17} Z'^{-0.14}\ {\rm M}_\odot\,{\rm km\,s^{-1}}. \tag{3.32}$$

To determine the phase of the blast wave, we compare χ to a transition mass ratio, which is obtained by equating the momentum of the snowplow (momentum conserving) phase $p_{\rm rad,KI}$ to the momentum expected from the Sedov-Taylor phase at transition $p_{\rm ad,tr} = \sqrt{2\chi_{\rm tr} N_{\rm SN} E_{\rm SN} M_{\rm ej} f_{\rm tr}}$. We then obtain

$$\chi_{\rm tr} = \max\left(\frac{p_{\rm rad,KI}^2}{2N_{\rm SN}E_{\rm SN}M_{\rm ej}f_{\rm tr}}, 1\right). \tag{3.33}$$

For each supernova, the momentum is hence injected following

$$\Delta p = \frac{1}{N_{\rm c}} \begin{cases} \frac{1}{f_{\rm p}} p_{\rm rad,KI} & \text{if } \chi \geq \chi_{\rm tr}, \quad (3.34a) \\ p_{\rm ad,KI} & \text{otherwise.} \quad (3.34b) \end{cases}$$

When injecting gas into the neighbouring cells, the assumption is made that they are one level of resolution higher. If it is not the case, and they are at the same level, momentum is injected four times, but with the direction of the hypothetical higher resolution cell. When adding them, a component of the momentum is cancelled, which leads to an underestimation of the momentum injected. $f_{\rm p} = 0.9387$ is a correction factor included to compensate this direct momentum cancellation. The ejecta is injected alongside the momentum with a metallicity $Z_{\rm ej} = Z_{\rm star} + \eta_Z(1 - Z_{\rm star})$ and a constant yield of $\eta_{\rm Z} = 0.075$.

"Geen boost"

Geen et al. (2015) found that the momentum injected could be increased through early photoionisation by massive stars. By lowering the density of the cell hosting the star through a pressure increase before the supernova, more momentum is conserved as the supernova shell loses less energy to its surrounding gas. They even found that with photoionisation, the momentum injected is almost independent of density, unlike in equations presented earlier. The method detailed here is an extension applied to Kimm et al. (2015) and follows Kimm et al. (2017) with momentum fitted from Geen et al. (2015).

The momentum of the supernova including photoionisation is then given by

$$p_{\rm sn+ph} = 5 \times 10^5 N_{\rm SN}^{16/17} Z'^{-0.14}\ {\rm M}_\odot\,{\rm km\,s^{-1}} \tag{3.35}$$

instead of Eq. 3.32 (there is no density dependence and the normalisation is higher by a factor two). If the simulation furthermore includes radiative transfer (Sec. 2.5, the momentum is considered slightly differently. To properly include photoionisation, the radius of the Strömgren sphere $R_{\rm st}$ needs to be resolved (see Eq. 1.3). Thus, the momentum $p_{\rm rad,KI}$ (Eq. 3.32) and $p_{\rm sn+ph}$ (Eq. 3.35) are combined so that either of them is mainly considered depending on how well the Strömgren sphere is resolved, following

$$p_{\rm sn} = p_{\rm rad,KI} {\rm e}^{-\Delta x/R_{\rm st}} + p_{\rm sn+ph}(1 - {\rm e}^{-\Delta x/R_{\rm st}}). \tag{3.36}$$

Whether there is RT or not, the maximum between the henceforth computed momentum and the original value is retained.

For the adiabatic phase, the radial momentum $p_{\rm ad,KI}$ is boosted by the additional factor

$$B_{\rm ph} = \sqrt{1 + \left(\left(\frac{p_{\rm sn}}{p_{\rm rad,Geen}}\right)^{1/0.9} - 1\right)\left(2 - \frac{2}{1+\exp\left(-\frac{1}{0.3}\frac{\chi+1}{\chi_{\rm tr}+1}\right)}\right)}, \tag{3.37}$$

if its radicand is positive. $p_{\rm rad,Geen}$ has the same expression as $p_{\rm rad,KI}$ but with exponents of 0.9 and -0.15 for the number of supernovae and the density instead of 16/17 and $-2/17$.

Finally, the two regimes are defined by

$$\Delta p = \frac{1}{N_{\rm c}}\begin{cases} \frac{1}{f_p} p_{\rm sn} & \text{if } \chi \geq \chi_{\rm tr}, \quad (3.38a) \\ B_{\rm ph} p_{\rm ad,KI} & \text{otherwise.} \quad (3.38b) \end{cases}$$

Supernova rate boost

The model used in Kimm et al. (2015) is overall the one followed in the SPHINX simulations of Rosdahl et al. (2018). In order to match the observed stellar mass to halo mass relation, the star formation rate to halo mass relation and the UV luminosity function in these simulations, an enhanced version of the feedback had to be introduced: the average mass of an SN progenitor was divided by four to artificially boost the SN rate and hence the feedback strength. It can be seen as compensation for numerical overcooling, uncertainties on the IMF-estimated average SN host mass and the non-modelling of SNIa. When using the model from Kimm et al. (2015), we thus also change the average stellar mass of a supernova from $M_{\rm SNII} = 20$ M$_\odot$ to $M_{\rm SNII} = 5$ M$_\odot$. Similarly, for Kretschmer & Teyssier (2020), we change it from $M_{SN} = 10$ M$_\odot$ to $M_{SN} = 2.5$ M$_\odot$. We do not include this boost in the model from Agertz et al. (2013), as it already includes SNIa and stellar winds from massive stars.

To conclude on the different approaches to supernova feedback, we have seen that there can be different approaches to compensate for the numerical overcooling associated with thermal feedback. The two most used are currently *delayed cooling feedback* and *mechanical feedback*. Even though they are all similar in principle, different flavours of mechanical feedback are implemented.

As presented in table. 3.1, the first difference is the transition radius between the Sedov-Taylor phase and the snowplow phase. While Agertz et al. (2013) and Kretschmer & Teyssier (2020) consider a cooling radius, Kimm et al. (2015) considers the expected mass swept-up by the supernova.

We summarise the momentum injected with the different approaches in table 3.2. With the approach of Kretschmer & Teyssier (2020), thermal energy is injected in all cases and complemented with momentum in the radiative phase. Contrastingly, both Agertz et al. (2013) and Kimm et al. (2015) inject momentum whether the supernova is expected to have developed at the Sedov-Taylor phase or the snowplow phase. We also show the momentum boost expected from unresolved photoionisation which is then combined with that shown for Kimm+15.

Table 3.1 – Criterion to determine whether the supernova is in the radiative or the adiabatic phase at the cell scale. Both Agertz+13 and Kretschmer+20 are based on a cooling radius, while Kimm+15 is based on the ejected mass.

Model based on	Quantity considered	Transition value
Agertz+13	$3\Delta x$	$30 N_{\rm SN}^{5/17} n_{\rm H}^{-0.43} (Z' + 0.01)^{3/17}$
Kretschmer+20	$4\Delta x$	$44 n_{\rm H}^{-0.42} Z^{-0.05}$
Kimm+15	$\frac{M_{\rm nei} + 1/N_{\rm c}\left(M_{\rm host} + M_{\rm ej}\right)}{\frac{1}{N_{\rm c}} M_{\rm ej}}$	$\frac{p_{\rm rad,KI}^2}{2 N_{\rm SN} E_{\rm SN} M_{\rm ej} f_{\rm tr}}$

Table 3.2 – Rough summary of the driving equations for momentum or energy injection. In the Sedov-Taylor phase, there is also thermal energy injected for Kretschmer+20 and no density dependence for Geen+15. In the adiabatic phase, the approaches vary more significantly.

	Radiative phase	Adiabatic phase
Agertz+13	$4.0 \times 10^5 N_{\rm SN}^{16/17} n_{\rm H}^{-2/17} Z'^{-0.2}$	$3.6 \times 10^4 N_{\rm SN}$
Kretschmer+20	$2.97 \times 10^5 N_{\rm SN} n_{\rm H}^{-0.19} Z^{-0.114} \eta_R$ & $E_{\rm th}$	$E_{\rm th}$
Kimm+15	$2.64 \times 10^5 N_{\rm SN}^{16/17} n_{\rm H}^{-2/17} Z'^{-0.14}$	$\sqrt{2\chi M_{\rm ej} f_{\rm e} E_{\rm SN}}$
Geen+15	$5.0 \times 10^5 N_{\rm SN}^{16/17} Z'^{-0.14}$	$B_{\rm ph}\sqrt{2\chi M_{\rm ej} f_{\rm e} E_{\rm SN}}$

3.4 Radiative transfer feedback

As mentioned in Sec. 3.3.3, feedback can originate or be enhanced through radiation. An example is the UVB (radiation from the reionisation) which induces photoionisation feedback that heats the gas and can prevent faint dwarf galaxies from accreting gas and quench them (Rey et al., 2020, 2022). Agertz et al. (2013) and Kretschmer & Teyssier (2020) respectively developed a subgrid model for radiation pressure and photoionisation feedback, but as it is done without tracking radiation, we removed these two implementations. We model photoionisation and radiation pressure from young stars more precisely by relying on RT, in which they are both modelled alongside radiative heating (Rosdahl et al., 2013; Rosdahl & Teyssier, 2015). We present briefly the main equations describing them below.

Photoionisation

HII regions are spaces surrounding stars where radiation has ionised the gas (Sec. 1.3.3). This gas is thus heated up, which prevents stars from forming. The implementation used in Kretschmer & Teyssier (2020) illustrates this effect perfectly as it consists in simply heating the gas of the cell hosting the star to 10^4 K and keeping it at this temperature until 20 Myr after their birth, the time at which the supernova cycle ends. In RT, the flux of photons $F(\nu)$ is tracked. From this, the photoheating rate

can be computed as (Rosdahl, 2012)

$$\mathcal{H} = \sum_{j}^{\text{HI,HeI,HeII}} n_j \int_0^\infty \sigma_j(\nu) F(\nu) \left[h\nu - \epsilon_j\right] \mathrm{d}\nu, \tag{3.39}$$

with ν the frequency of the photons, $\sigma_j(\nu)$ the cross-section of the ion, n_j its density and ϵ_j its photoionisation energies. The UVB heating is also included through a redshift-dependent heating rate and typically heats the ionised gas to 2×10^4 K, except in dense regions where self-shielding is modelled as exponential damping of the UVB with density (Rosdahl et al., 2015).

Radiation pressure

Another effect of radiation is to transfer momentum to its surrounding gas and dust (which we don't trace in the simulation) as radiation pressure. It is implemented in the model following Agertz et al. (2013) but we switched off their modelling as it is implemented in RT. The direct momentum absorption rate per unit volume is given by Rosdahl & Teyssier (2015)

$$\dot{\boldsymbol{p}}_\gamma = \int_{\nu=0}^\infty \frac{\boldsymbol{F}_\nu}{c} \left(\kappa_\nu \rho + \sum_{j}^{\text{HI,HeI,HeII}} \sigma_{\nu j} n_j \right) \mathrm{d}\nu, \tag{3.40}$$

with bold to denote the vectors and κ_i the dust opacity (depends on temperature, dust, and the shape of the radiation spectrum). This is injected in the Euler momentum equation and is furthermore complemented by radiative pressure from isotropic diffusive radiation to properly model the diffusion of photons of the infrared group in the diffusion limit when photons propagation is described by a random walk.

3.5 Stellar winds

The only approach that models stellar winds is that of Agertz et al. (2013), which describes winds for both low and high-mass stars.

high-mass stars
If there are stellar particles younger than 10 Myr, a fraction of the mass of the stellar particle will be lost through winds from high-mass stars. This mass loss is uniformly distributed over 10 Myr, as

$$f_{\text{HM}} \sim 0.0341 \log \left(\frac{Z_*}{4.60697 \times 10^{-4}} + 1 \right) \frac{\mathrm{d}t}{10}. \tag{3.41}$$

The mass ejected is then given by $M_{\text{HM}} = \min(M_{\text{init}} f_{\text{HM}}, M_+)$, with a metallicity of $Z_{*,\text{Fe}}$ for iron and $Z_{*,\text{Fe}}$ for oxygen.

low-mass stars
If there are stellar particles with stars within $0.5 - 8$ $\text{M}_\odot$, they are considered for low-mass winds (Kalirai et al., 2008). Even if the momentum from these

winds is negligible, the mass cast off during their asymptotic giant branch phase is considerable. The fraction of low-mass stars is expected to follow

$$f_{\rm LM} = 0.31491(N_{+,LM} - N_{-,LM}), \tag{3.42}$$

with $N_{\pm,\rm LM} = 0.3031 M_{\pm}^{-0.3}/(M_{\pm} - 2.97)$, based on the Chabrier IMF (Chabrier, 2003). The mass and the metallicity of the ejecta are defined as they are for fast winds.

Synthesis and global models

We have presented in this section several subgrid models relevant to galaxy formation. The first ones we describe in Sec. 3.1 characterise star formation. Agertz et al. (2013) uses a Schmidt law above a density threshold (sometimes combined with a temperature threshold) to allow star formation or not. This also rely on a constant *global* star formation efficiency. The two other star formation models are two versions of the multi-freefall model Federrath & Klessen (2012) in which there is a varying star formation efficiency depending on the local conditions (mainly described through the Mach number and the virial parameter). Kimm et al. (2017) and Kretschmer & Teyssier (2020) follow slightly different equations, based respectively on Padoan & Nordlund (2011) and Krumholz & McKee (2005). Also, while Kimm et al. (2017) makes a local estimate of the turbulence, there is a dedicated subgrid model in Kretschmer & Teyssier (2020). We then complement these star formation prescriptions in Sec. 3.2 with that of runaway stars, in which stellar particles are given at birth an additional velocity relative to their birth clouds in the form of a kick. This allows them to produce more efficient feedback in lower-density regions. We then presented different implementations of the main expected outflow source in Sec. 3.3, type II supernovae. The first one is *thermal feedback* and consists in injecting energy into the cell at which the supernova occurs. However, due to a lack of resolution, *overcooling* may ensue and all the energy is radiated away before forming a shockwave (Katz, 1992; Ceverino & Klypin, 2009). A first solution to this issue is *delayed cooling* in which radiation is turned off for a given amount of time which allows the shockwave to develop (Teyssier et al., 2013). However, this leads to unrealistically high temperatures. Another solution, *mechanical feedback*, consists in injecting instead this energy as momentum depending on which phase of the supernova is resolved. Resolution criteria can be based on a cooling radius (Agertz et al., 2013; Kretschmer & Teyssier, 2020) or the expected amount of mass swept up by the supernova at the cell length scale (Kimm et al., 2015). Then, while Agertz et al. (2013) and Kimm et al. (2015) inject momentum in both regimes, Kretschmer & Teyssier (2020) inject thermal energy in all cases and additionally injects momentum in the unresolved case as the thermal energy will naturally be radiated away. These models also differ in the ejected mass, its metallicity and how the momentum and this ejected mass are injected into the surrounding cells. Agertz et al. (2013) also models type Ia supernovae as well as stellar winds (in Sec. 3.5) which provide more feedback sources and generate stronger outflows. We include in Kimm et al. (2015) and Kretschmer & Teyssier (2020) an increase of factor four in their respective supernova rate, which can be seen as a compensation for these non-simulated

Table 3.3 – Description of the five models used in our simulations and their underlying subgrid models. We label them as KI, KI_rnw, KR, AG and DC. We show the references for their star formation (col. 2), supernova (col.3), additional physics boosting outflows (col.4) and radiative transfer (col.5). Each row is split in two, with the reference at the top and the physics described at the bottom.

	Star formation	Type II SN	Boost	RT
KI	Kimm+17 (multi-ff)	Kimm+15 ($p_{\rm rad}$ & $p_{\rm ad}$)	Rosdahl+18 (SN rate×4)	Rosdahl+13 + Geen+15
KI_rnw	"	"	+ Andersson+20 (runaway stars)	"
KR	Kretschmer+20 (multi-ff)	Kretschmer+20 ($p_{\rm rad}$ & $E_{\rm th}$)	Rosdahl+18 (SN rate×4)	Rosdahl+13
AG	Agertz+13 Schmidt's law	Agertz+13 ($p_{\rm rad}$ & $p_{\rm ad}$)	Agertz+13 (SNIa & SW)	Rosdahl+13
DC	Kimm+17 (multi-ff)	Teyssier+13 (delayed cooling)	None	Rosdahl+13

additional physics (Rosdahl et al., 2018). Lastly, we present in Sec. 3.4 how radiative transfer can generate feedback through radiation pressure and photoionisation. Their effect is respectively to transfer momentum to the surrounding gas and to heat the surrounding media, effectively acting as pre-SN feedback. As the lack of resolution also affects the pre-supernova feedback expected from photoionisation we further include a momentum boost following Geen et al. (2015) and Kimm et al. (2015).

For the next part of this work, we combine these subgrid models in five different ways to test their predictions. We label them as KI, KI_rnw, KR, AG and DC and summarise the subgrid models they respectively follow in table 3.3. KI, KR, and AG are three different approaches to star formation and feedback. In DC, only the feedback changes compared to KI; KI_rnw only changes from KI as runaway stars are included.

Chapter 4

Idealised galaxies

The first simulations we run are idealised, i.e. simulations where the galaxy is in an environment isolated from other galaxies and there is no cosmological context. We chose to run such simulations to first get a grasp on how various parameters of the subgrid model impacted galaxy evolution. We present the ICs and the simulations we run in Sec.4.1. We test model-dependent parameters in Sec. 4.2 and parameters common to all models in Sec. 4.3. We also check whether the models converge in stellar particle mass and spatial resolution in Sec. 4.4. After summarizing the results of the parameters tests, we calibrate the models so that they all end up with the same stellar mass in Sec. 4.5

4.1 The idealised simulations suite

In this first section, we introduce the initial conditions used to run the idealised simulations. We then list the simulations we run and detail the parameters we test in those simulations.

4.1.1 Initial conditions

We use the initial conditions of two idealised simulations from Rosdahl et al. (2015). Both the evolution of dark matter and baryonic physics are modelled in these simulations. The initial conditions are made with MakeDisc (Springel et al., 2005; Kim et al., 2014) and the DM halo follows an NFW density profile (Navarro et al., 1997). The galaxies are defined by their disc and their bulges, which are both initialised with gas and stars. The gaseous and stellar density profiles of the galaxy are decreasing exponentially with radius, and their height is Gaussian and centred on the mid-plane. The disc galaxies in the ICs have a respective baryonic mass of $3.5{\times}10^8$ $M_\odot$ and $3.5{\times}10^9$ $M_\odot$ and are called G8 and G9 as a reference to the exponent of their total baryonic mass. Half of this mass is gas and the other half is composed of stellar particles. The stellar mass of their bulge is respectively 3.5×10^7 $M_\odot$ and 3.5×10^8 $M_\odot$. In both of these ICs, the initial temperature of the disc is $T = 10^4$ K, with a metallicity of $Z = 0.1Z_\odot$, $Z_\odot = 0.02$ being Solar metallicity. The CGM is in pressure equilibrium with the disc, has a density $n_{\rm H} = 10^{-6}$ cm^{-3}, a temperature $T = 10^6$ K, and is devoid of metals. Lastly, while G8 has a virial radius of 41 kpc and a box size of 150 kpc, G9 has a virial radius of 89 kpc and a box size of 300 kpc.

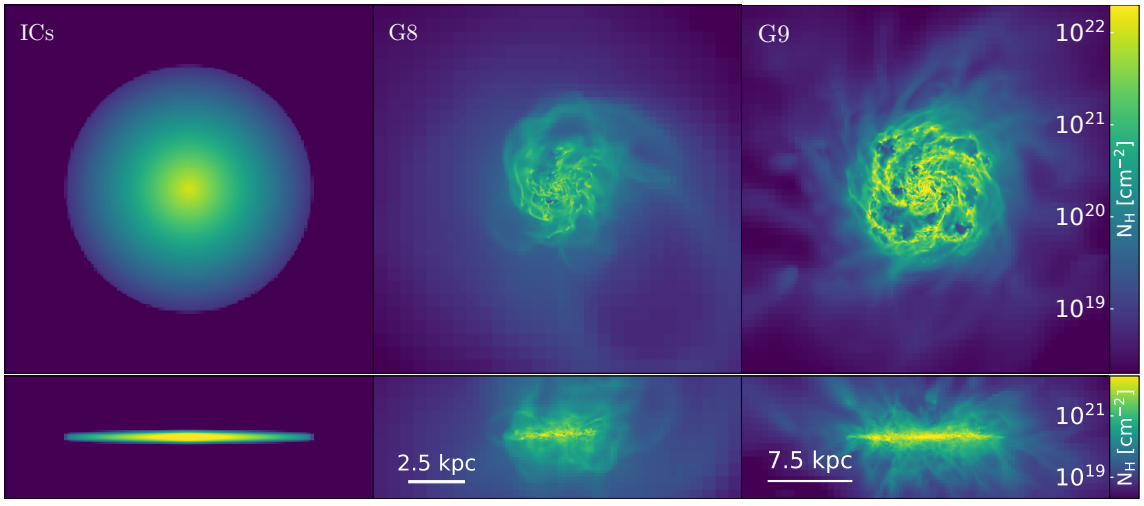

Figure 4.1 – Face-on and edge-on column density maps of hydrogen. We show the IC of the galaxies on the leftmost panels (the IC of G8 and G9 are similar but span different scales) and the galaxy after 515 Myr for G8 (middle column) and G9 (rightmost column) with the KI model and has a maximal resolution of 9.16 pc.

We illustrate the initial conditions and two galaxies formed with the simulations (G8 and G9) by showing in Fig. 4.1 their face-on (top row) and edge-on (bottom row) hydrogen column density.

4.1.2 List of simulations

We used both G8 and G9, as the mass of the galaxy has a great impact on the star formation regulation. A stronger gravitational potential means that the outflows will be ejected less far away and need to be stronger to avoid a raining back down on the galaxy. This is what makes supernovae inefficient in massive galaxies, with outflows having to be powered by AGNs. The effects of several parameters become more or less important depending on the galaxy considered, and can even lead to distinct effects. These simulations are run for 515 Myr with the models AG, KI and KR presented in chapter 3. We name the simulations with the chosen fiducial parameters Ag8, Ki8 and Kr8 (resp. Ag9, Ki9 and Kr9) for G8 (resp. G9). Unless otherwise specified, all results are extracted from the last output of the simulation.

Table 4.1 – List of the simulations run with AG. In order, the parameters tested are the mass of the galaxy, the spatial resolution, the density threshold, the global star formation efficiency, the minimal mass of stellar particles, the refinement level at which stars can be formed, the Jeans refinement criterion and the radiative transfer module. The asterisk on the runtimes symbolises simulations which had to be restarted due an issue with the computer. The real computing time is thus in reality slightly lower than written here.

	Galaxy	Δx [pc]	n_* [cm^{-3}]	$\epsilon_{\rm ff}$	$m_{*,\rm min}$ [M$_\odot$]	SF$_{\rm lmax}$	$\lambda_{\rm J,ref}$	RT	runtime [hCPU]
Ag8	G8	36.6	25	0.1	1600	T	T	T	1462
Ag8_HR	G8	**18.3**	25	0.1	1600	T	T	T	3886
Ag8_LR	G8	**73.2**	25	0.1	1600	T	T	T	344
Ag8_n10	G8	36.6	**10**	0.1	1600	T	T	T	1698
Ag8_n50	G8	36.6	**50**	0.1	1600	T	T	T	1218
Ag8_n100	G8	36.6	**100**	0.1	1600	T	T	T	1263
Ag8_e0.05	G8	36.6	25	**0.05**	1600	T	T	T	1524
Ag8_e0.2	G8	36.6	25	**0.2**	1600	T	T	T	1510
Ag8_m0.4	G8	36.6	25	0.1	**400**	T	T	T	1195
Ag8_m6.4	G8	36.6	25	0.1	**6400**	T	T	T	1680
Ag8_Nsflmax	G8	36.6	25	0.1	1600	**F**	T	T	1581
Ag8_NJeans	G8	36.6	25	0.1	1600	T	**F**	T	1692
Ag8_NRT	G8	36.6	25	0.1	1600	T	T	**F**	1584
Ag9	**G9**	36.6	25	0.1	1600	T	T	T	9341
Ag9_HR	G9	**18.3**	25	0.1	1600	T	T	T	35550*
Ag9_LR	G9	**73.2**	25	0.1	1600	T	T	T	1913
Ag9_NRT	G9	36.6	25	0.1	1600	T	T	**F**	10197

We present the simulations run with AG in table 4.1, those following KI in table 4.2 and those relying on KR in table 4.3. Each simulation is given a name depending on the quantity changed relative to the fiducial simulation, and we highlight these

changes in bold in the tables. For all models, we explore the effects of galaxy mass (G8 or G9), resolution (Δx), minimal stellar mass particle ($m_{*,\mathrm{min}}$), star formation limitation at the maximum level ($\mathrm{SF}_{\mathrm{lmax}}$), additional Jeans refinement ($\lambda_{\mathrm{J,ref}}$) and radiative transfer (RT). For AG, we explore the effect of different density thresholds (n_*) and star formation efficiencies (ϵ_{ff}). For KI, we consider different Jeans criteria for star formation ($\lambda_{\mathrm{J,turb}}$). For KR, we test different feedback implementations (p_{SN}). We give more detail on what these parameters are in the following sections, alongside the resulting galaxies.

Table 4.2 – List of the simulations run with KI. In order, the parameters tested are the mass of the galaxy, the spatial resolution, the Jeans criterion for star formation (a negative value meaning no criterion), the minimal mass of the stellar particles, the refinement level at which stars can be formed, the Jeans refinement criterion and the radiative transfer module. The asterisk on the runtimes symbolises simulations which had to be restarted due an issue with the computer. The real computing time is thus in reality slightly lower than written here.

	Galaxy	Δx [pc]	$\lambda_{\mathrm{J,turb}}$	$m_{*,\mathrm{min}}$ [$\mathrm{M}_\odot$]	$\mathrm{SF}_{\mathrm{lmax}}$	$\lambda_{\mathrm{J,ref}}$	RT	runtime [hCPU]
Ki8	G8	36.6	4	1600	T	T	T	1026
Ki8_EHR	G8	**9.16**	4	1600	T	T	T	6729*
Ki8_HR	G8	**18.3**	4	1600	T	T	T	2489
Ki8_LR	G8	**73.2**	4	1600	T	T	T	365
Ki8_ELR	G8	**146**	4	1600	T	T	T	154
Ki8_λ-1	G8	36.6	**-1**	1600	T	T	T	1190
Ki8_λ1	G8	36.6	**1**	1600	T	T	T	816
Ki8_m16	G8	36.6	4	**400**	T	T	T	853
Ki8_m256	G8	36.6	4	**6400**	T	T	T	1222
Ki8_Nsflmax	G8	36.6	4	1600	**F**	T	T	1090
Ki8_NJeans	G8	36.6	4	1600	T	**F**	T	1057
Ki8_NRT	G8	36.6	4	1600	T	T	**F**	850
Ki9	G9	36.6	4	1600	T	T	T	3567
Ki9_EHR	G9	**9.16**	4	1600	T	T	T	46679*
Ki9_HR	G9	**18.3**	4	1600	T	T	T	11355
Ki9_LR	G9	**73.2**	4	1600	T	T	T	902
Ki9_ELR	G9	**146**	4	1600	T	T	T	548*
Ki9_NRT	G9	36.6	4	1600	T	T	**F**	2195

4.2 Model-dependant parameters

Having presented the simulations, we now delve into parameters specific to each model. Specifically, we test the effect of various density thresholds and star formation efficiency in AG, the Jeans criterion for star formation in KI, and the strength of the feedback in KR.

Table 4.3 – List of the simulations run with KR. In order, the parameters tested are the mass of the galaxy, the spatial resolution, the minimal mass of stellar particles, the feedback implementation, the refinement level at which stars can be formed, the Jeans refinement criterion and the radiative transfer module. The asterisk on the runtimes symbolises simulations which had to be restarted due an issue with the computer. The real computing time is thus in reality slightly lower than written here.

	Galaxy	Δx [pc]	$m_{*,\mathrm{min}}$ [$\mathrm{M}_\odot$]	p_{SN}	$\mathrm{SF}_{\mathrm{lmax}}$	$\lambda_{\mathrm{J,ref}}$	RT	runtime [hCPU]
Kr8	G8	36.6	1600	weak	T	T	T	507
Kr8_EHR	G8	**9.16**	1600	weak	T	T	T	6406*
Kr8_HR	G8	**18.3**	1600	weak	T	T	T	1819
Kr8_LR	G8	**73.2**	1600	weak	T	T	T	176
Kr8_ELR	G8	**146**	1600	weak	T	T	T	84
Kr8_m0.4	G8	36.6	**400**	weak	T	T	T	295
Kr8_m6.4	G8	36.6	**6400**	weak	T	T	T	894
Kr8_Nmom	G8	36.6	1600	**no mom**	T	T	T	583
Kr8_Nboost	G8	36.6	1600	**no boost**	T	T	T	453
Kr8_str	G8	36.6	1600	**strong**	T	T	T	604
Kr8_Nsflmax	G8	36.6	1600	weak	**F**	T	T	510
Kr8_NJeans	G8	36.6	1600	weak	T	**F**	T	536
Kr8_NRT	G8	36.6	1600	weak	T	T	**F**	451
Kr9	G9	36.6	1600	weak	T	T	T	1743
Kr9_EHR	G9	**9.16**	1600	weak	T	T	T	31094*
Kr9_HR	G9	**18.3**	1600	weak	T	T	T	7028
Kr9_LR	G9	**73.2**	1600	weak	T	T	T	438
Kr9_ELR	G9	**146**	1600	weak	T	T	T	235*
Kr9_NRT	G9	36.6	1600	weak	T	T	**F**	1650

4.2.1 Density threshold in AG, n_*

The density threshold is only used in AG and consists in forming stars as soon as the gas density of a cell becomes greater than a chosen density threshold n_*. Setting this parameter correctly is of the utmost importance. Indeed, if the value is too high, gas clouds won't be able to collapse into stars whereas if it is too low, too many stars will be formed. As explained earlier, this value depends on the resolution of the simulation. In Agertz et al. (2013) and Agertz et al. (2020), the density thresholds are respectively 25 cm^{-3} and 300 cm^{-3} for a maximal resolution of 50 pc and 3 pc. The density threshold at the lowest resolution is based on the density at which molecular hydrogen reaches 50% (Gnedin & Kravtsov, 2011), and the other describes the density at which molecular hydrogen forms in cold clouds ($T < 100$ K). We thus test values of 10 cm^{-3}, 25 cm^{-3}, 50 cm^{-3} and 100 cm^{-3} for

the galaxies we simulated at a resolution of 37 pc.

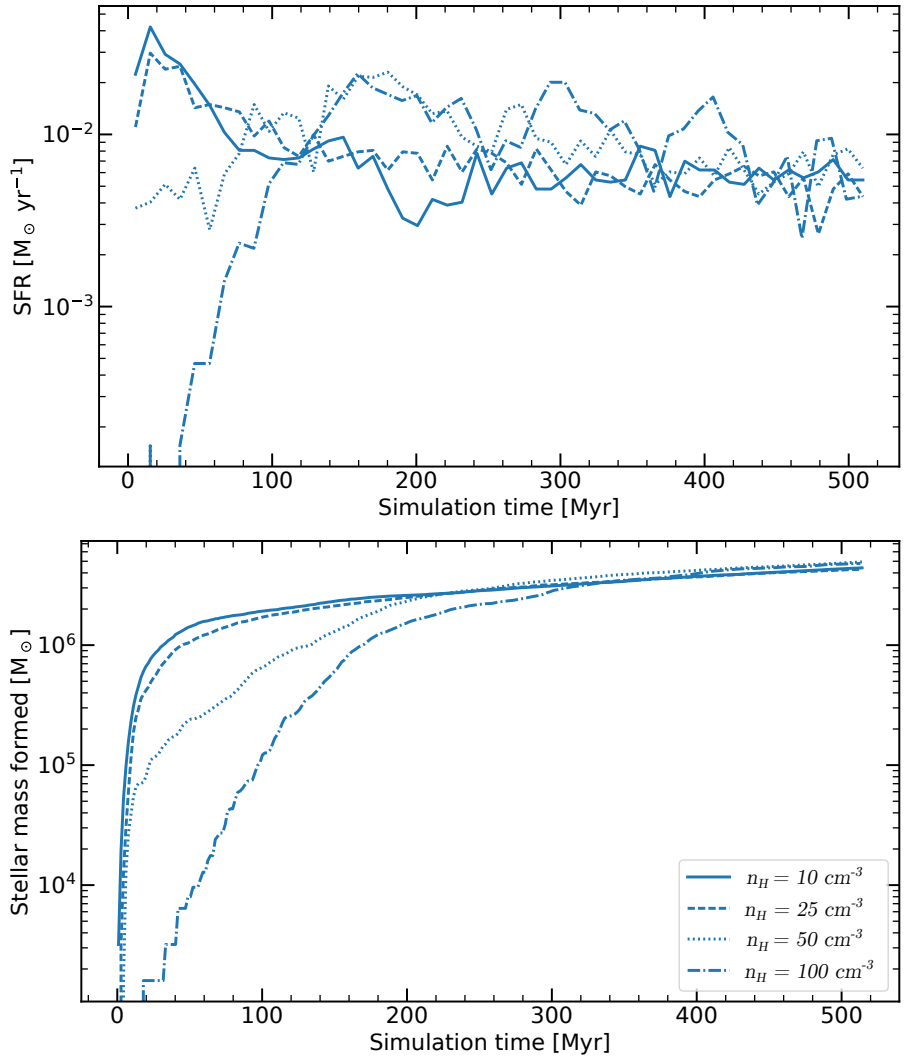

Figure 4.2 – SFR (upper panel) and stellar mass formed (lower panel) as a function of time, with AG using different density thresholds. We respectively consider density thresholds of 10 cm^{-3} (Ag8_n10), 25 cm^{-3} (Ag8), 50 cm^{-3} (Ag8_n50) and 100 cm^{-3} (Ag8_n100).

We show in Fig. 4.2 the SFR and the stellar mass formed as a function of time, with G8. The different lines denote different density thresholds for star formation in AG. The first direct consequence of a higher density threshold is that the gas takes longer to reach such densities and collapses to form stars. This is clearly shown in both plots. Looking at the SFR plot, the simulations with density thresholds of 10 cm^{-3} and 25 cm^{-3} begin to form stars with a high star formation rate of 0.02 M$_\odot$ yr^{-1} within the first 10 Myr. The medium density threshold of 50 cm^{-3} form 0.004 M$_\odot$ yr^{-1} from the beginning of the simulation. Lastly, the simulation with a high-density threshold of 50 cm^{-3} almost does not form stars within the first 20 Myr, and only reaches an SFR of 0.007 M$_\odot$ yr^{-1} after 110 Myr.

From this point on, two trends can be noted. The SFR of the simulations with the two lowest density thresholds decreases after the first peak and stabilises after 110 Myr at 0.006 M$_\odot$ yr^{-1}. Simulations with the higher thresholds exhibit

strong episodes of star formation, with star formation rates oscillating roughly within $0.005 - 2$ $M_\odot\,yr^{-1}$. Indeed, a higher density threshold leads to the condensation of more gas, which suddenly collapses into stars without giving time to feedback to stop the process. Conversely, a lower density threshold authorises star formation in many more regions and a smoother SFR.

Considering the integrated SFR, we show that the main difference comes from the speed at which the stellar mass is formed. As with the SFR, the lowest density threshold shows the earliest star formation, while the highest density threshold shows the latest. The lowest thresholds take respectively 15 Myr and 25 Myr to form 3×10^6 $M_\odot$, while the higher threshold simulations take 120 Myr and 170 Myr. Nonetheless, the final mass reached is similar for all of these simulations, albeit slightly higher for those with a higher density threshold. This is a result of this galaxy being in an idealised environment. Since there is a fixed budget of gas that can turn into stars, most of it is eventually converted into stars for all these simulations if given enough time. If this gas content was resplenished, stars would form earlier in the simulation with a lower threshold, while the gas would need to condense further to form stars with a higher density threshold. One would thus not expect a converged stellar mass but a stellar mass constantly higher the lower the density threshold. A fraction of the gas in our simulations can however leave it if ejected out of the simulation box. If there was a cosmological context and mergers, one could expect the galaxy to evolve drastically differently due to this delay in star formation. We discuss this effect in more depth in Sec. 4.5.

Fig. 4.3 shows the face-on and edge-on hydrogen column density of the galaxies simulated with AG and density thresholds of 10 cm^{-3}, 25 cm^{-3}, 50 cm^{-3} and 100 cm^{-3}. We find that the higher the density threshold, the more defined the spiral arms of the galaxies are. When the density threshold is low, the stars can form everywhere in the galactic disc, resulting in a smoother, diffuse shape. When the density threshold is high, the galaxy has time to condense gas and create higher density regions before forming stars. It is thus more difficult for feedback to eject gas out of the galaxy. The ejected gas is confined to the path of least resistance, while at a lower density threshold, gas is ejected in every direction. We show this effect with the edge-on maps. With a high-density threshold, outflows are only present in the galactic plane, while they are spread in a wider area around the galaxy with a lower density threshold. We note that in a cosmological context, the path of least resistance is expected to be along the minor axis of the galaxy (gas accreting through filaments along the major axis) and produce biconical outflows in this direction (Veilleux et al., 2001; Schroetter et al., 2019).

We also find that the density threshold affects the spread of the outflows on the edge-on maps. When the density threshold is high, the outflows are concentrated in the disc plane. When lowering this threshold, the outflows are spread in a wider area surrounding the galaxy. Indeed, with a low-density threshold, stars can form farther out of the disck plane than with a high threshold, allowing feedback to spread more easily.

Overall, a higher density threshold for star formation produces more well-defined spiral arms, outflows concentrated along the disc plane and delays star formation while making the SFR more bursty. A lower density threshold leads to a smoother galaxy with more isotropically spread outflows and a smooth SFR.

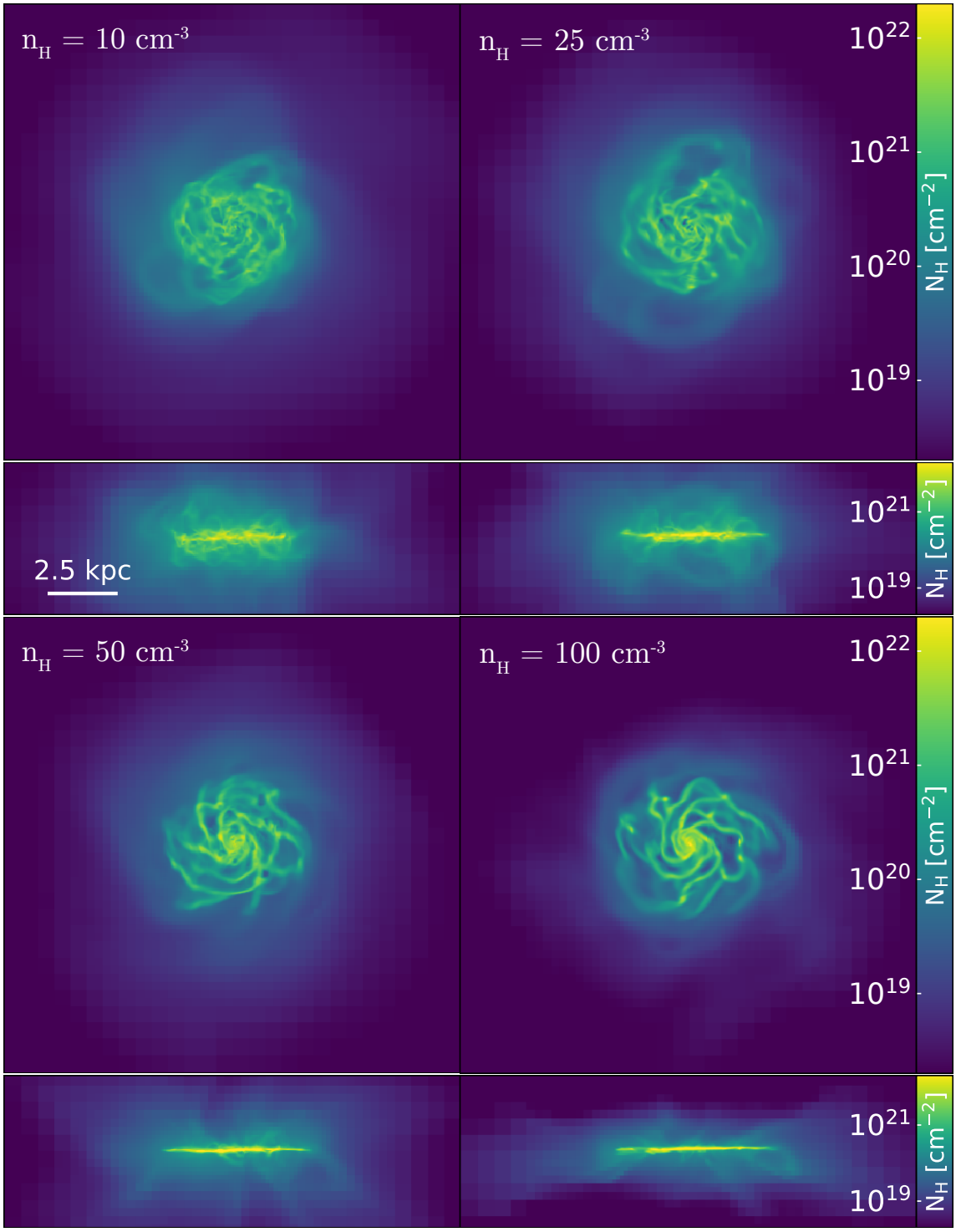

Figure 4.3 – Face-on and edge-on column density maps after 515 Myr in AG. From left to right, we show the simulations Ag8_n10 (10 cm^{-3}), Ag8 (25 cm^{-3}), Ag8_n50 (the fiducial 50 cm^{-3}) and Ag8_n100 (100 cm^{-3}).

4.2.2 Star formation efficiency in AG $\epsilon_{\rm ff}$

When the conditions are met and a stellar particle forms in a cell, a certain proportion of the gas from the birth cloud will collapse and form a star (see Sec. 3.1.1). The proportion of gas forming the star is referred to as the *local* SFE. Furthermore, the model for star formation used in AG uses a global efficiency which represents a mean over a whole galaxy. The quantity used is then a *global* SFE and also takes into account other phenomena that hinder star formation, such as neighbouring winds or turbulences. This parameter is described by $\epsilon_{\rm ff}$ in Eq. 3.2.

As mentioned in Sec. 3.1, we use a default value of 10% for the gas cloud fraction turning into the stellar particle (Grisdale et al., 2019; Agertz et al., 2020), as it leads to results similar to those found for individual giant molecular clouds. We nonetheless test less (5%) and more efficient (20%) values to see if they could impact the stellar mass formed.

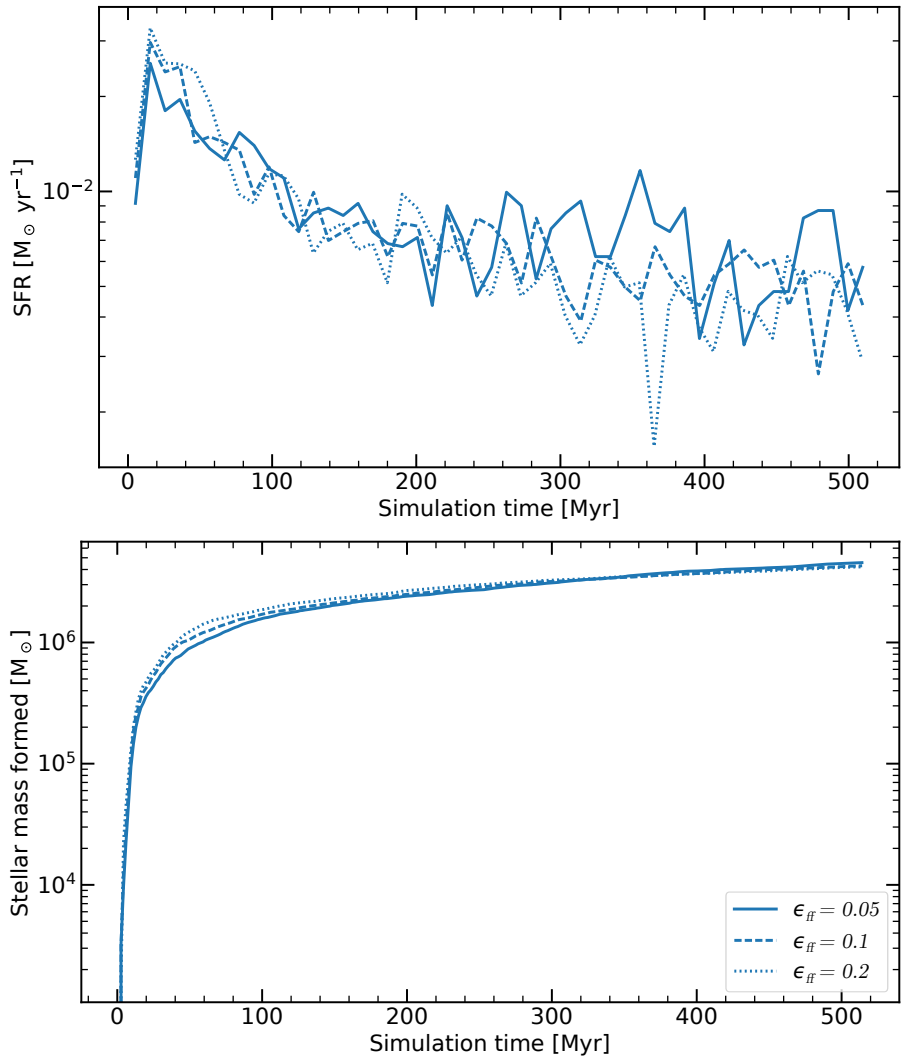

Figure 4.4 – SFR (upper panel) and stellar mass formed (lower panel) as a function of time, with AG using different global star formation efficiencies. We respectively consider efficiencies of 5% in Ag8_e0.05, 10% in Ag8 and 20% in Ag8_e0.2.

Fig. 4.4 shows the SFR and stellar mass formed for the galaxies simulated with AG, using these different global star formation efficiencies. We do not find much difference between these simulations with an SFR similar on average and a well-converged total stellar mass. It can also be noted that the first peak is slightly higher when the star formation efficiency is higher. Since the amount of gas turned into stars is almost linearly dependent on the star formation efficiency (Eq. 3.2), this could be interpreted as the model with a higher SFE forming more massive stars than those with lower SFE. However, this is not the case.

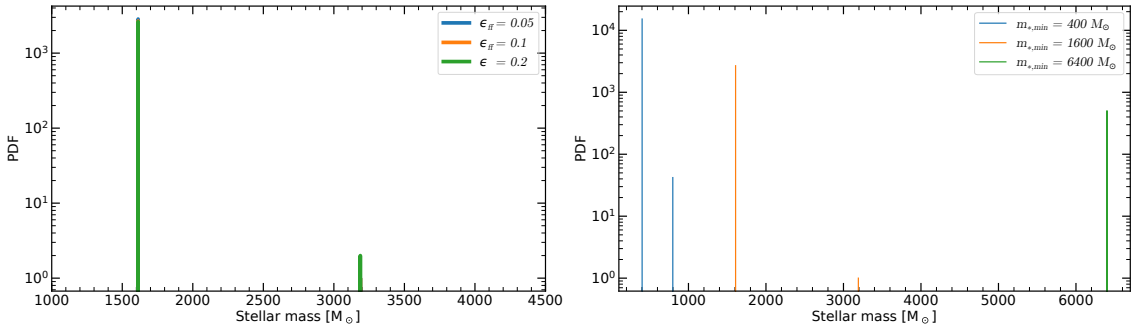

Figure 4.5 – Probability density function of the stellar particles' initial mass with AG using different star formation efficiencies (left) and different minimal stellar particles masses (right). The efficiencies used are as above and the minimal stellar particles masses we consider are respectively 400 $M_\odot$ for Ag8_m0.4, 1600 $M_\odot$ for Ag8 and 6400 $M_\odot$ for Ag8_m6.4.

To investigate this, we compare the distribution of the initial mass of stellar particles and find that only a few are more massive than $m_{*,\mathrm{min}}$. This is shown in the left panel of fig. 4.5. All three simulations exhibit a very similar distribution, with the main peak at 1600 $M_\odot$. There is also a second peak, but it is only present for Ag8_e0.2 and consists of only two stellar particles. This shows that the stellar particles form in media with different densities.

An important thing to understand is that the minimal mass of the stellar particles $m_{*,\mathrm{min}}$ also acts as a density threshold. 1600 $M_\odot$ roughly corresponds to a density threshold of 20 cm^{-3} with a resolution of 36.6 pc and an SFE of 10% and twice less with 20%. Even if the density threshold is reached in a cell, if the available mass for star formation is less than $m_{*,\mathrm{min}}$, no stellar particle will form until the density is high enough. What happens is that with lower efficiency, the cells must reach higher densities and star formation is thus slightly delayed. As the stellar particles have the same mass, they produce feedback in a similar medium with the same strength (more massive particles produce more powerful feedback), which leads to a very similar star formation rate overall.

With a lower mass for stellar particles, a more diverse stellar population can be reached amongst the simulations, and the impact of the global star formation efficiency is enhanced. This is what we see when considering simulations with different stellar particles mass (see Sec. 4.4.1 for more details). The right panel in fig. 4.5 shows different stellar particle masses, and we can see that at a given cell resolution, the height of the second peak increases with a lower stellar particle mass (in blue) while there is no peak with higher masses (in green).

The effect of the star formation efficiency is here akin to that of the star formation density threshold, as it leads to an initially slightly different SFR and a small delay in the formation of stellar mass. This is due to the stellar particle mass of our simulations, which constrains the stellar particle mass to a single value. If the mass resolution was high enough so that star particles would not act as density threshold, one would expect a higher stellar mass the higher the star formation efficiency. However, this would also lead to more massive particles and a stronger feedback which could inhibit star formation.

4.2.3 Jeans criterion for star formation in KI, $\lambda_{\mathrm{J,turb}}$

When using the multi-freefall model with the implementation from Kimm et al. (2017), there are various criteria to take into consideration before forming stars (see Sec. 3.1). In particular, $\lambda_{\mathrm{J,turb}} < 4\Delta x$, with $\lambda_{\mathrm{J,turb}}$ given by Eq. 3.7. As this criterion regulayy star formation and has a strong density dependence, it can seem similar to the star formation density threshold used in AG. However, while the density threshold in Agertz corresponds to an average description of the medium where star formation with a given efficiency, the role of the Jeans criterion is to adapt to the resolution limit. This criterion indeed determines whether a gas cloud should collapse further than resolution allows, and, in that case, enables star formation.

We test here how this criterion affects the results by removing the Jeans length (Ki8_sf_lam-1), resolving the Jeans length by four cells (Ki8) and considering a stronger criterion of resolving the Jeans length by one cell (Ki8_sf_lam1). Fig. 4.6 shows the SFR and stellar mass formed for the galaxies simulated with KI following these prescriptions. In the first $\sim$ 20 Myr, both the model without restriction and the one with a medium restriction quickly produce an SFR peak. However, the model with the strongest criterion of one Jeans length per cell takes longer to form stars and does not exhibit a significant peak. This is expected as $\lambda_{\mathrm{J,turb}}(\rho) \propto \rho^{-0.5}$. For the Jeans length to decrease and reach the resolution scale, higher density regions must form, and more time is needed. This can be seen in the stellar mass formed, as it seems that the star formation is "late" with a stricter criterion. This is similar to what we find in Sec. 4.2.1.

However, from $\sim$ 200 Myr, the SFR is systematically higher in this more restrictive model and the stellar mass formed is slightly higher than in the other two models after $\sim$ 400 Myr. The likely cause for this is that by forming stars later, denser regions have time to form before being subject to feedback. Thus, feedback happens in denser regions and is restricted to local scales by losing quickly its energy. Conversely, in lower-density regions, the supernova can expand freely to more extended scales and hinder the star formation of the next stars globally.

This hypothesis is backed by Fig. 4.7 which shows the face-on and edge-on hydrogen column density of the galaxies simulated with KI and Jeans lengths criterion of -1 (no criterion), 4 and 1. In the rightmost model (with the most restrictive criterion), the galaxy is globally smooth even though it is populated by several well-defined cavities with a very low-density caused by supernovae. However, in the leftmost panel, cavities are wider even though higher-density gas populates them. We can further see through the edge-on maps that those indeed eject gas on bigger scales, while the rightmost model does not eject as much gas out of the galaxy. This

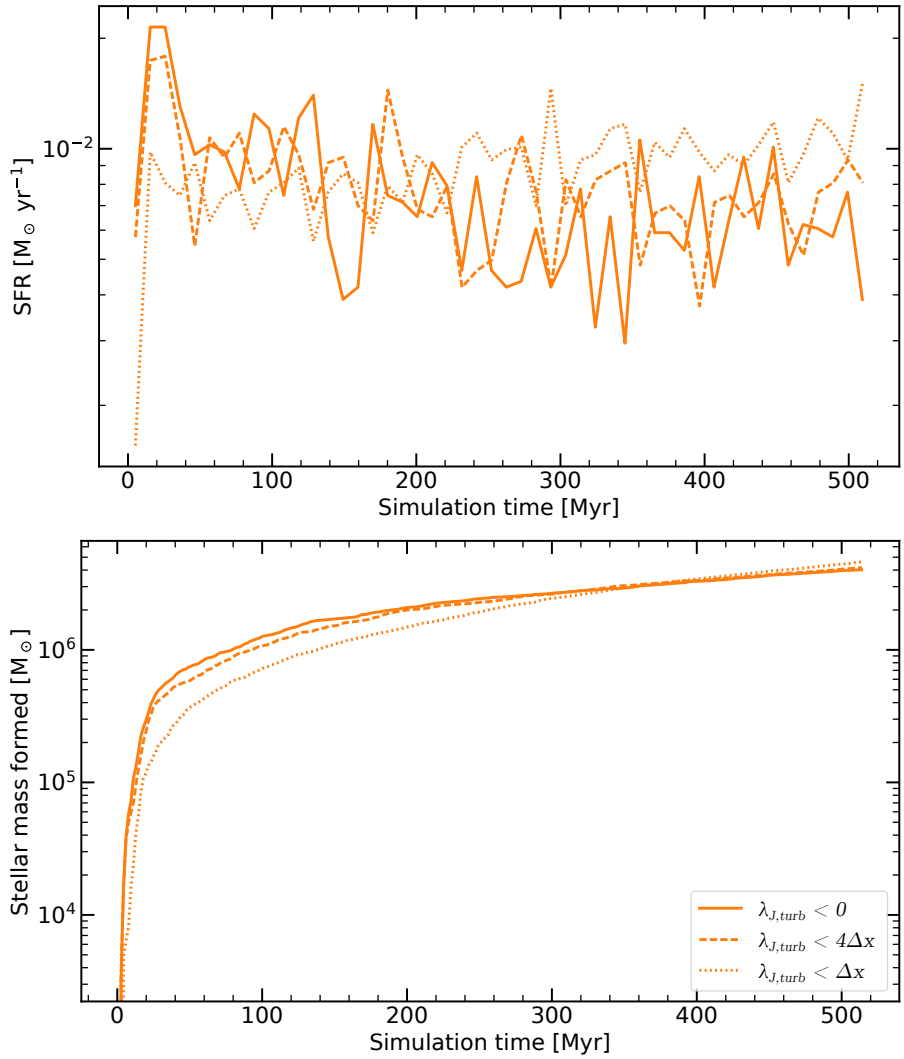

Figure 4.6 – SFR (upper panel) and stellar mass formed (lower panel) as a function of time, with KI using different criteria on the Jeans length for star formation. We respectively consider values of -1 (no criterion) in Ki8_sf_lam-1, a fourth of a Jeans length in Ag8 and one Jeans length in Ki8_sf_lam1.

can also be noticed in the face-on maps as there are traces of ejected gas in the CGM of the leftmost panel while the rightmost one still shows clearly the imprint of the initial conditions with a circular CGM.

In the end, being more restrictive in star formation leads to supernovae acting on a smaller scale than without a Jeans criterion, where gas is ejected further out of the galaxy. These differences nonetheless remain small, and the difference in star formation remains inconsequential.

4.2.4 Feedback strength with KR

In this part, we compare the effect of the different implementations of the momentum feedback used with KR. The first one we consider is to not inject any momentum, Kr8_Nmom (it is thus equivalent to thermal feedback). The second one is the model Kr8_Nboost, using the *weak feedback* from Kretschmer & Teyssier (2020), following

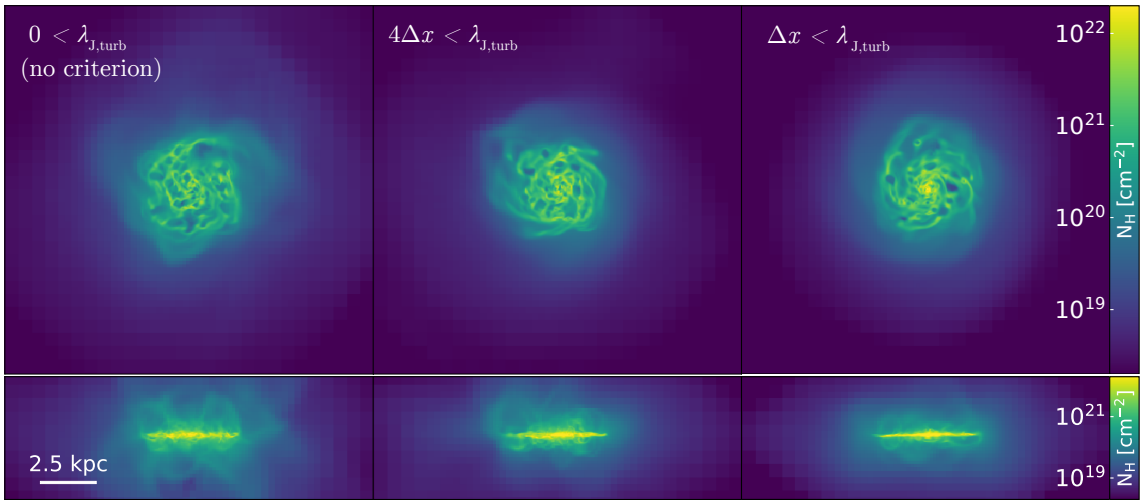

Figure 4.7 – Face-on and edge-on column density maps after 515 Myr in KI. From left to right, we show the simulations Ki8_sf_lam-1 (no Jeans length criterion), Ki8 ($4\Delta x < \lambda_{\rm J,turb}$) and Ki8_sf_lam1 ($\Delta x < \lambda_{\rm J,turb}$).

Eq. 3.25 and Eq. 3.26. The third model we consider, Kr8, is the same as the second but includes a factor four boost in the supernova rate. It is our fiducial model. The last model we consider is Kr8_str and relies on the *strong feedback* from Kretschmer et al. (2020), complemented by the same supernova rate boost. In this model, the exponents of the equations considered are changed so that the equations become

$$R_{\rm cool,Kr} = \mathbf{3.0} \left(\frac{n_{\rm H}}{100}\right)^{-0.42} Z'^{\mathbf{-0.082}} \text{ pc}, \tag{4.1}$$

$$P_{\rm st,Kr} = \mathbf{1.42} \times 10^5 \eta_R N_{\rm SN} Z'^{\mathbf{-0.137}} \left(\frac{n_{\rm H}}{100}\right)^{\mathbf{-0.16}} \text{M}_\odot \,\text{km}\,\text{s}^{-1}. \tag{4.2}$$

Fig. 4.8 shows the SFR and stellar mass formed for the galaxies simulated with KR using these different feedback prescriptions. We find that these simulations split into two distinct groups. The first pair comprises the simulation without momentum injection and the simulation without any boost in supernova rate. They both have an SFR globally higher than 0.01 $\text{M}_\odot\,\text{yr}^{-1}$ and form twice more stars than the second pair. Also, near 260 Myr, there is a small bump in SFR for Kr8_Nboost which is not present in the other simulations. This leads to a higher increase in stellar mass formed at the corresponding time and allows these models to have a very similar final mass. We thus see that the weak momentum injection from (Kretschmer & Teyssier, 2020) does not have much effect compared to the thermal feedback if it is not boosted. The other pair consists of the runs with boosted SN rate, either with the weak or strong feedback formulation. We find that the effect of strong feedback is comparable to that of weak feedback, as they lead to almost the same galaxy. Both of these models have a very similar SFR, varying around 0.008 $\text{M}_\odot\,\text{yr}^{-1}$, and a final stellar mass twice lower than without the boost.

We also looked at hydrogen column density maps of the galaxies simulated and found almost no change between the four simulations. The only difference is that models with the boost exhibit slightly more numerous small outflow bubbles.

Within ~ 5 kpc (roughly the galaxy, where supernovae explode), the medium has typically $n_{\rm H} > 10^{-4}$ cm^{-3} and $Z' > 0.15$ ($Z > 0.003$) which leads to $R_{\rm cool,Kr} \sim 1$ kpc.

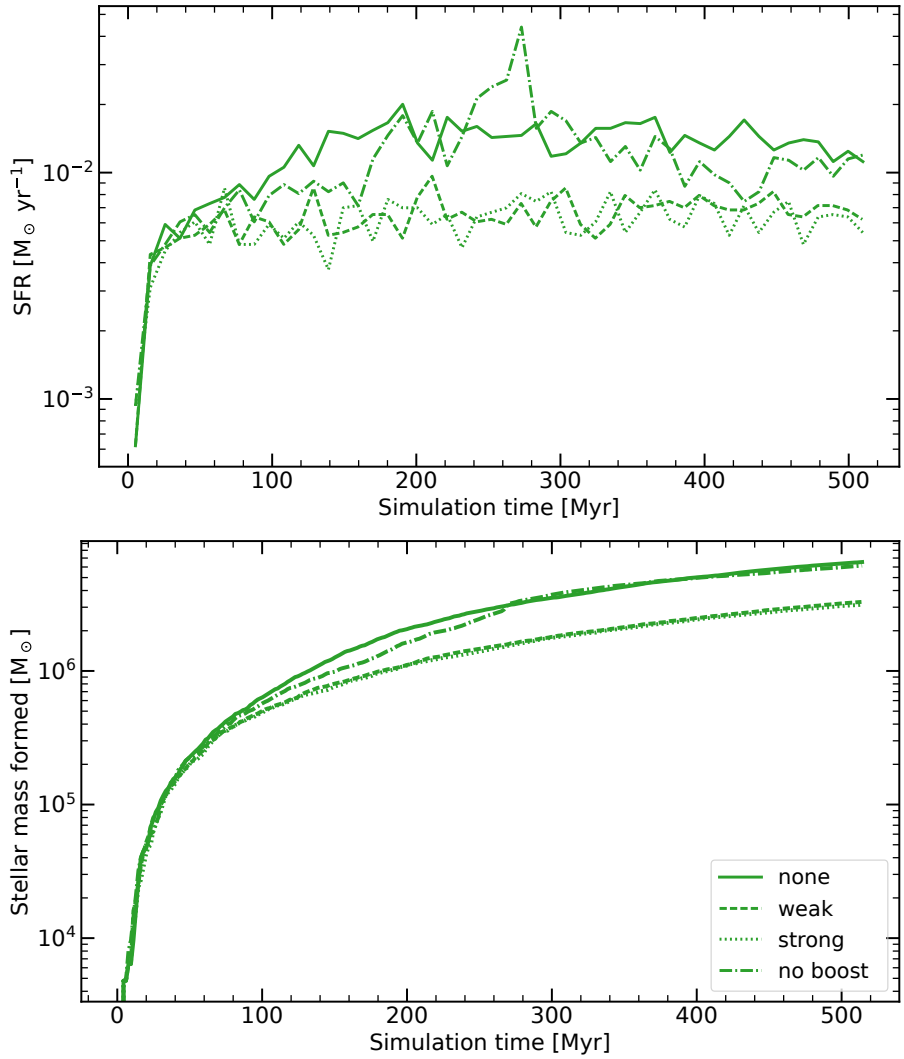

Figure 4.8 – SFR (upper panel) and stellar mass formed (lower panel) as a function of time, with KR using different feedback prescriptions. We respectively consider no momentum injection (Kr8_Nmom), no supernova rate boost (Kr8_Nboost), the *weak feedback* (Kr8) and *strong feedback* (Kr8_str).

However, a significant fraction of cells presents densities $n_{\rm H} > 1$ cm^{-3} which leads to $R_{\rm cool,Kr} \sim 24$ pc. The injection of momentum alongside thermal energy is thus a necessary component to produce stronger winds and compensate for overcooling at our resolution. However, we find that unless boosted, its effect is inconsequential in our simulations. Also, the small changes in the equations describing the momentum injection have a negligible effect on star formation. These effects were tested on a very low mass galaxy, and we expect that they will be even less pronounced in more massive galaxies.

4.3 Global simulation parameters

Having now tested the most important free parameters from the models, we now focus on parameters which are not dependent on the models used, but common to all the simulations we run.

4.3.1 Jeans refinement, $\lambda_{\mathrm{J,ref}}$

There is initially an additional refinement criterion in KI compared to AG and KR. This criterion consists in further increasing the resolution level depending on how well the Jeans length $\lambda_{\mathrm{J,ref}}$ (Eq. 2.1) is resolved. Note that the Jeans length considered here is different to that considered in the star formation criterion in Sec. 3.1 and Sec. 4.2.3 for KI as we do not include the turbulent speed of the gas (see Eq. 3.7). As we distinguish the subgrid models from the refinement strategies, we decided to include Jeans refinement in all the models. We verify here the extent of the impact of this parameter on the simulations.

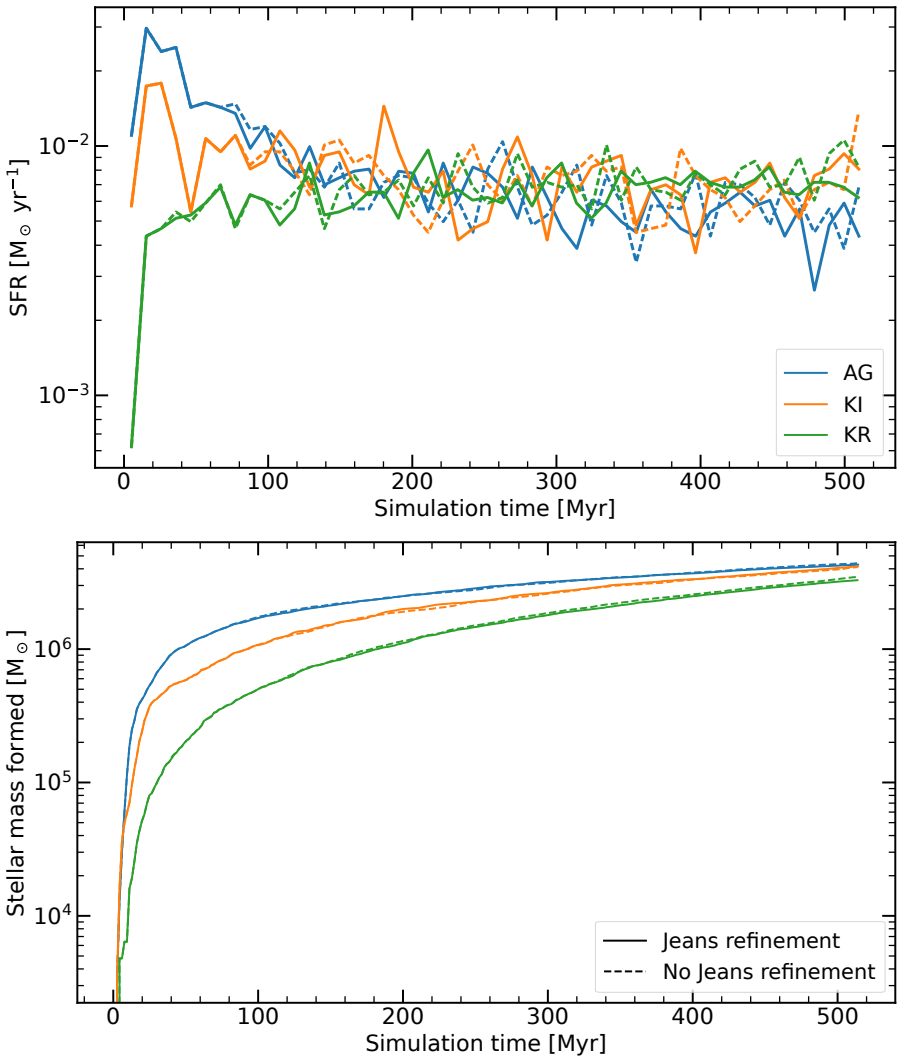

Figure 4.9 – SFR (upper panel) and stellar mass formed (lower panel) as a function of time, using or not the Jeans refinement.

Fig. 4.9 shows the SFR and stellar mass formed for the galaxies simulated with each model, with and without the Jeans refinement criterion. There is almost no difference in the curves shown respectively for each model, with AG and KI even being the same for the first $70 - 80$ Myr. This happens because the maximal resolution of 40 pc in these simulations is not high enough for the additional Jeans refinement to take place.

Table 4.4 – Table with the additional simulations run to test the impact of Jeans refinement on the simulations with each model for a higher resolution simulation. The four first are run with AG, the four following with KI and the last four are run with KR. The asterisk on the runtimes symbolises simulations which had to be restarted due to an issue with the computer. The real computing time is thus in reality slightly lower than written here.

	Galaxy	Δx [pc]	$\lambda_{\mathrm{J,ref}}$	$f_{\Delta \mathrm{x_{max}}}$	runtime [hCPU]
Ag8_HR	G8	18.3	T	4.84%	3886
Ag8_HR_NJeans	G8	18.3	F	2.16%	3413
Ag9_HR	G9	18.3	T	23.8%	35550*
Ag9_HR_NJeans	G9	18.3	F	18.0%	30432*
Ki8_HR	G8	18.3	T	4.77%	2489
Ki8_HR_NJeans	G8	18.3	F	3.91%	2590
Ki9_HR	G9	18.3	T	21.9%	11355
Ki9_HR_NJeans	G9	18.3	F	18.3%	10688
Kr8_HR	G8	18.3	T	6.6%	1819
Kr8_HR_NJeans	G8	18.3	F	4.6%	1818
Kr9_HR	G9	18.3	T	21.2%	7028
Kr9_HR_NJeans	G9	18.3	F	17.0%	6029

Both a more massive galaxy and a higher resolution simulation can lead to more significant differences in the results. As it will likely arise in the zoom simulations they will cover significantly more resolution levels, we run additional simulations presented in table 4.4. We also include $f_{\Delta \mathrm{x,max}}$ in the table, the fraction of cells which are at the maximum level in the simulation.

Fig. 4.10 shows the SFR and stellar mass formed for the galaxies simulated with KI, KR, and AG with and without the Jeans refinement criterion at a higher resolution for G8 and G9. We show in table 4.4 that the increase in the number of cells at maximum resolution is 0.9-2.7% in G8 and 3.6-5.8% in G9. As there are more numerous dense regions in G9 than in G8, it is expected to find a larger increase in the number of high-resolution cells. In G8, the star formation is slightly increased for AG and KR, leading to a slightly higher stellar mass, while there is almost no difference in KI. This can be linked to a lower difference in the number of resolved cells. However, we also find that there is no difference in total stellar mass formed in G9, even though there are up to $\sim$6% more cells at high resolution. The star formation history of the simulated galaxies with and without this additional

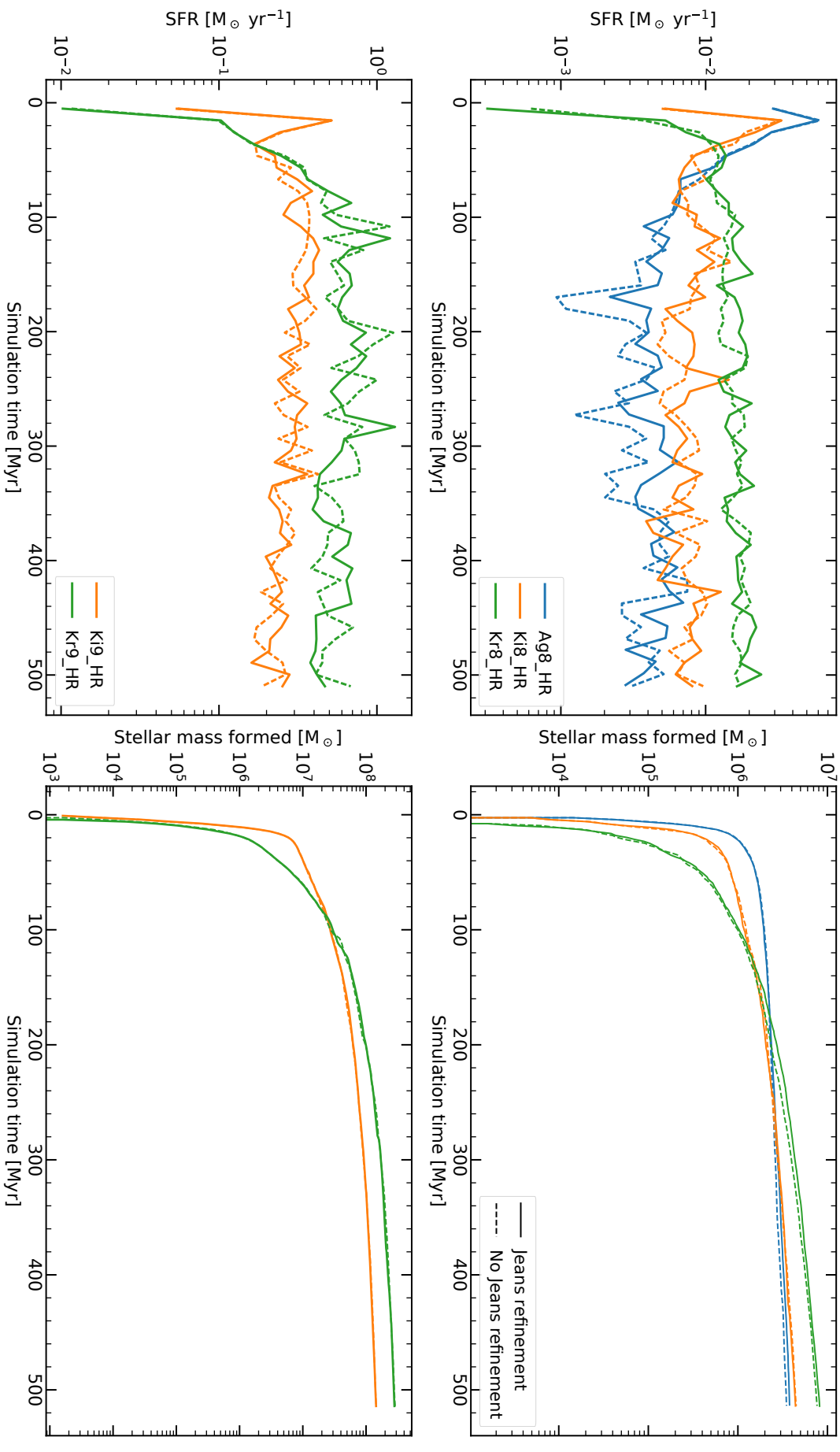

Figure 4.10 – SFR (left panels) and stellar mass formed (right panels) as a function of time, using or not the Jeans refinement. This is at one level higher resolution than the previous figure and runs for G8 (top row) and G9 (bottom row).

refinement criterion is also changed, but it remains insignificant. As these new high-resolution regions are one the outskirts of the extended arms of the galaxy, the explanation for this lack of difference is likely that these regions have a very low star formation rate. The regions with a higher star formation rate are denser and thus already resolved enough. We conclude that using this additional criterion on refinement should not affect much how the models respectively behave compared to their original version.

4.3.2 Restriction of star formation at the highest level, sf_lmax

As star formation should ideally occur on the smallest scale, one might want to restrict star formation to cells at the maximum level of refinement. We test the impact of this additional restriction, sf_lmax, in this section. An advantage of this approach is that it will make the simulations run faster as they will avoid unnecessary tests on lower-level cells, and the expensive computation of the star formation efficiency in these cells where star formation is not expected to occur.

Fig. 4.11 shows the SFR and stellar mass formed for the simulated galaxies, with each model with and without star formation restricted to the maximum level. While the results from KR are the same, there is only a small difference in SFR for AG and KI which is almost not noticeable in the stellar mass formed. This confirms that most stellar particles indeed already form at the maximum level and that this added criterion will not affect the results significantly.

4.3.3 Radiative transfer

A major physical ingredient in our code is radiative transfer (Rosdahl et al., 2013; Rosdahl & Teyssier, 2015). The radiative transfer module has different impacts, but the most important one regarding feedback comes in the form of pre-SN feedback, as detailed in Sec. 3.4. We test for G8 and G9 how the subgrid models fare when these additional physics are implemented or not. With RT, two main effects can lead to the suppression of star formation. The first is photoheating, which heats the gas to temperatures high enough to prevent it from collapsing and forming stars. The second is radiative pressure, which pushes the gas away and lowers the density of the medium surrounding the stars. This then allows the wind from the forthcoming supernova to travel much further and push more gas out of the galaxy, effectively reducing the star formation rate of the galaxy. Without RT, as the stars remain in a denser local environment, the supernovae are trapped and will transmit much more of their momentum to the local medium, without having much impact at the galactic scale.

Low mass galaxy: G8

Fig. 4.12 shows the SFR and stellar mass formed for the G8 galaxies simulated with each model with and without RT. AG exhibits a significantly more drastic effect than the other two models. Not including RT allows a large initial star formation burst, which then depletes the galaxy of its gas. Not being hindered by the pre-SN feedback from RT, the gas can collapse freely in Ag8_NRT and very efficiently form stars up until the first supernovae. The SFR decreases more and more as more supernovae

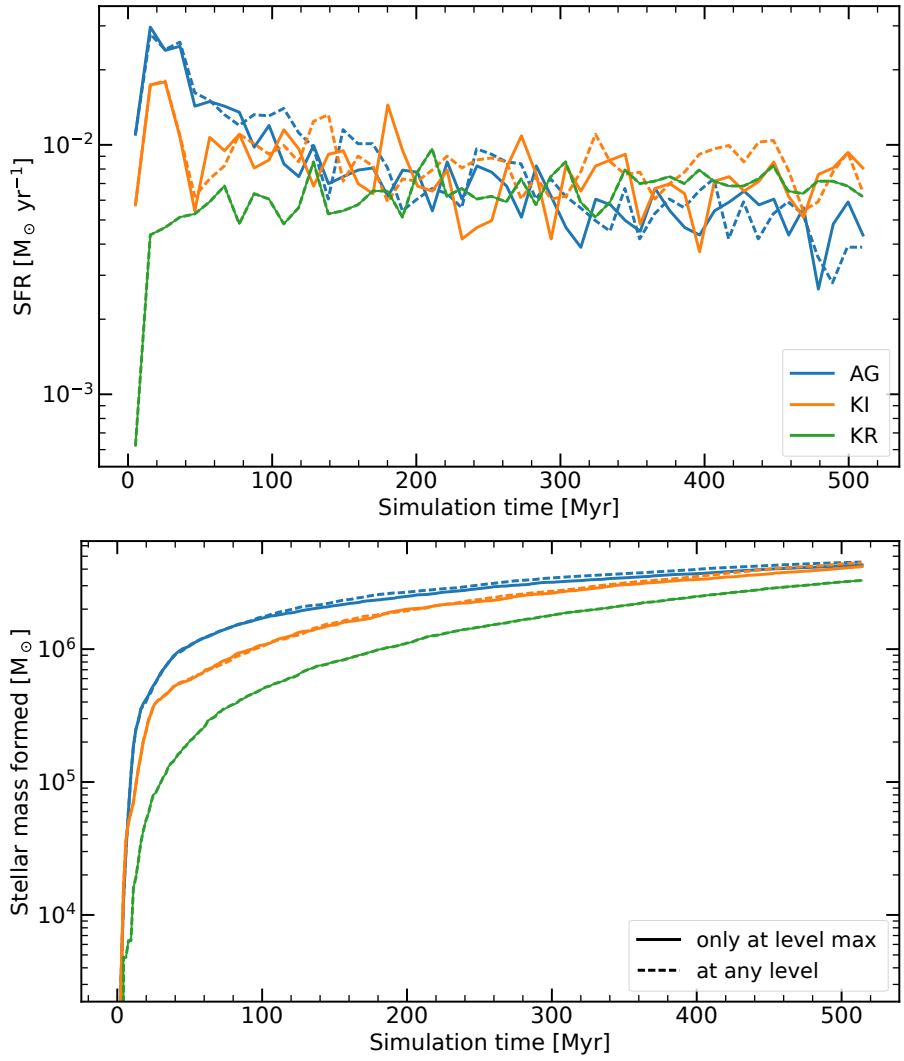

Figure 4.11 – SFR (upper panel) and stellar mass formed (lower panel) as a function of time, with (solid line) or without (dashed line) restriction on the star formation level.

events occur and the gas in the galaxy gets depleted. After some time, the star formation oscillates between efficient star-forming events and gas depletion due to very efficient feedback (as no radiative feedback lowered the density around stars). In KI, the effect is similar but to a significantly lower extent and the stellar mass formed reaches similar values. Lastly, KR behaves differently. As with the other models, the star formation rate is initially higher. However, it is not followed by a decrease in SFR and the star formation remains higher than with radiative transfer. This likely exhibits outflows which are inefficient in reducing star formation when there is no pre-SN feedback and leads to a twice higher stellar mass.

Fig. 4.13 shows the face-on and edge-on hydrogen column density of the galaxies simulated with and without RT in G8. Without RT, the cavities caused by the supernova feedback are significantly more pronounced than when it is included for AG and KI. Especially in AG, this leads to a galaxy with highly inefficient star formation. The total mass reached is nonetheless still significantly higher due to the

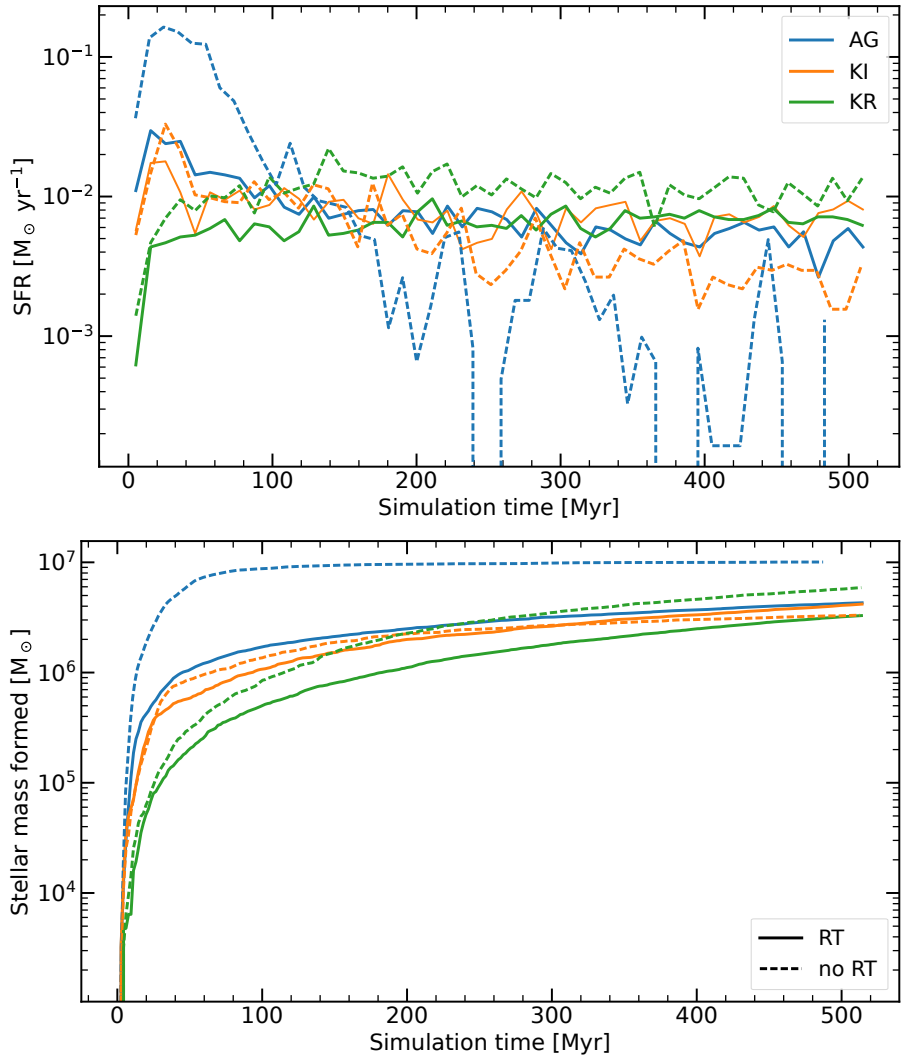

Figure 4.12 – SFR (upper panel) and stellar mass formed (lower panel) in G8 as a function of time, with (solid line) or without (dashed line) radiative transfer.

first peak in SFR, which only starts to decrease after ~ 50 Myr. Such a peak would likely not be produced in a cosmological simulation. Indeed, ideal simulations are initialised with an already formed gaseous disc in which stars can suddenly form. This leads to a sudden excessively high SFR, which would not be found had they formed alongside the disc. With KI, removing the radiation feedback similarly leads to a higher initial SFR. With time, the SFR decreases and reaches values below those from the RT simulation from $\sim 150 - 200$ Myr. As the effect is less striking than with AG, the cause is more ambiguous. We can however see in the maps that, as with AG, the average density of the galaxy is lower without RT and that significantly more gas was ejected out of the galaxy. This means that the initial burst of star formation was sufficiently high without RT to push more gas out of the galaxy and slowly quench the galaxy. We can see in the maps that more gas is ejected out of the galaxy without RT. Then, having more gas available, the model with RT eventually catches up and ends up with a slightly higher final stellar mass. Lastly, we can see in KR that the CGM is unaffected by the inclusion or not of radiative transfer.

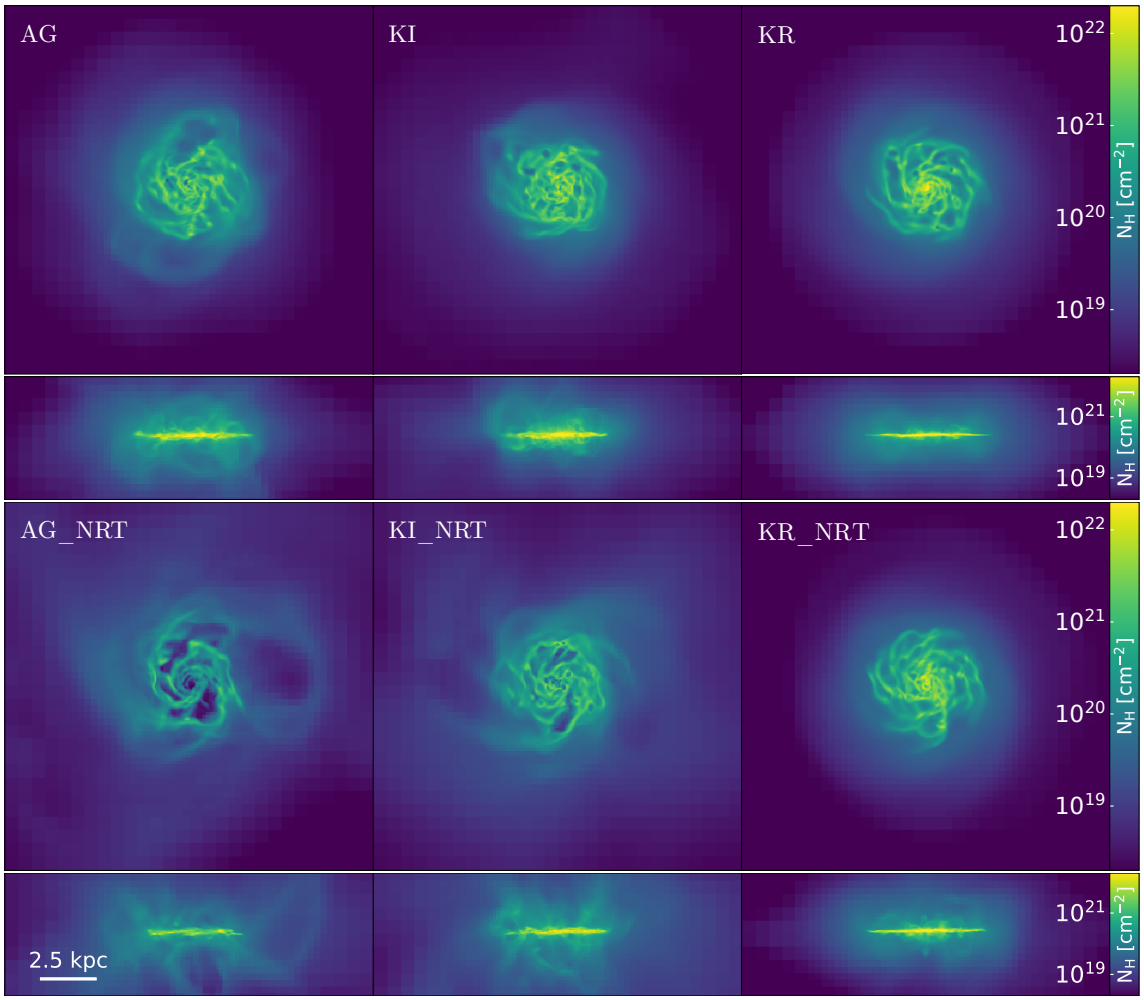

Figure 4.13 – Face-on and edge-on column density maps after 515 Myr with (top rows) and without (bottom rows) radiative transfer in G8. From left to right, we show the simulations Ag8, Ki8 and Kr8.

However, with RT, small cavities can be found in the column density maps whereas they are non-existent or more diffuse without RT. In both cases, the supernovae are highly local and inefficient in driving gas out of the galaxy. The feedback just loses efficiency when the source of pre-SN feedback is removed, possibly due to explosions occurring in a higher-density medium. It then leads to a higher SFR which remains almost constant, unlike the other two models. This then translates into a twice higher stellar mass formed.

With G8, we thus see that in AG and KI, the absence of radiative transfer leads to more efficient star formation, followed by more efficient feedback. This depletes the galaxy of its gas content (see the face-on column density maps) and then leads to a lower star formation rate. In the end, AG produces significantly more stars due to the initial burst which produced most of the stellar mass in the first 100 Myr, while in KI the difference is insignificant. The behaviour in KR does not change much either, except that without RT, the supernovae are less efficient at all times, which leads to a higher SFR and a higher final stellar mass.

Higher mass galaxy: G9

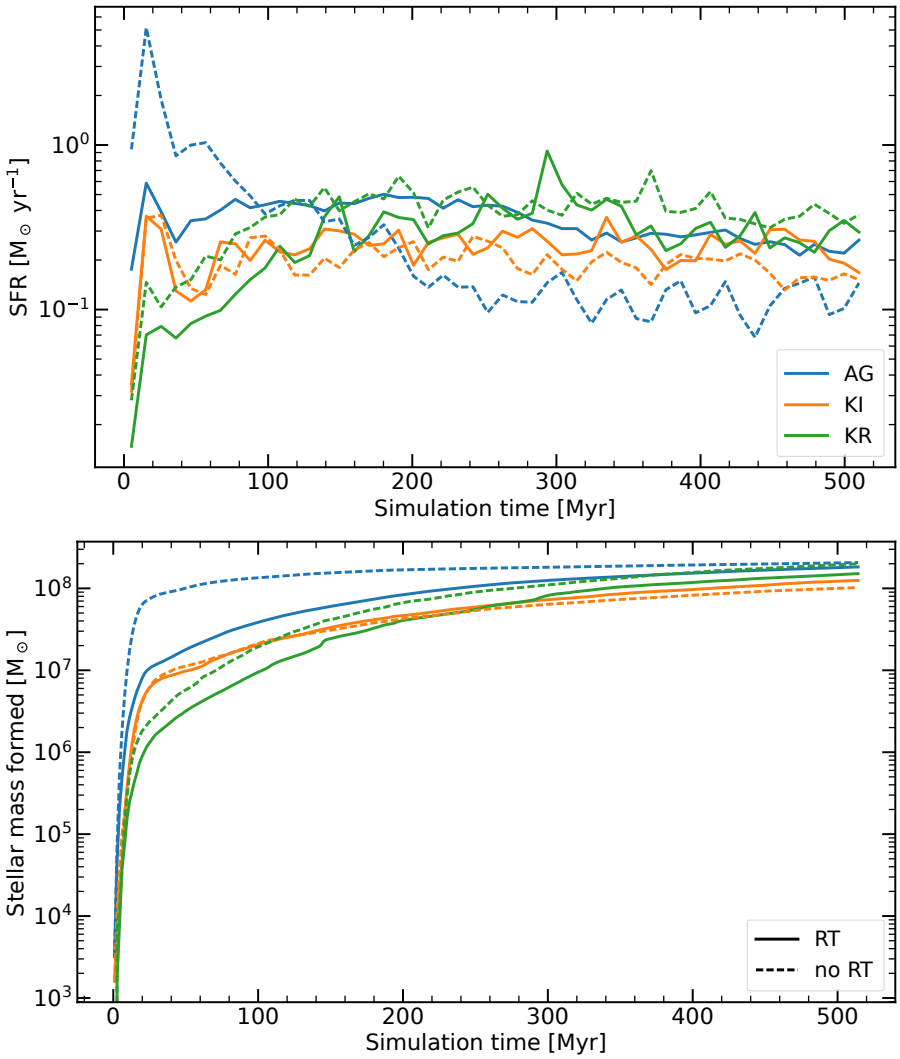

Figure 4.14 – SFR (upper panel) and stellar mass formed (lower panel) in G9 as a function of time, with (solid line) or without (dashed line) radiative transfer.

We now consider the effect of radiative transfer on the more massive galaxy G9. We show in Fig. 4.14 the SFR and stellar mass formed for the galaxies simulated with each model with and without RT. For all three models, the effect is similar to those found with G8, but to a lower extent. As for G8, AG presents a significantly stronger initial burst of star formation without RT, which is followed by a steady decrease in SFR. As the galaxy is more massive, some gas is retained and the galaxy continues to form stars, unlike the bursty cycle of star formation followed by starvation seen in G8. Furthermore, the final stellar mass is similar both with and without RT. This is actually due to G9 providing stronger gravitational support for gas. The effect is twofold. First, the higher gravitational potential makes the supernovae eject gas less far than in G8 in which gas is more easily unbound and more likely to never fall back. Then, the gas is accreted back into the galaxy more quickly than in G8 for the same reason. We can thus reasonably assume that given sufficient time, the same would have occurred for G8 as the simulations are idealised and there is no exterior

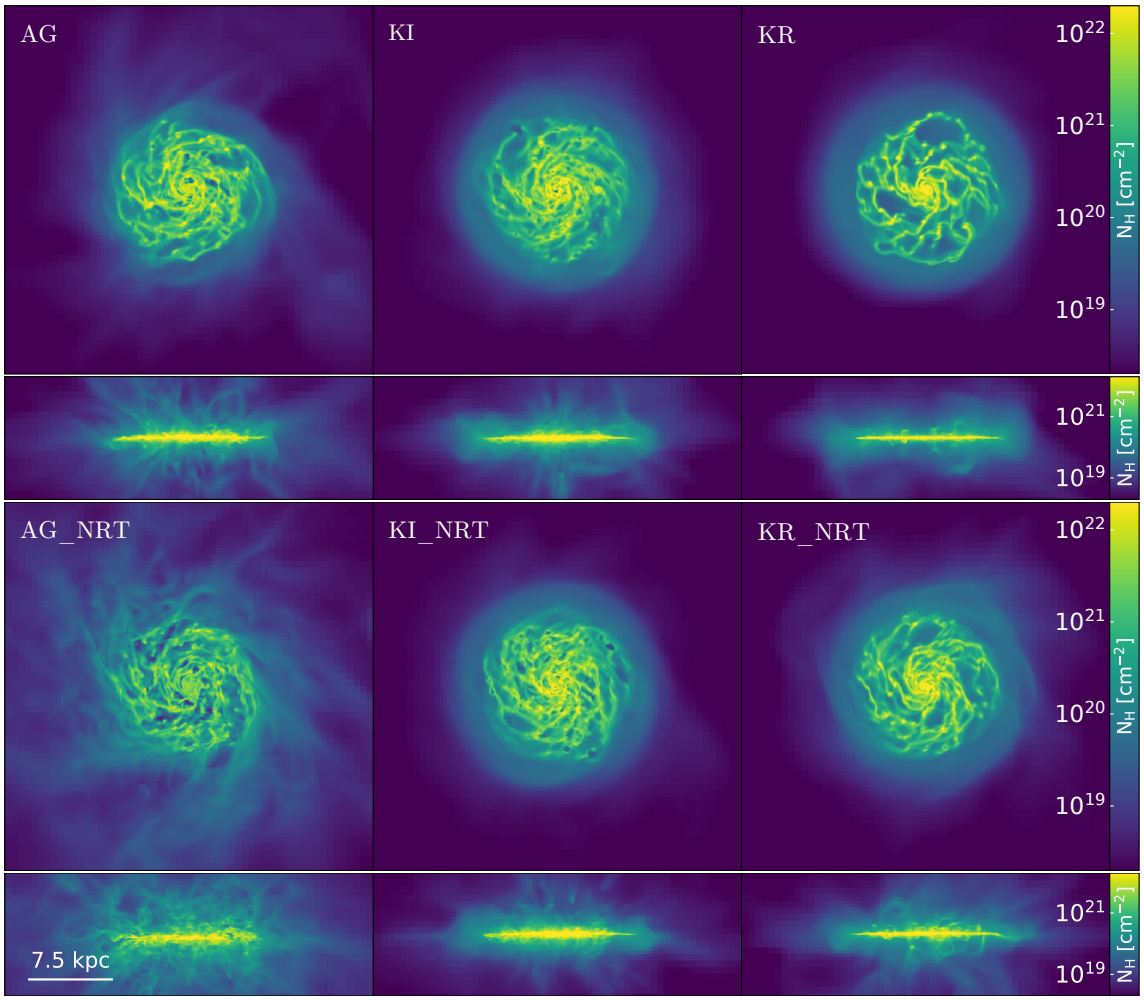

Figure 4.15 – Face-on and edge-on column density maps after 515 Myr with (top rows) and without (bottom rows) radiative transfer in G9. From left to right, we show the simulations Ag9, Ki9 and Kr9.

hindrance preventing the CGM gas from falling back. Note however that not all the gas can fall back due to outflowing boundaries. If the gas is ejected further than 150 kpc from the galaxy centre (out of the simulation box), it is removed from the simulation. We further consider the face-on and edge-on hydrogen column density of the galaxies simulated with and without RT in G9, as shown in Fig. 4.15. These maps clearly confirm the origin of the difference in the stellar mass formed in AG with and without RT. There is significantly more gas in the CGM without RT (bottom left panels) than with RT (top left panels). As explained above, this gas was likely mainly ejected shortly after the first star formation burst and is slowly falling back onto the galaxy. One can also see that the gas column density of this galaxy remains high enough to allow star formation, unlike what has been seen in G8, in which the galaxy got depleted of its gas content. In KI, the initial burst is very similar to with and without RT. Unlike what we found with G8, there is no high burst of star formation triggering early efficient feedback and depleting the galaxy of its gas. Combined with a higher potential well, we find in the column density maps that the CGM is effectively very similar in both simulations with and

without RT. Having the same reservoir for star formation and the RT only inducing a slight difference in the feedback efficiency, both simulations produce a very similar stellar mass. Finally, in KR the SFR is consistently higher without RT except for a single peak as with G8. However, the cause for the differences in star formation can be seen here more clearly than with G8. Indeed, the cavities produced with RT are wider than without it. This is effectively the combined effect of pre-SN and SN feedback being able to create more extended cavities, leading to slightly lower star formation.

In conclusion, by removing RT in G9 we find an effect similar to the one found in G8 but to a lower extent. This lower difference is due to a stronger gravitational potential in G9, preventing the gas from being ejected at large distances and allowing it to fall back on shorter timescales. In AG without RT, powerful outflows drive a considerable amount of gas out of the galaxy which slowly falls back on it, only causing a delayed star formation and producing a galaxy with a CGM significantly richer than with RT. In KI, the feedback is not efficient enough in pushing gas out of the galaxy (unlike in G8) and this leads to two very similar simulations. In KR, we find the same result. With RT, the supernova feedback is slightly more efficient locally in preventing stars from forming and leads to a lower final stellar mass formed.

We can compare these results to Rosdahl et al. (2015), who also tested the impact of RT in G8 and G9. Unlike us, the main effect was found with G9, where adding RT led to lower stellar mass. Interestingly, these authors found that the impact of RT was to smooth the galaxies and hinder star formation, not by disrupting molecular clouds but by suppressing star formation through photo-heating. In our results with AG, we find almost no effect in G9 and when we do not include RT, there is a high initial star formation rate followed by strong feedback ejecting gas out of the galaxies. These two pictures are coherent, but differences in subgrid physics likely drive them. Indeed, the explanation for the initial absence of high star formation burst with RT is likely that photoionisation prevents star formation. In Rosdahl et al. (2015), thermal feedback is used and is less powerful than the one used in AG. Thus, the episode of intense star formation in AG is followed by strong feedback, while it is not powerful enough in Rosdahl et al. (2015) to eject a significant proportion of gas out of the galaxy. For the other two simulations, we believe that the lower impact of RT on our results stems from a combination of a different star formation subgrid model which provides stricter star formation criteria (multi-freefall instead of a Schmidt law with a density threshold) and more powerful feedback which minimises the role of the RT feedback on the galaxy.

4.4 Convergence

Having studied how most parameters that we deem important affect our simulations, we now move on to test how the models behave when changing two different types of resolution. The first is the mass resolution of the stellar particles, i.e. the minimal mass which particles can have in a simulation. The second is spatial resolution, which dictates how small cells can be. As the simulation resolution increases, it resolves structures better. Precise models should thus exhibit better convergence within the limits of the physics they describe.

4.4.1 Stellar particles minimal mass, $m_{*,\mathrm{min}}$

The minimal mass of the particles is an important parameter which depends on the spatial resolution and physics as it is a biased tracer of the gas density field. While a low $m_{*,\mathrm{min}}$ is more computationally costly, feedback schemes relying on an averaged IMF also break down on such scales, as the stellar populations described are too small (Smith, 2021). If the minimal mass of stellar particles is too high, no star will form or only extremely massive ones. Then, the feedback produced will be stronger than it is supposed to be since SN events will be clumped together and synergise into more powerful outflows. We thus test here the impact induced by changing its value for the three models. For AG and KR, the minimal mass of a stellar particle is given by the parameter m_star, while it is determined by nsn2mass for KI. In KI, we computed nsn2mass so that the masses tested were the same as in AG and KR.

AG

We first consider AG, Fig. 4.16 shows the SFR and stellar mass formed for the galaxies simulated with AG using different minimal stellar particle masses. The simulation with the highest stellar particle mass (6400 $\mathrm{M}_\odot$) quickly forms a lot of stars with an SFR of 0.04 $\mathrm{M}_\odot\,\mathrm{yr}^{-1}$. It then decreases quickly, exhibiting cycles of SFR bursts of 0.003 $\mathrm{M}_\odot\,\mathrm{yr}^{-1}$ followed by non-star-forming periods after $\sim$ 100 Myr. The strong decrease in SFR is not seen in the fiducial model, even though there is initially a similar SFR peak. This is because in the simulations with high $m_{*,\mathrm{min}}$, the more massive stellar particles lead to more powerful feedback by having the energy of more supernovae combined. Fig. 4.17 shows the face-on and edge-on hydrogen column density of the galaxies simulated with AG and minimal stellar particle masses of 400 $\mathrm{M}_\odot$, 1600 $\mathrm{M}_\odot$ and 6400 $\mathrm{M}_\odot$. As with what we found by removing RT, the simulation with the more massive stellar particles (rightmost panel) exhibits a lower column density in the galaxy than the other simulations but expelled more gas, as we see denser and more extended gas in the CGM. This leads to self-starvation of the galaxy until a sufficient density is reached and stars can form once again. Then, the cycle repeats itself with strong feedback from these particles. Also, the extent of the cavities we find shows the strength of the SN feedback.

Conversely, if we consider the simulation with a lower minimal mass for particles, we can see that the initial burst of star formation is lower and significantly less extended in time. This is because stars can form earlier with a lower stellar particle mass and can thus generate feedback earlier, which will keep other stars from forming. The SFR then increases slightly and remains relatively constant at $\sim$ 0.01 $\mathrm{M}_\odot\,\mathrm{yr}^{-1}$. In the end, this model produces more stars as the SFR allows this mass to increase steadily with less powerful outflows hindering it. If we now consider the morphology of the corresponding galaxy, we find that the arms show a more distinct filamentary structure than with more massive stellar particles. This effect resembles what is found with a higher density threshold for star formation (see Fig. 4.3). Indeed, with an efficiency of 10% and considering that at most 90% of the gas in a cell can be converted into stellar mass, a minimal stellar mass of 1600 $\mathrm{M}_\odot$ corresponds to a density of $\sim$ 15 cm^{-3}, while 6400 $\mathrm{M}_\odot$ corresponds to a density of $\sim$ 58 cm^{-3}. As we use a density threshold of $\sim$ 25 cm^{-3} in these simulations, forming stellar particles with higher masses can effectively translate into a

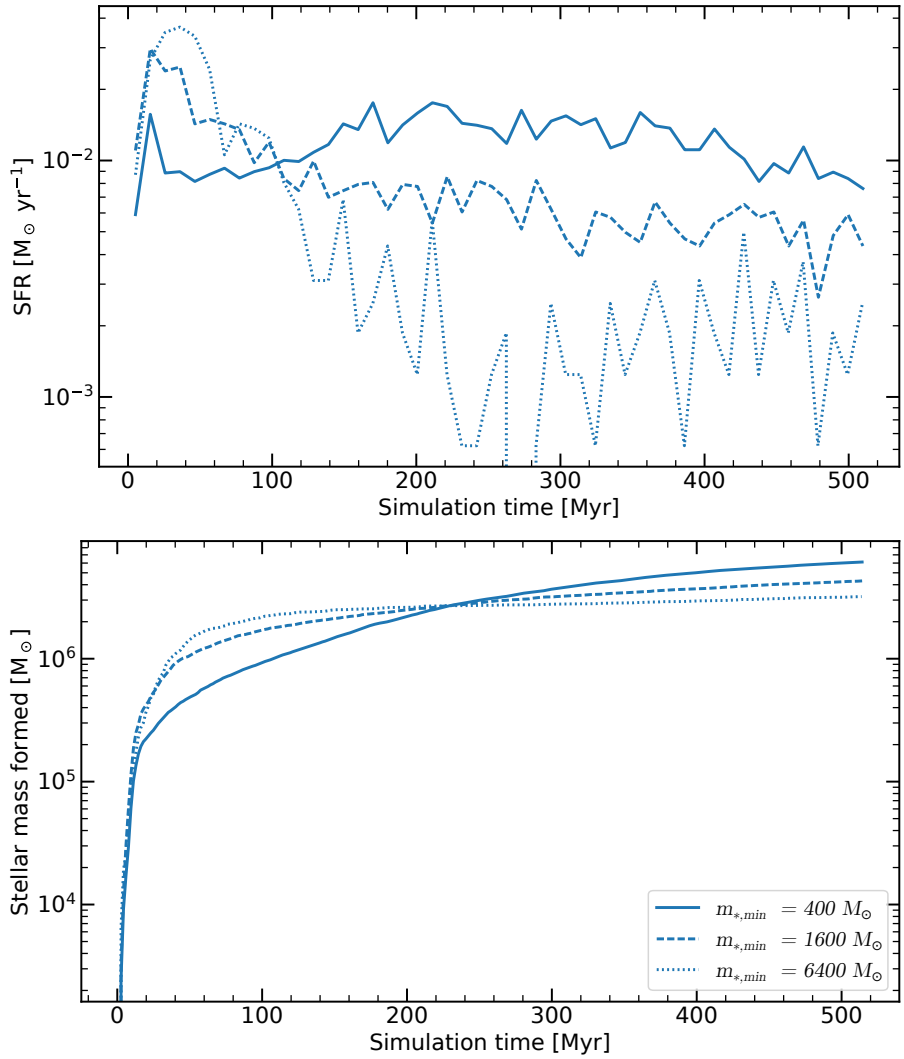

Figure 4.16 – SFR (upper panel) and stellar mass formed (lower panel) as a function of time, using different $m_{*,\mathrm{min}}$ with AG. We respectively consider minimal stellar particle masses of 400 $M_\odot$ in Ag8_m0.4, 1600 $M_\odot$ in Ag8 and 6400 $M_\odot$ in Ag8_m6.4.

criterion more stringent than the density threshold. However, the processes behind this filamentary structure are quite different. Firstly, lowering the minimal stellar particles mass will not affect the density threshold for star formation, as a stellar mass of 1600 $M_\odot$ already corresponds to densities below ~ 25 cm^{-3}. Secondly, the creation of the filamentary structure actually goes in the opposite direction, it appears when the density threshold is higher and when $m_{*,\mathrm{min}}$ is lower[1]. When looking more precisely at the structure of the two filamentary galaxies, it can be noted that there are fewer spiral arms which are more distant from one another in the galaxy with a higher threshold and that its core is smaller. The simulation with a low $m_{*,\mathrm{min}}$ produces less efficient feedback, allowing more gas to fall into the centre of

[1]The model with a higher $m_{*,\mathrm{min}}$ does not behave similarly to the simulation with a high-density threshold because the higher mass of stellar particles leads to stronger feedback which disrupts the galaxy and prevents a filamentary structure from forming.

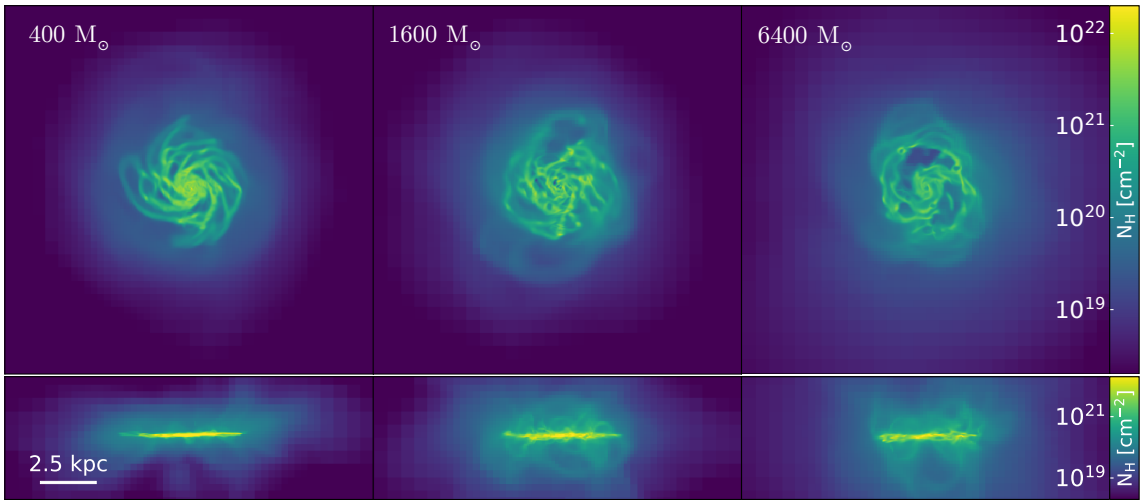

Figure 4.17 – Face-on and edge-on column density maps after 515 Myr with different minimum stellar particle mass in AG. From left to right, we show the simulations Ag8_m0.4 (400 $M_\odot$), Ag8 (the fiducial 1600 $M_\odot$) and Ag8_m6.4 (6400 $M_\odot$).

the galaxy and producing a larger core. Also, through the lack of powerful feedback regulating efficiently star formation, the gas naturally collapses into a dense filamentary structure. However, in the simulation with a higher density, the arms form as the gas has time to collapse into very dense regions, but when stars are formed they induce stronger feedback which regulates the shape of the galaxy and leads to a galaxy with less numerous and better-defined filaments.

Overall, the mass of the stellar particles drives the efficiency of the resulting SN-induced feedback, which shapes the galaxy morphology. On the one hand, a higher $m_{*,\mathrm{min}}$ mass gives stars more time to form as gas clouds have to concentrate further and lead to a higher initial star formation burst. On the other hand, we find a more efficient early feedback with a low stellar particle mass, which is an artefact due to earlier star formation. With a high $m_{*,\mathrm{min}}$, the galaxy is then starved by highly efficient feedback, unlike with a lower $m_{*,\mathrm{min}}$ mass where stars can form continuously and we find more efficient early feedback. A factor 16 difference in the minimal mass of stellar particles can lead to a factor 6 difference in the total stellar mass formed after 515 Myr. This dependence in resolution (either in stellar mass or through the density threshold) is a weakness of the star formation subgrid model in AG. As we have seen with RT, if this was tested on G9, a stronger gravitational potential would allow gas to fall back more efficiently onto the galaxy, reducing the effect of the more efficient feedback on the stellar mass (one would still see cavities more pronounced).

KI

We then test different minimal stellar particle masses with KI. Fig. 4.18 shows the SFR and stellar mass formed for the galaxies simulated with KI, using different $m_{*,\mathrm{min}}$. For the fiducial model and the simulations with a lower minimal stellar particle mass, the results are very similar, with the same initial peak of ~ 0.02 $M_\odot\,\mathrm{yr}^{-1}$ and then oscillating relatively stably within $\sim 0.005-0.01$ $M_\odot\,\mathrm{yr}^{-1}$. For higher mass particles, as seen with AG, the first SFR peak is higher, reaching ~ 0.03 $M_\odot\,\mathrm{yr}^{-1}$ and then decreasing below the two other simulations, seemingly reaching stability at

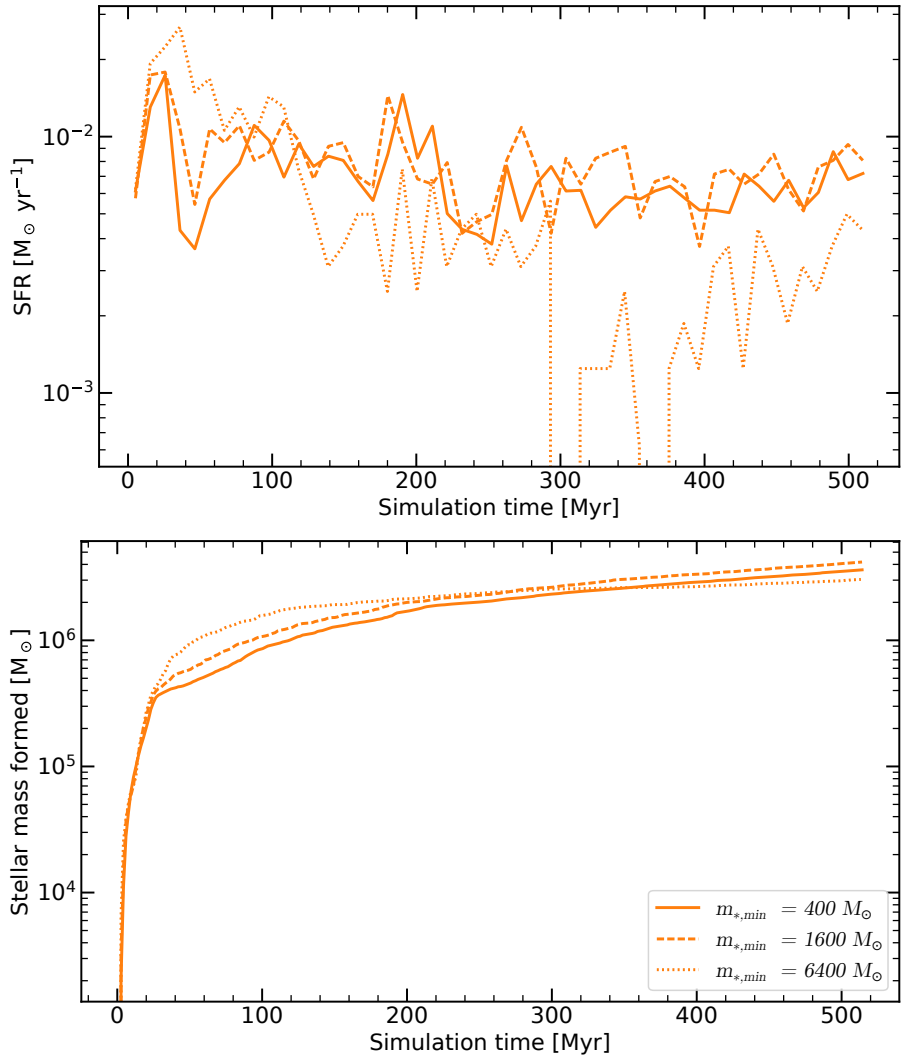

Figure 4.18 – SFR (upper panel) and stellar mass formed (lower panel) as a function of time, with KI using different $m_{*,\mathrm{min}}$. We respectively consider minimal stellar particle masses of 400 $\mathrm{M}_\odot$ in Ki8_m0.4, 1600 $\mathrm{M}_\odot$ in Ki8 and 6400 $\mathrm{M}_\odot$ in Ki8_m6.4.

~ 0.004 $\mathrm{M}_\odot\,\mathrm{yr}^{-1}$ before exhibiting starvation followed by a slowly increasing SFR.

Fig. 4.19 shows the face-on and edge-on hydrogen column density of the galaxies simulated with KI and the three stellar particle masses. After 500 Myr, we find that there are bigger cavities in the models with a high $m_{*,\mathrm{min}}$ and that the CGM is significantly enriched in gas compared to the other two simulations. As with AG, stellar particles of higher mass lead to stronger outflows. At small stellar particle masses, it can also be seen that the feedback is weaker as outflows are unable to affect the CGM.

We now focus on the sudden drop in SFR at $\sim$ 300 Myr with the bottom row of Fig. 4.19 in which we show the same maps as previously but at 300 Myr. As expected, we find that with a high $m_{*,\mathrm{min}}$, the galaxy at this time has been ripped apart by powerful feedback. The resulting galaxy has lost its structure and presents a very thin disc, ejecting strong outflows. This leads to gas depletion and leaves

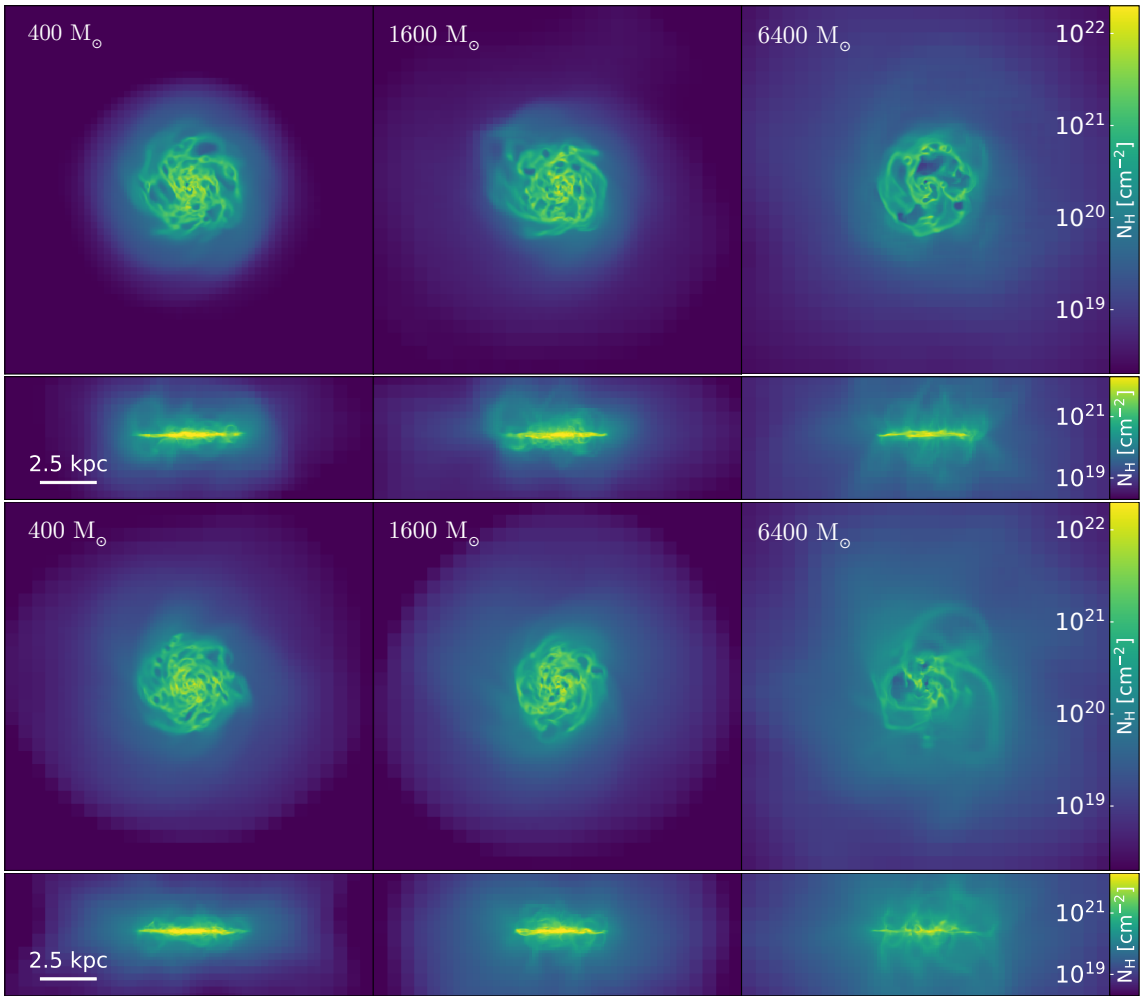

Figure 4.19 – Face-on and edge-on column density maps after 500 Myr (top row) and 300 Myr (bottom row) in KI. We also consider different minimum stellar particle masses. From left to right, we show the simulations Ki8_m0.4 (400 $M_\odot$), Ki8 (the fiducial 1600 $M_\odot$) and Ki8_m6.4 (6400 $M_\odot$).

the galaxy in a non-star-forming state. By looking at earlier maps, we see that the galaxy is already shattered before the sudden drop in SFR. The destruction of the galaxy was thus likely a slow process. At 300 Myr, there is a turning point that makes the galaxy unable to form any more stars, possibly due to the density finally getting sufficiently low. Then, the ejected gas is slowly re-accreted with time and begins to form a new generation of stars, as we see with the slowly increasing SFR following the drop. When enough stars are formed, the feedback will once again get more efficient and this phenomenon will probably repeat itself, forming a saw wave-like SFR.

In the two simulations with a lower $m_{*,\mathrm{min}}$, we find that there is almost no difference in their morphology at 300 Myr. This shows that the difference between these at 500 Myr came afterwards. Also, as the extent of the disc in the CGM is larger at this time, the difference between the fiducial simulation (with gas in its CGM) and the one with the lowest stellar particle mass (almost no gas in its CGM) stems from the fiducial model being better in preventing gas from falling into the

galaxy. The feedback is stronger than with a lower $m_{*,\min}$, in which the gas falls more easily, forming a halo of gas in the shape of a disc around the galaxy. This is unlike other simulations, where the more irregular shape is due to outflows.

Nevertheless, even though these simulations prove to form galaxies with different morphologies, the stellar masses formed are very similar, the differences becoming insignificant after 200 Myr. We could attribute this to the fact that we are studying a closed system, but the results from AG and KR (previous and next subsection) show that even with a closed system the stellar mass does not necessarily converge. This seems that the models used in KI converge better with mass resolutions.

KR

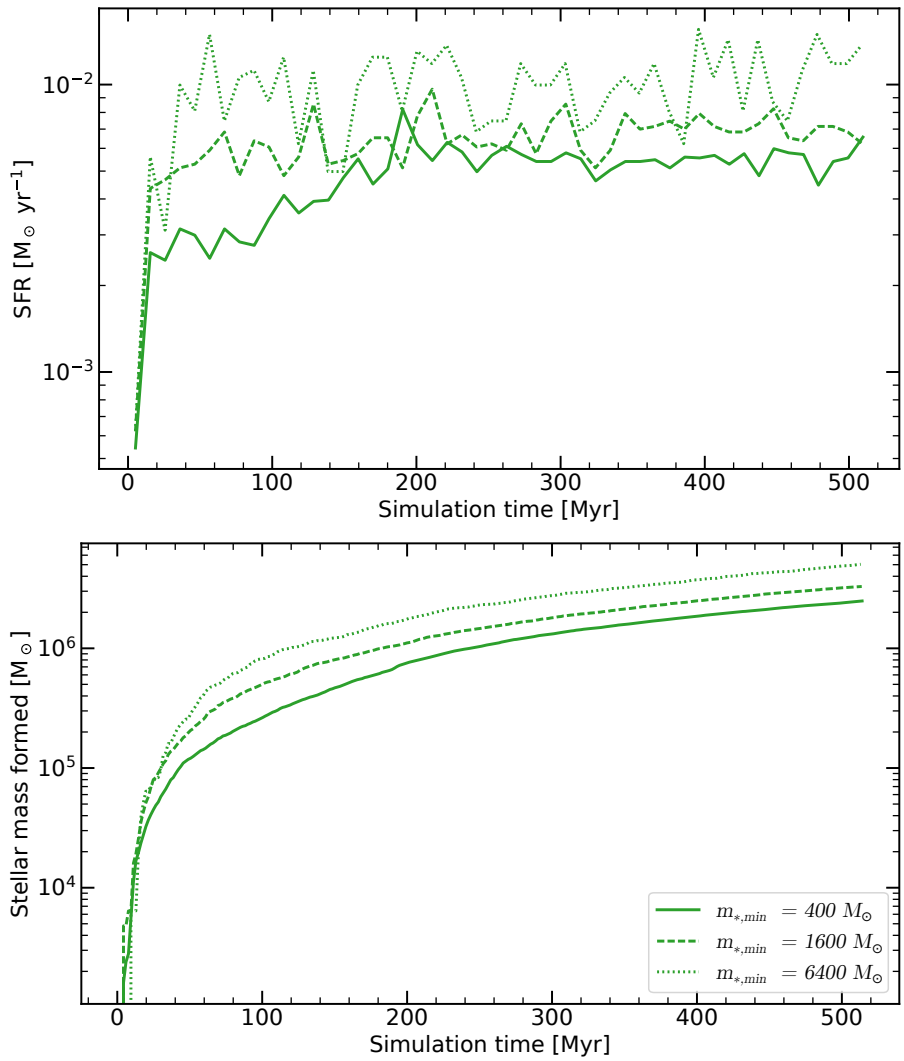

Figure 4.20 – SFR (upper panel) and stellar mass formed (lower panel) as a function of time, with KR using different $m_{*,\min}$. We respectively consider minimal stellar particle masses of 400 M$_\odot$ in Kr8_m0.4, 1600 M$_\odot$ in Kr8 and 6400 M$_\odot$ in Kr8_m6.4.

Finally, we test the effect of $m_{*,\min}$ on KR. Fig. 4.20 shows the SFR and stellar mass formed for the galaxies simulated with KR using different minimal stellar

particle masses. We find here that when the stellar particle masses are higher, the SFR and the total stellar mass formed are also higher. This is opposed to what we found in the two previous models, where feedback was stronger when $m_{*,\mathrm{min}}$ was higher and led to lower mass galaxies. We nonetheless note the higher burstiness of the SFR for the simulations with the highest $m_{*,\mathrm{min}}$, which is a hint for stronger feedback. Fig. 4.21 shows the face-on and edge-on hydrogen column density of

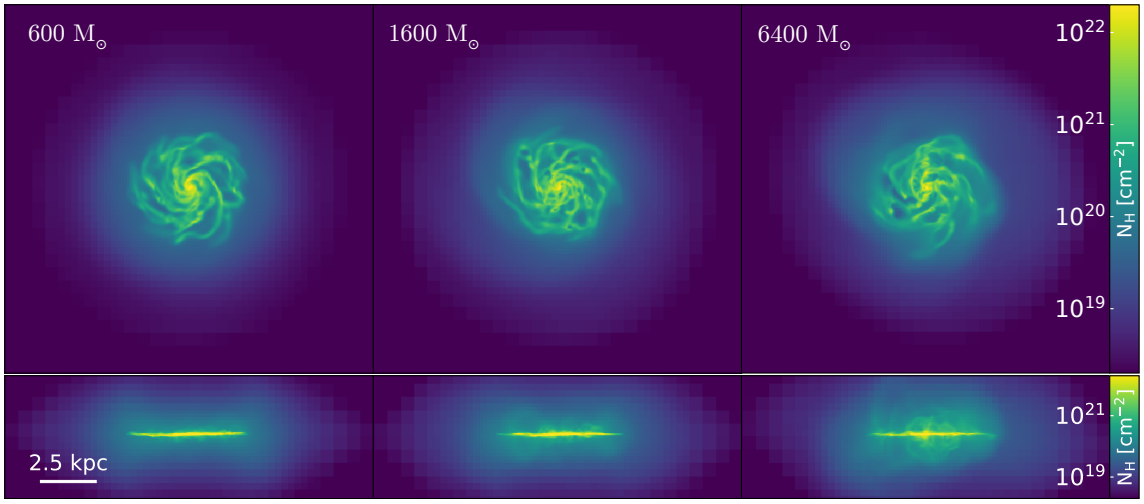

Figure 4.21 – Face-on and edge-on column density maps after 515 Myr with different minimum stellar particle mass in KR. From left to right, we show the simulations Kr8_m0.4 (400 $\mathrm{M}_\odot$), Kr8 (the fiducial 1600 $\mathrm{M}_\odot$) and Kr8_m6.4 (6400 $\mathrm{M}_\odot$).

the galaxies simulated with KR and the three stellar particle masses. These maps confirm that a higher $m_{*,\mathrm{min}}$ induces more powerful feedback, as we found in the other models. The galaxy with the lowest $m_{*,\mathrm{min}}$ presents relatively well-defined arms — which we identified as a potential signature of inefficient feedback — while it is less noticeable for the one with the highest $m_{*,\mathrm{min}}$. A direct signature of stronger feedback is that on the edge-on maps, we can see that galaxies with a higher $m_{*,\mathrm{min}}$ exhibit ejecta more extended than in the other simulations. However, none of these galaxies seems to be able to eject gas in the CGM through outflows and the cause for a higher SFR with more efficient feedback remains a mystery into which we won't delve further. A lead to investigate the process might be to study the star formation sites, as feedback might actually favour star formation through a form of positive feedback: turbulent compression (see Sec. 6.1).

Summary on the convergence with $m_{*,\mathrm{min}}$

For the three models, we found that feedback became more efficient with increasingly high $m_{*,\mathrm{min}}$ and more massive stellar particles. In AG, the higher mass of stellar particles allows a higher and larger initial SFR burst to form, in which most of the stellar mass is formed. The galaxy is then depleted of its gas and struggles to form stars. We found a similar effect in KI, but to a significantly lower extent. Surprisingly, it goes in the other direction in KR and the stellar mass formed is higher with higher stellar particle mass.

Also, the stronger feedback seen with higher stellar particle masses leads to a drastic change in the morphology of the simulated galaxies, with AG showing the

largest difference and KR the smallest one. Overall, the stellar mass is stable in KI, slightly less in AG (it would nonetheless probably increase with time) and very different with KR. Also, the morphology of the galaxy is less impacted in KR and significantly more in AG.

4.4.2 Spatial resolution, $\Delta x_{\rm min}$

We now consider the convergence of each model when changing its spatial resolution. This is one of the most important challenges when considering simulations, as their main limitation is resolution and subgrid models are meant to represent what would happen at higher resolution.

AG

Fig. 4.22 shows the SFR and stellar mass formed for the G8 and G9 galaxies simulated with AG at different spatial resolutions. We test resolutions of 18.3 pc, 36.6 pc, and 73.2 pc. The trends are very similar for both G8 and G9, but less marked for G9.

With a higher resolution, the stars are formed faster than in the fiducial model. With a lower resolution, the SFR takes longer to set off and remains quite low compared to the fiducial simulation. Indeed, with a lower resolution, the cells are on average at a lower density. The density threshold of the higher resolution simulation is consequently not adapted. This results in a galaxy with a lower stellar mass. Conversely, the difference with respect to the fiducial simulation is less pronounced at higher resolution.

Table 4.5 – List of the simulations run with AG, testing different resolutions and adapting the star formation threshold value. The asterisk on the runtimes symbolises simulations which had to be restarted due to an issue with the computer. The real computing time is thus in reality slightly lower than written here.

	Galaxy	Δx [pc]	n_* [cm^{-3}]	runtime [hCPU]
Ag8	G8	36.6	25	1462
Ag8_HR	G8	**18.3**	25	3886
Ag8_LR	G8	**73.2**	25	344
Ag8_HR_n56	G8	**18.3**	**15**	3560
Ag8_LR_n15	G8	**73.2**	**56**	455
Ag9	**G9**	36.6	25	9341
Ag9_HR	G9	**18.3**	25	35550*
Ag9_LR	G9	**73.2**	25	1913
Ag9_HR_n56	G9	**18.3**	**56**	33583*
Ag9_LR_n15	G9	**73.2**	**15**	2073

We thus also compare how AG behaves with a star formation density threshold scaled with resolution. Comparing the density thresholds in Agertz et al. (2013,

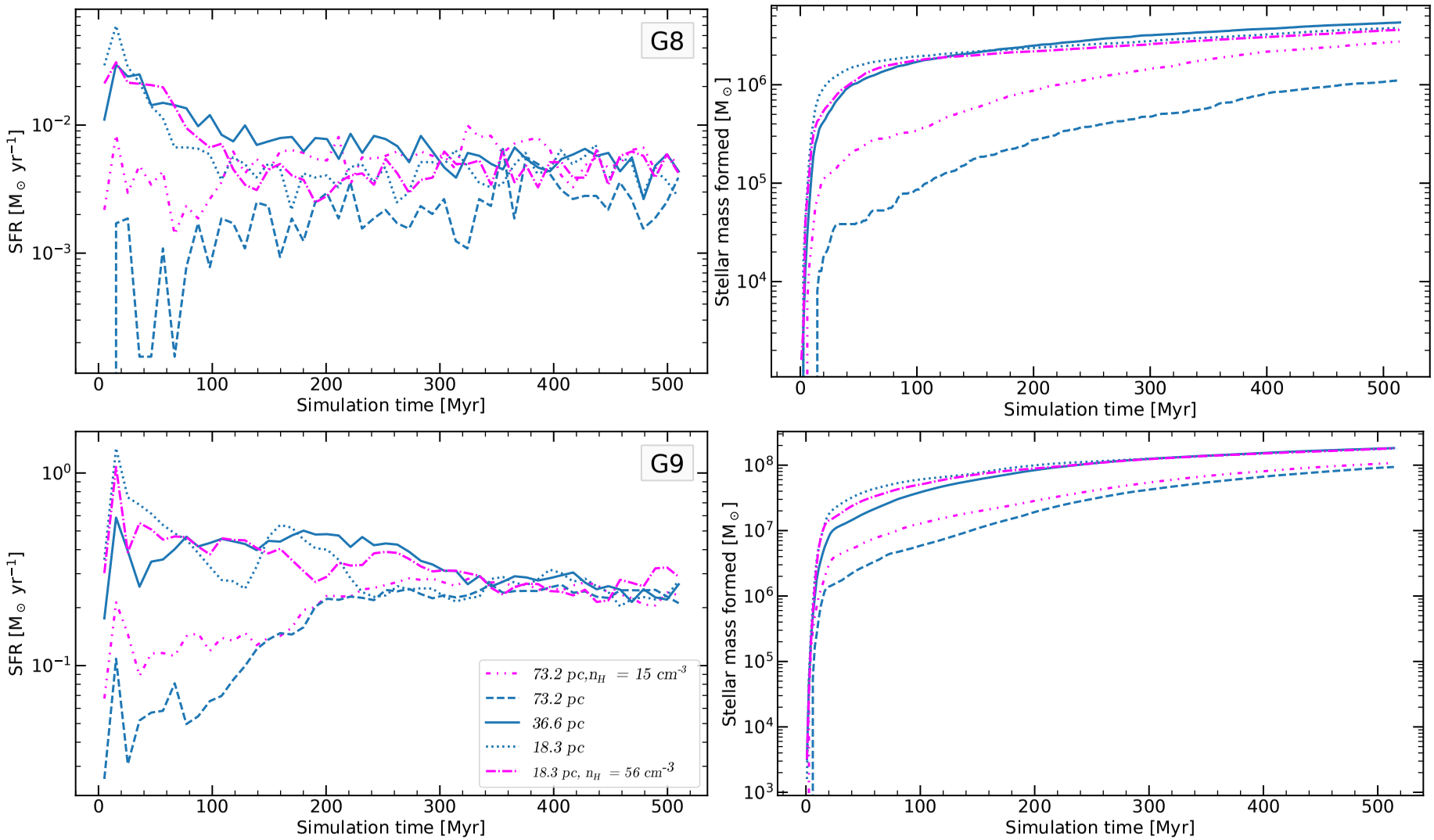

Figure 4.22 – SFR (upper panel) and stellar mass formed (lower panel) in G8 (top row) and G9 (bottom row) as a function of time at low (dashed line), fiducial (solid line) or high (dotted line) resolution. We also show simulations with an adapted density threshold using bolder lines.

2020) and assuming that they depend on resolution, we estimate that the choice of the density threshold should be roughly inversely proportional to the resolution. In this spirit, we compute from these references that the density threshold at 18.3 pc (resp. 73.2 pc) should be within $49-68$ cm^{-3} (resp. $12-17$ cm^{-3}) so we pick a value of 56 cm^{-3} (resp. 15 cm^{-3}). If we also consider that $t_{\rm ff} \propto \rho^{-1/2}$, one should expect the density threshold to scale as $(\Delta x)^{-1.5}$. Following this second approach, we find a range of possible density thresholds even larger than with a simple proportionality and roughly overlapping with the prior values (the upper limit at 73.2 pc would then be 14 cm^{-3}). We thus choose to keep the values computed with a straightforward proportionality. We show the new list of simulations considered in table 4.5 and show the two additional curves in bold. For the high-resolution simulation, we still find a good convergence when comparing the model with an adapted threshold to the fiducial model. It even produces closer to the fiducial simulation, especially in G8, where the difference is more noticeable. For the low-resolution simulations, the difference in the fiducial final stellar mass goes from a factor of four to a factor less than 1.3 with a more suitable density threshold in G8, reaching a far better agreement. The star formation history is not so different compared to the higher resolution simulations, except for the first burst of star formation. Shortly after this burst, both the low-resolution simulation and the high-resolution simulations converge at a nearly constant rate. Based on our findings in Sec. 4.4.1, this shows that this adaptation of the density threshold should also probably be combined with an increased stellar particle mass so that it corresponds to the higher resolution simulations (assuming these latter have converged). Indeed, as the main impact of $m_{*,\rm min}$ lies in the height and width of the first star formation burst, a lower $m_{*,\rm min}$ could compensate for the initial lack of star formation found at low resolution by leading to a larger initial star formation rate.

Fig. 4.23 shows the face-on and edge-on hydrogen column density of the three simulations. We find that the morphology of the galaxy also changes drastically with resolution. When going to higher resolution in both G8 and G9, substructures are more resolved and the CGM is significantly richer in gas, similarly for both the fiducial and the higher resolution simulations. With a lower resolution, the arms are smoother and the CGM retains a disc shape originating from the initial conditions. Due to a higher gravitational potential, this effect is more marked in the case of G9. This is very similar to what we find with a higher stellar particle mass or a higher density threshold, which both lowered the impact of feedback and led to the formation of a more well-defined spiral structure and an empty CGM.

KI

Fig. 4.24 shows the SFR and stellar mass formed for the G8 and G9 galaxies simulated with KI at resolutions of 9.16 pc, 18.3 pc, 36.6 pc, 73.2 pc, and 146 pc (see table 4.2). The comparison of the fiducial model to the higher-resolution simulations shows an excellent convergence, with the only difference being that at higher resolution, a more massive initial burst is found. For G8, lowering the maximal resolution by one level produces an inconsequential difference. The lowest maximal resolution however leads to a significantly underestimated stellar mass, a factor ~ 3 lower than the other simulations. This is due to a stronger cycle of star formation followed by very efficient disruptive feedback, as seen in the galaxy star formation rate. This is

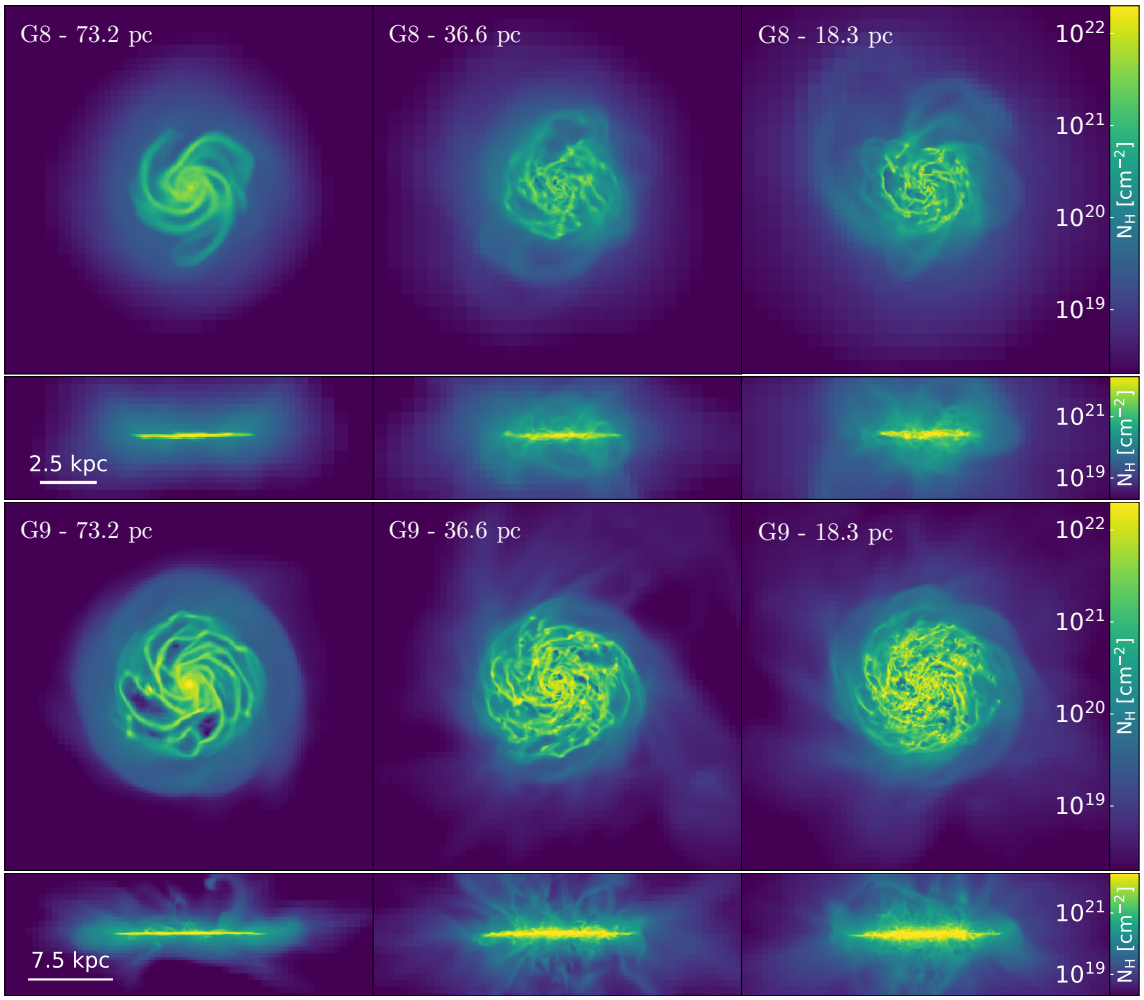

Figure 4.23 – Face-on and edge-on column density maps after 515 Myr with different maximal resolutions in AG. From left to right, the simulations shown have a maximal resolution of 73 pc (left panel), 37 pc (middle panel) or 18 pc (right panel). The leftmost and rightmost figures are the versions with an adapted threshold, we do not show the others as they are very similar.

directly caused by more massive particles forming in Ki_ELR (resolution of 146 pc). While in all the other simulations the mass of the stellar particles is $1 - 2m_{*,\mathrm{min}}$, a significant proportion of them is more massive than $2m_{*,\mathrm{min}}$ in Ki_ELR and even reaches $5m_{*,\mathrm{min}}$. As explained earlier, these more massive particles thus represent a larger stellar population and this leads to a clumped feedback which is overly efficient (Kimm et al., 2015). This effect is not seen with the G9 galaxy, as it possesses a stronger potential well, which likely makes the feedback less disruptive at the galaxy scale. This discrepancy emphasises an important point as this simulation has a very low resolution of 146 pc. These subgrid models describe what happens at the scale of molecular clouds. If the resolution is too low and cannot resolve molecular clouds, such models should not work.

The initial burst and large-scale evolution of the SFR (i.e. not considering the oscillations) are very similar from one simulation to another, especially in G9 where the initial peak is the same for all simulations, even with the lowest maximal spatial

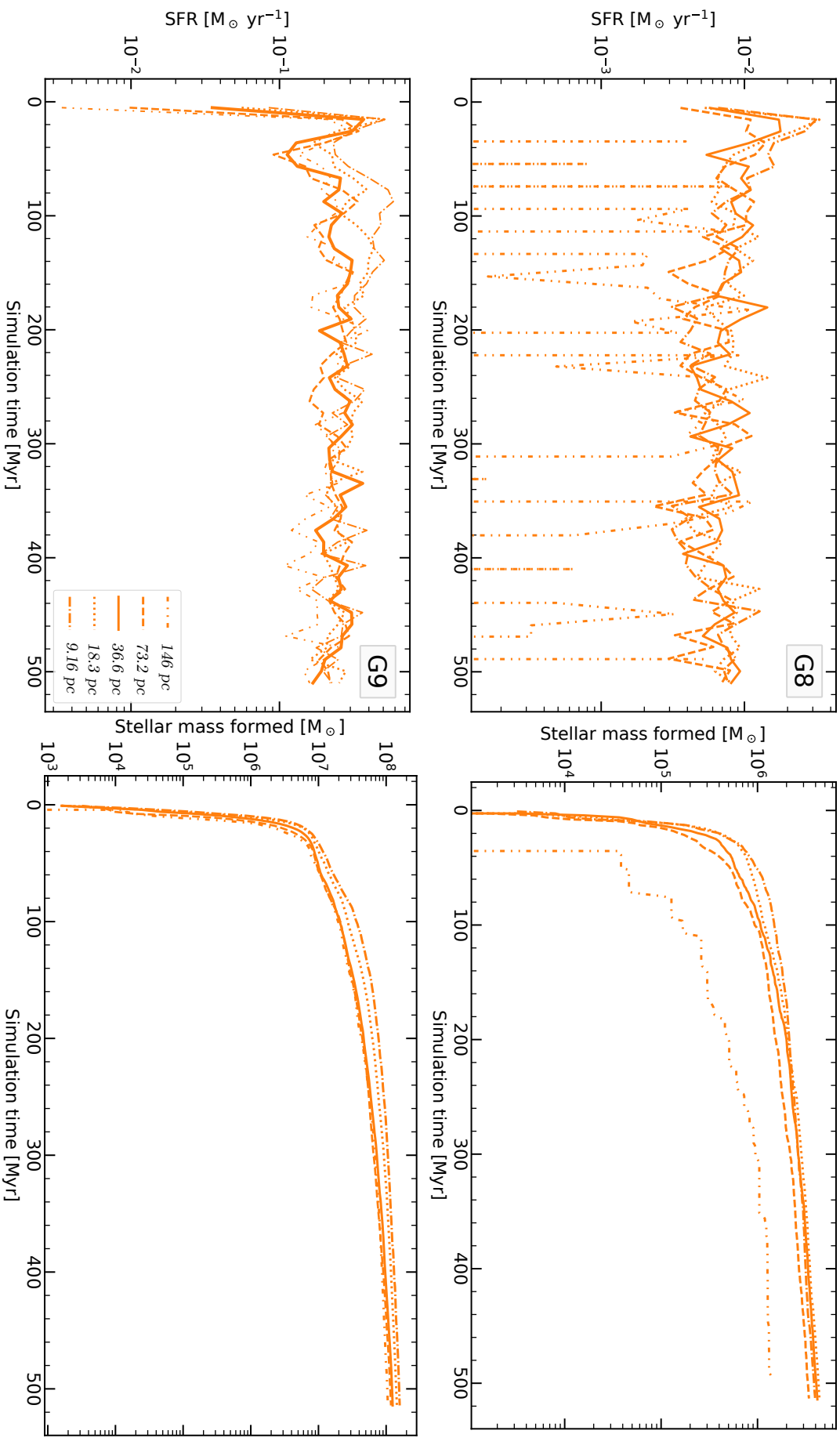

Figure 4.24 – SFR (upper panel) and stellar mass formed (lower panel) in G8 (top row) and G9 (bottom row) as a function of time, with five different maximum resolution lengths.

resolution. This shows that this model is very efficient in self-regulating itself at different scales and is seemingly scale-free (as long as the formation of clumps is resolved, $\Delta x \lesssim 100$ pc), unlike AG where the parameters have to be adapted carefully depending on the resolution.

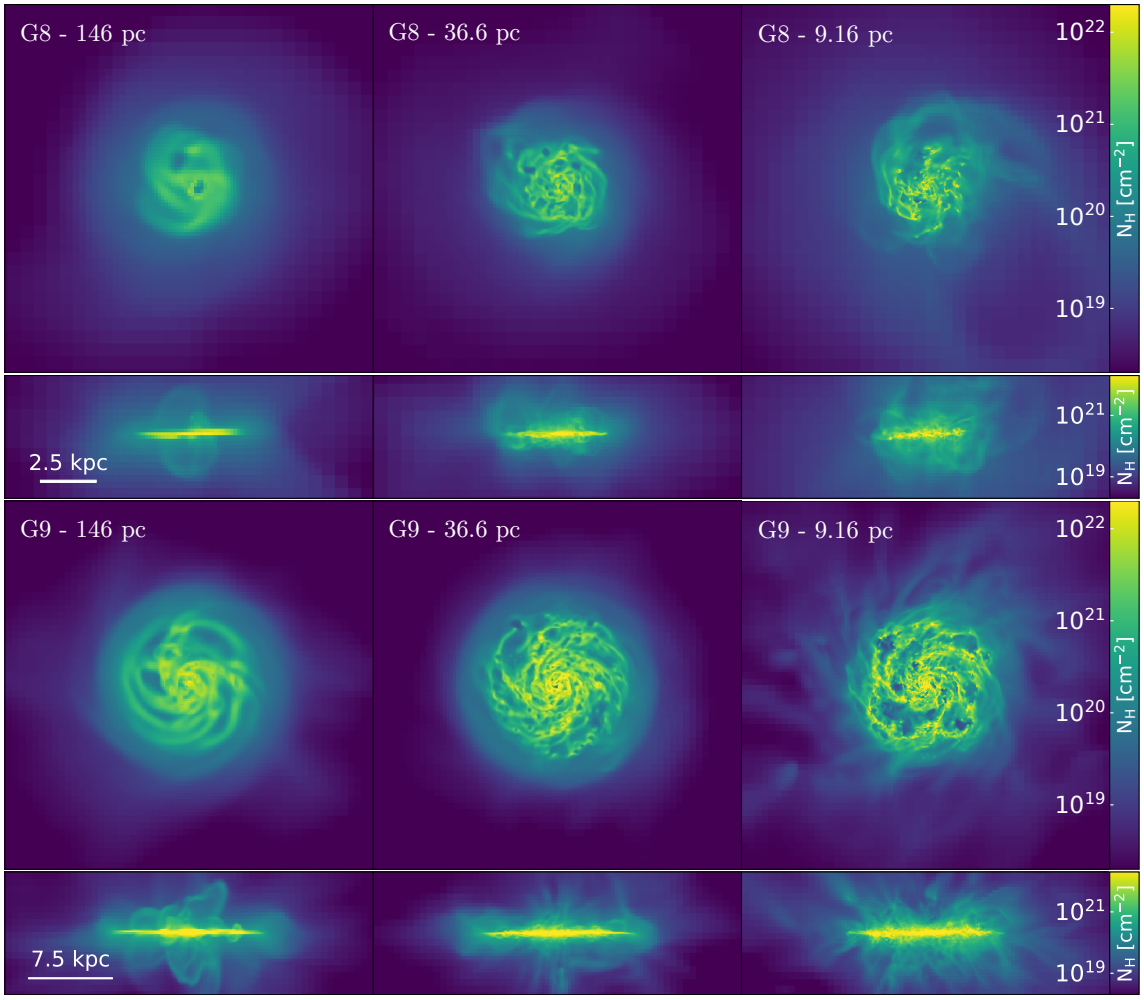

Figure 4.25 – Face-on and edge-on column density maps after 515 Myr with different maximal resolutions in KI. From left to right, the simulations shown have a maximal resolution of 146 pc (left panel), 37 pc (middle panel) or 9 pc (right panel).

Fig. 4.25 shows the face-on and edge-on hydrogen column density of the galaxies simulated with KI and a maximal spatial resolution of 9 pc, 37 pc and 146 pc. We only show the extreme resolutions and the fiducial ones, as the evolution of morphology with the resolution is relatively consistent. As with AG, the more resolution there is, the more defined the substructures are. In G8 at low resolution, we find an irregular structure, not showing arms as defined as with AG but relatively similar to the fiducial galaxy. We can also see a cavity which gets more defined with increased resolution. When considering the simulation with the highest resolution, these become more extended and eventually puncture the galaxy, as seen in the top-right panel of Fig. 4.25. When considering G9, the same behaviour can be found with increasingly numerous and defined holes.

We also find that the CGM is strongly influenced by resolution, as it leads to more

efficient feedback. The halo leftover from the initial conditions gets smaller when increasing the resolution from 37 pc to 18 pc. However, when further increasing the resolution, outflows become more noticeable and can be seen to impact the CGM in both highest resolution maps.

KR

Fig. 4.26 shows the SFR and stellar mass formed for the G8 and G9 galaxies simulated with KR at resolutions of 9.16 pc, 18.3 pc, 36.6 pc, 73.2 pc, and 146 pc (see table 4.3). Unlike the previous simulations, there is a striking difference, with the stellar mass directly scaling with resolution. This difference in total stellar mass formed directly comes from the star formation scaling with resolution. In G8, an increase in maximal resolution by one level leads to an increase in the SFR and the total stellar mass formed by more than a factor of two up to the penultimate level. The same effect can be observed with G9, showing almost no convergence. However, at the highest resolutions, this effect diminishes and a potential hint of convergence appears, likely as most of the gas available has been converted into stars.

Fig. 4.27 shows the face-on and edge-on hydrogen column density of the galaxies simulated with KR and a maximal spatial resolution of 9 pc, 37 pc and 146 pc. We only show the extreme resolutions and the fiducial ones, as the evolution of morphology with the resolution is relatively consistent. We see that the galaxy tends to form spiral arms when going to a lower resolution, in G8 as well as in G9. When increasing resolution, more substructures are visible, not retaining the spiral structure, as seen with AG. The CGM is also more enriched when increasing resolution. This can especially be noticed in the edge-on column density maps of G9.

Interestingly, AG exhibits significantly better convergence than KR in stellar mass, but the effects seen on the morphology of the galaxy are very similar. This effectively shows that the gaseous morphology is a powerful complementary constraint to the stellar mass when considering different feedback models.

Summary on the convergence in spatial resolution

We summarise here our results on spatial convergence. For all three models, a relatively similar evolution in gas morphology is found. With decreasing resolution, the details of the galaxies are blurred out and their CGM shows strong relics from the initial conditions, with a disc not impacted by outflows. In AG and KR, spiral arms form, while KI retains a similar structure as in the fiducial simulation. Increasing resolution produces smaller substructures and leads to a CGM enriched in gas due to stronger outflows. This is especially noticeable in G9 with KI.

We considered the impact of resolution on the stellar mass. The convergence in resolution is relatively good in AG but needs to be adjusted by changing the density threshold for star formation. We also speculate that an additional scaling in the minimal mass of stellar particles might allow for better convergence.

In KI, the simulations are well converged from a resolution of 73 pc in G8 and all produce the same stellar mass in G9. The difference in G8 at a resolution of 146 pc arises from the extreme burstiness of star formation, showing extreme episodes of star formation followed by periods without star formation due to extremely massive

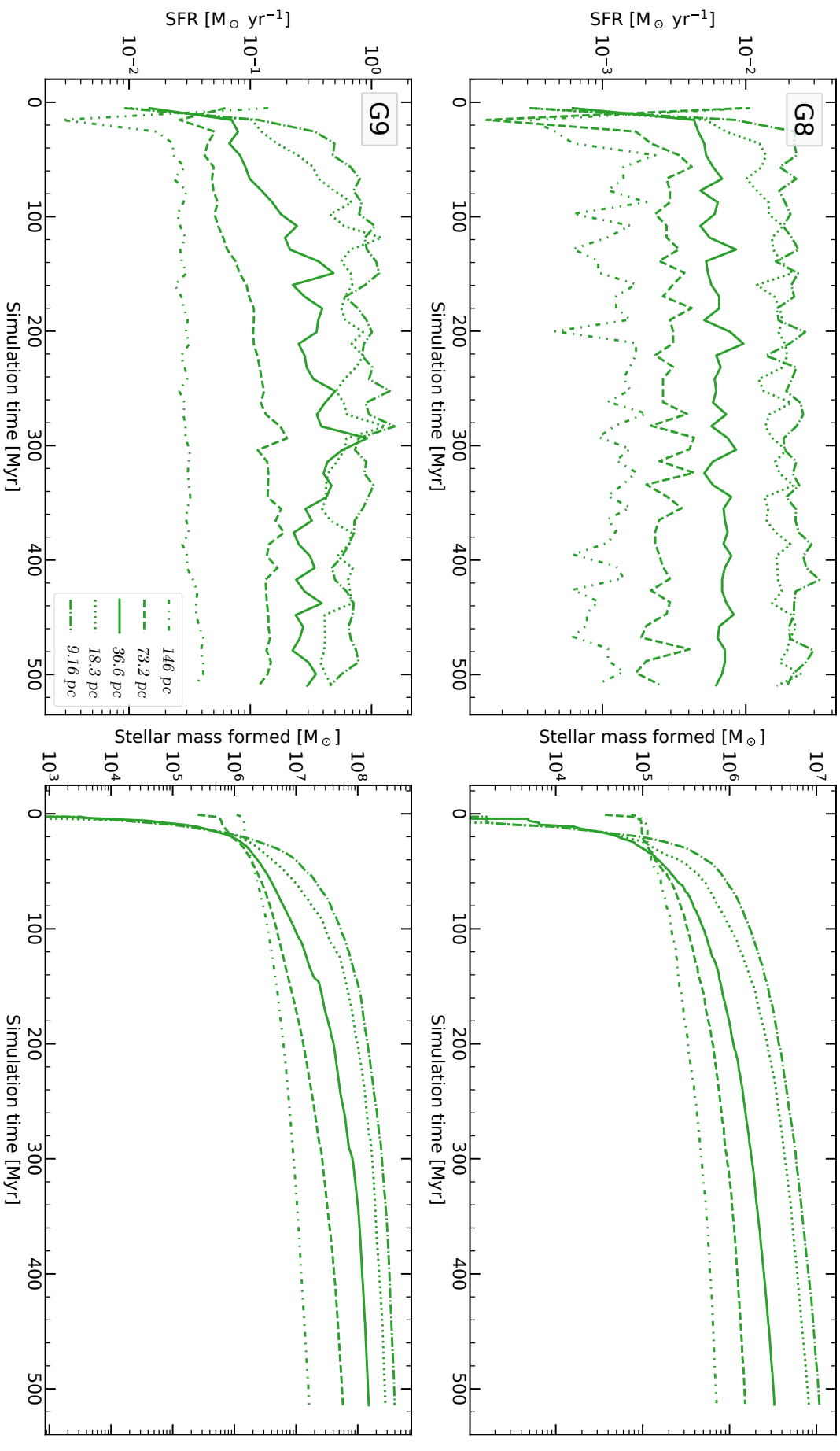

Figure 4.26 – SFR (upper panel) and stellar mass formed (lower panel) in G8 (top row) and G9 (bottom row) as a function of time at low (dashed line), fiducial (solid line) or high (dotted line) resolution.

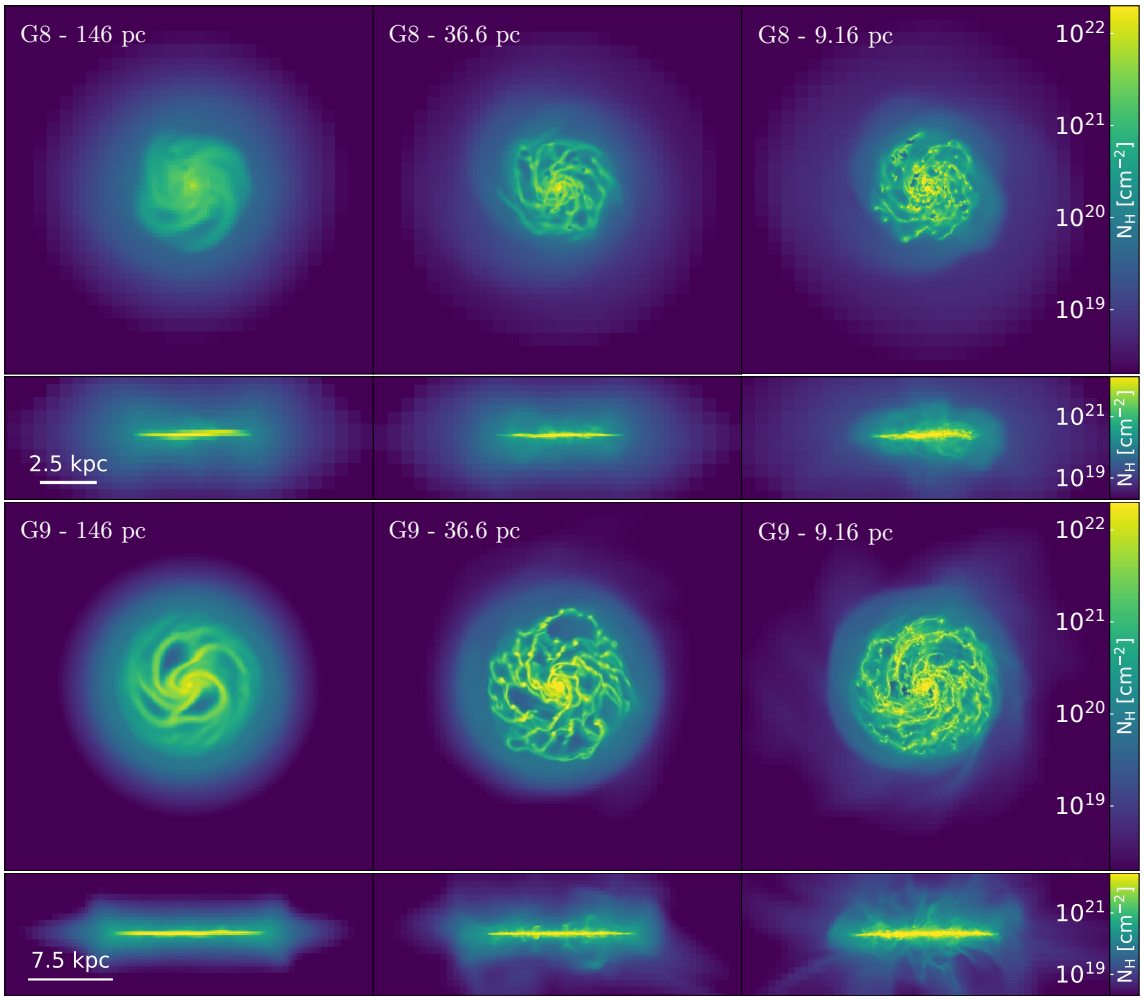

Figure 4.27 – Face-on and edge-on column density maps after 515 Myr with different maximal resolutions in KR. From left to right, the simulations shown have a maximal resolution of 146 pc (left panel), 37 pc (middle panel) or 9 pc (right panel).

stellar particles. This model still produces overall an excellent convergence with resolution.

Lastly, the simulations ran with KR exhibit poor convergence with the resolutions we tested. This difference is the same as the one seen when varying the minimal mass of the stellar particle. However, unlike the lowest resolution in Ki8_ELR, this does not seem to arise from too high a particle stellar mass as there is little sign of burstiness in the SFR and most of the particles are at the minimal mass (except for Kr8_ELR).

4.5 Tests summary and calibration

We have studied many parameters, model-dependent parameters as well as model-independent parameters and tested the convergence of the different models against a variation in the stellar particle mass resolution and the spatial resolution. We summarise these tests in the next section and use this knowledge to calibrate the different models in stellar mass.

4.5.1 Summary and highlights

We summarise in table 4.6 our conclusions on the role of the various parameters tested and, as we have seen similar effects when changing different parameters (an altered initial star formation burst, disparate outflow strength and a distinct morphology), we outline once again their effect in this section.

We have seen multiple times that there is an initial burst of star formation in the simulations, and it was significantly impacted in AG when changing the star formation density threshold, removing radiative transfer and changing either the stellar mass or the spatial resolutions. There was no such impact on the star formation efficiency, but it was likely due to the resolution in stellar mass not being high enough in our simulations. It was also seen to a lower extent in KI when changing the mass and spatial resolution. In KR, these differences did not impact the initial SFR but uniquely led to an SFR which remained stable but at a different average value. In all these cases of changed initial SFR burst, the reason is similar, as changing these parameters changed how efficient the galaxy was in forming stars. This led to a galaxy being over-efficient in forming stars in its early stages, which consumed its fuel quickly and eventually became depleted in gas. This can especially be noticed when removing RT or going to high stellar particle masses, as the feedback is also more powerful and can lead to galaxies alternating rapidly between star-forming and non-star-forming states. Conversely, when it is harder for stars to form (e.g. a high-density threshold), there is no initial burst and the star formation takes longer to take off. This results in a delayed star formation, which leads in several of our simulations to the same stellar mass formed after 515 Myr. With a more complete and complex medium including inflows and mergers, the results might differ significantly due to this major delay as other physics will interfere and change the timescales involved. In a cosmological simulation, a parameter inducing stronger feedback such as a higher mass for stellar particles would prevent gas from falling on the galaxy more efficiently than counterpart simulations with lower particle masses, and this could lead to significantly different final stellar masses.

In the simulation with a higher stellar particle mass, not only does the SFR take longer to rise, but it is also lower because there is more efficient feedback, which is the second consequence of these parameter changes. The strength of the feedback can be seen in both the SFR of the galaxy (as it leads to very bursty star formation alternating between star-forming and non-star-forming states) and in its CGM (through the presence of more gas). As mentioned above, with a low-density threshold, the cell has to reach a higher density before forming a stellar particle. This results in star particles being located in similar places and combining their effect into stronger feedback. This effect is even more notable without RT in AG, where the initial peak is 1 dex higher and leads to an overall density too low to form stars in the galaxy. When lowering the stellar particle mass, the outflows also get stronger and lead to a diffuse galaxy with a low star formation. These lead to more gas ejection, as we have seen with the edge-on and face-on column density maps. This can be seen in all simulations when changing the stellar mass or spatial resolution. This highlights how sensitive the CGM is against different subgrid models. Increasing the spatial resolution or the stellar particle mass both result in stronger outflows.

These outflows lead to a third major difference in our simulations, which is the

Table 4.6 – Summary of the impact of the parameters tested on idealised simulations. We use ↗ and ↘ to denote whether the parameter considered increases or decreases when it is relevant.

		AG	KI	KR
Density threshold (AG) / SF Jeans criterion (KI)	↗	Absence of initial burst of SFR followed by a strong cycle of star formation and feedback but still converged. More well-defined spiral arms with outflows along the minor axis.	Lower initial SFR burst but nonetheless reached convergence.	
	↘	Slightly higher initial SFR burst and smoother morphology.	Very similar in stellar mass. The outflows eject gas further out of the galaxy.	
Star formation efficiency	↗	No significant impact, the conclusions might be different with different stellar particle masses.		
	↘	No significant impact, the conclusions might be different with different stellar particle masses.		
Feedback strength				Momentum injection is the same as thermal feedback if there is no boost. Otherwise, lower star formation rate. Strong and weak feedback do not show any significant difference.
Jeans refinement		More high-resolution cells but no significant impact.	More high-resolution cells but no significant impact.	More high-resolution cells but no significant impact.
sf_lmax		No significant impact.	No significant impact.	No significant impact.
Removing RT		Consequent initial star formation burst followed by gas depletion and significantly more stars in G8. The cavities are significantly bigger without RT. Similar in G9 but of a lower extent.	Slightly higher initial star formation burst but the stellar mass formed is still close in both cases. The cavities are slightly bigger without RT.	Less efficient feedback which leads to a twice higher SFR and stellar mass formed. No significant difference in morphology.
Stellar particle mass	↗	Significantly stronger initial burst of star formation followed by very strong feedback emptying the gas reservoir by ripping apart the galaxy.	Very close SFR and stellar mass but galaxy ripped apart by stronger feedback.	Bursty SFR and stronger feedback which however produces higher stellar mass.
	↘	Lower initial SFR burst, resulting in a higher constant SFR. Structure with numerous filaments.	No significant impact on star formation but less effective feedback allowing the gas to fall unhindered on the galaxy.	Lower SFR and lower stellar mass formed.
Spatial resolution	↗	Good convergence and closer in SFH with an adapted star formation density threshold. More substructures with gas everywhere in the galaxy and stronger outflows.	Exquisite convergence and similar but more resolved morphology.	Significantly higher SFR and stellar mass formed with more substructures in the galaxy and stronger outflows.
	↘	Lower stellar mass but slightly better convergence with an adapted star formation density threshold. Blurry spiral arms and less gas in CGM. No gas permeates the CGM.	Exquisite convergence except for G8 at 146 pc where SFR becomes very bursty. Similar morphology but blurred.	Significantly lower SFR and stellar mass formed. Spiral arms with no gas permeating the CGM.

gas morphology of the galaxies formed. When the outflows are not strong enough or when there is sufficient time before forming stars, the gas is allowed to collapse freely, forming a filamentary structure which is wrapped around the central gravitational potential, a spiral galaxy. Galaxies formed notable spiral arms when decreasing the star formation density threshold, considering a lower stellar particle mass, and lowering the resolution in AG. Conversely, removing RT or decreasing the stellar particle minimal mass led to seemingly stronger outflows, which shattered the galaxy for both AG and KI. However, unlike AG, KI remained able to form a similar stellar mass. Gas morphology could thus also be a powerful probe to discriminate different subgrid models.

To summarise, the initial burst of star formation, the outflow strength and the morphology are all linked together but can change independently of one another. It is well illustrated by the fact that in KI, the SFR and stellar mass of the galaxy is similar in all simulations, but its morphology can change considerably. Contrarily, KR can exhibit widely different stellar masses formed while retaining a similar morphology. Also, the feedback can occur on local scales, impacting the galaxy morphology and/or leading to short non-star-forming states, but also on a global scale, ejecting gas in the CGM and depleting the gas budget accessible to form new stars. Comparing simulations against the stellar mass as well as against outflows tracers thus grants two complementary constraints and should effectively allow simulations to reach a better agreement both against one another and against observations.

4.5.2 Calibration

One of our goals is to create a list of parameters for each subgrid model which would be as close as possible to their original versions while producing galaxies of similar stellar masses. To do so, our reference run for this calibration was KI as it proved to be the most stable against the variation of most parameters, especially in mass and spatial resolution.

As the resolution and the star formation density threshold in AG are degenerate, we first set m_star, and then calibrate the stellar mass relying on the stellar particle mass. In KR, as we find that the SFR is scaling with the stellar particle mass, we directly calibrate the model with the star particle mass. We then finally test and confirm that this calibration holds when considering the more massive galaxy G9. We show the SFR and total stellar mass formed in the calibrated simulations in Fig. 4.14, both for G8 and G9.

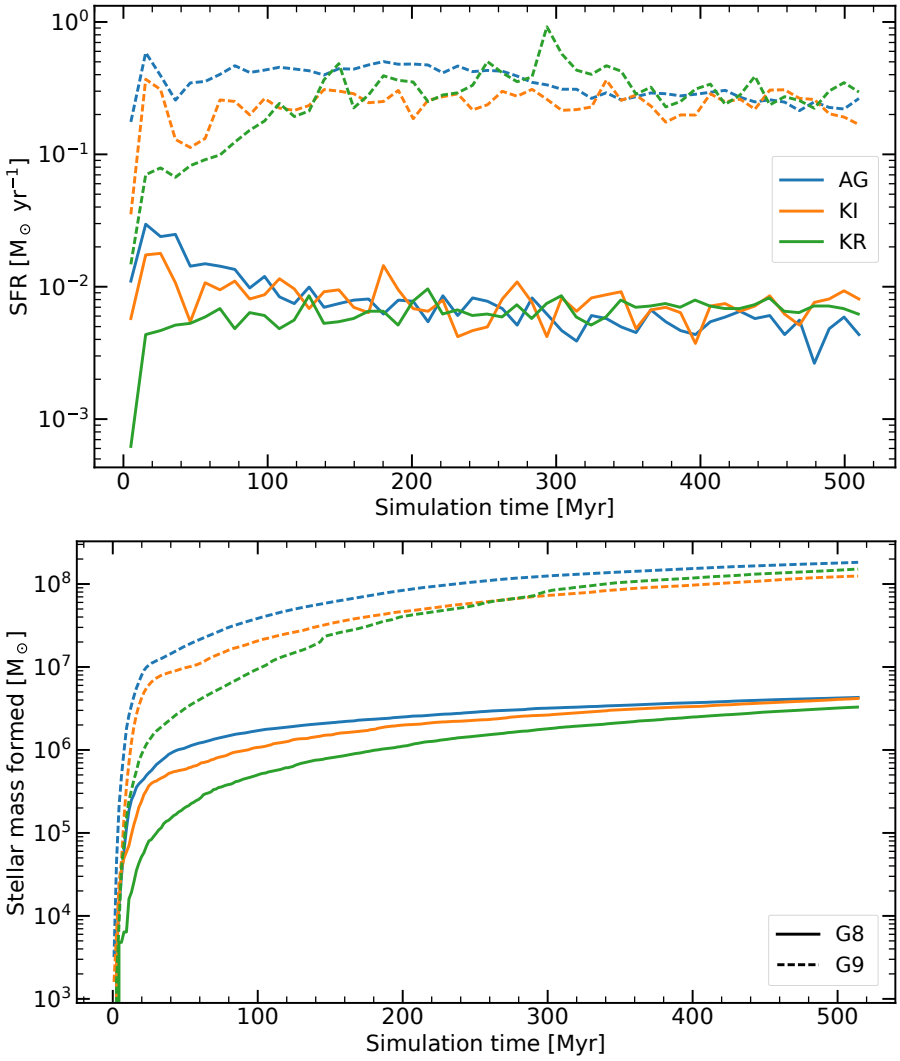

Figure 4.28 – SFR (upper panel) and stellar mass formed (lower panel) as a function of time, for the calibrated models AG, KI, and KR. We show in solid line the resulting calibration of G8, and in dotted line the same calibration for G9.

Chapter 5

Zoom simulations

In chapter 4, we have shown the importance of subgrid models for star formation and stellar feedback in the context of galaxy formation simulations. These simulations can be very sensitive to the free parameters of the subgrid models, and we thus need to constrain them. Models are often calibrated on the stellar mass to halo mass relation Behroozi et al. (2010, 2013, 2019); Moster et al. (2013, 2021). However, diverse models — relying for instance on different physics — have been developed and can satisfy this constraint. We did it in Sec. 4.5.2 by calibrating in stellar mass an idealised galaxy simulated with three different models. In this chapter, we simulate the formation of galaxies in a cosmological context instead of using idealised simulations. In section 5.1, we thus present and test our calibration on the first set of initial conditions, which corresponds to a halo of $\sim 5 \times 10^{10}$ $M_\odot$. This first galaxy is relatively isolated, and we present in section 5.2 a less isolated galaxy with a second set of ICs with a halo of $\sim 5 \times 10^{11}$ $M_\odot$.

Having calibrated the simulated galaxies in mass, a complementary constraint is necessary to be able to discriminate subgrid models. As we expect the CGM to be very sensitive to the outflows induced by different subgrid models, we investigate its properties in the simulated galaxies through quasar absorption lines. We present these results in 5.3. In sections 5.4 and 5.5, we further our studies by testing the spatial convergence of the subgrid models in the cosmological context and the inclusion of runaway stars. We conclude on these results in sections 5.6

5.1 Isolated galaxy

In this section, we run cosmological zoom simulations of a relatively isolated galaxy with a high resolution of 20 pc. The initial aim of these simulations was to test cosmological zoom simulations and check whether the calibration made with isolated galaxies was still valid in this context. The ICs we use in this section were selected from a first sample in which haloes were restricted to masses of $3 \times 10^{10} - 10^{12}$ $M_\odot$ and the conditions of having less than 10% of their mass in substructure and no neighbour more massive than 30% of their mass within 7 R_{vir}. We then select a random subsample of this set within which we chose ICs leading to a rather isolated (and faster to run) halo with a mass of $\sim 5 \times 10^{10}$ $M_\odot$ at redshift $z = 0.5$ in a DM-only simulation.

Table 5.1 – List of cosmological simulations of an isolated galaxy. We show here the simulation name, the model followed, whether star formation is limited at the maximum level, whether the simulation includes Jeans refinement, the simulation time reached at the end of the simulation, and the corresponding computation time. RNW means that the simulation was made with runaway stars. For the fiducial KR_weak simulation, the log file for the first few days of the simulation was erased. the corresponding running time was thus estimated to be 96h from the time at which the files were written and the maximal running time which was possible on the machine used.

Simulation	Model	SF_{lmax}	$\lambda_{J,ref}$	SN boost	$t_{sim.}$ [Gyr]	Redshift z	$t_{comp.}$ [khCPU]
AG	AG	T	T	F	1.59	3.96	119
KI	KI	T	T	T	1.93	3.33	65.3
KI_rnw	KI + RNW	T	T	T	1.98	3.26	49.0
KR_weak[1]	KR	T	T	F	1.73	3.66	42.8
KR_str	KR	T	T	F	1.74	3.65	42.8
KR_boost	KR	F	F	T	2.73	2.43	20.3
AG_{NJeans,sf_lmax}	AG	F	F	F	2.12	3.07	123
KR_{NJeans,sf_lmax}	KR	F	F	F	2.12	3.06	29.9

The time at which we ran simulations using these ICs corresponds to the point at which we added the boost to KR and the Jeans refinement and level max star formation for both AG and KR. Thus, we also show here the comparison of feedback strength and the effect of adding the Jeans refinement and limiting star formation at the maximum level in a cosmological zoom-in simulation. This is also the point at which we introduced the modelling of runaway stars, so we include it in our comparison of the *fiducial* models. We present these simulations in table 5.1.

[1]The log file for the first few days of this simulation was erased. The corresponding running time is thus estimated to be 96h by looking at the time at which the files were written. Since it corresponds to the maximal running time of a single job of the queue chosen on the computing machine, this is a reasonable assumption.

5.1.1 Jeans refinement and star formation at the maximum level

We first present the effect of removing Jeans refinement and allowing stars to form at any level with the AG and KR models. As it was included by default in KI, we did not test the difference induced on this model, and we tested its effect on KR without the boost for KR (it was not included at the time). We remind the reader that for idealised galaxies, both parameters had no significant impact on simulations except for the cell tree structure in the case of Jeans refinement.

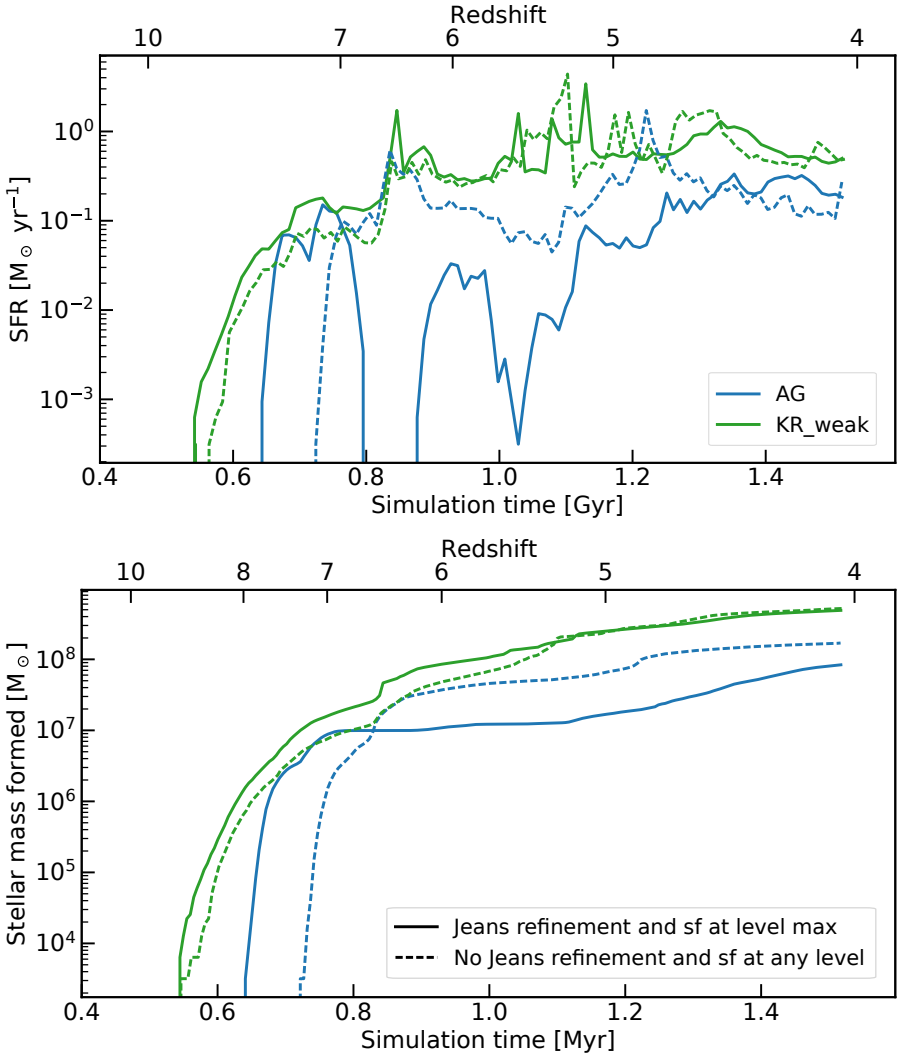

Figure 5.1 – SFR (upper panel) and total stellar mass formed (lower panel) in AG and KR with and without the Jeans refinement criterion and the restriction of star formation to the maximum spatial resolution level.

In Fig. 5.1, we show the star formation rate and total stellar mass formed in AG and KR with and without these two criteria. In the case of KR, these parameters have no significant impact on the stellar mass. Concerning the SFR, even though the stellar mass formed is initially slightly lower in $\mathrm{KR}_{\mathrm{NJeans,sf\_lmax}}$, it becomes very similar from redshift $z \sim 5$. In the case of AG, including the Jeans refinement and the restriction of star formation to the cells at the highest resolution leads

to an earlier star formation rate which is significantly more bursty and lower on average. This difference leads to a stellar mass slightly more than twice higher in AG_{NJeans,sf_lmax} than in AG.

At redshift $z = 4.04$ in AG, while there are 0.2% cells at the maximum level (resp. 0.8% at the penultimate level) without Jeans refinement, there are 5.7% (resp. 8.0%) when using it. Without the Jeans refinement, cells are at a lower resolution level and need more time to reach the star formation threshold. Indeed, since their volume is at least eight times larger (for a difference of only one level), more mass needs to be accreted in the lower-resolution cells. However, once this threshold is reached and stars are allowed to form (since they can form at any level), there is a sudden increase in the star formation rate as the cells have accumulated more mass. This is what we can see with the two bursts slightly before redshift $z \sim 6$ and slightly after redshift $z = 5$.

By looking at density-temperature phase diagrams of these simulations shown in Fig. 5.2, we see for both models that including the Jeans refinement criterion and restricting star formation to the maximum level leads to a larger spread in gas properties in density and in temperature. Due to more numerous refined cells which are typically in the ISM, the gas can reach denser values with jeans refinement, which leads to a wider spread in the cold phase of the phase diagram. For the hot gas and low-density phase of the diagram, the mechanism is different and traces feedback. The same region is populated both with and without Jeans refinement and the limitation on star formation. This phase being more densely populated with the Jeans criterion shows how it induces more feedback. We however remind the reader that this is the case for both simulations and, as the total mass is the same with and without Jeans refinement in KR, it likely solely changes the state of the gas without having a significant impact on star formation.

In cosmological simulations, we thus find that including Jeans refinement and forcing stars to form at the maximum level will not lead to much difference in the stellar content of KR, but has a notable impact on AG, unlike in idealised simulations. Indeed, including Jeans refinement leads to a smoother star formation history. The thermal content of both galaxies is also affected by these changes, as they lead to a larger spread in both density and temperatures

5.1.2 Feedback strength in KR

We now look at the effect of the two different feedback schemes presented in Kretschmer & Teyssier (2020) and Kretschmer et al. (2020) and of an increased supernova rate. We remind the reader that the *weak* and the *strong* feedback approaches produced negligible differences and that they were equivalent to the thermal feedback unless a boost was included, lowering their SFR in isolated galaxies.

We initially compared the effect of the boost to KR_{NJeans,sf_lmax}, and the effect of weak and strong feedback after implementing the Jeans length refinement criterion and the limitation of star formation at the maximum level. To include KR_boost in the comparison of KR_weak to KR_str we should thus run another simulation based on KR_boost including Jeans refinement and star formation restriction at the maximum level. As we find that these parameters have a negligible effect on the simulation for KR, we consider that the result would be similar and only compare

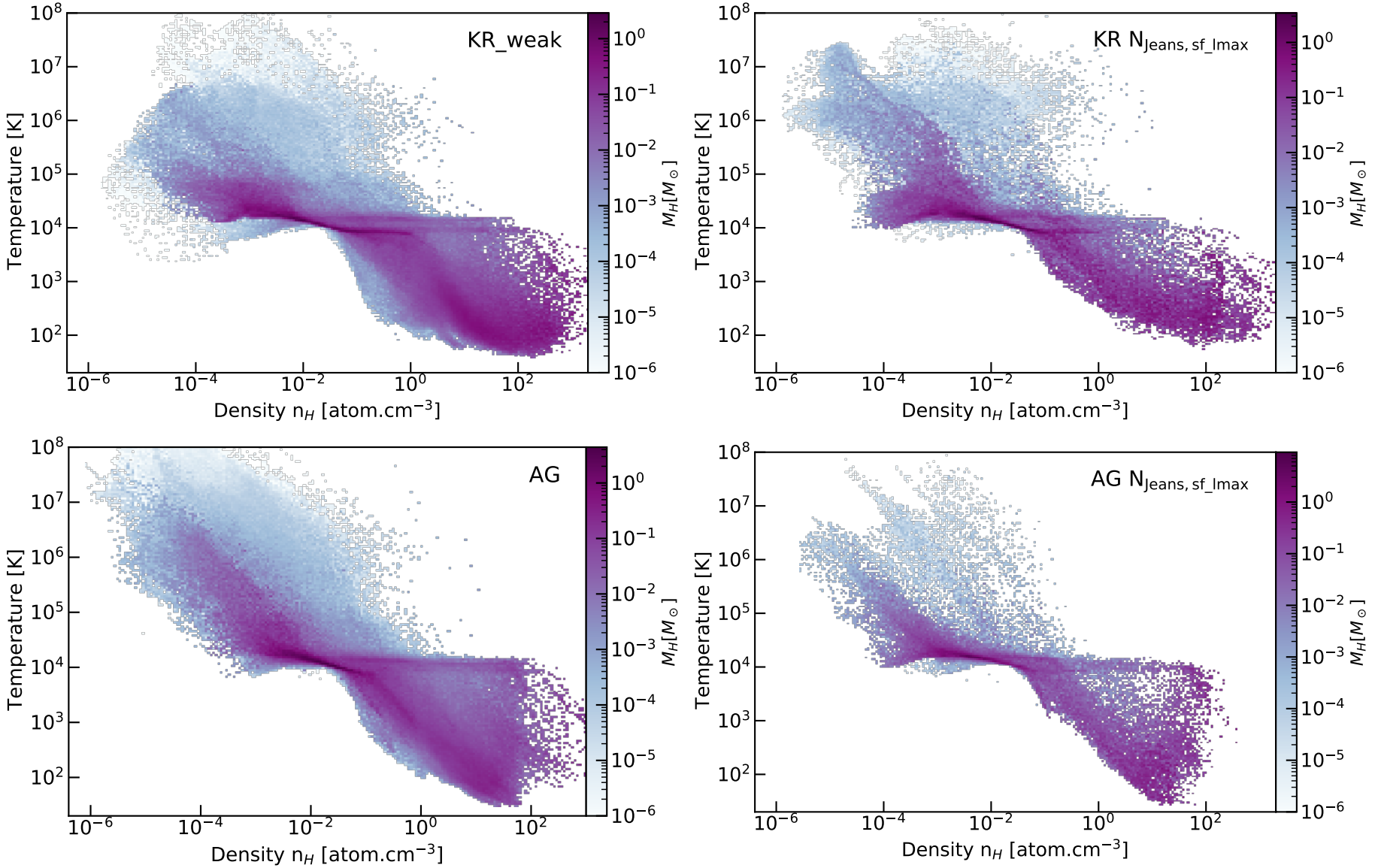

Figure 5.2 – Density-temperature phase diagram of KR for the cosmological zoom-in isolated galaxy with (left panel) and without (right panel) Jeans_refine and sf_lmax.

it to KR_boost.

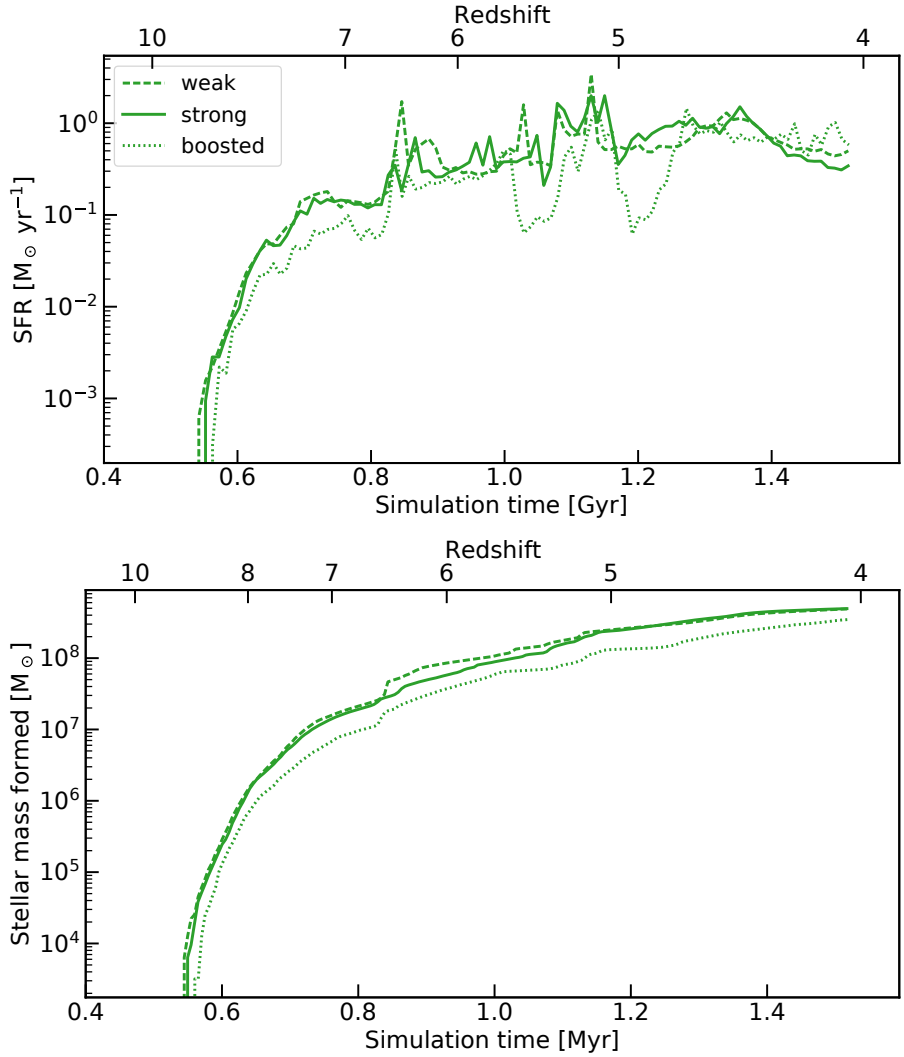

Figure 5.3 – SFR (upper panel) and total stellar mass formed (lower panel) in KR, with different feedback modelling.

We show the SFR and stellar mass formed in KR with these three approaches in Fig. 5.3. Once again, we do not see much difference between the weak and the strong feedback models. The only difference is that while the weak feedback produces a few rare and short high bursts of star formation, the strong feedback approach produces more of them, but to a lower extent and more spread in time. This nonetheless does not affect much the total stellar mass formed. Contrastingly, when boosting the supernovae rate in the weak feedback model, the SFR decreases slightly, being almost systematically below the other two simulations except for a few bursts. More strikingly, there are three episodes of significantly lower star formation reaching 0.1 $M_\odot\,yr^{-1}$, while the other simulations are relatively stable around 1 $M_\odot\,yr^{-1}$.

We show in the upper panels of Fig. 5.4 the density-weighted projections of the hydrogen density of the galaxy at redshift $z = 5.58$. This redshift is the beginning of the first depression in KR_boost relative to the two other simulations. While we

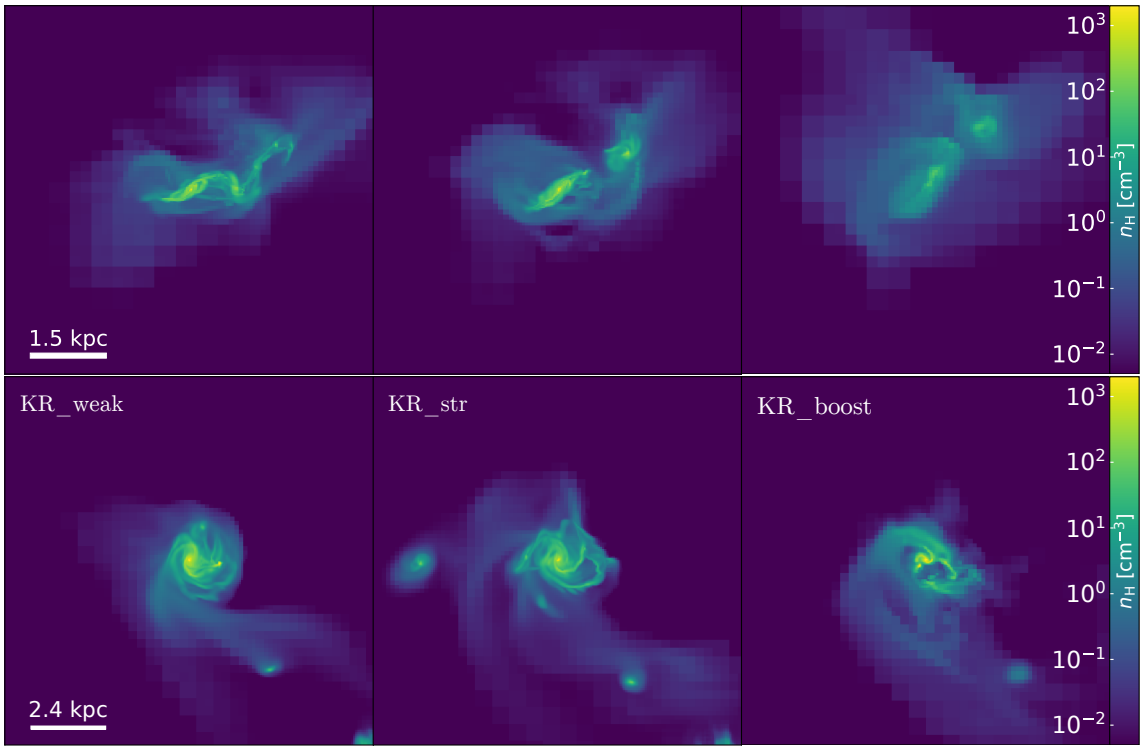

Figure 5.4 – Density-weighted projections of the hydrogen density of KR with different feedback recipes in the isolated cosmological simulations. From left to right we show KR_weak, KR_str and KR_boost. The upper panels correspond to $z = 5.58$ and the lower panel to $z = 4.04$

can only find minor differences between the weak and the strong feedback, the boost drastically diminishes the density of the galaxy (and hence the more numerous lower resolution pixels). This is possibly due to the merger we see, triggering clustered star formation followed by significantly stronger feedback in KR_boost. This feedback is strong enough to actually disrupt the galaxy and lower the SFR for a short time. After some time, the gas falls back and the galaxy reaches an SFR close to the other two simulations. We show in the lower panel of Fig. 5.4 the same maps at redshift $z = 4.04$, and find that at later times, even if the SFR is slightly higher with the boost, traces of the galaxy disruption remain as the spiral shape of the galaxy is relatively well-defined without the boost while it is irregular with the boost and still show signs of strong feedback with deeper cavities carving the galaxy morphology.

Lastly, we show the density-temperature phase diagram of the galaxy at redshift $z = 5.58$ in Fig. 5.5. We only show the weak supernova model with and without the boost, as the strong feedback model is very similar to the weak feedback. Interestingly, we see that when the boost is included, the gas populating the galaxy is mainly concentrated around 10^4 K there is no hot gas and no star-forming gas. Contrastingly, when there is no boost, we can find the gas ejected from supernova higher than 10^5 K and star-forming gas lower than $\sim 10^3$ K at densities higher than 1 cm^{-3}. This effectively shows how the gas can be ejected further than $R_{200} \sim 11.8$ kpc thanks to the boosted feedback (the region in which we plot the phase diagram) at this redshift, and how it can destroy star-forming regions and leave imprints on the galaxy formed. The mass of the halo is very similar in both simulations, while the

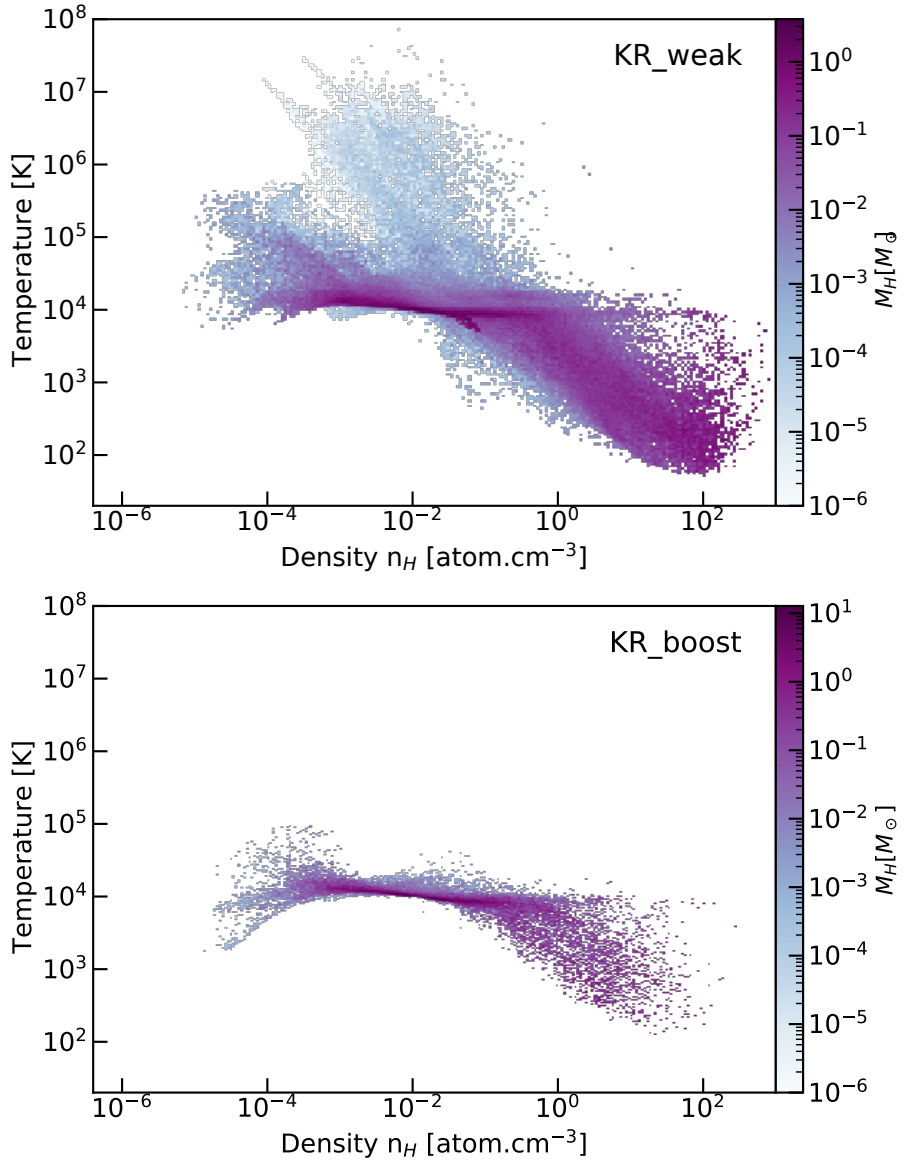

Figure 5.5 – Density-temperature phase diagram of KR for the cosmological zoom-in isolated galaxy with (right panel) and without (left panel) the supernova boost using the weak feedback scheme of KR at $z = 5.58$.

gas mass is halved within R_{200} when adding the boost, and the stellar mass is five times lower. By $z = 5.58$ the phase diagram of the boosted simulation resembles that of the other simulations as the gas composing the galaxy falls back on the galaxy.

To summarise, we once again find that the weak and strong feedback schemes of the KR model produce very similar results and that boosting the supernova rate by a factor four decreases the stellar mass, albeit only by a small coefficient. We nonetheless find that it alters notably the SFH, leading to the disruption of the galaxy at several distinct times, leading to a different morphology.

5.1.3 Fiducial simulations

In this section, we now compare the three models AG, KI and KR_boost alongside KI with runaway stars. We compare these simulations to KR_boost, as it is closest to the *fiducial* parameters defined in the previous chapter. It does not include the Jeans refinement criterion nor the limitation of star formation at the maximum level, but we saw these have a negligible impact on the KR model. The results presented here should thus be comparable.

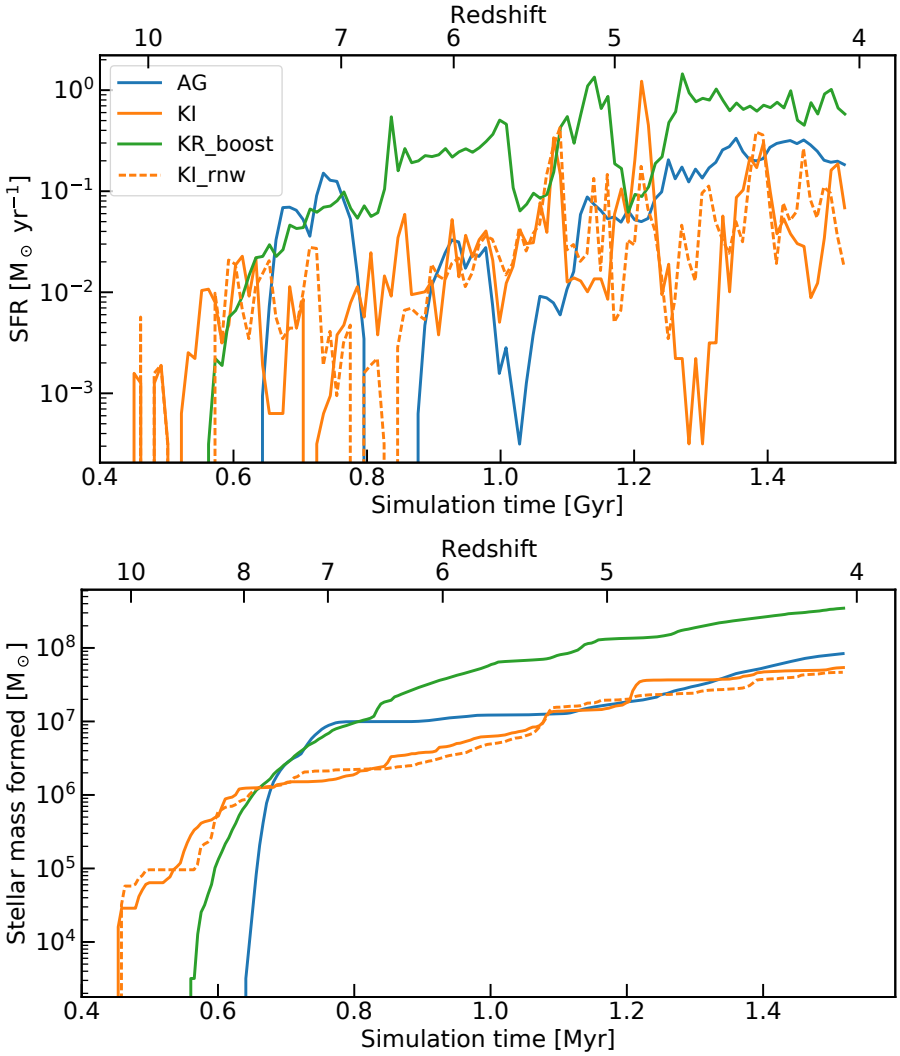

Figure 5.6 – SFR (upper panel) and total stellar mass formed (lower panel) in AG, KI, KR and KI_rnw.

We show in Fig. 5.6 the star formation rate and total stellar mass formed in these four simulations. The first difference is that KR exhibits a significantly higher SFR, five to fifty times higher than the other simulations from redshift $z \sim 7$ even though there are drops in star formation, which likely corresponds to an after-merger epoch (see the previous section). KI with and without runaway stars both produce very similar results and exhibit a very bursty star formation rate. AG presents two strong bursts at redshift $z \sim 6-7$ which destroy the galaxy (see Sec. 5.1.1) and has a then slowly increasing SFR, eventually producing a similar total stellar mass as KI. The

calibration made in the idealised simulation thus did not hold in the cosmological context. We believe it might be due to the peculiar nature of this isolated dwarf galaxy, and study a more massive galaxy in the next section. Indeed, in the idealised simulations, the reservoir of gas available for star formation is essentially set by the ICs and hardly affected by star formation and feedback. Obtaining convergence in the mass of stars formed in such conditions is thus not sensitive to the large-scale impact of feedback, but only to its small-scale regulation of the star formation efficiency. In cosmological simulations, the amount of gas available for star formation is the result of accretion and may be strongly impacted by feedback at large scales (Tollet et al., 2019; Mitchell et al., 2018; Mitchell & Schaye, 2022). The results of Fig. 5.6 suggest that the KR model is less efficient at preventing gas accretion, while the other three may reduce significantly the gas budget.

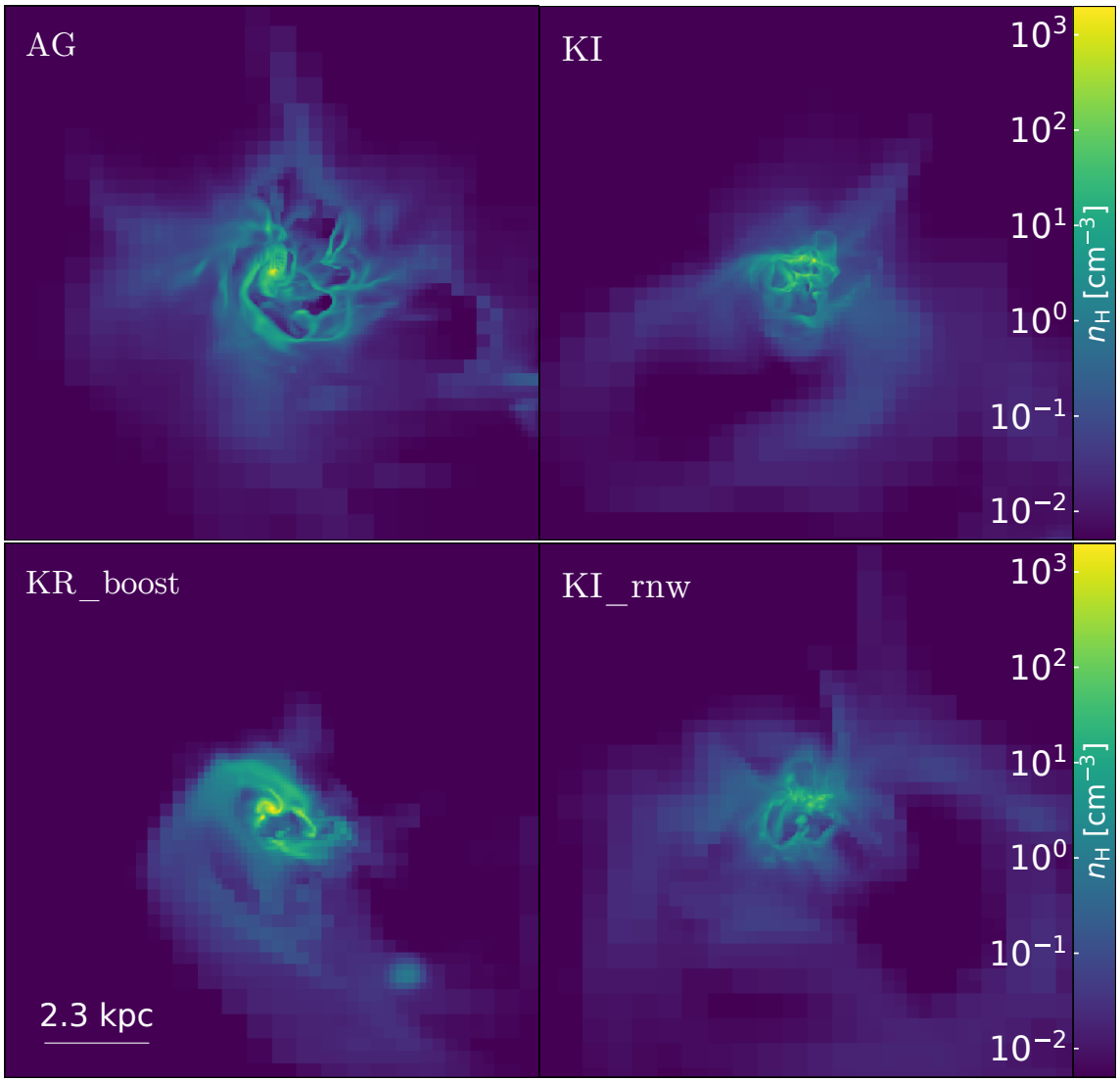

Figure 5.7 – Density-weighted projections of the hydrogen density of AG, KI, KR, and KI_rnw with the isolated cosmological simulation at redshift $z \sim 4$. From left to right and from top to bottom, we show AG, KI, KR, and KI_rnw.

In Fig. 5.7, we show hydrogen maps of the four models AG, KI, KR, and KI_rnw. We see that all galaxy morphologies are relatively disturbed, showing that they all

exhibit strong feedback. In KR and both simulations relying on KI, this is due to the boost, while in AG this is due to the implementation of more feedback sources through winds and SNIa. We also note that there is not much difference in the morphology of the galaxy when adding runaway stars, even though galaxies of such masses are more sensitive to supernovae feedback than more massive ones. The sole difference between KI and KI_rnw comes from the fact that the snapshots are not *exactly* at the same point in time, and the image is consequently slightly more rotated in one than in the other. Finally, except for KR, all galaxies are relatively disrupted by the feedback.

5.2 A more massive galaxy

We found through these tests that this galaxy was too isolated and peculiar[2], and thus studied another one, with ICs taken from a second subsample. In that set of ICs, the haloes were selected to be within $3 \times 10^{11} - 3 \times 10^{12}$ $M_\odot$, less than 10% of their mass in substructure and no neighbour more massive than 20% of their mass within 3 R_{vir}. Amongst those, we picked ICs leading to a halo of $\sim 5.3 \times 10^{11}$ $M_\odot$ at $z = 0.5$ in a DM-only simulation.

Table 5.2 – List of cosmological simulations of a galaxy run with different variations of AG. We show here the simulation name, the adjustment made compared to the fiducial one, the simulation time reached at the end of the simulation and the corresponding computation time. In these runs, we also adapted the load balancing at each restart by calibrating the subcycling depending on the computation time of the coarse timesteps.

Simulation	Main adjustment	$t_{sim.}$ [Myr]	$t_{comp.}$ [khCPU]
AG	Default simulation	1280	360
AG_6e8	Changed T_{max} to 6×10^6 K	799	41.1
AG_8e8	Changed T_{max} to 8×10^6 K	811	49.1
AG_6e8_384	Changed T_{max} to 6×10^6 K + ran on 384 cores	831	66.0
AG_nbug	Code improvement to avoid useless computations.	783	49.1
AG_512	Simulation ran on 512 cores	839	98.1
AG_384	Simulation ran on 384 cores	1690	920

With these new ICs, we found that AG became significantly slower than the other models, and thus tested different approaches to find what was the origin of this difference. We list these simulations in table 5.2. As we expected this model to produce hotter outflows than KI and KR, the first test we did was to reduce slightly the maximal temperature of the simulation. Indeed, decreasing the maximal temperature of the gas leads to a lower sound speed and thus longer CFL timesteps.

[2]From another set of simulations, we find that the galaxy stops forming stars after $z = 2$ as there is no more cosmic accretion.

Longer timesteps give rise to a lower number of timesteps for a given simulation time and thus fewer computations. However, this did not produce much change in the computation time. At the same time, we improved the subcycling between the different resolution levels of the simulations and the frequency of the load balancing to optimise the computation time. This was calibrated on the computation time of a coarse timestep as we found that the simulation was faster when coarse timesteps were approximately 200 s. We also tried to decrease the computation time by using more cores, but AG runs were still much slower than KI and KR. Finally, we reviewed the code and improved several parts which were adapted during its merging into the *ramses_cral* version. An example is that during star formation, the loop to form stars was made on each cell of the simulation when some should have been avoided as they didn't pass the first star formation criteria. This corresponds to the simulation AG_nbug. Lastly, we tried to use the code from Oscar Agertz alongside the fixes made using the same parameters as in the previous namelist and finally confirmed that the slower simulation time was effectively simply due to a longer computation time for similar timesteps in the simulation, and due to the subgrid model itself.

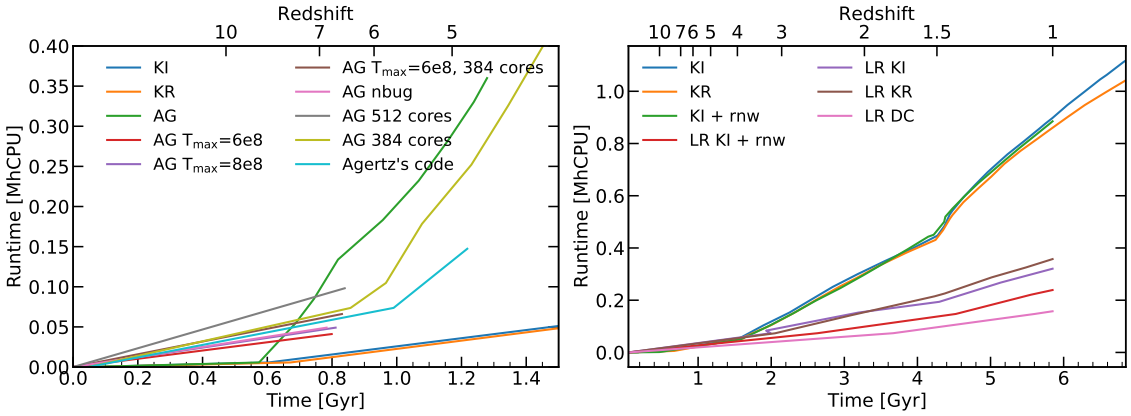

Figure 5.8 – Simulation runtime against the time within the simulation for the cosmological simulation of the less isolated galaxy. The left side corresponds to simulations run with AG, alongside different adjustments made in an attempt to make it faster. The right plot corresponds to the fiducial galaxies KI and KR at two resolution levels, KI with runaway stars and DC at the lower resolution.

We show on the left panel of Fig 5.8 the computation time of the corresponding simulations from AG, alongside KI and KR for reference. While a simulation time of ~ 2 Gyr took $30 - 60$ khCPU, it typically took ~ 120 khCPU for AG to reach a simulation time of ~ 1.5 Gyr. As the computational cost of idealised simulations or even the isolated galaxy is typically smaller, this effect was not as significant in the simulations presented earlier but became problematic for the larger halo. We thus abandoned the AG model and tested DC instead. Also, as it would have otherwise not been finished by the end of this work, we ran DC one resolution level lower than the previous simulations and re-ran KI and KR at this same resolution.

We refer to the higher resolution simulations with the suffix *-HR*. We show in the right panel of Fig 5.8 the simulation time of all the final simulations considered. A high-resolution simulation typically took 6 months to run, while at one resolution level lower, it took 1.2 months. We show that the simulation time between KI and

KR is comparable, and that including runaway stars makes the simulation slightly faster. We also find a smaller computation time when using DC, which is likely due to more efficient and disruptive feedback (see Sec. 5.3) which leads to lower densities than with the other models. We present in table 5.3 the simulations used in the next sections.

Table 5.3 – List of cosmological simulations of a galaxy run with the main simulations of this work. We show here the simulation name, the model followed, the maximal resolution and the total computation time. All simulations were run down to redshift $z = 1$ (5.85 Gyr) except for KI and KR, which were run slightly further (6.85 Gyr). In these runs, we also adapted the load balancing at each restart by calibrating the subcycling depending on the computation time of the coarse timesteps.

Simulation	Model/physics	Resolution [pc]	$t_{comp.}$ [khCPU]
KI_HR	KI	20.1	1120
KR_HR	KR	20.1	1040
KI_HR + RNW	KI + runaway stars	20.1	885
KI + RNW	KI + runaway stars	40.3	239
KI	KI	40.3	321
KR	KR	40.3	357
DC	DC	40.3	158

5.3 Impact of subgrid models on the CGM (paper)

Using the ICs presented in Sec. 5.2, we now test the impact of the subgrid models KI, KR, and DC presented in chapter 3 on cosmological zoom-in simulations of galaxy formation. We first investigate the properties of the simulated galaxies and confirm their calibration in stellar mass. Then, we detail the gas phases traced by the four ions we chose (H I, Mg II, C IV, and O VI) and how we simulated the observation of column densities. Finally, we analyse the properties of the CGM by comparing the simulated column densities to observations made with quasar absorption lines.

MNRAS 000, 1–17 (2022) Preprint 23 November 2022 Compiled using MNRAS LATEX style file v3.0

The impact of subgrid physics on the properties of the circum-galactic medium.

Maxime Rey,[1]★ Jérémy Blaizot[1]
[1]ENS de Lyon, Univ. Lyon, Univ. Lyon1, CNRS, Centre de Recherche Astrophysique de Lyon UMR5574, 9 av. Charles André, 69230 Saint-Genis-Laval, France

Accepted XXX. Received YYY; in original form ZZZ

ABSTRACT

Galaxy evolution is driven by star formation and stellar feedback, which occur at scales that cannot be resolved by current high-resolution cosmological simulations. Precise subgrid models are thus necessary, and different approaches have been developed. They are however degenerate and often mostly calibrated to produce resonable stellar masses. In order to explore these degeneracies, we introduce three state-of-the-art zoom-in simulations of the same galaxy, which implement different subgrid models, and compare their respective circum-galactic media through quasar absorption sightlines. These simulations use RAMSES-RT and are post-processed with KROME and RASCAS to generate simulated column densities of H I, Mg II, C IV and O VI. The simulated column densities are well-described by an exponential profile combined with a plateau and exhibit a sharp drop near the disc edge which is lower for higher ions. We find a significant discrepancy between observed and simulated column densities for most ions. This disagreement stems from a combination of feedback not pushing enough enriched gas out of the galaxy and an incorrect ionisation state of the CGM, likely due to an inaccurate thermal state. QSO lines are however highly efficient in lifting the degeneracy between different subgrid models. Finally, we find that delayed cooling with a single supernova explosion is more efficient than mechanical feedback with time-sampled explosions enriching the CGM in metals.

Key words: keyword1 – keyword2 – keyword3

1 INTRODUCTION

To be able to grasp the underlying physics regulating galaxy formation and produce accurate theoretical predictions, one needs to consider highly non-linear equations covering a broad range of scales and numerous physical processes. To this aim, we need hydrodynamical cosmological simulations. Many of them can match observational probes (Schaye et al. 2015; Nelson et al. 2019), but at the cost of tuning their simulations and not through a resolved modelling of the feedback processes involved. Simulations with increasingly high resolutions and relying less on calibration often struggle in describing properties such as the baryon fraction in galaxies (Silk & Mamon 2012). As the stellar mass of simulated galaxies depends highly on feedback and is often higher than expectations from observations (Kimm et al. 2015; Rosdahl et al. 2017), modelling these processes correctly is one of the key challenges of current galaxy formation simulations.

While gas accretion fuels the galaxy to form stars, different phenomena can hinder it and are expected to drive this discrepancy, such as turbulence (Padoan et al. 2012) or outflows (Hopkins et al. 2011). For low mass galaxies, it is expected that outflows are mainly driven by stellar feedback (Dekel & Silk 1986; Oppenheimer & Davé 2006; Agertz & Kravtsov 2015). Proper modelling of stellar processes such as star formation and supernovae is thus crucial for galaxy formation. However, one of the shortcomings of simulations is that the scale of these stellar processes is far below the maximal resolution that can be reached while simulating the cosmological context which is necessary as it determines the accretion history of the galaxy. Hence, we need subgrid models which describe the effects of unresolved physics at the scale of the simulation resolution.

Simulations often calibrate subgrid model parameters so as to reproduce the stellar mass to halo mass relation (Behroozi et al. 2019; Moster et al. 2021), and manage to match it even though the underlying methods can be widely different. Other properties such as the luminosity function can also be used be are still not enough to identify degeneracy between different subgrid models. It is thus important to find other ways of comparing simulations and observations, and a powerful new constraint might lie in the circum-galactic medium (CGM).

As the CGM is the place where hot outflows from the galaxy interact with cold inflows from cosmic filaments (Hafen et al. 2019), it is a complex multiphase medium. Its contents depend on how efficiently the galaxy ejects gas and how cosmological accretion fuels filaments falling onto the galaxy. The CGM could thus be very sensitive to subgrid models. To test this hypothesis, we want to compare the simulated CGM obtained with different subgrid models and test them against observations. To do so, quasar absorption lines are a very powerful tool, as they grant access to the content of the

★ E-mail: maxime.rey@univ-lyon1.fr

CGM of observed galaxies through various metal species. However, the observational points are scarce and matching such observations from the CGM is a complex challenge which simulations struggle against. Some simulations lack cold gas Liang et al. (2016), others manage to produce cold gas comparable to observations but lack hot gas Ford et al. (2016), and the ones seemingly matching both are scarce Shen et al. (2013). Even with different subgrid models (Hummels et al. 2013), additional physics Oppenheimer et al. (2016); Suresh et al. (2017) or an enhanced resolution in the CGM (Hummels et al. 2019), matching these observables remains a challenge for simulations.

In this work, we run three high-resolution radiative hydrodynamic simulations based on the same initial conditions. Each simulation uses a different set of star formation and supernova feedback models, taken from Kretschmer & Teyssier (2020) (hereafter KR), (Kimm et al. 2017) (KI), and a mix of (Kimm et al. 2017) and Teyssier et al. (2013) (DC). In all of them, we model star formation relying on the multi-freefall approach (Hennebelle & Chabrier 2011; Federrath & Klessen 2012), which models how stars form in their natal molecular cloud (Kennicutt & Evans 2012; Girichidis et al. 2020) and how its efficiency varies depending on its turbulent state (Elmegreen & Scalo 2004; Scalo & Elmegreen 2004). KI and KR use two variations of the multi-freefall model (Padoan & Nordlund 2011; Krumholz & McKee 2005). While KI estimates turbulence locally (Kimm et al. 2017), KR relies on a dedicated subgrid model (Kretschmer & Teyssier 2020). Concerning the feedback, KI relies on mechanical feedback from Kimm et al. (2015), KR on a combination of thermal and mechanical feedback Kretschmer et al. (2020) and DC relies on delayed cooling (Teyssier et al. 2013). DC also models supernovae as a single explosion, while it is sampled through time in KI and KR. We constrain these models with the stellar mass to halo mass relation and aim to find if their respective CGM can be used as a complementary constraint using quasar absorption lines. We describe the numerical code used for the simulations and the subgrid models in section 2. We investigate the properties of the simulated galaxies in section 3 and then compare the properties of their CGM through quasar absorption lines in section 4. Finally, we discuss our results in section 5 and summarise our conclusions in section 6.

2 NUMERICAL METHODS

In this section, we briefly describe the code we used to run our simulations and how we generate the initial conditions. We also list the physics included in the simulations and detail how the subgrid models work, insisting on the differences in our three approaches.

2.1 Numerical setup

We perform our simulations with the hydrodynamical code RAMSES (Teyssier 2002, 2010), relying on an Adaptive Mesh Refinement strategy and based on the Euler conservation equations in presence of self-gravity and cooling. Non-equilibrium cooling is included alongside radiative transfer (Rosdahl et al. 2013; Rosdahl & Teyssier 2015). Dark matter and stars are modelled as collisionless particles interacting gravitationally by following an N-body scheme similar to Kravtsov et al. (1997). Their minimal masses are respectively 3.47×10^5 $M_\odot$ and 3.2×10^4 $M_\odot$.

We use MUSIC (Hahn & Abel 2011, 2013) to generate cosmological initial conditions for the simulations presented here assuming the standard ΛCDM parameters $\Omega_\Lambda = 0.6825, \Omega_m = 0.3175, \Omega_b = 0.049$. From these initial conditions at $z = 150$, we run a dark-matter-only simulation down to redshift $z = 0$. We identify our central halo using the ADAPTAHOP halo finder (Aubert et al. 2004; Tweed et al. 2009). We select a halo of 5.33×10^{11} $M_\odot$ without massive substructures and no neighbour halo more than 20% of the target virial mass within $3R_{vir}$. We then select dark matter particles up to three times the virial radius, trace them back to the initial conditions and use them to generate zoom-in initial conditions which provide a high-resolution description of the halo (no low-resolution particle within $3R_{vir}$ at any time down to $z = 1$). From this point on, we run the simulation once more, but as zoom and including RHD. The RAMSES simulations consist of cells that can be refined further by being split equally into 8 children cells characterised by their level, 0 being the level of the box. Our simulations describe a 30 Mpc h^{-1} wide box resolved from level 7 to level 11 and up to level 20 ($\sim$ 40 pc) in the zoom region. The general simulation setup and physics included follow closely those used in SPHINX (Rosdahl et al. 2018).

We use the stellar spectral energy distributions from the Binary Population and Spectral Synthesis code (Stanway & Eldridge 2018) and trace the generated photons in the simulations using three groups defined by the ionisation energy of H I, He I and He I, respectively 13.6 eV, 24.59 eV and 54.42 eV (we do not account for radiation below the Hydrogen ionisation energy). We thus trace all ionisation states of Hydrogen and Helium, while we track metals through a single variable Z, describing the metal mass fraction. The interactions simulated for these groups are photoionisation, heating, and momentum transfer (Rosdahl & Teyssier 2015). As radiation flows through the grid, it is constraining the Courant condition. We thus use the reduced speed of light approximation with $c_{sim} = 0.005$ c (Gnedin & Abel 2001; Rosdahl et al. 2013) to limit the computational cost. We turn on a uniform ionisation UV field modelling emission from unresolved surrounding galaxies at $z = 8.5$, following Faucher-Giguère et al. (2009). We also take into account self-shielding with an exponential damping factor above densities of 10^{-2} cm^{-3}.

Non-equilibrium cooling is computed for Hydrogen and Helium by including photoionisation, collisional ionisation and excitation, recombination, bremsstrahlung, homogeneous Compton cooling/heating off the cosmic microwave background, and dielectronic recombination. Above 10^4 K, metal cooling is modelled following CLOUDY tables (Ferland et al. 1998, version 6.02) assuming photoionisation equilibrium with the UV background from Haardt & Madau (1996). Below 10^4 K, fine structure metal cooling rates from Rosen & Bregman (1995) are used down to 10 K.

In the zoom region, there are two criteria that can trigger a resolution increase in the AMR grid. The first criterion follows density and essentially consists in increasing the resolution when the matter in a cell is greater than a selected threshold. In practice, for the cell to be refined, the condition is $m_{DM,\,cell} + f_b m_{b,\,cell} \geq 8 m_{DM,\,part}$ where $m_{DM,\,cell}$ is the dark matter mass in the cell, $f_b = \Omega_m/\Omega_b$ the universal baryon fraction, $m_{b,\,cell}$ the baryonic mass in a cell (gas + stellar mass) and $m_{DM,\,part}$ the mass of a single dark matter particle. The second refinement criterion aims to keep the local thermal Jeans length resolved by at least 4 cells (Truelove et al. 1997), i.e. a cell if refined whenever

$$\Delta_x \leq 4\lambda_J = 4\sqrt{\frac{\pi c_s^2}{\rho G}}, \quad (1)$$

where $c_s^2 = \gamma P_{th}/\rho$ with $P_{th} = (\gamma - 1)E_{th}/\Delta_x^3$ and G the gravitational constant.

2.2 KI simulation

Unresolved phenomena have to be simulated through *subgrid models*, which describe their effect at the simulation resolution scale. Two such phenomena which are very important in galaxy formation are star formation and feedback. Our first model uses the implementation of Kimm et al. (2017) for star formation and Kimm et al. (2015) for supernova feedback, we thus refer to it as KI. The next section describes how the multi-freefall model for star formation works and how it is applied in KI. Then, we describe the radiative feedback used in all our simulations alongside the modelling of supernovae feedback in KI.

Star formation

In KI, the first set of criteria to allow star formation is that the cell must have a gas density higher than 10 cm^{-3}, be a local maximum in density compared to its six neighbouring cells, the flow must be convergent ($\nabla(\rho\vec{v}) \leq 0$), and the turbulent Jeans length given by

$$\lambda_{\rm J,turb}(\rho) = \frac{\pi\sigma_{\rm 1D}^2 \pm \sqrt{36\pi c_{\rm s}^2 G\Delta x^2\rho + \pi^2\sigma_{\rm 1D}^4}}{6G\Delta x\rho}, \quad (2)$$

must be larger than four cells. The one-dimensional gas velocity dispersion $\sigma_{\rm 1D}$ is computed locally as the norm of the gradient of the velocity field.

Star formation is a process expected to depend on the environment of the star-forming region (Murray 2011; Padoan et al. 2012) and Hennebelle & Chabrier (2011) and Federrath & Klessen (2012) described it through a *multi-freefall* approach. The two main assumptions are that star formation occurs in a supersonic turbulent medium and that the density distribution follows a log-normal function. Then, the star formation efficiency is the integral of the normalised probability distribution function of density multiplied by density-weighted by the free-fall time. By integrating it from a critical density $s_{\rm crit}$ to infinity, the star formation efficiency can be computed as

$$\epsilon_{\rm ff} = \frac{\epsilon}{2\phi_{\rm t}} \exp\left(\frac{3}{8}\sigma_{\rm s}^2\right)\left[1 + {\rm erf}\left(\frac{\sigma_{\rm s}^2 - s_{\rm crit}}{\sqrt{2\sigma_{\rm s}^2}}\right)\right]. \quad (3)$$

Here, erf is the Gauss error function and $\sigma_{\rm s}$ is the standard deviation of the density distribution. It is expressed as a function of the Mach number $\mathcal{M}$ and the turbulent forcing parameter $b = 0.4$ (which describes if the turbulence is in a solenoidal or compressive mode) as $\sigma_{\rm s}^2 = \ln\left(1 + b^2\mathcal{M}^2\right)$. The Mach number $\mathcal{M} = \sigma_{\rm 1D}/c_{\rm s}$ depends on the sound speed $c_{\rm s}$ and the one dimensional velocity dispersion $\sigma_{\rm 1D}$. The model from (Padoan & Nordlund 2011) which we use in KI uses

$$s_{\rm crit} = \ln\left[0.62\alpha_{\rm vir}\mathcal{M}^2\right], \quad (4)$$

where

$$\alpha_{\rm vir} = \frac{5}{\pi\rho G}\frac{\sigma_{\rm 1D}^2 + c_{\rm s}^2}{\Delta_x^2} \quad (5)$$

is the virial parameter describing the gravitational stability of the cloud. The *local* star formation efficiency $\epsilon = 0.5$ is a constant used to account for unresolved physics such as protostellar jets removing gas from the star-forming region and $\phi_{\rm t} = 0.57$ (best-fit of an update of the results from Federrath & Klessen (2012)) is used to take into account the estimated error on the timescale for the gas to become unstable (Krumholz & McKee 2005).

When a cell fulfils the criteria for star formation, the number of stars formed is obtained by sampling a Poisson distribution with a mean depending on the star formation efficiency of Eq. 3, the density of the cell, its length, the simulation integration step and the minimal mass of a stellar particle. The stellar particle created represents a single stellar population defined through its mass, metallicity, age, position, and velocity. We set the unit mass of the stellar particles in our simulation to ~ 3200 M$_\odot$. This also sets an additional star formation threshold, as density needs to be high enough to have sufficient mass in a cell to create one stellar particle. At a resolution of 40 pc, this is equivalent to a density threshold of ~ 1.8 cm^{-3}.

Feedback

The first form of feedback present in all our simulations is in the form of photo-ionisation, heating and radiation pressure from young stars modelled with RT (Rosdahl et al. 2013; Rosdahl & Teyssier 2015).

The second and most important form of feedback for such galaxies is supernova feedback. The minimum age of a stellar particle to undergo supernova is within 0 – 2.3 Myr and depends on its metallicity. It also needs to be younger than 50 Myr. From the Kroupa initial mass function (Kroupa 2001), the average mass of a supernova progenitor is $M_{\rm SNII} = 20$ M$_\odot$. Following Rosdahl et al. (2018), we divide by four to artificially boost the supernova rate. This is a calibration which was done to match the stellar mass to halo mass relation, the star formation rate to halo mass relation and the UV luminosity function at high redshift in the SPHINX simulation (Rosdahl et al. 2018). It can be seen as compensation for unaccounted physics such as cosmic rays, type Ia or stellar winds. We consider that supernovae eject 20% of their mass ($\eta_{\rm SN} = 0.2$, Few et al. 2012). This results in a total number of supernovae for a single stellar particle given by $\eta_{\rm SN} m_{\rm star}/M_{\rm SNII}$, with $m_{\rm star}$ the initial mass of the stellar particle. Based on this number, the lifetime of massive stars is randomly sampled following a polynomial fit to the SNII rate calibrated on the STARBURST99 code (Leitherer et al. 1999, SB99). It depends both on the stellar population age and on its metallicity and allows us to sample individual supernovae explosions through time for a single stellar particle (see Kimm et al. (2015)). This results in a number of supernovae $N_{\rm SN}$ for a given timestep.

This model then relies on the mechanical feedback formulation of Kimm et al. (2015), which splits the supernova into two phases. The first one corresponds to the Sedov-Taylor (energy conserving) phase and the second to the snowplough (momentum conserving or radiative) phase. To determine the momentum injected, the ratio of the mass swept up by the supernova to the mass of the ejecta is computed as

$$\chi_{\rm nei} \equiv \frac{{\rm d}m_{\rm W}}{{\rm d}m_{\rm ej}} = \frac{m_{\rm nei} + \frac{1}{N_{\rm c}}\left(m_{\rm host} + m_{\rm ej}\right)}{\frac{1}{N_{\rm c}}m_{\rm ej}}. \quad (6)$$

$m_{\rm host}$ and $m_{\rm nei}$ are respectively the mass of gas in the host and neighbouring cells, and $m_{\rm ej} = M_{\rm SNII}N_{\rm SN}$ is the mass ejected by the supernova. All computations are made assuming the central cell and the neighbouring cells are one level higher, so that $N_{\rm c} = 52$ is the number of cells sharing at least two vertices with the central cell plus the central cells. $\chi_{\rm nei}$ is compared to a threshold obtained by equating the momentum expected in the adiabatic phase $p_{\rm rad,Ki}$ to the momentum expected at the transition between the adiabatic and the radiative phases as

$$\chi_{\rm tr} = \frac{p_{\rm rad,Ki}^2}{2N_{\rm SN}E_{\rm SN}m_{\rm ej}f_{\rm tr}}, \quad (7)$$

with a minimum of unity. $E_{\rm SN} = 10^{51}$ erg is the energy released by a single supernova with a fraction in kinetic energy of $f_{\rm tr} = 0.676$ Blondin et al. (1998).

For the unresolved radiative phase, the momentum is given by (Blondin et al. 1998; Thornton et al. 1998; Kim & Ostriker 2015; Martizzi et al. 2015)

$$p_{\rm rad,Ki} = 2.5 \times 10^5 N_{\rm SN}^{16/17} n_{\rm H,1}^{-2/17} Z'^{-0.14}\ {\rm M_\odot\,km\,s^{-1}}, \quad (8)$$

with $Z' = \max(Z/Z_\odot, 0.01)$, $Z_\odot$ being the solar metallicity, Z the metallicity of the cell, and $n_{\rm H,1}$ its density in cm^{-3}. However, this model does not account for unresolved radiative feedback from photoionisation which is given by (Geen et al. 2015)

$$p_{\rm sn+ph} = 5 \times 10^5 N_{\rm SN}^{16/17} Z'^{-0.14}\ {\rm M_\odot\,km\,s^{-1}}. \quad (9)$$

As we include RT, this feedback can already be accounted for depending on the resolution of radiative feedback which is quantified through the Strömgren radius $R_{\rm st}$. We thus combine the two previous equations as (Kimm et al. 2017)

$$p_{\rm sn} = p_{\rm rad,Ki} e^{-\Delta x/R_{\rm st}} + p_{\rm sn+ph}(1 - e^{-\Delta x/R_{\rm st}}). \quad (10)$$

In the adiabatic phase, the expected momentum from the supernova is given by

$$p_{\rm ad,KI} = \sqrt{2\chi m_{\rm ej} f_{\rm e} E_{\rm SN}}, \quad (11)$$

and is combined to a boost factor $B_{\rm ph}$ to account for unresolved photoionisation. Finally, the model can be described by

$$\Delta p = \frac{1}{N_{\rm c}} \begin{cases} \frac{1}{f_P} p_{\rm sn} & \text{if } \chi \geq \chi_{\rm tr}, \quad (12a) \\ B_{\rm ph} p_{\rm ad,KI} & \text{otherwise.} \quad (12b) \end{cases}$$

$f_{\rm e}$ is a coefficient ensuring a smooth transition between the two propagation phases of the supernova. The momentum is then injected in the 48 neighbouring cells sharing at least two vertices with the host cell. The parameter $f_{\rm p} = 0.9387$ is a correction coefficient which compensates an underestimation of the momentum injected when the neighbouring cells are effectively at the same level as the host cell. This is always the case here, as we enforce star formation at the maximum level. As stars host stellar nucleosynthesis, we model the mass fraction of metal in the ejecta with a yield of 7.5%, as $Z_{\rm ej} = Z_{\rm star} + 0.075(1 - Z_{\rm star})$.

2.3 KR simulation

We now detail the subgrid models used in the simulation KR, which come from Kretschmer & Teyssier (2020).

Star formation

In this star formation model, the only criterion is that the cell density should be above 0.1 cm^{-3} for the same reasons as in KI. We confirmed that it has no impact on star formation, as no stars are forming in cells with densities below 10 cm^{-3}. The other major difference from the previous model is the definition of one-dimensional turbulence. Kretschmer & Teyssier (2020) use a subgrid turbulence model relying on numerical diffusion from the large eddy simulation (LES) (Smagorinsky 1963; Schmidt et al. 2006). There, the turbulence is introduced through the turbulent kinetic energy of the medium as

$$K_T = \frac{1}{2}\bar{\rho}\left(\sqrt{3}\sigma_{\rm 1D}\right)^2, \quad (13)$$

with $\bar{\rho}$ an averaged large-scale density. No turbulent diffusion is injected, and numerical diffusion is instead used to provide an implicit LES model (Semenov et al. 2016). Also, the critical density used to compute the star formation efficiency in Eq. 3 is given by (Krumholz & McKee 2005)

$$s_{\rm crit} = \ln\left[\alpha_{\rm vir}\left(1 + \frac{2\mathcal{M}^4}{1+\mathcal{M}^2}\right)\right]. \quad (14)$$

Also, the KR model sets $\phi_{\rm t} = 1 = \epsilon$ in Eq. 3 as all the gas is here expected to fall onto the star.

Feedback

The model from Kretschmer & Teyssier (2020) includes a subgrid description of radiative feedback. As we already include RT, we turn it off to avoid double-counting. Concerning supernovae feedback, the age at which the stellar particles explode ranges from 3 Myr to 20 Myr and the total number of supernovae for a given stellar particle follows the same principle as in KI but is then sampled uniformly through time instead of following a best-fit to an SNII rate. To avoid alignment effects, the location at which the supernovae explode is chosen randomly over the eight cells comprised in the oct where the stellar particle is located. Whether the phase considered is the adiabatic phase or the radiative phase, the energy of the supernova is injected as thermal energy into the host cell. Kretschmer & Teyssier (2020) compute a cooling radius as (Martizzi et al. 2015)

$$R_{\rm cool} = 43.6 n_{\rm H,1}^{-0.42} Z'^{-0.05}\ {\rm pc}. \quad (15)$$

If this cooling radius is not resolved by at least four cells, the momentum expected at the adiabatic phase

$$p_{\rm ad,Kr} = 2.66 \times 10^5 \eta_R N_{\rm SN} Z'^{-0.114} n_{\rm H,1}^{-0.19}\ {\rm M_\odot\,km\,s^{-1}} \quad (16)$$

is injected into a neighbouring cell to compensate for overcooling, where η_R is a factor dependent on how resolved the cooling radius is. A further difference with KI is that this energy is not simply injected as momentum in the surrounding cells but also treated as a source term at the solver level, following Agertz et al. (2013). The ejected mass is obtained by taking the product of the number of supernovae and their average mass and has a metal yield of 10%.

2.4 DC simulation

Star formation

We use the same star formation recipe as for KI here.

Feedback

We refer to this last model as DC, as it follows the delayed cooling feedback model from Teyssier et al. (2013). The feedback here is injected in the same fashion as in the *thermal feedback* scheme. When the star particle is 50 Myr, the energy from the supernovae is injected at once into the host cell as thermal energy, assuming a typical supernova progenitor mass of 10 M$_\odot$. The mass ejected is defined by $m_{\rm ej} = \eta_{\rm SN} m_{\rm star}$ (same idea as KI and KR but with a larger value as it is integrated over time) with $\eta_{\rm SN} = 0.2$, and has the same metal yield as in KI. With this approach, cooling is turned off in the host region for a given amount of time to avoid overcooling. To do so, an additional variable $\epsilon_{\rm DC}$ is used in the numerical scheme and is increased by a value based on the ejected mass every time a supernova occurs. This quantity is advected with the gas and is only used as a passive scalar which is exponentially dampened at

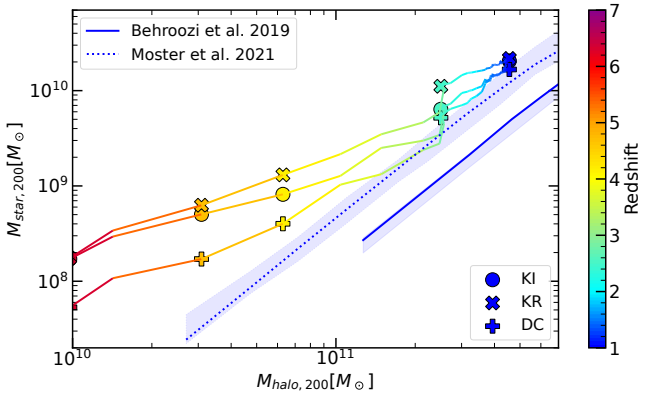

Figure 1. Stellar mass to halo mass relation, with each style of marker representing a different simulation. The colour code corresponds to the redshift, and the simulations go down to redshift $z = 1$. The solid lines and shaded areas correspond to predictions from observations from Behroozi et al. (2019) and Moster et al. (2021) and are also colour coded, blue at $z = 1$.

each cooling timestep with a characteristic dissipation timescale of 10 Myr (Williams & McKee 1997; Teyssier et al. 2013). Where this scalar is higher than a given threshold, cooling is turned off.

We summarise the main differences between KI, KR, and DC in table 1. The major modification for star formation is the difference estimation of the velocity dispersion σ_{1D}. For feedback, major changes are the boost, the time sampling of the supernova (single explosion in DC) and how the supernova is modelled: mechanical feedback (KI), thermal feedback combined with mechanical feedback (KR) or delayed cooling (DC). KI also includes compensation for unresolved H II regions.

3 GALAXY PROPERTIES

In this section, we present the properties of the galaxies formed in our simulations and compare their stellar masses and their gas content.

3.1 The $M_* - M_h$ relation

In Fig. 1, we show the stellar mass to halo mass relation for our three simulations. For each point, the stellar mass is measured as the mass of stars within 0.1 R_{200}, and the halo mass is measured from a twin dark-matter-only simulation to match the approach made in Behroozi et al. (2019) and Moster et al. (2021)[1].

The first thing we note is that the three models produce the same galaxy stellar mass (within a factor < 2) at $z = 1$, and are thus well calibrated. Even though the stellar mass is initially more than twice lower in DC than in the other two models, all three models are in very good agreement by redshift $z = 1$. The step in the evolution of the stellar mass at a halo mass of $M_h \sim 3 \times 10^{11}$ $M_\odot$ corresponds to simultaneous satellite mergers.

The second thing we note is that at $z = 1$, the simulated galaxies are slightly above the observed stellar mass to halo mass relation for all three models. As a galaxy gets more massive, its gravitational potential becomes too strong for supernovae alone to regulate star formation, and AGN (which are not simulated here) may take over as the driver of feedback to solve this problem (Silk & Rees 1998; Somerville & Davé 2015; Naab & Ostriker 2017). It is nonetheless also possible that this is simply a feature from the particular history of the simulated galaxy, as we only follow a single set of initial conditions. Some uncertainties also weigh on these relations, such as a possibly underestimated observed stellar mass and its correction almost halving the stellar mass in simulations (Munshi et al. 2013; Graham et al. 2005), the IMF dependence on the measurement aperture (van Dokkum et al. 2017) or the stochasticity of such simulations (Keller et al. 2019; Genel et al. 2019).

3.2 Gas properties

We now want to probe the gas content within the halo to check whether it is similar or not amongst our simulations. Fig. 2 shows the density-temperature distribution of the gas within the virial radius of each simulation. The panels show the phase diagram of 100 outputs from redshift $z \sim 1.30$ down to redshift $z = 1.00$, which we stack together. We can see three main phases in all three simulations. The first phase is the shock-heated gas ($10^5 - 10^6$ K) at low density ($10^{-5} - 10^{-3}$ cm^{-3}). At higher densities, cooling becomes efficient, and the gas reaches the second phase of the phase diagram, around 10^4 K. Below this temperature, cooling is inefficient, and another peak can be seen in the temperature PDF. This gas is spread in density from $\sim 10^{-4}$ cm^{-3} to 10^{-1} cm^{-3}, above which cooling becomes efficient again because of its dependency oh n_H^2. The last phase is the dense ($30 - 300$ cm^{-1}) cold gas ($10^2 - 10^3$ K) in which star formation may occur.

We find a striking difference between DC and the two other models: gas in DC populates the high-density, high-temperature part of the diagram where cooling is supposedly efficient. This is a direct effect of the delayed cooling, as cooling is turned off in such gas to avoid numerical overcooling. Nonetheless, the corresponding mass represents less than a percent of the total gas mass within 0.1 R_{200} at redshift $z = 1.00$ and significantly less in the CGM. This hot dense gas is concentrated around stars and has no impact on the results we produce, which focus on the CGM.

Focusing now on the density distribution in the simulations, KR exhibits a notable difference compared to KI and KR, with the gas mass within R_{200} being almost equally split between the ISM and the CGM, while in the other simulations the density is mainly at low values[2]. Even though the stellar masses of our three simulations are similar, their baryonic content differs.

4 COMPARISON TO OBSERVATIONS

Now that we have seen how different models lead to different situations, we discuss in this section how they compare to observational constraints on the CGM.

4.1 Ionic tracers

We choose to focus on H I, Mg II, C IV, and O VI which span a wide temperature range and which commonly appear in observations. Since the non-equilibrium ionised hydrogen fraction is tracked in each cell, the H I content of our galaxies and their CGM is a direct prediction of our radiative hydrodynamic simulations. It is thus

[1] Using the dark-matter-only simulations instead of the simulation including baryons leads to an increase in dark matter mass of $\sim 23\%$.

[2] At a higher resolution, most of the gas is at low densities in KR, bringing its distribution of gas closer to the other simulations.

Table 1. Summary of the main differences between the subgrid models used in KI, KR, and DC. The three first rows describe the differences in the star formation subgrid models, and the following ones are the differences in the feedback subgrid models.

	KI	**KR**	**DC**
$s_{\rm crit}$	$\ln\left[0.62\alpha_{\rm vir}\mathcal{M}^2\right]$	$\ln\left[\alpha_{\rm vir}\left(1+\frac{2\mathcal{M}^4}{1+\mathcal{M}^2}\right)\right]$	$\ln\left[0.62\alpha_{\rm vir}\mathcal{M}^2\right]$
ϵ	0.5	1	0.5
$\phi_{\rm t}$	0.57	1	0.57
Turbulence $\sigma_{\rm 1D}$	Local estimation	Subgrid turbulence model	Local estimation
Supernova sampling	Random time sampling over a fit to the SNII rate	Uniform time sampling	Single explosion
Time of supernova	0 – 2.3 to 50 Myr	0 to 20 Myr	50 Myr
Supernova average mass	5 $\rm M_\odot$	2.5 $\rm M_\odot$	10 $\rm M_\odot$
Thermal energy injection	None	Random cell within the 8 parent cell	In central cell + cooling turned off
Adiabatic phase	$\sqrt{2\chi m_{\rm ej} f_{\rm e} E_{\rm SN}}$	None	None
Transition	$\chi \equiv \frac{{\rm d}m_{\rm W}}{{\rm d}m_{\rm ej}}$	$R_{\rm cool} = 43.6 n_{\rm H,1}^{-0.42} Z'^{-0.05}$ pc	None
Radiative phase [$\rm M_\odot\,km\,s^{-1}$]	$2.5{\times}10^5 N_{\rm SN}^{16/17} n_{\rm H,1}^{-2/17} Z'^{-0.14} {\rm e}^{-\Delta x/R_{\rm st}} + 5\times10^5 N_{\rm SN}^{16/17} Z'^{-0.14}(1-{\rm e}^{-\Delta x/R_{\rm st}})$	$2.66\times10^5 \eta_R N_{\rm SN} Z'^{-0.114} n_{\rm H,1}^{-0.19}$	None
Momentum injection sites	Neighbouring cells	Neighbour cells + source term	None
Metal yield	7.5%	10%	7.5%

the most robust comparison point. For other species, we first need to model the abundance of each ion in post-processing. For this, we infer the fraction of O, Mg and C from the metallicity variable traced in the simulation and assuming Solar abundances of $A_{\rm Mg,\odot} = 3.98\times10^{-5}$, $A_{\rm C,\odot} = 2.69\times10^{-4}$ and $A_{\rm O,\odot} = 4.9\times10^{-4}$ (Grevesse et al. 2010). We then post-process the outputs of the simulations using KROME (Grassi et al. 2014) to obtain the ionisation state of these elements. We do so following Mauerhofer et al. (2021) and solving the ionisation balance to the equilibrium for the chosen elements, relying on the cell's metallicity, density, temperature and ionising radiation flux.

We now describe the gas phases traced by these ions by showing in Fig. 3 the same phase diagrams as Fig. 2 but now weighted by the mass of the different tracers. They are similar for all simulations, and we only show results from KI. We see here that the neutral hydrogen, H I, traces cold and dense gas at $40-4\times10^4$ K. As it traces the same gas phases as H I and almost yields the same temperature and density distribution, we do not show the corresponding figure for Mg II. C IV exhibits a major peak in the dense phase with temperatures near 10^4 K. As most of the gas in this peak has densities higher than 10 $\rm cm^{-3}$, it traces the ISM of the galaxy. The CGM is probed by the second peak, which is close to 10^5 K and traces a shallower region of the phase diagrams shown previously. Lastly, O VI traces hot gas (10^5 K to 10^6 K) at low densities ($\sim 10^{-4}$H $\rm cm^{-3}$). O VI preferentially traces the lower part of the hot region with a distribution peaking at $\sim 2\times10^5$ K. This is slightly lower than the peak in the distribution of hot gas, at $\sim 4-5\times10^5$ K. O VI is thus not necessarily the optimal tracer for the hotter phase of the galaxy, and O VII could prove to be a better match with a maximal fraction at higher temperatures and a larger extent in temperature (Tumlinson et al. 2017). For more massive galaxies, a bigger fraction of gas can reach higher temperatures, and we need even higher ions to probe it.

In the top panels of Fig. 4, we show the density-weighted projection of the hydrogen density for KI, KR, and DC. We can see the presence of more diffuse gas in KI and DC than in KR. The presence of this diffuse gas actually exhibits the difference that we pointed out earlier, which is that there is significantly more mass in the CGM of KI and DC than in KR. While the CGM gas mass is $M_{\rm KR,CGM} \sim 4.3\times10^9$ $\rm M_\odot$ in KR, the gas mass in KI and DC is respectively $M_{\rm KI,CGM} \sim 19.6\times10^9$ $\rm M_\odot$ and $M_{\rm DC,CGM} \sim 11.2\times10^9$ $\rm M_\odot$. This exhibits the degeneracy of subgrid models (all having the same stellar mass but a different gas content), and that these different models are effectively ejecting gas differently. We also find that the metallicity in KR is higher than that of DC, which is in turn larger than that of KI. This leads to an overall metal content in KR comparable to KI, but lower than DC.

To get a clearer image of the location of the different ions in our simulations, we also show in Fig. 4 the face-on column density maps of H I, C IV and O VI in KI, KR, and DC. The distribution of H I (and Mg II) is very concentrated in and around the galaxy, its satellites and the filaments of cold gas connecting them. This is expected as it is where the cold gas traced by these ions is located. Beyond, there is close to no H I as gas is hotter and H becomes H II. As seen in the phase diagrams, the C IV traces gas which is in the ISM, but there is also a remarkable amount of diffuse C IV throughout the CGM. This shows how C IV also traces gas in a warmer phase, which is more extended than gas in a colder phase. The gas in C IV is more extended in DC than in KR, and more extended in KR than in KI. This is directly due to the mass of metals in the CGM, which is ~ 1.5 times higher in DC than in KR and ~ 1.6 times higher in KR than in KI. Finally, O VI almost permeates the whole CGM and is widely distributed with no obvious link with inflows or outflows from the galaxy. Even more than with C IV, DC exhibits significantly higher O VI column densities than both KI and KR due to its higher metal content. The difference between KI and KR is smaller. In KI, O VI is mostly present in the outer part of the CGM. Conversely, O VI is more concentrated in the inner CGM with KR than in the outskirts. As O VI traces hot gas, this difference could show how the two simulations eject gas through outflows at different scales.

4.2 Cold gas: H I and Mg II

After computing the ion populations, we compute the simulated column densities along random lines of sight by propagating 10^5 rays in each snapshot with RASCAS (Michel-Dansac et al. 2020a,b). In practice, we draw for each ray a random direction $k_{\rm obs}$ and two ran-

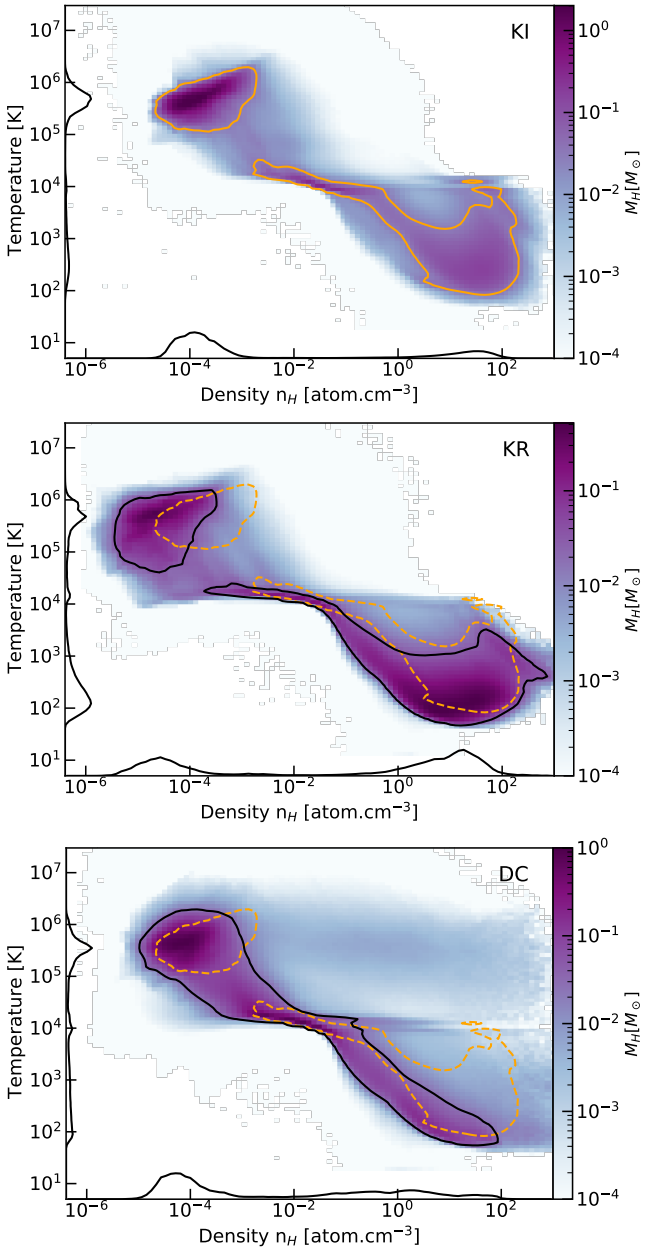

Figure 2. Phase diagrams of the gas contained within R_{200} for each simulation, stacked over 1 Gyr. From top to bottom are KI, KR, and DC with a colour code that corresponds to the mass probability density function. The full line contour encompasses 90% of the mass within R_{200}, and the contour in the orange dotted line is that of KI. We show on the left and lower sides of each panel the temperature and density distribution of the corresponding simulation.

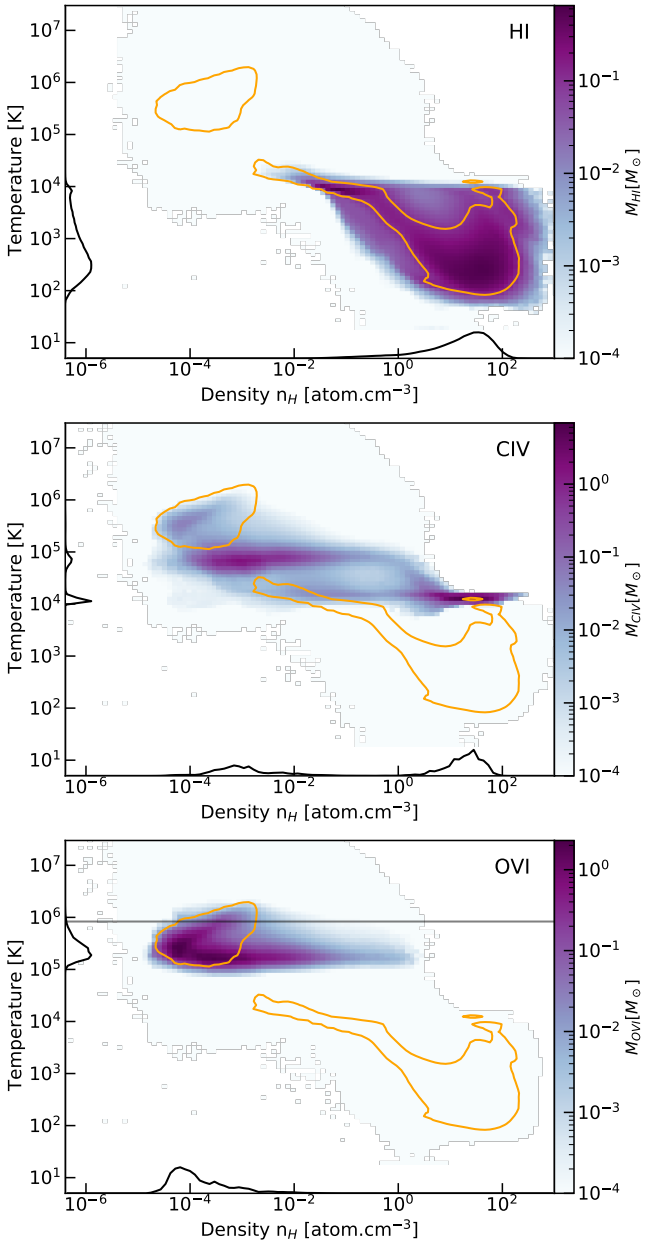

Figure 3. Phase diagrams of the gas contained within R_{200} in KI, stacked over 1 Gyr. From top to bottom, the phase diagram is weighted by the mass of H I, C IV and O VI. The solid line contour is the same as in Fig. 2 and encompasses 90% of the mass within R_{200} in KI. We show on the left side and at the bottom of each panel the stacked mass-weighted probability distribution function of temperature and density of the corresponding simulation.

dom coordinates, $x_\perp$ and $y_\perp$ on the plane perpendicular to $k_{\rm obs}$. We retain only rays with $r_\perp = \sqrt{x_\perp^2 + y_\perp^2} \leq 2\ R_{\rm vir}$. We integrate the rays over 5 $R_{\rm vir}$ along the line of sight and centred on the plane perpendicular to $k_{\rm obs}$.

In Fig. 5, we compare these simulated column densities to observations of H I (Prochaska et al. 2011; Johnson et al. 2015; Prochaska et al. 2017; Wilde et al. 2021), and Mg II (Chen et al. 2010; Werk et al. 2013). These rely on QSO lines of sight from Keck with HIRES (Werk et al. 2013), the MagE spectrograph (Chen et al. 2010) or HST with GHRS (Prochaska et al. 2011) and COS (Johnson et al. 2015; Prochaska et al. 2017; Wilde et al. 2021). Data from Chen et al. (2010) is taken from Hummels et al. (2013) who converted equivalent widths into column densities following Draine (2011). These data cover halo masses of $10^{10.6}$–10^{13} $M_\odot$. Prochaska et al. (2017) contains the same absorption lines as Werk et al. (2014) but with new measurements and either a different estimate of the gas metallicity or a consistent lower limit. Werk et al. (2013), Prochaska et al. (2017), and Johnson et al. (2015) cover a range of stellar masses of $10^{8.4}$ – $10^{11.5}$ $M_\odot$. We restrict the data we take from Wilde et al. (2021) to a subsample of galaxies with a stellar mass within $10^{9.9}$ – 10^{11} $M_\odot$. Prochaska et al. (2011) cover luminosities of 0.007 – 2.6 L_*. All observed column

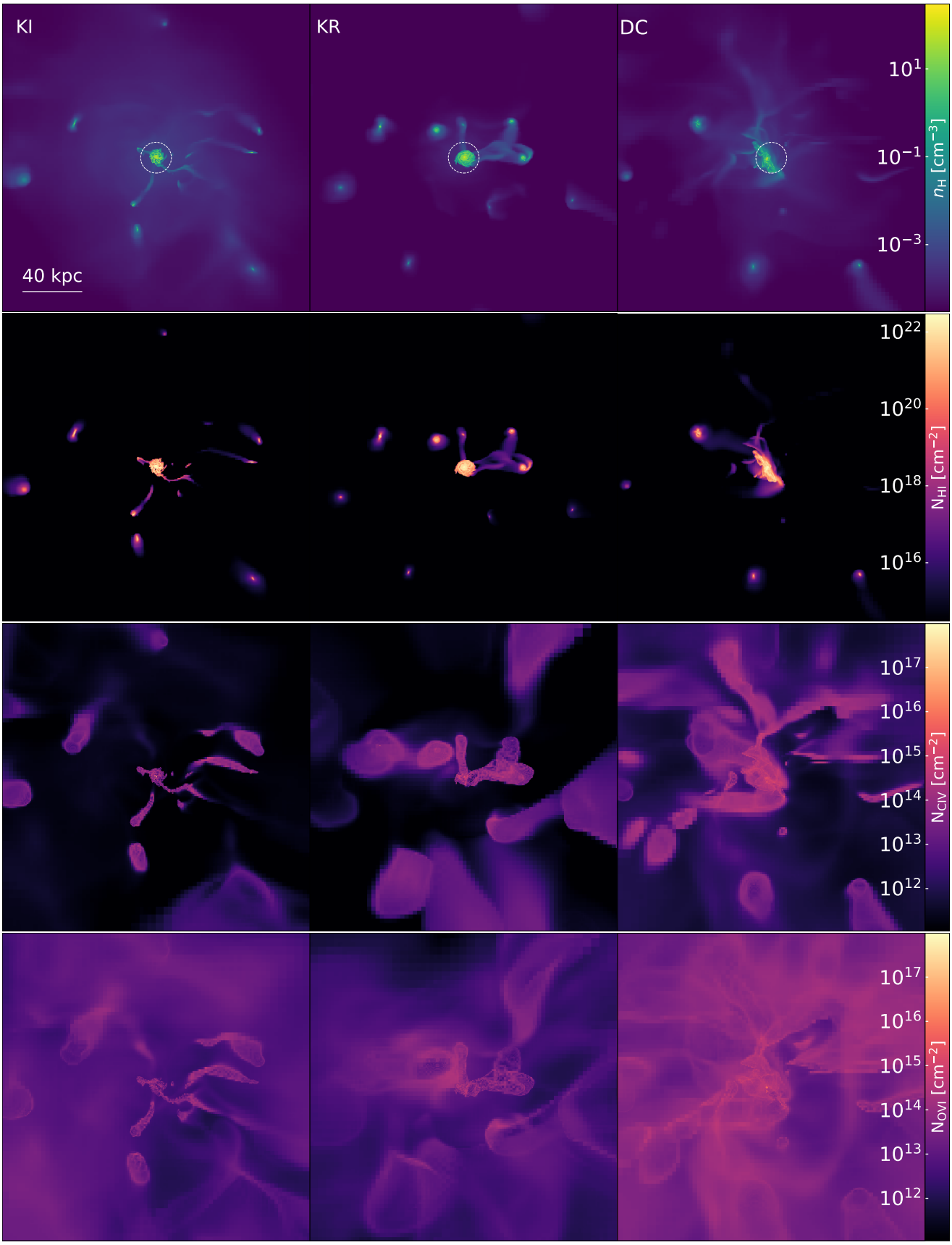

Figure 4. Maps of the galaxy at $z = 1.0$ for KI, KR, and DC (from left to right). From top to bottom is shown the density-weighted projection of the hydrogen density and the column density of H I, C IV and O VI. The column density map of Mg II is not shown as it is very similar to that of H I. The images are 2 R_{200} on a side. The dashed white circle in the top panels is centred on the galaxy, with a radius of 0.1 R_{200}.

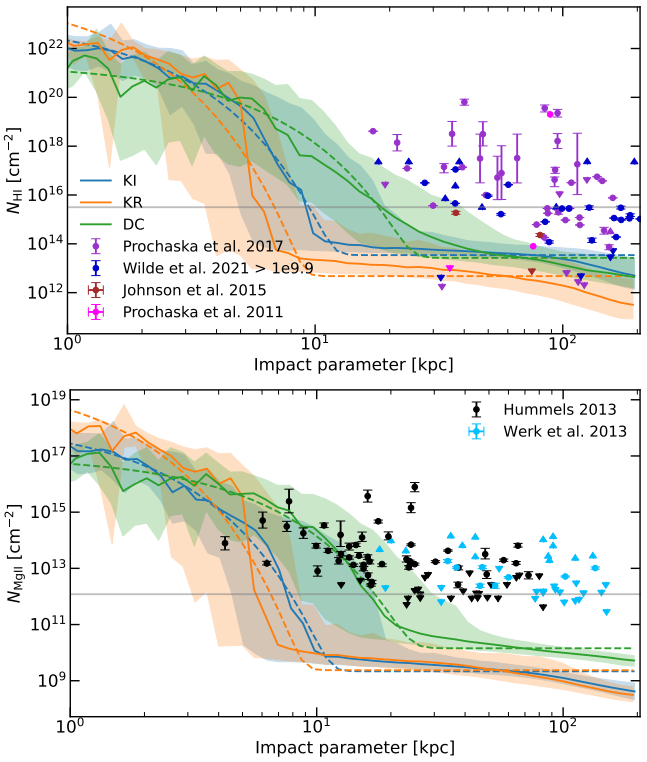

Figure 5. Column density as a function of impact parameter for H I (top) and Mg II (bottom). The simulated data are shown in solid lines, with the shaded area denoting the 15.9 and 84.1 percentiles. The dotted line corresponds to an exponential best fit of the median. Galaxy-selected observational points are shown by different markers for different references. Upward-pointing arrows denote lower limits and downwards-pointing arrows denote upper limits. The horizontal grey line shows the value used for the minimum threshold in the covering fractions.

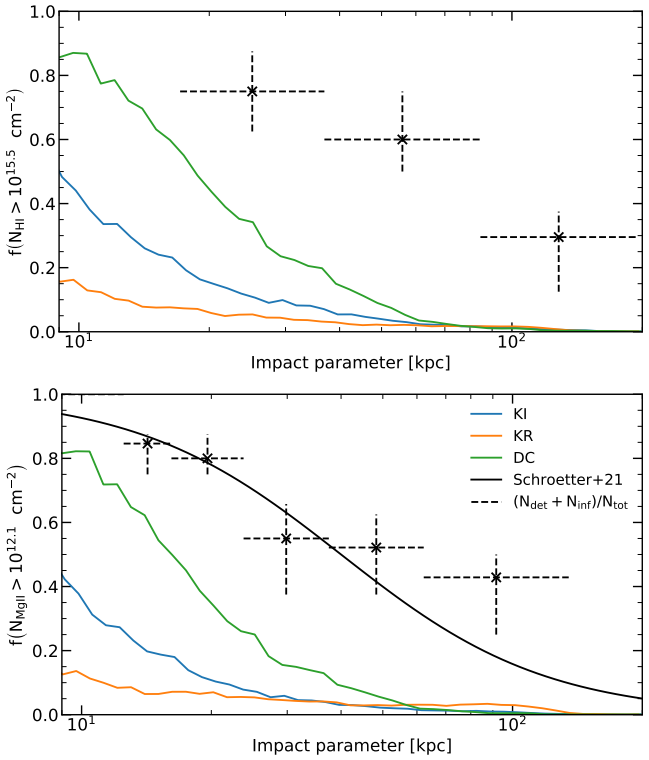

Figure 6. Covering fraction as a function of impact parameter for H I (top) and Mg II (bottom). The simulated data is shown in coloured solid lines with the same colour code as used in previous plots. The lower threshold above which the covering fraction is computed for the simulated data is arbitrarily chosen for H I and is computed from the minimal equivalent width from Schroetter et al. (2021) for Mg II. Their inferred covering fraction for Mg II as a function of impact parameter is plotted in full black line. The markers denote the binned fraction of detection for the observations used in this study.

densities are at redshift $z < 0.4$. Due to scarce observations, the range in mass and luminosity of the surveys we selected is wide and extends over up to three orders of magnitude. We remind that the three simulations produce galaxies with stellar masses of $1.7 - 2.2 \times 10^{10}$ $M_\odot$ within 0.1 R_{200}.

In Fig. 5, we show the median column density of H I and Mg II as a function of the impact parameter. H I and Mg II both trace cold gas, but H I traces both pristine and enriched gas while Mg II traces only enriched gas and we may thus expect differences. However, they both yield similarly-shaped profiles. KI and KR present a similar behaviour, with the column density slowly decreasing, until $\sim$ 5 kpc where a steep drop occurs. Further than $\sim$ 10 kpc, the column density reaches a plateau. Interestingly, the plateaus in KR and KI are very close for Mg II but are separated by an order of magnitude in H I with KI matching the values from DC. DC exhibits a slower drop at the edge of the galaxy (i.e. $\sim 5 - 10$ kpc), which is likely explained by a more extended disc than in the other two simulations (see the top panel in Fig. 4).

In H I, there are no observations of the inner CGM. Most observational points are located in the plateau zone and the outer regions of the CGM. There, most column densities from observations are between one and four orders of magnitude above the simulated ones. In the case of Mg II, the inner CGM is also probed thanks to the data from Chen et al. (2010). These data points are in excellent agreement with the median of DC and have some overlap with the upper percentiles of KI, but agree badly with KR. Further than $\sim$ 30 kpc from the centre, most observations are upper limits plateauing above $\sim 10^{12}$ cm^{-2}, while the few detections are two to four dex above the simulations.

To account for the fact that many observational points are upper limits, we compute the *covering fraction* as the fraction of absorbers above a given column density threshold. This threshold is often chosen to be the minimum value that can be detected in observations. If the surveys are complete, the covering fraction should represent well the fraction of simulated column densities above a chosen detection threshold. For Mg II, we base our column density threshold on observations from Schroetter et al. (2021) where the minimal equivalent width is $W_{\mathrm{Mg\,II}} = 0.05$ Å. We convert it into a column density $N_{\mathrm{ion}} = 1.136 \times 10^{14} W_{ion}/f_{12}\lambda^2_{1000}$, which assumes an optically thin regime. With f_{12} the oscillator strength for Mg II, this gives $N_{\mathrm{Mg\,II,min}} = 1.2 \times 10^{12}$ cm^{-2}. For H I, we choose arbitrarily a column density threshold based on our set of observations. Taking a threshold too low can make the covering fraction lose its significance, as it would overestimate the detection limit in several samples. Conversely, taking a column density threshold too high should impact similarly the observations and the simulations, but would produce less constraining results. This leads to the choice of $N_{\mathrm{H\,I,min}} = 3.2 \times 10^{15}$ cm^{-2}. The thresholds used are also reported on the column density figures as horizontal grey lines.

In Mg II, we compare our results to observations from Schroetter et al. (2021). In H I, we do not have such a measure and build a covering fraction combining our previous sample of observations.

Then, we define our covering as the fraction of observations composed of either lower limits or detections ("detections" from now on). We show it with black markers. The bins in impact parameters were made to contain at least ten observational points, and the horizontal dashed lines are extended to the size of the bin. The vertical dashed error bars show the 15.9 and 84.1 percentiles[3], which we estimate with bootstrapping. To do so, we produce 100 random realisations of a sub-sample of eight data points for each bin and then compute the fraction of detections in each of them. We also show covering fractions measured this way in Mg II and find that the covering fraction estimated this way is in excellent agreement with the one determined in observations (Schroetter et al. 2021). We also find similar results for both H I and Mg II. Since we find that they trace the same gaseous phases, it leads us to believe that this approach and the selection of our threshold are reasonable.

Fig. 6 shows the covering fraction of H I and Mg II as a function of impact parameter. For both observations and simulated data, the covering fraction decreases with increasing the impact parameter. This is expected because we expect gas to be more diffuse the further we get away from the galaxy. The results in H I and Mg II are very similar. All three models produce covering fractions significantly below the observed values at all radii. Similar to what was seen for the column densities as a function of the impact parameter, the closest match is DC, while KR seems to most severely lack cold gas in the CGM. Nonetheless, all three simulations appear to significantly lack cold gas in the CGM.

4.3 Warm gas: C IV

We now look at the warm gas traced by C IV. We compare our simulations to observations from Chen et al. (2001) and Bordoloi et al. (2014b), with Bordoloi et al. (2014b) using COS. As with Chen et al. (2010), points from Chen et al. (2001) are taken from Hummels et al. (2013) who converted equivalent widths into column densities following Draine (2011). These points cover stellar masses of $10^{9.5} - 10^{11.5}$ $M_\odot$. This is also the only data set with redshifts higher than $z = 0.4$, going up to $z = 0.8920$. Data from Bordoloi et al. (2014b) cover a stellar mass range of $10^{8.2} - 10^{10.1}$ $M_\odot$.

The upper panel in Fig. 7 shows the median column density of C IV as a function of the impact parameter. As for cold gas, we can see a transition at the disc edge for all three models, which occurs once again further out for DC than for KI and KR. The drop in the simulated column densities is of 2.5 – 3 dex, far less than for H I and Mg II, which both drop by ~ 8 dex. The KI and KR simulations do not agree well with observations from Hummels et al. (2013) and Bordoloi et al. (2014a), but also note that these observations are mostly upper limits and plateau above ~ 10^{13} cm^{-3}, as seen in Mg II. DC is in good agreement with the observations up to ~ 60 kpc from the galaxy centre, showing column densities remarkably higher than the two other models.

In the lower panel of Fig. 7, we now show the covering fraction of C IV against the impact parameter. As done with Mg II, we use a detection limit of $W_{\rm C\,IV} = 0.05$ Å (Schroetter et al. 2021) and convert it into a column density, which results in a column density threshold of $N_{\rm C\,IV,min} = 1.3 \times 10^{13}$. The most apparent feature is that DC is consistently above the observed covering fraction up until ~ 100 kpc, which means that there is *at least* enough column densities above the chosen threshold. Conversely, KI is consistently below observations and has column densities which are too low. KR produces covering fractions between the other two models which are compatible with the covering fraction we estimate but too low compared to expectations from (Schroetter et al. 2021).

[3] For a normal data set, this corresponds to the standard deviation σ.

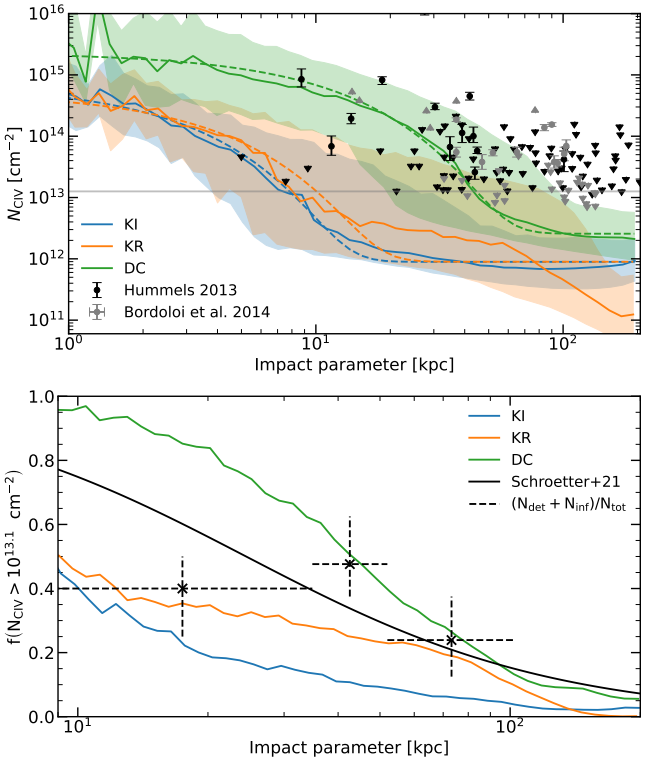

Figure 7. Column density (top) and covering fraction (bottom) of C IV as a function of impact parameter. The same notation as Fig. 5 (resp. Fig. 6) is used for the top (resp. bottom) plot. The covering fraction from Schroetter et al. (2021) for C IV is plotted in full black line.

4.4 Hot gas: O VI

The last ion we examine is O VI. The observational data we compare our results to are taken from Prochaska et al. (2011), Tumlinson et al. (2011) and Johnson et al. (2015), with Tumlinson et al. (2011) using COS. As in the previous sections, the data included all have a redshift $z < 0.4$. The stellar mass ranges of the data cover $10^{9.5} - 10^{11.5}$ $M_\odot$ (Tumlinson et al. 2011), $10^{8.4} - 10^{11.1}$ $M_\odot$ (Johnson et al. 2015) and luminosities of 0.007 – 2.6 L∗ (Prochaska et al. 2011).

The upper panel of Fig. 8 shows the median column density of O VI as a function of impact parameter. The decrease in the simulated column density between the innermost and the outermost regions is significantly less pronounced than for the previous plots, and the scatter is only ~ 1 dex (it is approximately eight dex for the cold gas and three dex for the warm gas). Most detections of O VI shown are from Tumlinson et al. (2011) and are in the range ~ $10^{14} - 10^{15}$ cm^{-2}, approximately one to two dex above the simulated column densities from KI and KR. On the other hand, DC is almost constant at $N_{\rm O\,VI} = 5 \times 10^{14}$ cm^{-2} up to 20 kpc and is in quite good agreement with observations up to large distances.

The lower panel of Fig. 8 shows the covering fraction of O VI, with $N_{\rm O\,VI,min} = 1.5 \times 10^{14}$ cm^{-2}. Most column densities in KI and KR are below the minimal threshold and their fraction of sightlines above it thus barely reaches 10%, showing a significant lack of hot gas in both simulations. DC is significantly above them and matches

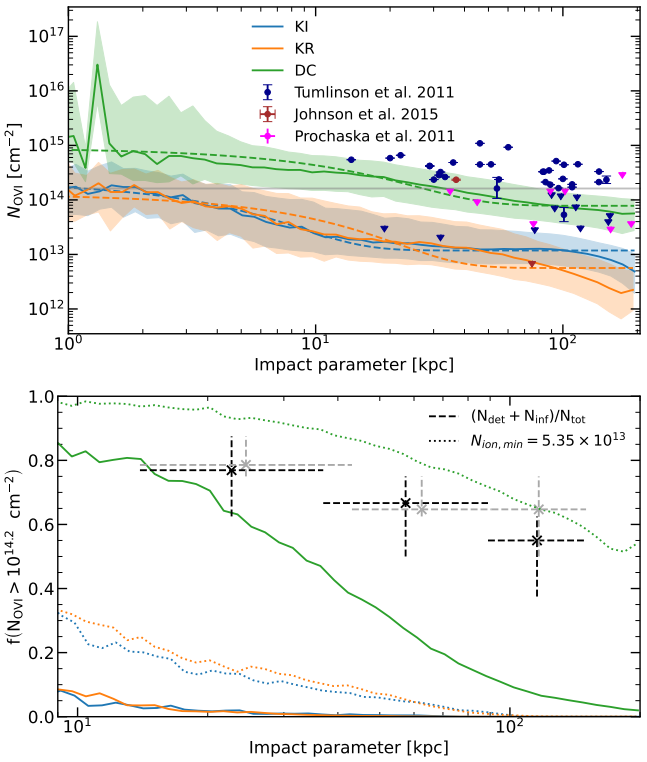

Figure 8. Column density (top) and covering fraction (bottom) of O VI as a function of impact parameter. The same notation as Fig. 5 (resp. Fig. 6) is used for the top (resp. bottom) plots. We also show in dotted lines the simulated covering fraction using the lowest detection as a density threshold.

observations in the inner the CGM. It however decreases to values lower than observations at higher radii.

4.5 Limits of the covering fraction

The covering fraction is quite sensitive to the detection threshold for observations as well as for simulations, and it has to be approached with caution. In our sample, there is a significant amount of sightlines producing upper limits. In this case, the column density threshold must be taken above most of these upper limits. Comparing our estimation of the covering fractions with those from Schroetter et al. (2021), we estimate our approach to be realistic. For simulations, if there is a considerable change in the simulated column densities near the density threshold (as for H I and Mg II), changing the value of the density threshold will not affect the covering fractions much. However, in the case of a smaller drop as in O VI, changing the column density threshold can have a significant impact on the covering fractions.

We illustrate this by using the lowest detection from our observational sample as the column density threshold for O VI. We show the results with dotted lines on the lower panel of Fig. 8. The column density threshold is then $N_{\mathrm{O\,VI,min}} = 5.35 \times 10^{13}$ cm^{-2}. While the observations still place a similar constraint (light grey markers), the change in the simulations is considerable. DC stands close to unity in the whole range probed, significantly above observations. In this case, DC is actually overestimating the O VI column density. KI and KR also show a far better match to observations, with a decrease similar to previous simulated covering fractions. If we take an arbitrary density threshold between the previous values of $N_{\mathrm{O\,VI,min}} = 7 \times 10^{13}$ cm^{-2}, the only difference is that DC is just enough to match observations. As this is still largely below most detections, the observations remain similar.

We thus see how a single isolated detection can significantly drive the results if located below most others. This shows the impact of the threshold chosen and how subtle its choice is when the number of observations is so limited. More observations and a well-defined detection density threshold are thus necessary to drive a more robust conclusion regarding column densities in the CGM.

4.6 Summary

In this section, we have seen that cold gas is a problem for our simulations, especially at large distances. In C IV, the simulations are not far from a match with observation depending on the model considered and might be overestimated in DC. O VI proves to be the best ion to constraint different feedback models, even though the results are quite sensitive to the density threshold. As a significant proportion of the gas phases is probed through these ions, this means that either there is not enough gas ejected, the metallicity is too low, or that the gas is in a different phase (it might be slightly too hot in all phases).

4.7 Exponential profile

Other than the height of the column densities profiles, we show in our results that different models and different ions produce distinct simulated column density profiles. We focus here on two major differences related to the presence of a sudden drop in column density, and present for all the ions we trace. The first is the extent of this drop in column density, and the second is the characteristic distance at which it occurs.

The presence of this column density drop is supported by several observational papers, notably in Bordoloi et al. (2014b) and Johnson et al. (2015) in which they find a boundary for C IV. Several authors find an exponential profile to be the best-fit for the radial equivalent widths or column density profiles (Nielsen et al. 2013; Borthakur et al. 2015; Tchernyshyov et al. 2022). Some others however favour the Schechter function by combining a power law and an exponential law (Hasan et al. 2020). In simulations, this drop is also seen (Hummels et al. 2013), and has been described as a "metal boundary" but was interpreted by Liang et al. (2016) as the natural evolution of an exponentially decreasing profile. We thus want to characterise our simulated column density profiles and choose to describe them by combining an exponential profile and a constant following

$$N_{\mathrm{ion}} = \alpha \exp^{-r/r_{\mathrm{d}}} + \beta. \quad (17)$$

α, β and r_{d} are free parameters which we fit using non-linear least squares on the log distribution of the median of column densities. The fit parameters are listed in table 2. The curves corresponding to the best fits are plotted in dashed lines in Fig. 5, 7 & 8 with the same colour coding as the solid lines. Except for a few curves, most of these prove to be a very close match to the simulation points with a coefficient of determination $R^2 \gtrsim 0.95$. The fits with the lowest coefficient of determination are KR and DC with O VI. On the other hand, the exponential best fit proves to be a very good match with KI for all ions.

Unlike (Hummels et al. 2013) and Liang et al. (2016), we show that our simulated column densities plateau from a certain distance. We thus find a drop less sharp, which remains at higher column densities at large radii and reaches a better agreement with observations.

We now investigate two characteristic scales for this drop: its characteristic distance to the galaxy centre r_{d} and its extent. We find that

Table 2. best-fit parameters for an exponentially decreasing column density profile combined with a constant value, as described by 17.

	H I			Mg II			C IV			O VI		
	$\alpha/10^{22}$ [cm^{-2}]	r_d [kpc]	$\beta/10^{13}$ [cm^{-2}]	$\alpha/10^{18}$ [cm^{-2}]	r_d [kpc]	$\beta/10^{9}$ [cm^{-2}]	$\alpha/10^{14}$ [cm^{-2}]	r_d [kpc]	$\beta/10^{11}$ [cm^{-2}]	$\alpha/10^{14}$ [cm^{-2}]	r_d [kpc]	$\beta/10^{13}$ [cm^{-2}]
KI	13.8	0.54	3.45	1.69	0.55	2.17	7.08	1.92	8.93	2.06	3.57	1.18
KR	207	0.34	0.47	66.6	0.36	2.37	5.23	2.63	8.96	1.23	8.33	0.56
DC	0.24	1.33	2.66	0.10	1.52	14.3	23.0	8.33	25.7	8.14	12.5	7.80

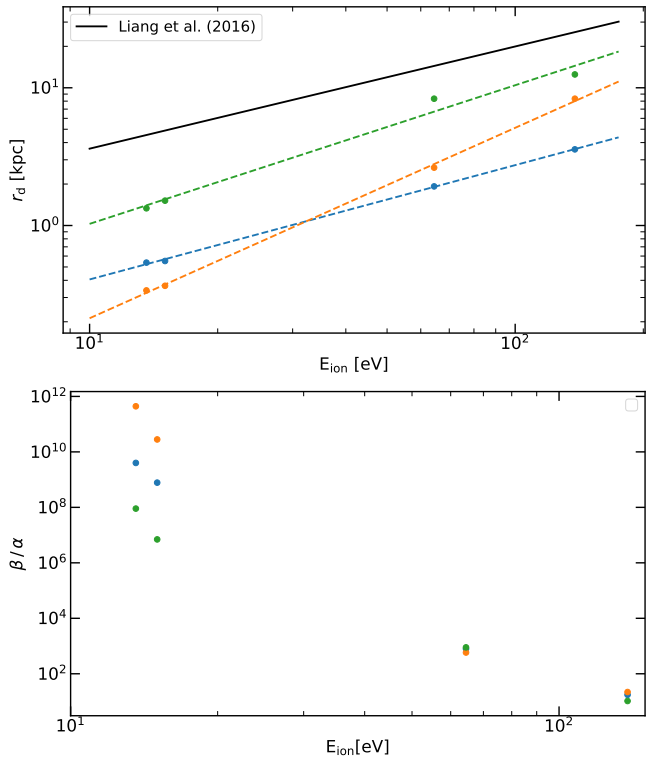

Figure 9. Scale length (upper panel) and column density drop (lower panel) against the ionisation energy of H I, Mg II, C IV and O VI. In the upper panel, the dotted line corresponds to the best fit and the full black line corresponds to 0.74 E$_{ion}$ (Liang et al. 2016).

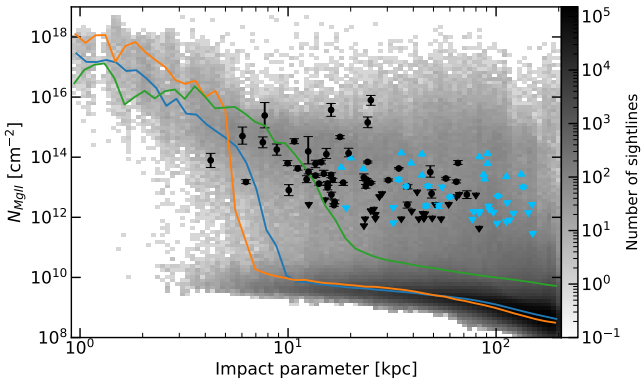

Figure 10. Histogram of the simulated and observed Mg II column densities as a function of impact parameter between in the redshift range $z = 1.3 - 1$ for KI. The observations are shown with the same colour code as in Fig. 5 and the darker pixels show the most densely populated area of the histogram.

the drop is dependent on the disc size. As KI and KR have similar gaseous disc sizes, it happens in a similar location. It is however more extended in DC, so this drop happens further out. When normalising scale heights by R$_{vir}$ as done in Liang et al. (2016), we find that all the simulation models produce r_d significantly lower than those found by these authors for Mg II and O VI, even though it comes closest for C IV. The difference between cold and hot gas comes directly from the column density dropping at a lower radius in our study while for warm gas, the drop is at $\sim$ 40 kpc, closer to what is found in Liang et al. (2016). As done in Liang et al. (2016), one can further find a relation between the typical scale r_d and the ionisation energy E_{ion}, as shown in the upper panel of Fig. 9. This scaling between the ionisation energy and the scale height reasonably stems from the propensity of low ions to reside in high-density and low-temperature media, while higher ions reside in a hotter and less dense environment. As the median density decreases with radius while the median temperature increases, the typical length for higher ions is naturally larger. Assuming $r_d \propto E_{ion}^{\gamma}$, with γ a free parameter and using a least-squares linear fit, we find respective slopes of 0.83, 1.34 and 1.00 for KI, KR, and DC. While there is a remarkable consistency between the four ions studied, there is a large discrepancy between the different simulations. In KI, the steepness is close to the value of 0.74 found in Liang et al. (2016), while it is significantly higher in KR.

We also characterise the height of the drop for the different ions through α/β with α the maximal height of the peak and β the plateau value as shown in the lower panel of Fig. 9. The higher α/β is, the bigger the drop. As we have shown in the column densities, we find a strong anti-correlation, with higher ionisation energy for a given species inducing a smaller drop. Indeed, while hot gas extends far into the CGM, cold gas traces preferentially gas in the galaxy and is more dependent on the size of the gaseous disc. Thus, as H I and Mg II trace the cold dense gas, the drop in such ions is steeper than for ions tracing shallower densities and warmer temperatures, such as C IV and O I.

4.8 Limits

A complex distribution

Even though an exponential profile describes satisfyingly the column density profiles, there is an extremely large scatter in the simulated data. H I and Mg II exhibit very similar behaviour and both range over more than eight orders of magnitude in column densities, while C IV and O I cover respectively a little more than four dex and two dex. This scatter actually stems from a bimodal distribution. Fig. 10 shows the full distribution of column densities of Mg II as a function of impact parameter. Seeing the complexity of this distribution, we stress how important it is to analyse it as a whole and not just as a single quantity. In this figure, most absorption lines are shaping a slightly decreasing plateau at $10^8 - 10^{10}$ cm^{-2} but a second trend also shows up, decreasing from 10^{18} cm^{-2} at 1 kpc and joining the bulk of the distribution further out. The observations match surprisingly well with this second trend, and the same can be seen with H I. We find

the same bimodality when looking at the distribution of sightlines in KR and DC. As the drop in column is of lower extent for C IV and O VI, this effect is of lower magnitude with these ions.

The detection limit

Since observations are limited by their sensitivity, they are biased towards higher column densities. The absence of the lower column density sightlines in observations could thus also be interpreted as observations only probing the upper part of the distribution. We discuss this hypothesis in the following paragraph. To create galaxy-absorber pairs, one can either rely on detected absorber lines and find galaxies matching them or include all galaxies within a QSO sightline and attempt to match these to absorbers by comparing their redshifts. While the first method biases the results towards higher column densities, the second one allows for upper limits and non-detections. We thus choose to only include galaxy-selected surveys to produce a complete set of data with upper limits. If the surveys are indeed complete, the covering fractions showed in the previous figures are comparable to the simulated data, as they give a lower limit to the fraction of observed sightlines that should be in a certain column density range. The limitation in sensitivity should thus have no impact on our study. Prochaska et al. (2011) (H I and O VI) and Wilde et al. (2021) (H I) estimate their samples to be nearly fully complete, respectively up to magnitudes $m = 19.5$ within 150 kpc of the absorber and within 2 arcmin (~ 230 kpc at their lowest redshift of $z = 0.1$) with an i-band magnitude lower than $m = 22$. Johnson et al. (2015) (O VI) also mentions a completeness of 80% for $L > 0.1L_*$, $z < 0.4$ and radii lower than 500 kpc. There is no completeness estimation for the other surveys. There might thus still be undetected low-mass neighbours closer to the sightline producing the absorption features. These would shift the observed distribution to the left and bring it closer to a match, but we deem it unlikely as the surveys are still highly complete.

A small integration length

Also, while observations integrate absorptions over a range of a few hundred km s^{-1}, our results are integrated over only $\delta v \sim \pm \int H(z)dz \sim \pm 30 - 35$ km s^{-1}. As the sightlines could cross the CGM of more galaxies by extending this integration length, we might miss additional absorption features. We extended our integration length from $\sim$ 500 kpc to $\sim$ 600 kpc but it produced no significant difference. As it is close to the size of our zoom region at redshift $z = 1$, we cannot extend this measure further. Wilde et al. (2021) finds that slightly more than half of the galaxies with $M_* < 10^{10}$ M$_\odot$ have $M_* > 10^{10}$ M$_\odot$ neighbours within 300 kpc and 1000 km s^{-1} of the sightline and that low mass galaxies with nearby massive neighbours tend to have elevated HI covering fractions out to $\sim 2 - 3$ R$_{\rm vir}$ compared to galaxies with no detected massive neighbours. In our simulations, we choose to model a quite isolated galaxy, with no neighbour halo more than 20% of the target virial mass within 3R$_{\rm vir}$. This leads to an under-representation of the satellite's population in our simulations. There is only one galaxy in our sightlines, but this assumption is realist, as the probability of finding another galaxy in the volume over which the observations are integrated (a cylinder of radius 250 kpc spread over δv) is negligible based on the luminosity function.

The last caveat is that the statistics we have for observations are relatively low. Mg II and C IV are respectively only probed by two and three surveys, some of which rely on strong priors (Chen et al. 2001, 2010; Hummels et al. 2013).

5 DISCUSSION

Both KI and KR show very similar results for all four ionic species, while DC presents generally higher column densities in the CGM. Nonetheless, except for DC in C IV, none of the simulations reproduces the observations.

We could expect to find column densities slowly decreasing with increasing radius as stellar feedback not only regulates star formation but also ejects gas from the galaxy, enriching the surrounding media, but we find that there is a sudden drop in the simulated column densities. The cause for this drop in column densities and the lack of all ionic species in the CGM can be understood in two ways. Either the feedback is not efficient enough in expelling metal-enriched gas out of the galaxy, or the gas is in an incorrect ionisation state or both.

5.1 What the simulations lack

There are several possible causes that could give rise to the discrepancy between our simulations and observations. We describe here the two most plausible reasons, which are a lack of refinement causing incorrect temperatures or feedback which is not efficient enough in removing gas for the galaxy.

As Mg II exhibits similar results as H I which is traced through the simulation with a dedicated ionisation bin, we expect that the photoionisation modelling is reasonable. An incorrect temperature in the CGM could then be the cause for too low ionisation states. Studies suggest that the cold CGM is actually in the form of small dense clouds (see McCourt et al. (2018) for a compilation of such studies). Through $N_{\rm H}$ and $n_{\rm H}$ (respectively the column density and the density of hydrogen), observations computed the path length of cold absorbers as $l_{cool} \equiv N_{\rm H}/n_{\rm H}$. This resulted in typical scales of $\sim 1 - 100$ pc. Another way to see that is that cold gas is found with a large covering fraction alongside a very low volume filling factor, which also suggests that it resides in small dense clouds (Gronke et al. 2022). McCourt et al. (2018) sets the origin of these cold droplets in shattering, a rapid fragmentation of the cold gas caused by cooling and external pressure. These would reach scales down to $c_{\rm s}\, t_{\rm cool} \sim 0.1 {\rm cm}^{-3}/n$ pc, with n the volume density in cm^{-3}. However, other results suggest that such small clouds could not survive and Gronke et al. (2022) defines a critical radius of ~ 8 pc which depends on the local properties of the gas, and above which a cloud could survive in a turbulent environment. These paint the picture of a CGM described by a fog comprised of cold clouds defined by a scale of $10 - 100$ pc. Such objects are largely unresolved in our simulation, where the resolution significantly drops beyond the disc. If fragmentation were to occur in our simulation, the clouds that should be formed are instead mixed with hotter gas in larger cells and evaporate. This results in a higher temperature, effectively decreasing the amount of cold gas traced by H I and Mg II. The idea of the bimodality of the simulated absorption lines is hence supported, as clouds would populate the first trend in the upper left part of Fig. 10 and slowly decrease in strength with increasing radius until the resolution is too low, and they transition to the plateau by evaporating. A solution to the problem of thermal mixing induced by the lack of resolution is simply to increase the resolution in the CGM. This was done in Hummels et al. (2019) by forcing the simulation to reach a fixed minimal resolution in a defined region around the galaxy. They find first that it changes the thermal balance of the CGM by increasing the cold gas content while lowering the warm/hot gas content. It also allows cool gas clouds to survive longer while allowing them to reach smaller scales. van de Voort et al. (2019) also test the same, going from a single mass refinement criterion to a 1 kpc minimal CGM

resolution, and also finds increased column densities and covering fractions (the CGM resolution in our simulation ranges roughly over 1.2 – 5 kpc). In Peeples et al. (2019), the CGM resolution is increased to 183 kpc, but the changes in column densities and covering fractions remain small, even though the size of cold clouds changed greatly.

The second phenomenon inducing a mismatch with observations can be inferred by analysing the clear lack of O VI in all simulations presented. The column density drop seen in O VI is of a significantly lower extent than with cold gas. The observed discrepancy is thus seemingly more of a global lack of gas in the O VI state rather than a local phenomenon causing it in the CGM. This difference with observations can come from either the gas column density $N_{\rm O\,VI}$ (treated in the next subsection), its metallicity Z or the ionisation fraction $f_{\rm O\,VI}$. It was found that including active galactic nuclei (AGN) could increase O VI column densities by 1.5 dex (Sanchez et al. 2019) and allow for a better match with observations. This is enabled by heating the CGM to a temperature corresponding to the ionisation fraction peak of O VI ($10^{5.5-5.8}$ K) (Suresh et al. 2017) while enriching it in metals (Nelson et al. 2018). We thus think that AGN might allow the simulations to reach a higher O VI column density and reach a good match with observations, but we leave such an analysis for a future study.

A last possible solution may lie in cosmic rays (CR) as it was seen that they can push colder outflows out of the galaxy (Liang et al. 2016; Farcy et al. 2022).

However, these considerations are purely theoretical and only presented as possible explanations. Our simulations do not allow us to test the effect of AGN feedback, CR feedback or an increased resolution. Since they are both heavily related, simply looking at a density radial profile or a temperature radial profile is inconclusive when trying to determine whether an incorrect temperature or an insufficient metal content is mainly responsible for the low column density. Indeed, as the resolution is following density, if the cold gas is in the form of cold clouds and is dependent on resolution, the cold gas content is ultimately dependent on density.

5.2 An incorrect ionisation state ?

To compare the role of the temperature to the role of the outflows, we compute the column density of each element with the density of the element j given by $n_j = n_{\rm H} A_{j,\odot} Z/Z_\odot$. As previously, we use solar abundance of $A_{\rm Mg,\odot} = 3.98 \times 10^{-5}$, $A_{\rm C,\odot} = 2.69 \times 10^{-4}$ and $A_{\rm O,\odot} = 4.9 \times 10^{-4}$ (Grevesse et al. 2010). We show the computed column density of each element in Fig. 11. The first difference in the four ions we show is that all the Mg in the ISM is in Mg II, except for DC, with an Mg II column density slightly below that of Mg. This is not the case for higher ions, as they tracer hotter gas. As they are well above the minimum detection threshold, we find that the covering fractions are all at unity for most impact parameters except for KI and KR in O VI which undergo a sudden strong decrease close to the virial radius. As expected, the shape of the dotted line in Fig. 11 is the same for $N_{\rm Mg}$, $N_{\rm C}$ and $N_{\rm O}$ as they correspond to the metal content corrected by a given factor depending on the element. There is a constant decrease with increasing impact parameters, and all ions reach values within the upper observational points. For hydrogen, the column densities computed are consistently 5 dex above the lower points in observations, meaning that a H I fraction of 10^{-5} is *sufficient* to match observations. For magnesium and carbon, the sufficient fraction of Mg II and C IV is 0.01 at 40 kpc and decreases to 0.1 at R_{200}. For oxygen, it is $\sim$ 0.1 at 40 kpc and 1 at R_{200}. We

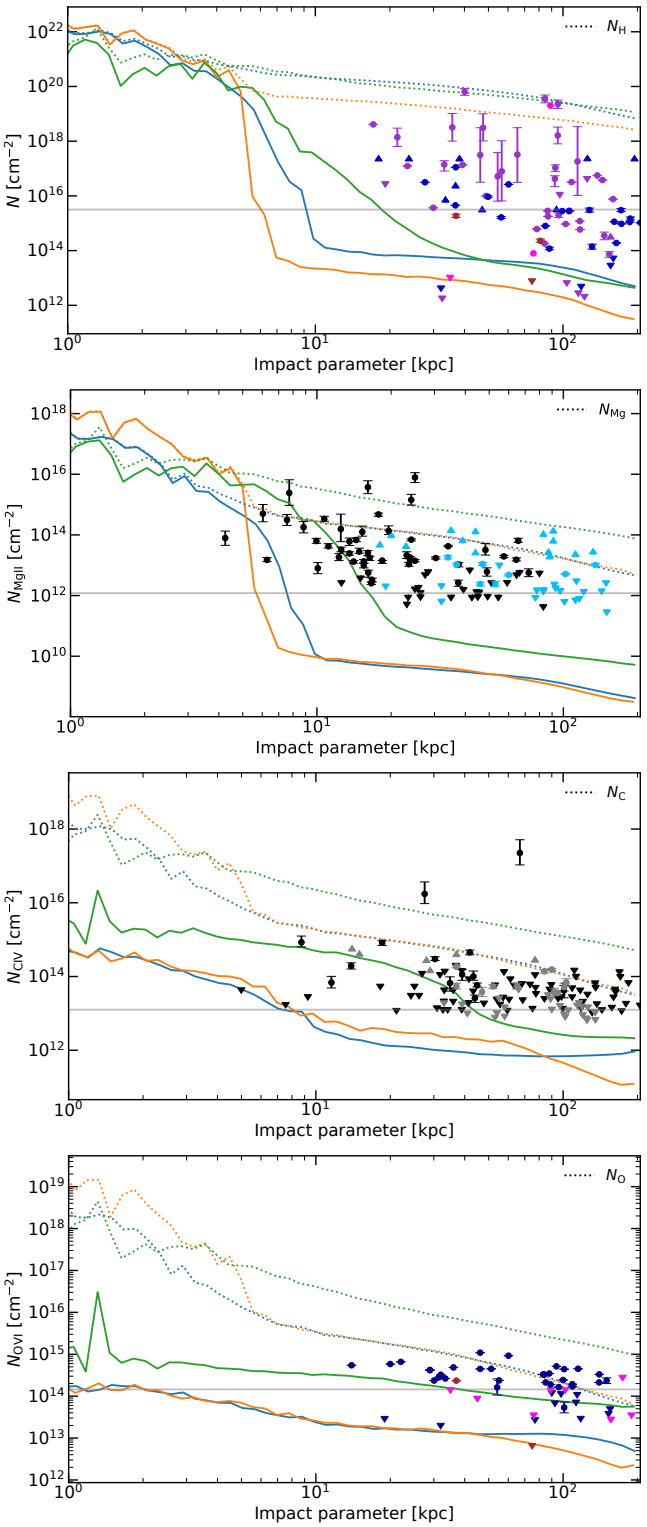

Figure 11. Column density of Mg II (top), C IV (middle) and O VI (bottom) as a function of impact parameter. We furthermore show in dotted line the column density of Mg, C and O which corresponds to the maximal column density attainable for each ion. Otherwise, the same notation and colour code as the previous figures is used.

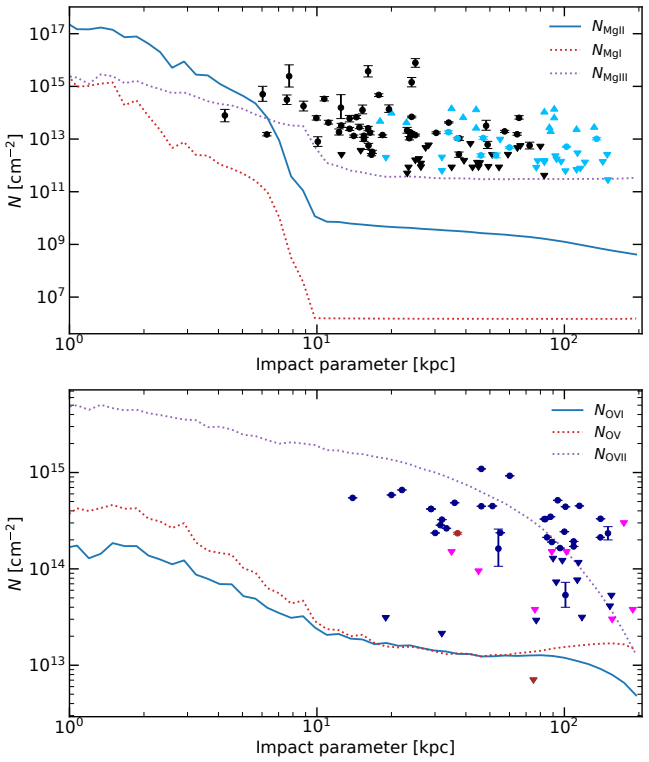

Figure 12. Column density of Mg I, Mg II and Mg III (upper panel) and O V, O VI and O VII (bottom panel) as a function of impact parameter in KI. Otherwise, the same notation and colour code as the previous figures is used.

thus see that there is a reasonable margin allowing for an incorrect ionisation state in H I but that there is almost none for O VI.

We now look at gas in the ionisation state just above and just below Mg II and O VI to check if the gas might be in a slightly incorrect ionisation state. We respectively show in the upper and lower panel of Fig. 12 the column density of Mg I, Mg II and Mg III and the column density of O V, O VI and O VII. We find in the bottom panel that there is significantly more O VII than O VI at all radii. Thus, if the temperature was slightly lower, the computed column density could be significantly higher and match observations. This is consistent with the interpretation of O VI being maximal when the virial temperature of the halo is close to its ionisation peak (Hummels et al. 2013; Oppenheimer et al. 2016). As the virial temperature of the simulated galaxies is 8×10^5 K, it implies that the CGM of the simulated galaxy is too hot. This is also consistent with the peak in the O VII which we find at 6×10^5 K. If all of this gas was at a lower temperature, it would be in O VI which would then provide a better match with observations. However, this is not all as the peak in O VII is also significantly wider compared to O VI. The distribution of O VII ranges over $1.5 - 10 \times 10^5$ K while that of O VI is narrower, only ranging over $1.5 - 2 \times 10^5$ K and making it more sensitive to the temperature of the CGM. It is thus expected to find more O VII than O VI. If we now look at the results of the upper panel, we also find significantly more Mg III than Mg II, but only in the CGM, where it stands ~2 dex above. The galaxy can still be interpreted as too hot since a colder CGM would allow a better match between observations and simulations, but in this case, ions from higher states would need to recombine down to match observations.

5.3 An incorrect gas mass ?

Another solution that could explain the mismatch between observations and simulations might lie in the inefficiency of outflows in ejecting gas out of the galaxy. As it was seen in Fig. 1 that the stellar mass is higher than expected from observations, it is a sensible solution.

If we consider once again Fig. 11, it can be noticed that the column density of each element is higher in the first few kiloparsecs for KR than for the other models. As these elements trace the metal content of the gas (the only difference being the abundance assigned to them), it means that the metal content is higher in KR than in the other two simulations in this region. This is due to a different metal injection scheme in both star formation models. In KI and DC, the metals ejected depend on the metallicity of the star, while in KR is it systematically 1 $M_\odot$ per stellar particle. Furthermore, we notice that there is a small drop in KR, which makes it reach the values found in KI. For DC, the metal content is at the same level as KI and lower than KR in the inner regions, but is consistently 1 dex above both in the CGM. It shows directly that the metal-enriched gas is more efficiently pushed out of the galaxy through the feedback model from DC than through the mechanical feedback schemes used in KR and KI. The higher metal content thus ejected directly leads to higher column densities for all ions, even though they might have the same ionisation fractions.

We thus see that the mismatch between observations and simulations of the CGM can be explained by two processes. First, there is a lack of gas due to the feedback not being efficient enough in pushing gas out of the galaxy. Second, an incorrect CGM temperature can lead to an incorrect ionisation fraction and too low column densities. Further studies following a similar approach and testing complementary or more precise physics are thus needed to be able to conclude what drives the difference between observations and simulations of the CGM.

6 CONCLUSIONS

In this work, we run three cosmological zoom-in simulations with different subgrid models for star formation and feedback to find whether the CGM could provide a complementary constraint to the stellar mass to halo mass relation. We refer to our three models as KI (Kimm et al. 2017), KR (Kretschmer et al. 2020) and a variation of KI with supernova feedback modelled through delayed cooling (Teyssier et al. 2013), DC. We calibrate our simulations in stellar mass, and, relying on KROME, we post-process them to compute the ionisation fraction of various elements, specifically focusing on H I, Mg II, C IV and O VI. We further use RASCAS to model the propagation of light rays and estimate the column density which we would measure in these galaxies. Our results can be summarised as follows.

- *There is a significant lack of most ions for the three simulated galaxies.* Except for C IV with DC, the modelled column densities are all significantly below observations. We reach the same conclusion by computing the covering fraction, which describes how statistically likely our simulations are. However, these results are sensitive to the lower threshold used.
- *The column density profile can be described by an exponential profile combined with a plateau.* We find that an exponential fit matches well the column density simulated with each ion if we combine it with a plateau value. We also find that there is a significant

drop in column density, the lower the ionisation energy is, the larger the drop is.

- *Outflows more efficient in removing gas from the galaxy would allow for a better match with observation, but might not be sufficient.* We find one of the models (DC) has a higher metal content than the other models, and that this difference is due to a model producing feedback ejecting enriched gas more efficiently in the CGM. This leads to higher column densities for all ions probed.
- *A lower CGM temperature could significantly increase the simulated column densities of the ions probed.* On the one hand, there is a significant reservoir of metals which would allow simulations to match observations, even with small ionisation fractions of H I, Mg II and C IV (for O VI, the margin is considerably smaller). On the other hand, while there is a significant amount of gas in O VII, the amount of gas in Mg III alone would not be enough to match observations.
- *CGM quasar absorption lines are a powerful complementary probe to the stellar mass to halo mass relation.* While our three simulations present very similar masses, the differences we find in their CGM column densities are considerable, and we even find differences in models with similar feedback schemes such as KI and KR. Covering fractions yield even more striking differences between the simulations.

We found that the simulated column densities are lower than expected from observations and established that they are a very powerful complementary probe to the stellar mass to halo mass relation. Adding additional physics such as AGN could bring the simulations closer to observations by fuelling stronger outflows and enriching the CGM. Cosmic rays could also play a role by propagating colder outflows. Finally, increasing the CGM resolution could allow simulations to resolve its complex multiphase character and allow cold gas clouds to sustain themselves for longer times, eventually leading to higher simulated column density.

ACKNOWLEDGEMENTS

Simulations necessary for this work were executed on the CCF (Common Computing Facility) of the LABEX Lyon Institute of Origins (ANR-10-LABX-0066) and most simulations were achieved thanks to the computing resources of the PSMN (Pôle Scientifique de Modélisation Numérique) of the ENS de Lyon. We acknowledge the use of Python (Van Rossum & Drake Jr 1995), Matplotlib (Hunter 2007), NumPy (Harris et al. 2016) and Astropy (Astropy Collaboration et al. 2013, 2018)

DATA AVAILABILITY

REFERENCES

Agertz O., Kravtsov A. V., 2015, ApJ, 804, 18
Agertz O., Kravtsov A. V., Leitner S. N., Gnedin N. Y., 2013, ApJ, 770, 25
Astropy Collaboration et al., 2013, A&A, 558, A33
Astropy Collaboration et al., 2018, AJ, 156, 123
Aubert D., Pichon C., Colombi S., 2004, MNRAS, 352, 376
Behroozi P., Wechsler R. H., Hearin A. P., Conroy C., 2019, MNRAS, 488, 3143
Blondin J. M., Wright E. B., Borkowski K. J., Reynolds S. P., 1998, ApJ, 500, 342
Bordoloi R., et al., 2014a, ApJ, 794, 130
Bordoloi R., et al., 2014b, ApJ, 796, 136
Borthakur S., et al., 2015, ApJ, 813, 46
Chen H.-W., Lanzetta K. M., Webb J. K., Barcons X., 2001, ApJ, 559, 654
Chen H.-W., Helsby J. E., Gauthier J.-R., Shectman S. A., Thompson I. B., Tinker J. L., 2010, ApJ, 714, 1521
Dekel A., Silk J., 1986, ApJ, 303, 39
Draine B. T., 2011, Physics of the Interstellar and Intergalactic Medium. Princeton Series in Astrophysics
Elmegreen B. G., Scalo J., 2004, ARA&A, 42, 211
Farcy M., Rosdahl J., Dubois Y., Blaizot J., Martin-Alvarez S., 2022, arXiv e-prints, p. arXiv:2202.01245
Faucher-Giguère C.-A., Lidz A., Zaldarriaga M., Hernquist L., 2009, ApJ, 703, 1416
Federrath C., Klessen R. S., 2012, ApJ, 761, 156
Ferland G. J., Korista K. T., Verner D. A., Ferguson J. W., Kingdon J. B., Verner E. M., 1998, PASP, 110, 761
Few C. G., Courty S., Gibson B. K., Kawata D., Calura F., Teyssier R., 2012, MNRAS, 424, L11
Ford A. B., et al., 2016, MNRAS, 459, 1745
Geen S., Rosdahl J., Blaizot J., Devriendt J., Slyz A., 2015, MNRAS, 448, 3248
Genel S., et al., 2019, ApJ, 871, 21
Girichidis P., et al., 2020, Space Sci. Rev., 216, 68
Gnedin N. Y., Abel T., 2001, New Astron., 6, 437
Graham A. W., Driver S. P., Petrosian V., Conselice C. J., Bershady M. A., Crawford S. M., Goto T., 2005, AJ, 130, 1535
Grassi T., Bovino S., Schleicher D. R. G., Prieto J., Seifried D., Simoncini E., Gianturco F. A., 2014, MNRAS, 439, 2386
Grevesse N., Asplund M., Sauval A. J., Scott P., 2010, Ap&SS, 328, 179
Gronke M., Oh S. P., Ji S., Norman C., 2022, MNRAS, 511, 859
Haardt F., Madau P., 1996, ApJ, 461, 20
Hafen Z., et al., 2019, MNRAS, 488, 1248
Hahn O., Abel T., 2011, MNRAS, 415, 2101
Hahn O., Abel T., 2013, MUSIC: MUlti-Scale Initial Conditions (ascl:1311.011)
Harris C. R., et al., 2016, Nature, 585, 357
Hasan F., et al., 2020, ApJ, 904, 44
Hennebelle P., Chabrier G., 2011, ApJ, 743, L29
Hopkins P. F., Quataert E., Murray N., 2011, MNRAS, 417, 950
Hummels C. B., Bryan G. L., Smith B. D., Turk M. J., 2013, MNRAS, 430, 1548
Hummels C. B., et al., 2019, ApJ, 882, 156
Hunter J. D., 2007, Computing in Science & Engineering, 9, 90
Johnson S. D., Chen H.-W., Mulchaey J. S., 2015, MNRAS, 449, 3263
Keller B. W., Wadsley J. W., Wang L., Kruijssen J. M. D., 2019, MNRAS, 482, 2244
Kennicutt R. C., Evans N. J., 2012, ARA&A, 50, 531
Kim C.-G., Ostriker E. C., 2015, ApJ, 802, 99
Kimm T., Cen R., Devriendt J., Dubois Y., Slyz A., 2015, MNRAS, 451, 2900
Kimm T., Katz H., Haehnelt M., Rosdahl J., Devriendt J., Slyz A., 2017, MNRAS, 466, 4826
Kravtsov A. V., Klypin A. A., Khokhlov A. M., 1997, ApJS, 111, 73
Kretschmer M., Teyssier R., 2020, MNRAS, 492, 1385
Kretschmer M., Agertz O., Teyssier R., 2020, MNRAS, 497, 4346
Kroupa P., 2001, MNRAS, 322, 231
Krumholz M. R., McKee C. F., 2005, ApJ, 630, 250
Leitherer C., et al., 1999, ApJS, 123, 3
Liang C. J., Kravtsov A. V., Agertz O., 2016, MNRAS, 458, 1164
Martizzi D., Faucher-Giguère C.-A., Quataert E., 2015, MNRAS, 450, 504
Mauerhofer V., Verhamme A., Blaizot J., Garel T., Kimm T., Michel-Dansac L., Rosdahl J., 2021, A&A, 646, A80
McCourt M., Oh S. P., O'Leary R., Madigan A.-M., 2018, MNRAS, 473, 5407
Michel-Dansac L., Blaizot J., Garel T., Verhamme A., Kimm T., Trebitsch M., 2020a, RASCAS: Resonant line transfer in AMR simulations (ascl:2002.002)
Michel-Dansac L., Blaizot J., Garel T., Verhamme A., Kimm T., Trebitsch M., 2020b, A&A, 635, A154
Moster B. P., Naab T., Lindström M., O'Leary J. A., 2021, MNRAS, 507, 2115
Munshi F., et al., 2013, ApJ, 766, 56

Murray N., 2011, ApJ, 729, 133
Naab T., Ostriker J. P., 2017, ARA&A, 55, 59
Nelson D., et al., 2018, MNRAS, 477, 450
Nelson D., et al., 2019, Computational Astrophysics and Cosmology, 6, 2
Nielsen N. M., Churchill C. W., Kacprzak G. G., 2013, ApJ, 776, 115
Oppenheimer B. D., Davé R., 2006, MNRAS, 373, 1265
Oppenheimer B. D., et al., 2016, MNRAS, 460, 2157
Padoan P., Nordlund Å., 2011, ApJ, 730, 40
Padoan P., Haugbølle T., Nordlund Å., 2012, ApJ, 759, L27
Peeples M. S., et al., 2019, ApJ, 873, 129
Prochaska J. X., Weiner B., Chen H. W., Mulchaey J., Cooksey K., 2011, ApJ, 740, 91
Prochaska J. X., et al., 2017, ApJ, 837, 169
Rosdahl J., Teyssier R., 2015, MNRAS, 449, 4380
Rosdahl J., Blaizot J., Aubert D., Stranex T., Teyssier R., 2013, MNRAS, 436, 2188
Rosdahl J., Schaye J., Dubois Y., Kimm T., Teyssier R., 2017, MNRAS, 466, 11
Rosdahl J., et al., 2018, MNRAS, 479, 994
Rosen A., Bregman J. N., 1995, ApJ, 440, 634
Sanchez N. N., Werk J. K., Tremmel M., Pontzen A., Christensen C., Quinn T., Cruz A., 2019, ApJ, 882, 8
Scalo J., Elmegreen B. G., 2004, ARA&A, 42, 275
Schaye J., et al., 2015, MNRAS, 446, 521
Schmidt W., Niemeyer J. C., Hillebrandt W., 2006, A&A, 450, 265
Schroetter I., et al., 2021, MNRAS, 506, 1355
Semenov V. A., Kravtsov A. V., Gnedin N. Y., 2016, ApJ, 826, 200
Shen S., Madau P., Guedes J., Mayer L., Prochaska J. X., Wadsley J., 2013, ApJ, 765, 89
Silk J., Mamon G. A., 2012, Research in Astronomy and Astrophysics, 12, 917
Silk J., Rees M. J., 1998, A&A, 331, L1
Smagorinsky J., 1963, Monthly Weather Review, 91, 99
Somerville R. S., Davé R., 2015, ARA&A, 53, 51
Stanway E. R., Eldridge J. J., 2018, MNRAS, 479, 75
Suresh J., Rubin K. H. R., Kannan R., Werk J. K., Hernquist L., Vogelsberger M., 2017, MNRAS, 465, 2966
Tchernyshyov K., et al., 2022, ApJ, 927, 147
Teyssier R., 2002, A&A, 385, 337
Teyssier R., 2010, RAMSES: A new N-body and hydrodynamical code (ascl:1011.007)
Teyssier R., Pontzen A., Dubois Y., Read J. I., 2013, MNRAS, 429, 3068
Thornton K., Gaudlitz M., Janka H. T., Steinmetz M., 1998, ApJ, 500, 95
Truelove J. K., Klein R. I., McKee C. F., Holliman John H. I., Howell L. H., Greenough J. A., 1997, ApJ, 489, L179
Tumlinson J., et al., 2011, Science, 334, 948
Tumlinson J., Peeples M. S., Werk J. K., 2017, ARA&A, 55, 389
Tweed D., Devriendt J., Blaizot J., Colombi S., Slyz A., 2009, A&A, 506, 647
Van Rossum G., Drake Jr F. L., 1995, Python reference manual. Centrum voor Wiskunde en Informatica Amsterdam
Werk J. K., Prochaska J. X., Thom C., Tumlinson J., Tripp T. M., O'Meara J. M., Peeples M. S., 2013, ApJS, 204, 17
Werk J. K., et al., 2014, ApJ, 792, 8
Wilde M. C., et al., 2021, ApJ, 912, 9
Williams J. P., McKee C. F., 1997, ApJ, 476, 166
van Dokkum P., Conroy C., Villaume A., Brodie J., Romanowsky A. J., 2017, ApJ, 841, 68
van de Voort F., Springel V., Mandelker N., van den Bosch F. C., Pakmor R., 2019, MNRAS, 482, L85

This paper has been typeset from a TEX/LATEX file prepared by the author.

5.4 High resolution simulations

In this section, we test how converged the simulations from 5.3 are by comparing them to higher resolution simulations which were run with one more level of refinement. As explained earlier, this comparison is only made for KI and KR. We show in Fig. 5.9 the star formation rate of KI and KR at 20.1 pc and 40.3 pc alongside the total stellar mass formed. We find that in KI, the SFR is almost constantly slightly higher at a higher resolution than in the fiducial simulation. In KR, the SFR seems similar at both resolutions up to redshift $z \sim 2$, after which the SFR of the higher resolution simulation becomes constantly a few times higher than the fiducial simulation. In the end, increasing the resolution leads to higher stellar mass formed in both simulations. In KI, the effect is relatively small (increase by a factor ~ 1.3) while in KR, the stellar mass is increased by a factor ~ 1.6 with resolution. In the idealised simulations, KI was well converged with resolution while the stellar mass in KR was increasing with the resolution, as we see here. In the idealised simulation, we found that this higher star formation rate was actually due to less efficient feedback.

We show in Fig. 5.10 the temperature-density phase diagrams of the four simulations studied in this section. When increasing the resolution, we find that the phase of the gas at high densities tends to be at higher densities than in the fiducial simulations, and slightly colder in the case of KI. This is due to gas being able to concentrate in smaller cells when the resolution is higher, leading to more cells at high density. This leads to a medium more prone to star formation and an increased stellar mass formed. We also find in the gas density distribution that at higher resolution, there is a smaller fraction of cold dense gas with KR. This gas was likely turned into stars at higher resolution. Concerning the hot phase, while there is not much difference in KI (the gas is only slightly hotter), the gas reaches lower densities at higher resolutions in KR. Finally, at higher resolution, the phase diagrams of KI and KR also look closer to each other than at lower resolution. This can also be seen with the density distribution, as the fraction of hot gas increases in KR, bringing it closer to KI_HR while KR is dominated by its cold gas content.

We now compute the column density of the four ions H I, Mg II, C IV and O VI, and show them as a function of impact parameter in Fig. 5.11. For the cold tracers, KI and KI_HR show very similar results, while KR exhibits a drop in column density significantly sharper than KR_HR, going from a match with observations slightly better than KI to a slightly worse match. In the CGM, the plateau is one dex lower in KR than for the three other simulations, but only in H I, and not in Mg II. This is because H I is not impacted by the metallicity of the gas but solely by its amount, and we have shown in Sec. 5.3 that KR has a small fraction of gas in the CGM while KI exhibits a fraction almost six times higher there. For warmer gas, traced by C IV and O VI, there is a slightly larger difference between KI and KI_HR, in the first few kiloparsecs, but both remain very similar in the CGM. We find the same feature in O VI. In KR, we find the same difference as with KI in C IV, although a difference arises at large radii. However, it is of a significantly greater extent in O VI. The higher resolution simulation exhibits column densities more than three times higher than the lower resolution simulation, which diminishes even more from $\sim$ 40 kpc. This difference brings the simulation with the KR model significantly

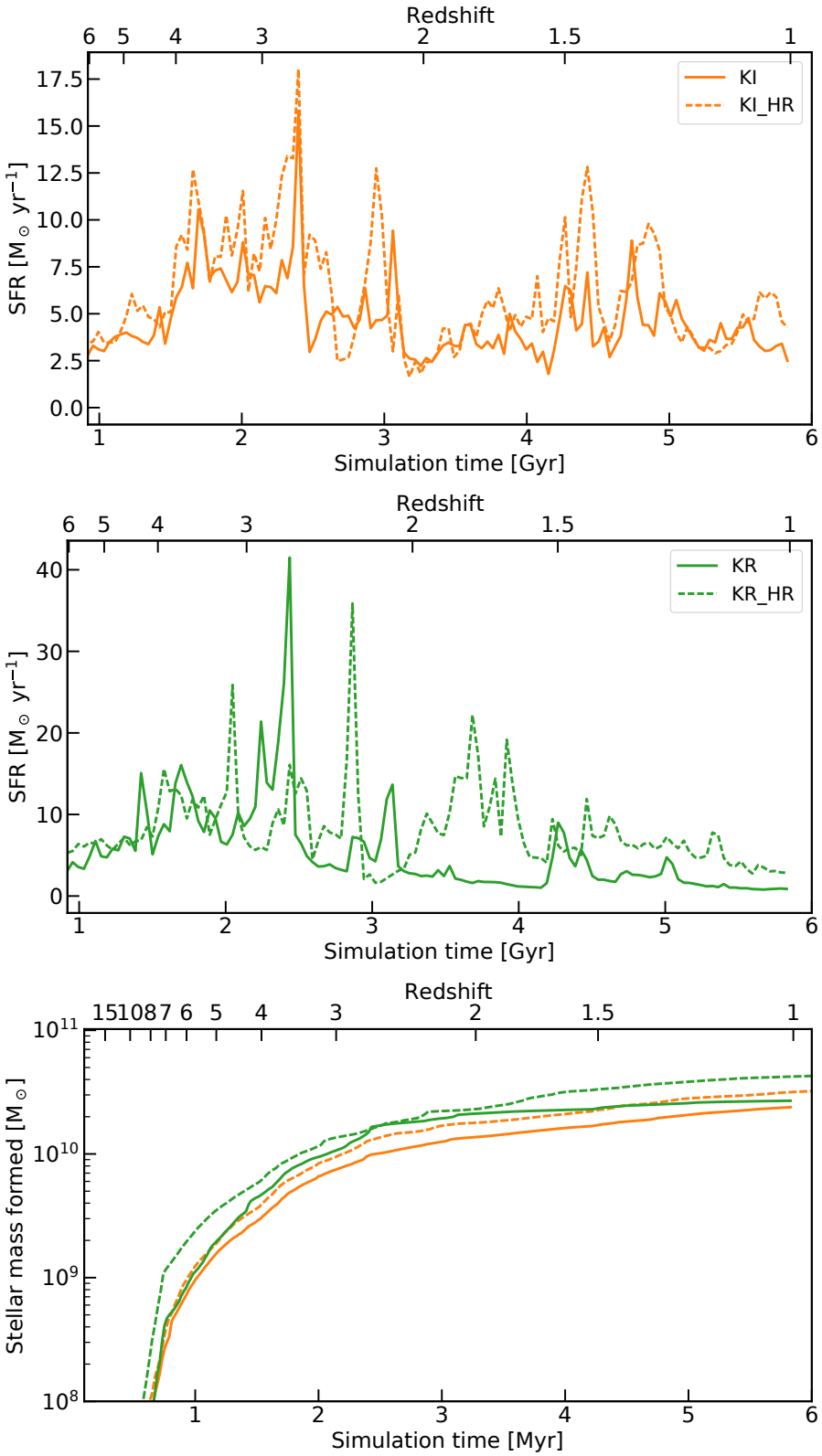

Figure 5.9 – SFR (upper and middle panel) and total stellar mass formed (lower panel) in cosmological simulations of galaxy formation made with KI (upper panel) and KR (middle panel) at resolutions of 20.1 pc and 40.3 pc.

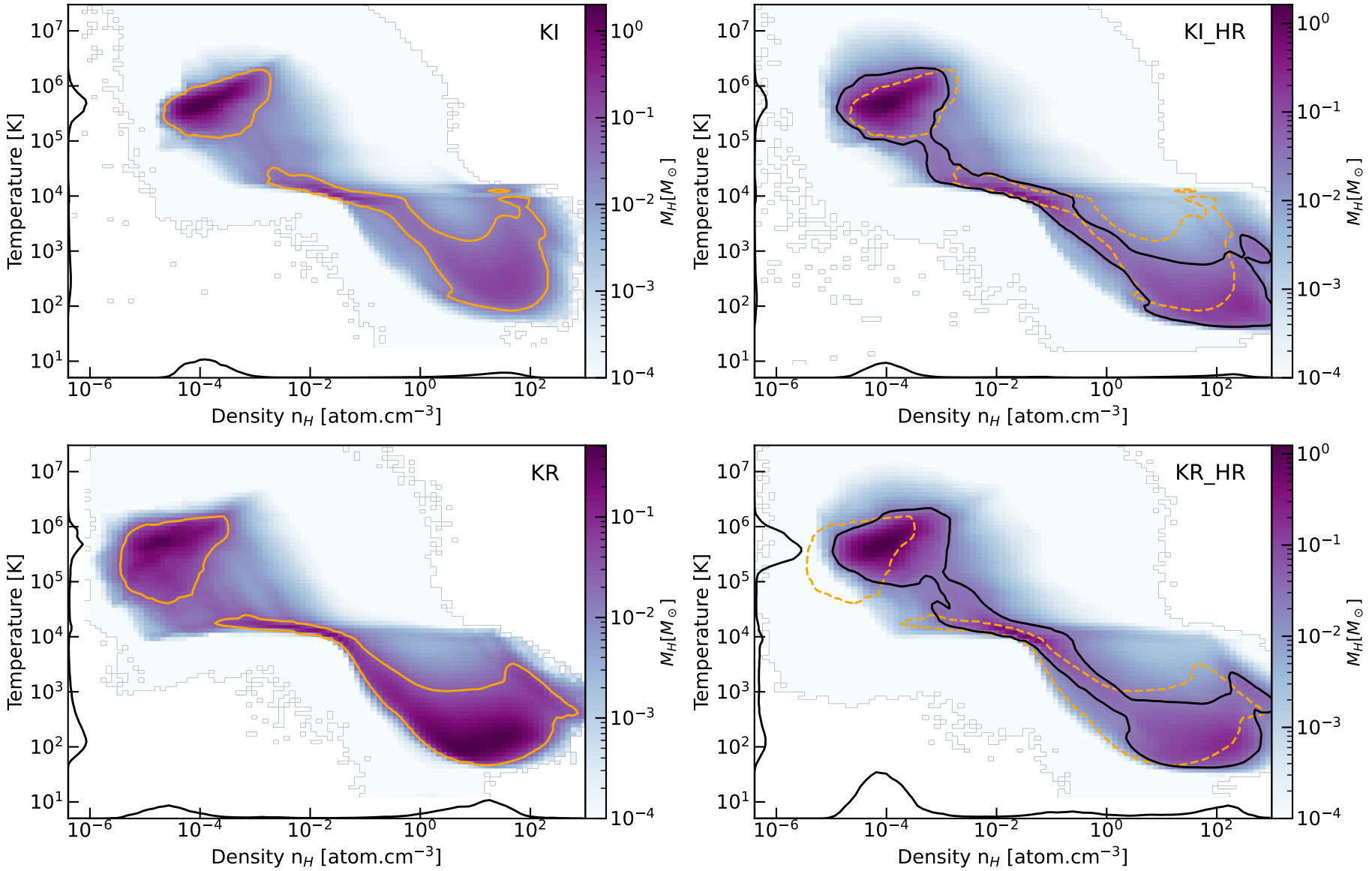

Figure 5.10 – [Phase diagram of KI and KR at fiducial resolution (left panels) and two times higher (right panels). We show a mass contour with a full blue or black line. The mass contour of the simulations without runaway stars (left panels) is reproduced as a dashed line on the phase diagrams of the simulations at higher resolutions (right panels).

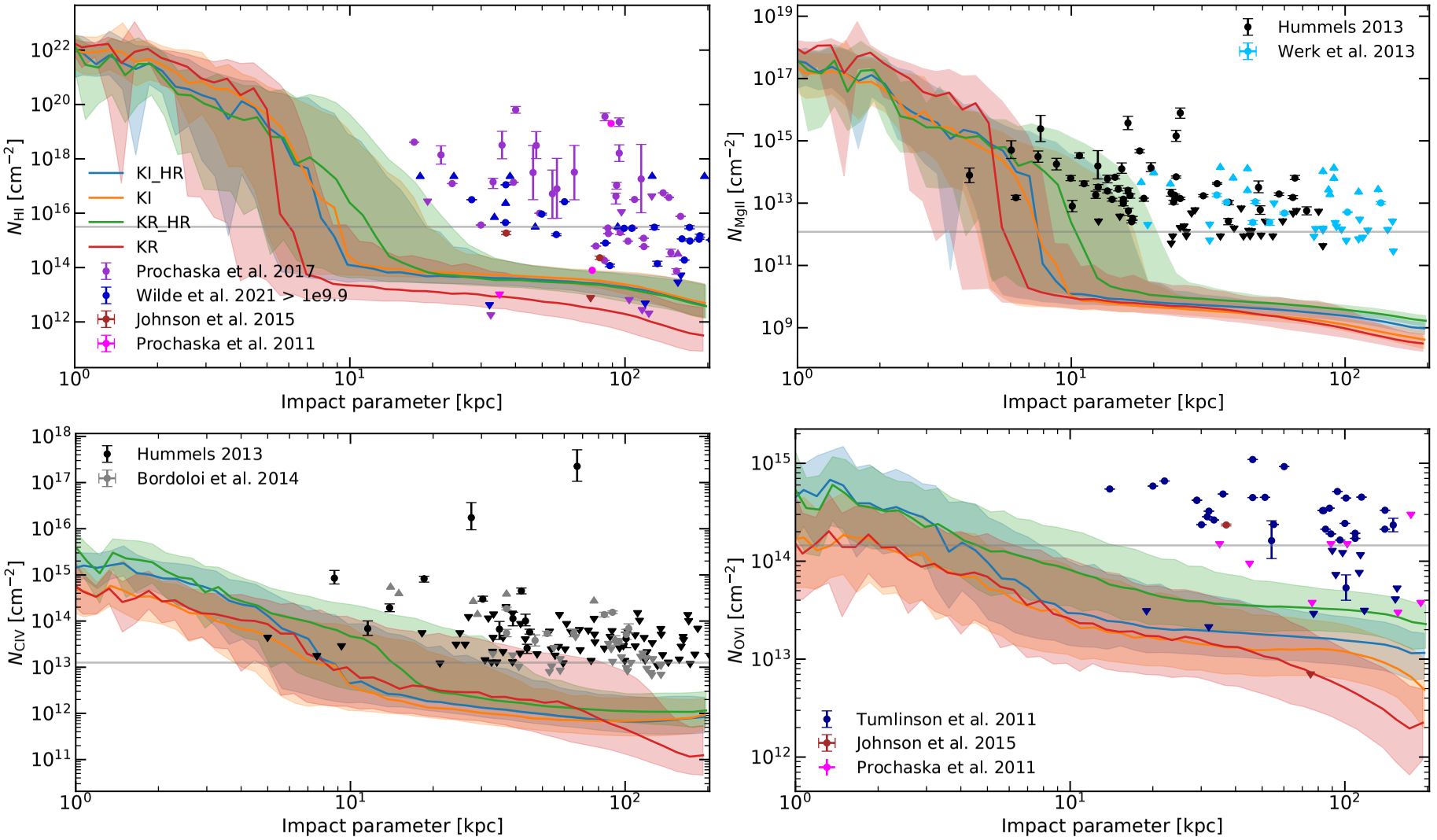

Figure 5.11 – Column density for KI and KR at fiducial and high resolution as a function of radius for H I (top left), Mg II (top right), C IV (bottom left) and O VI (bottom right). The simulated data is shown in full line, with the shaded area denoting the 15.9 and 84.1 percentiles. Galaxy-selected observational points are shown by different markers for different references. Upward-pointing arrows denote lower limits and downwards-pointing arrows denote upper limits.

closer to observations. A last point is that in O VI, both KI_HR and KR_HR exhibit column densities three times higher than their lower resolution counterpart, but that KI_HR shows the typical drop in column density while in KR_HR it is of a significantly smaller extent. This potentially shows that in this case, KR_HR exhibits outflows pushing gas more efficiently further out of the galaxy than KI_HR (since outflows are traced by hot gas).

To conclude, we find that changing the resolution impacts the SFR of both KI and KR, and eventually leads to a slightly higher stellar mass formed. The phase diagrams are close to each other in KI while there are slightly more distinct in KR with gas being slightly denser for both the hot and cold phases. KI also exhibits slightly colder and denser gas at high densities, which is expected due to a direct effect of an increased simulation resolution. In KI, increasing the resolution does not change the column density, and the model globally exhibits an overall good convergence. In KR, increasing the resolution significantly impacts the sharpness of the column density drop for all ions, and leads to the presence of higher column densities in hot gas traced by O VI, where the difference can reach more than a factor of three. Anyhow, both models still fail to reproduce CGM observations at large radii, even at higher resolution (Sec. 5.3).

5.5 Runaway stars

We now show our results on the inclusion of runaway stars with KI. Fig. 5.12 shows the impact of runaway stars on the SFR and total stellar mass formed with KI at two resolutions. We find that at both fiducial and higher resolution the SFR is not highly impacted by the presence of not of runaway stars, being sometimes both slightly above and slightly below the simulation without runaway stars. We confirm in the bottom panel of Fig. 5.12 that these slight variations only lead to a small difference in total stellar mass and that the simulations with and without runaway stars have the same stellar mass at $z = 1$. The negligible impact from runaway stars is opposed to the results from (Andersson et al., 2020), where idealised simulations with runaway stars produced more powerful outflows and lower stellar masses.

As runaway stars can travel out of their birth cloud before exploding as a supernova, one could expect to find hotter gas when they are included in the simulations. However, when comparing the temperature-density phase diagrams, we find that including runaway stars does not change the gas content of the galaxy for both the fiducial and the high-resolution simulations, showing that this model does not affect much the medium in which they explode.

We then compare the column density of the four ions H I, Mg II, C IV and O VI in Fig. 5.13. For the cold tracers H I and Mg II, we find an opposite effect from the inclusion of runaway stars at *low* and at *high* resolution. At low resolution, including runaway stars slightly increase the column densities, shifting the column density drop to the right, while it is shifted towards the galaxy centre at higher resolution. For tracers of warmer gas, we find that including runaway stars does not induce any difference in column density, the shift seen being due to the higher resolution as explained in the previous section.

To conclude, we find that unlike what was found in idealised galaxy formation simulations, including runaway stars in our simulations with the model from KI does

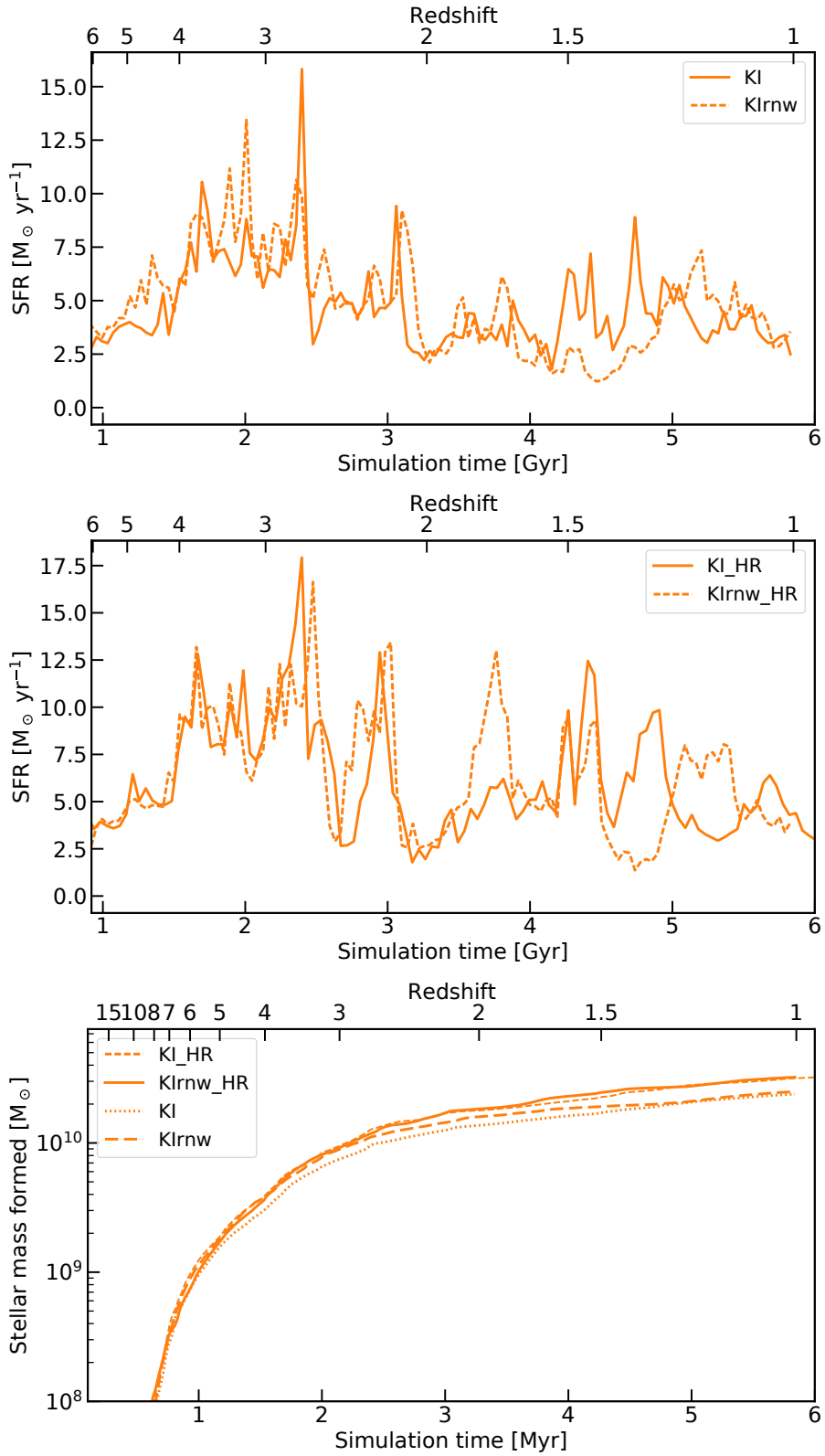

Figure 5.12 – SFR (upper and middle panel) and total stellar mass formed (lower panel) of cosmological simulations of galaxy formation made with KI (upper panel) and KI_HR (middle panel) with and without runaway stars.

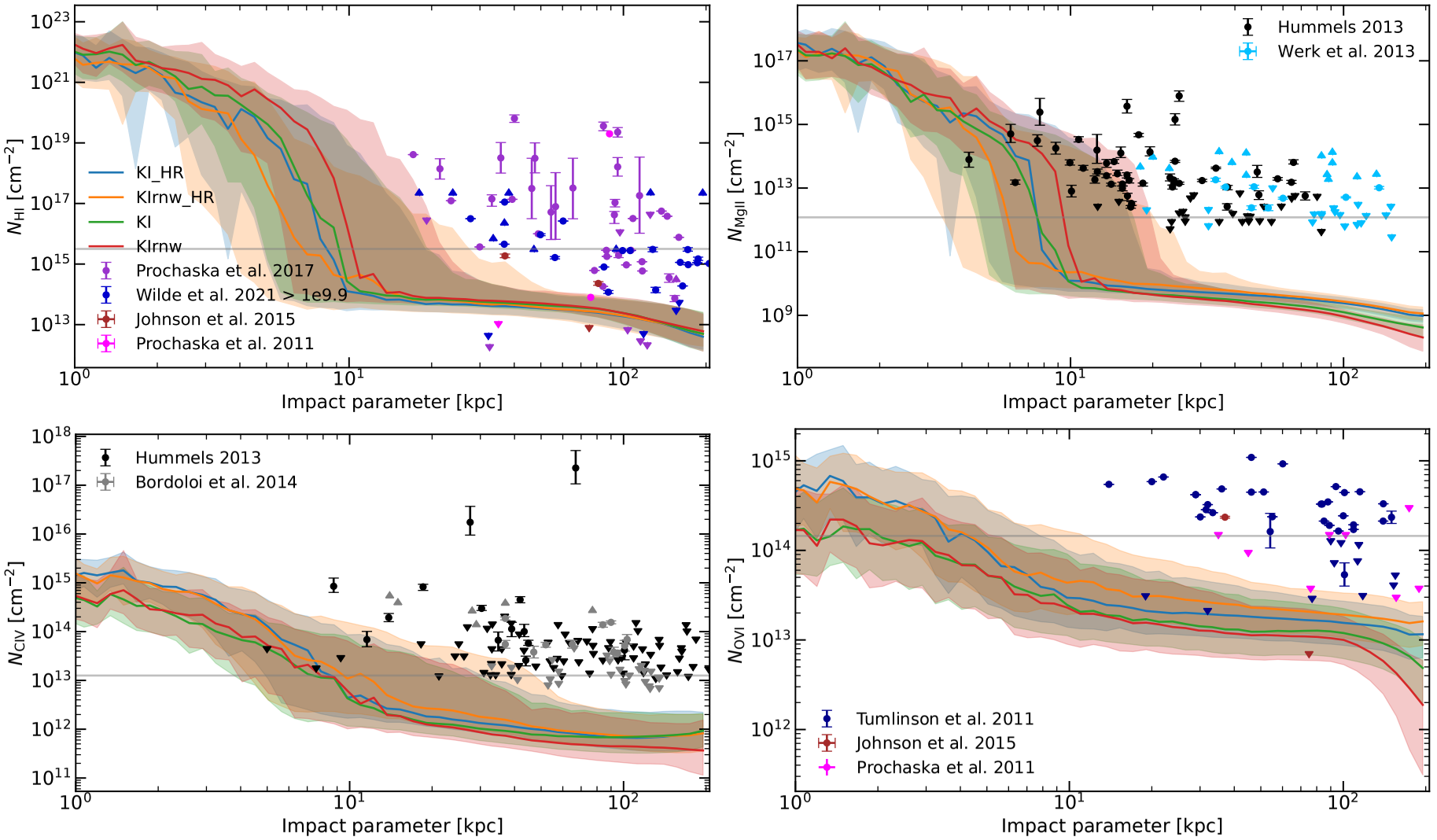

Figure 5.13 – Column density for KI with and without runaway stars as a function of radius for H I (top left), Mg II (top right), C IV (bottom left) and O VI (bottom right). The simulated data is shown in full line, with the shaded area denoting the 15.9 and 84.1 percentiles. Galaxy-selected observational points are shown by different markers for different references. Upward-pointing arrows denote lower limits and downwards-pointing arrows denote upper limits.

not produce any noticeable difference in the stellar mass of simulated galaxies. A puzzling effect is the opposite effect of runaway stars on cold gas at low and at high resolution. However, this only affects the galaxy and not its CGM, so we do not investigate this effect further. The absence of impact from runaway stars on warm gas in the CGM shows how they are unable to affect feedback in our simulations. As runaway stars moving away from their birth cloud is similar to reducing the density of their surrounding, the effect can be compared to that of pre-SN feedback. In this sense, the lack of impact from runaway stars might come from the fact that we use different subgrid models or the inclusion of RT in our simulations, which was not present in Andersson et al. (2020). RT in the form of radiation pressure already diminishes the density of the medium in which stellar particles reside in KI without runaway stars and making them move away further from their birth clouds leads to a less notable difference. Also, the cosmological context impacts greatly the dynamics of the galaxy, which might considerably minimise the effect of runaway stars as the evolution of the galaxy is overall much more pronounced.

5.6 Conclusion on the zoom simulations

We summarise here our main results on the cosmological zoom-in simulations of galaxy formation. We first used initial conditions for a relatively isolated galaxy. This led to a divergence of the different models studied, with KI and AG still being converged but KR ending with a stellar mass $\sim$1 dex higher than both of them. This shows clearly the underlying degeneracy there is between different subgrid models, as these models can be calibrated in stellar mass for a given galaxy but still produce a different stellar mass for another galaxy. The cause of this difference is likely more complex than just a difference in the energy injected, as changing the equations or boosting the supernova rate in KR did not have an impact big enough to compensate for this discrepancy. Anyhow, in this case, it was likely due to this galaxy having a peculiar environment.

We then ran simulations of a less isolated galaxy and found that AG could not be run in a realistic amount of time due to a higher computational cost than the other models, and instead compared KI and KR against DC. We found that there is a bimodality in the simulated column densities, with a trend at higher values matching observations and most points plateauing at a lower value. This effect is of a lower extent for higher ions and results in a median profile well described by an exponential law combined with a plateau. Also, almost none of the median column densities of the simulations match the observations. Each model exhibits too low column densities, except for KR, which seems to produce too much C IV. This mismatch might be effectively explained by outflows inefficient in pushing gas out of the galaxy or an incorrect ionisation fraction. Indeed, outflows might not push enough gas enriched in metals out of the galaxies for KI and KR, as we find that the metal content of DC is $\sim$ 1 dex higher in the CGM (this is what causes DC to produce higher column densities). Also, the discrepancy between observations and simulations might stem from an incorrect ionisation fraction. This could be explained by an inaccurate temperature modelling, potentially due to a lack of resolution in the CGM. Finally, we find that modelling the CGM through quasar absorption lines is a very powerful approach to break the degeneracy between different subgrid models,

complementary to the stellar mass to halo mass relation.

We also tried to include runaway stars in our simulations with a velocity kick model which should lead to bigger differences than found in Andersson et al. (2020) but found that they had almost no impact on neither the mass of the galaxy formed nor on its gas content nor the column density found in its CGM. This is likely due to the inclusion in our simulation of the cosmological context alongside radiative transfer, which plays a similar role to runaway stars by reducing the density around stellar particles.

We also tested the convergence of the models of KI and KR and found a similar gaseous content and a satisfying convergence in stellar mass for both models, albeit slightly higher at higher resolution. KI exhibits a very good convergence regarding simulated column density for all ions studied, while the drop in column densities shifts with resolution in KR. Also, the hot gas content traced by O VI is increased by a factor higher than three at high resolution with KR.

Chapter 6

Auxiliary results and open questions

In the previous section, we simulated the formation of galaxies using different subgrid models and calibrated them in mass. We then confirmed that the CGM can be an efficient tool to break the degeneracy between subgrid models, but also found that there was a discrepancy between simulated and observed column densities for almost all models. We started to investigate this matter and found that there might be two reasons for this mismatch. The first is that in two of the three simulated galaxies, the outflows are not efficient enough in pushing gas far out of the galaxy and enriching it in metals. The other is that the thermal state of the CGM might be inaccurately modelled. In this section, we extend the analysis of our simulations (KI, KR, and DC) by comparing other properties of the simulated galaxies. We first look at the burstiness of the simulated galaxies and the processes that drive star formation (gravitational instability or turbulent compression). Then, we compare the morphological properties of the simulated galaxies and compare them to results from Kretschmer et al. (2020). Finally, we investigate how the metal content of the CGM evolves with time by comparing covering fractions.

6.1 Star formation processes

During the analysis of the three first simulations for the paper presented in Sec. 5.3 (the high-resolution simulations of KI, KR, and KI_rnw), we found that the burstiness of the galaxies simulated with different models was disparate. While the shape of the star formation rate history was extremely similar in the three simulations, KR exhibited significantly more numerous bursts of star formation. We thus investigated the origin of this difference. These results were initially obtained to be published alongside the paper from Sec. 5.3 and were thus made with KI, KR, and DC.

6.1.1 A different burstiness

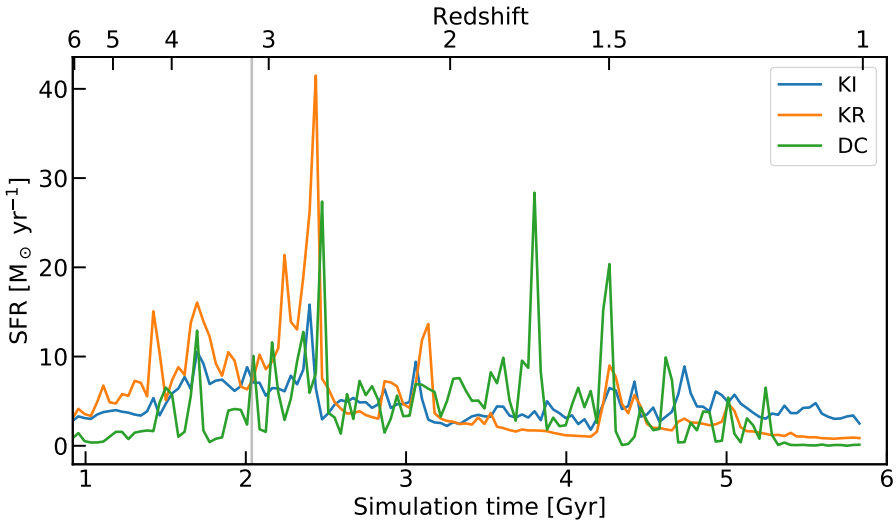

Figure 6.1 – Star formation rate for each of the three simulations: KI, KR and DC. KI is less bursty than KR and DC, which is significantly different from both other models. The vertical grey line shows the time at which simulations were restarted to survey the environment of star formation sites.

Fig. 6.1 shows the star formation history for KI, KR, and DC. We show that the simulation KR is significantly more bursty than the KI simulation, with numerous and intense peaks of star formation, in particular at high redshift. The simulation DC also shows a bursty star formation history, with bursts even in the later stages of the galaxy evolution ($z < 2$), when the SFR of the two other simulations becomes smoother. We investigate below the origin of these differences.

Each simulation has a minimal mass for stellar particles of $M_{\rm init} = 3200$ M$_\odot$. Depending on the medium where star formation occurs, the mass of the stellar particle created can be higher than this minimum value, massive star particles thus trace intense events of star formation. On the one hand, the KI simulation mainly forms stars of $M_{\rm init} = 3200$ M$_\odot$, up to $\sim 54 M_{\rm init}$. On the other hand, both the KR and the DC simulations have a significant proportion of more massive stars, with a maximum stellar particle mass of $\sim 358 M_{\rm init}$. In order to access the conditions in which such stars are formed, we re-ran both simulations from redshift 3.09 where

all simulations have a similar SFR (vertical grey line in Fig. 6.1) up until $\sim 2 \times 10^4$ stellar particles were formed. This corresponds to $\sim$ 6 Myr for KI and KR and $\sim$ 32 Myr for DC. From this, we saved properties such as the Mach number $\mathcal{M}$, the virial parameter $\alpha_{\rm vir}$, the local density n_H and the star formation efficiency $\epsilon_{\rm ff}$.

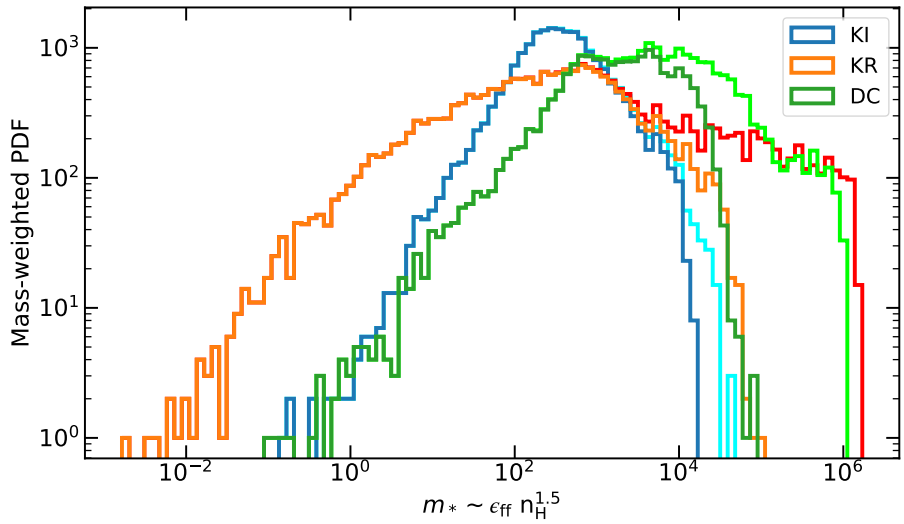

Figure 6.2 – Mass-weighted probability density function of the estimate of the stellar mass formed as described per Eq. 6.1. The three colours represent the three models and the second colour for each model represents the more massive stellar particles of the simulations (cyan for blue, orange for red, and light-green for green).

The mass of the star formed in a cell can be roughly described by

$$m_* \propto \epsilon_{\rm ff} \frac{\Delta t}{t_{\rm ff}} m_{\rm cell} \propto \epsilon_{\rm ff} n_H^{1.5} \Delta x^3 \Delta t, \tag{6.1}$$

where Δt is the duration of the timestep (it is comparable in all simulations), $m_{\rm cell}$ the mass of gas in the cell, and n_H its density. By combining the star formation efficiency and density in each cell, we compute the estimated mass of stellar particles in each cell, as described in Eq. 6.1. We plot the result in Fig. 6.2. As expected, from what we described in the previous paragraph, we see that a considerable fraction of stellar particles are more massive in KR and DC than in KI. While in KR and DC the estimated masses reach more than 10^6 $M_\odot$, in KI they do not present masses higher than 3×10^4 $M_\odot$. This difference means that despite the similar SFR values in the three runs, galaxies form stars very differently in the KI simulation compared to the KR and DC simulations. Looking at Eq. 6.1 and taking into account that star formation is restricted to the highest resolution level, we can deduce that the difference in the mass of the stellar particles formed originate either in the density of the host cell or in the star formation efficiency $\epsilon_{\rm ff}$.

6.1.2 The star formation rate efficiency

We first investigate the possibility of the star formation rate efficiency causing the difference in stellar masses formed. If it is indeed the cause of this discrepancy, it is either because the properties of the local star-forming regions are different,

or because the underlying models describing $\epsilon_{\rm ff}$ are different (the KI/DC and KR simulations are respectively relying on models from PN11 and KM05).

Properties of the star-forming regions

We can first analyse the local properties of the media influencing $\epsilon_{\rm ff}$, namely the Mach number and the virial parameter. The virial parameter is the ratio of the kinetic energy of the cell to its gravitational potential. Thus, a high virial parameter means higher kinetic energy and more dispersion in the cloud. On the contrary, a low virial parameter denotes a more gravitationally bound cloud, which favours star formation. The Mach number describes the compressibility of the fluid and a higher Mach number implies stronger and denser local compressions and consequently, more star formation but also more resistance to gravity as it leads to a higher $\lambda_{\rm J,turb}$ and a higher $s_{\rm crit}$ (see Eqs. 3.7, 3.10 and 3.15).

We show the probability density function of both of these quantities in the upper and middle panels of Fig. 6.3. We see that star formation happens in very different conditions in the KI and DC simulations compared to the KR simulation. In the KR simulation, star formation sites are strongly supersonic with $\overline{\mathcal{M}} \sim 45$[1]. The star formation there is thus completely due to turbulent compression. For KI and DC, star formation happens in a mildly turbulent media, with respectively 49% and 64% of the stellar mass formed in a supersonic state and 33% and 42% of the mass is gravitationally unstable in the sense that $\alpha_{\rm vir} < 1$. We also find that a large proportion of star-forming gas is subsonic.

We show the star formation efficiency in the bottom panel of Fig. 6.3 which is a combination of $\overline{\mathcal{M}}$ and $\alpha_{\rm vir}$. We see that even though the differences between KI and DC compared to KR are striking in the Mach number and the virial parameter as star formation is driven by distinct processes, the resulting star formation efficiency is relatively close (although both the shape and the position of the peak are different).

PN11 or KM05

We can then compare the impact of the underlying model (PN11 or KM05) to the impact of the turbulent state of the gas by comparing both the equations of each model and the outputted $\mathcal{M}$ and $\alpha_{\rm vir}$. We first consider the simulated values of $\mathcal{M}$ and $\alpha_{\rm vir}$ from the KI and KR simulations and compute the corresponding $\epsilon_{\rm ff}$ with each underlying model. We find in this case that the values from KI are systematically higher and also mainly concentrated towards the maximal ones, while KR presents a more bell-shape profile (as we can see in the bottom panel of Fig. 6.3). We then test the opposite approach and compute $\epsilon_{\rm ff}$ with both PN11 and KM05 using the data from KI and then iterate using the data from KR. In both cases, we find that PN11 produces slightly higher star formation efficiencies than KM05. The same result is found by taking the ratio of both $\epsilon_{\rm ff,PN11}$ and $\epsilon_{\rm ff,KM05}$. At high efficiency (high Mach number or low virial parameter) the values from PN11 are slightly above those from KM05 and the lower the efficiency, the bigger the difference between both models.

[1]Following Larson's law (σ km s^{-1} = 1.1L$^{0.38}$ pc, Larson, 1981), we expect a velocity dispersion of $\sigma \sim 4.5$ for a cloud size of $L = 40$ pc. However, in the molecular clouds from the KR models, from $T \sim 10^2$ K and $\mathcal{M} \sim 100$, we obtain $\sigma \sim 100$km s^{-1}. The results of KR thus seem unrealistic.

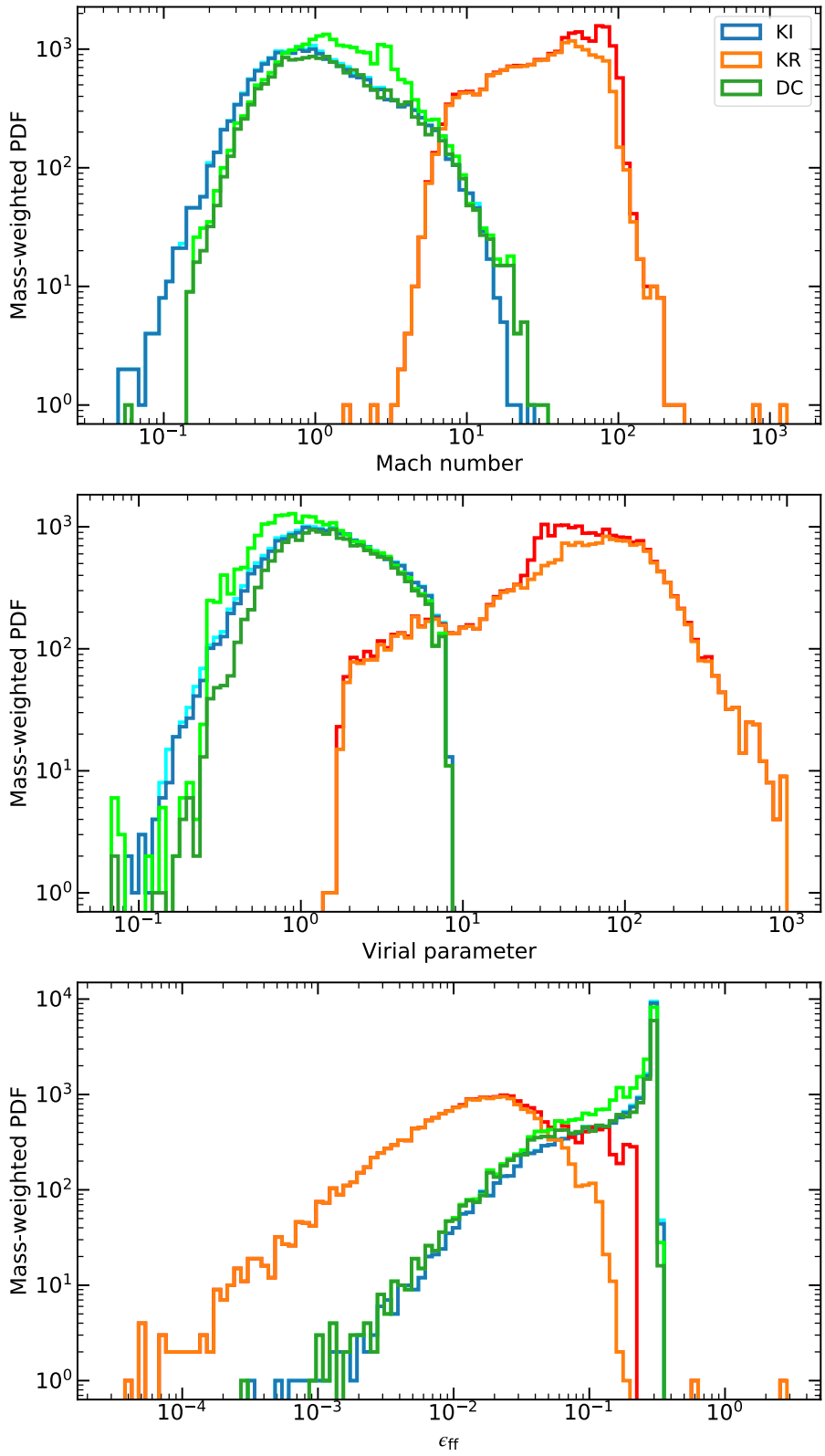

Figure 6.3 – Mass-weighted probability density functions at the sites of star formation at redshift $z = 3.09$. We show the Mach number (top), the virial parameter (middle panel) and the star formation rate efficiency (bottom) as defined by Eq. 3.6. The colour code is the same as in Fig. 6.2.

To sum up, the star formation efficiency $\epsilon_{\rm ff}$ is higher in KI than in KR and is mainly concentrated at the highest values of the distribution. This is mainly due to the local properties of the media and slightly enhanced by the different underlying models used. This is thus not what causes the burstiness of the simulations.

6.1.3 The density of star formation sites

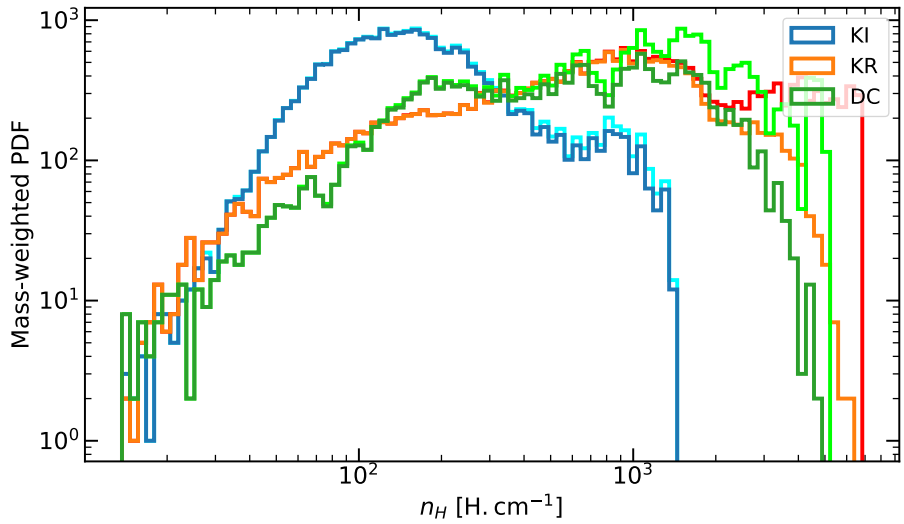

Figure 6.4 – Mass-weighted probability density function of the density of the cell in which stars form. The colour code is the same as in Fig. 6.2

This higher efficiency in KI could seem surprising as the simulation producing the most massive stars is KR, but a hint that the origin of the burstiness actually lies elsewhere. We show the density of the cells at which the stellar particles are formed in Fig. 6.4. We find that the densities reached are higher in KR and DC than in KI with a significant proportion of cells higher than 10^3 cm^{-3}. The high end of the PDF resembles closely what is found in Fig. 6.2, making high densities the main ingredient to form massive stars.

One of the origins of these high-density regions has been hypothesised to be merger events which lead to high-density cells (Kretschmer & Teyssier, 2020). However, the initial conditions are the same for both simulations, it should then also happen in KI. Furthermore, even though peaks are earlier for KR, DC presents bursts of star formation at all times, even at low redshift when mergers are rarer. As both KI and DC simulations rely on the same star formation subgrid model and DC reaches higher densities, this implies that the origin of lower densities in KI does not lie in the star formation subgrid model but in the feedback subgrid model.

Short summary

We attempted to understand the burstiness produced in each of the simulated galaxies and found that it is traced by the massive stellar particles. We investigated the local properties of the star-forming gas and found two interesting results. The first is that even though the total mass of stars is similar in the three simulations,

the process driving their formation can be very different. In KR, star formation is turbulence-driven, with all star formation sites in a highly supersonic turbulent state ($\overline{\mathcal{M}} \sim 45$), while in KI and DC, roughly half of them are subsonic and with a low virial parameter (gravitationally bound), leading to gravitation-driven star formation. This is due to the modelling of turbulence in both approaches for star formation, which impacts both the Mach number and the virial parameter. The second result is that for KR and DC, some stars form in regions of very high density ($n_{\rm H} > 10^3$ cm^{-3}). The existence of these high-density regions is tied to the feedback models. KI efficiently disrupts molecular clouds before they reach catastrophic densities, while KR and DC generate runaway structures which cause intense bursts and favour the formation of more massive and more numerous massive particles. These particles represent 2% of the particles in KI, 7% in KR and 15% in DC (it is higher in DC since they form in both a denser medium and with higher efficiency). As there are significantly fewer high-resolution stellar particles in DC than in the other simulations, this results in an overall lower star formation rate at non-bursty epochs.

6.2 Morphology

An important difference we found amongst the simulations is that the morphology of the galaxies was different depending on the subgrid models used, possibly showing another major impact they can have on the galaxies formed. We focus here on the difference in morphology between KI and KR. These results are particularly interesting as Kretschmer et al. (2020) found that the origin of extended thin discs in galaxies depended on the direction of gas accretion relative to the disc rotation, while we do not reach similar conclusions.

6.2.1 A difference in morphology

We show in the upper panels of Fig. 6.5 the morphology of the high-resolution galaxies simulated with KI, KR, and KI_rnw at $z = 1$[2]. There are a few differences we can note. The first and most notable difference is that KR exhibits very smooth and extended arcs located in a more diffuse environment than in KI and KI_rnw. These arcs are distinct from the galaxy and are additionally in a different plane than the galaxy. Focusing on the denser part of the simulations, KI_rnw presents the most extended dense structure with well-defined arms, populated by small clumps. KI has a similar core but less defined arms which seem to begin to fall and merge with the core, as well as a more diffuse environment than KI_rnw. Conversely, KR exhibits a smaller core with almost indistinguishable arms nearly merged with it. We thus see how KR is significantly different in morphology from KI and KI_rnw.

Although a slightly smaller core is found for KR at $z = 1$, all three simulations are very similar at z$\sim$1.5 and this feature is not present down to z$\sim$1.3. At this point in time, all models are in a state similar to KI_rnw with a small core and elongated clump-rich arms going out from it. While retaining a similar maximal

[2]As we compare our results to Kretschmer et al. (2020), we follow the same colour scheme as their paper for the figures in this section.

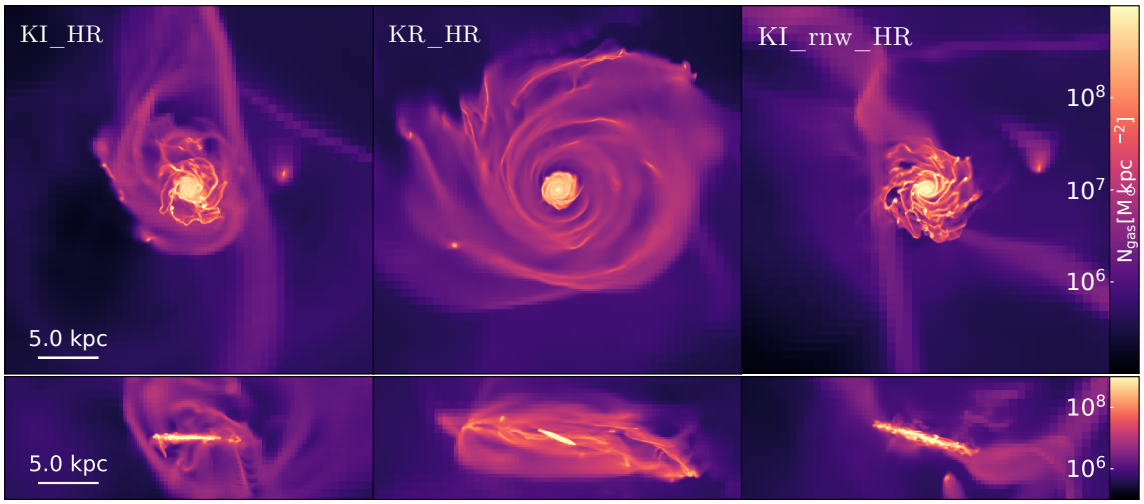

Figure 6.5 – Face-on and edge-on column density maps of hydrogen at $z = 1$. From left to right, we show KI, KR, and KI_rnw. We see with these figures how KR forms an extended gaseous disc, while the galaxy is more compact in KI and KI_rnw. We use scales and colour schemes following those from Kretschmer et al. (2020).

central density, the densest part of the core in KR got smaller much more rapidly than the other two models, producing a very small core at z∼1.0 with arms almost indiscernible from it. At the same time, unlike KI and KI_rnw where the satellites fell on the galaxy quite quickly and fuelled it by merging with its extended arms, the accretion in KR took longer, not going directly onto the galaxy but following a circular motion, and forming arcs rotating around it. Those eventually produce a flatter density profile reaching 10^{-2} $n_H cm^{-3}$ at a radius of 11 kpc, while the same value is reached at approximately 6 kpc for both KI and KI_rnw simulations. The three simulations match up in density at a distance of 14.5 kpc from the centre.

It might seem that KI_rnw correspond to the earliest stages of this morphological evolution with the galaxy still possessing well-defined arms and that KI is at a later stage with its arms starting to merge with its core. If this was indeed the case, we could expect KI and KI_rnw to match KR evolution later on. It would mean that, somehow, either this model accelerates the morphological evolution of the galaxy or that both KI and KI_rnw slow it down. Both KI and KR were run down to redshift $z \sim 0.78$. Yet, KI did not exhibit signs of large arcs forming, showing that being at a different evolutionary stage is not the explanation for the morphological difference.

Another explanation for this difference might lie in the stochasticity of such simulations. Indeed, ICs with the same models can lead to slightly different galaxy environments and merger histories. In our simulations, KI and KI_rnw are very similar in essence, and we do not expect their difference to significantly alter the trajectory of a galaxy. Nonetheless, we find that the satellites in KI and KI_rnw are not all coming from exactly the same direction. We can note from the bottom panels of Fig. 6.5 that both KR and KI_rnw are tilted compared to KI when looking at them edge-on. The small differences due to stochasticity lead to slightly different incidence angles, which in turn lead to a different orientation of the resulting merged

galaxy. This is thus a side effect due to the stochasticity of the simulations and not directly dependent on the model (Genel et al., 2019; Keller et al., 2019). As this difference seems to arise from the speed at which satellites are merged with the central galaxy, this hypothesis might be a possible solution. However, the direction from which satellites fall is relatively similar among simulations, even though it can be delayed and exhibit a slightly different trajectory. This is unlikely the cause as these extended arms are only seen in KR among our simulations and no sign of such evolution is seen in the other two simulations. It thus seems to come from the subgrid model.

6.2.2 Comparison to Kretschmer et al. (2020)

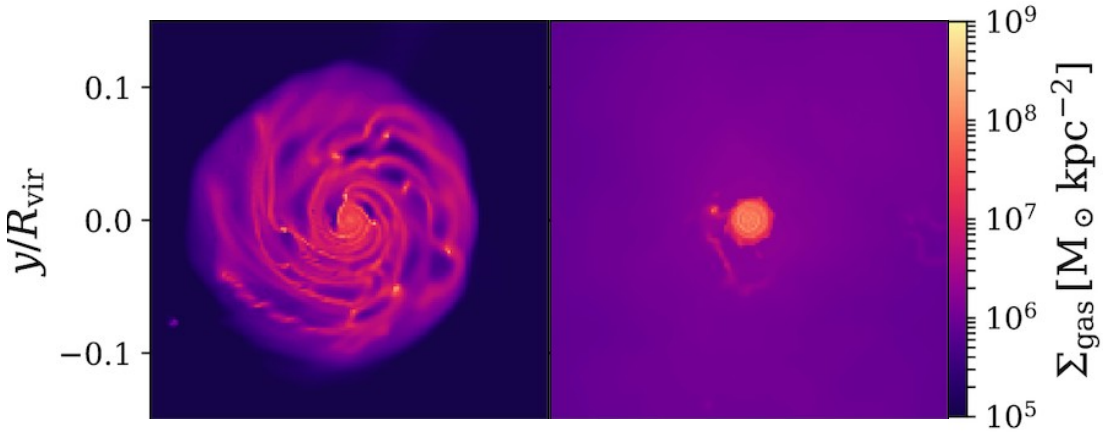

Figure 6.6 – Maps of the gas surface density of a disc-dominated and a bulge-dominated galaxy in (Kretschmer et al., 2020) at $z = 0$.

This behaviour resembles strongly the epoch of the *Grand Twirl* that is mentioned in Kretschmer et al. (2020). In this paper, the authors investigate how elliptical galaxies or razor-thin spiral galaxies are formed with the same feedback model. They simulate the formation of two galaxies, which we show in Fig. 6.6. They are referred to as a *disc-dominated* (left panel) and a *bulge-dominated* (right panel) galaxies. In their work, they notice a rapid disc growth of these two simulations, with their respective gas half-mass radius doubling in less than a Gyr from redshift $z \sim 1.5$. Then, while the bulge-dominated one contracts down to ~ 2 kpc, the size of the disc-dominated one keeps on increasing and reaches 10 kpc at $z = 0$. In the disc-dominated galaxy, a similar extended thin disc formed around the galaxy whereas the other is more compact. The origin of the difference comes from their accretion history, adding angular momentum either constructively or destructively.

In the simulations presented here, when considering the same criterion for the half-mass radius as Kretschmer et al. (2020) (gas within 0.1 R_{200} and T lower than 5×10^4 K), there is no epoch during which such growth is seen for any of the galaxies as the temperature threshold it too strict. Nonetheless, when removing the temperature criterion, the gas half-mass radius in KR indeed experiences a sudden growth from 1.5 kpc to 4.5 kpc in nearly 400 Myr near redshift $z = 1$. Although it is similar in nature, this expansion begins later in our simulation ($z = 1$ against $z = 2$), and is faster (the gas half mass radius is tripled in less than 400 Myr against

a doubled size in 750 Myr in Kretschmer et al. (2020), and is of lower extent. Additionally, unlike what is found in Kretschmer et al. (2020), there is no stellar mass increase similar to the gas mass in our galaxies and maps of the stellar particles highlight no difference between the three models.

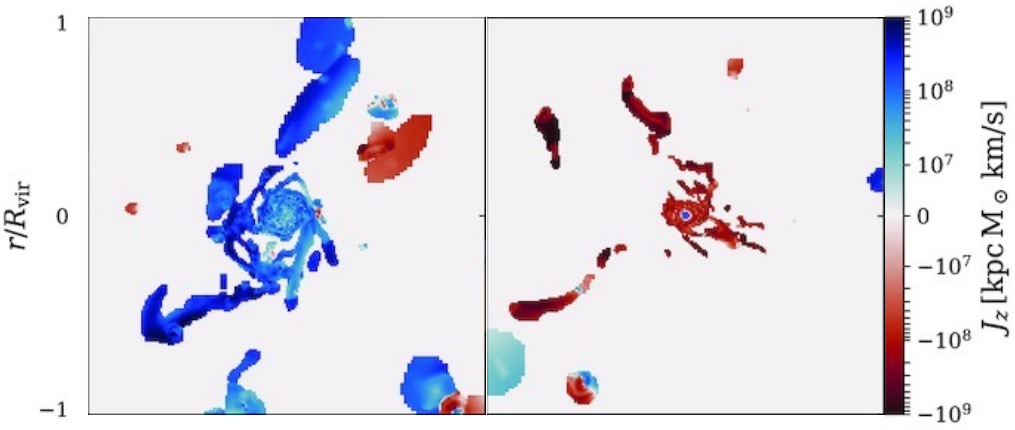

Figure 6.7 – Angular momentum of cold gas for both the disc-dominated and the bulge-dominated galaxies in Kretschmer et al. (2020) at $z \sim 1$. The one with corotating (or *additive*) accretion of gas leads to an extended thin disc, while the one with counterrotating (or *destructive*) accretion of gas leads to a compact galaxy. We use scales and colour schemes following those from Kretschmer et al. (2020).

The origin of this difference in Kretschmer et al. (2020) is explained by how the gas accretes from satellites onto the galaxy. We show in Fig. 6.7 the component of the orbital angular momentum[3] along the rotational axis of the cold gas of the disc-dominated (left panel) and the bulge-dominated (right panel) galaxy. Their main result is twofold. On the one hand, the gas was accreted constructively in the disc-dominated galaxy and formed an extended gas disc, as we can see in the left panel of Fig. 6.7 with both the galaxy and the satellites having the same angular momentum. On the other hand, as we can see with the galaxy having an angular momentum opposite to that of the satellites, gas is accreted destructively in the bulge-dominated galaxy, ripping off the gas of a potentially extended structure.

Following their approach, we plot in Fig. 6.8 the component of the angular momentum along the rotational axis of the galaxy for cold gas in our three simulations. We find that in KR, the external gas disc is counter-rotating compared to the central part of the galaxy. Following the angular momentum hypothesis from Kretschmer et al. (2020), we can expect to form a *bulge dominated* galaxy in which gas accreted destructively. However, we form a disc-dominated galaxy. Furthermore, the three simulations should exhibit a comparable accretion history. Thus, if this morphological difference was due to how satellites accrete, it should have been reflected in all three simulations, which is not the case. As both KI and KI_rnw are very similar in their modelling and do not present this feature, this might be a hint for the extended disc being formed due to the different subgrid models used in KR. However, these results only rely on three simulations and more of them would be needed to confirm this effect.

[3]The orbital angular momentum is similar to the momentum (i.e. a conserved quantity) for a rotation. It is defined as $\mathbf{L} = \mathbf{r} \times \mathbf{p}$, with $\mathbf{p} = m\mathbf{v}$ the linear momentum.

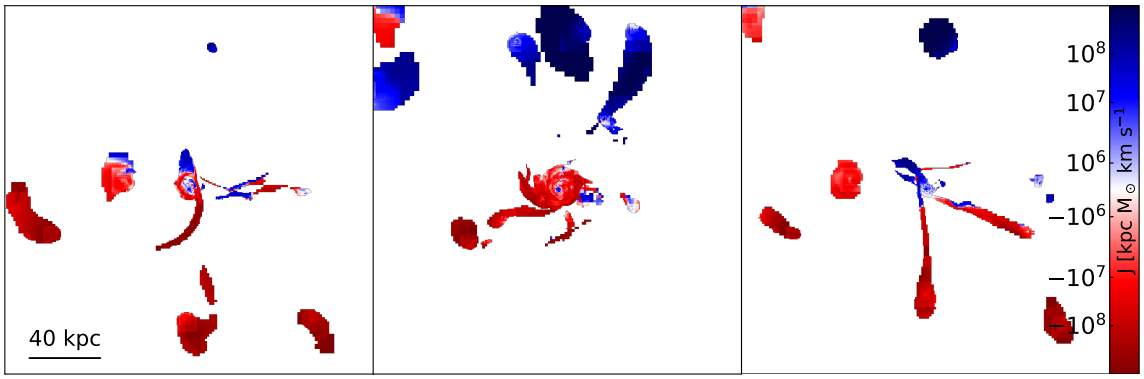

Figure 6.8 – Angular momentum of cold gas in KI_HR, KR_HR, and KI_rnw_HR. While KI and KI_rnw show both additive and destructive accretion, the disc surrounding the central part of KR exhibits a counter-rotating disc relative to its core. In Kretschmer et al. (2020), this is expected to lead to galaxies with compact morphologies.

6.2.3 Leads for further investigation

Finding a correlation between the morphology of the galaxy and the angular momentum of accreted gas contrary to what is found in Kretschmer et al. (2020) is intriguing, but sadly, we did not have enough time to investigate this effect. We present in the next paragraphs two approaches that may be able to bring about a better understanding of this discrepancy.

Similar resolution

The resolution in Kretschmer et al. (2020) reaches at best 55 pc, while our simulations have a maximal resolution of 20.1 pc. We thus also apply this comparison to our lower resolution simulation of the same galaxies ($\Delta x = 40.3$ pc). We show in Fig. 6.9 the same plots as previously. The upper panels show the morphology of the three galaxies, and the lower panels show their angular momentum. In these simulations, all three galaxies show similar morphology to that seen in KI or KI_rnw at higher resolution with well-defined arms and traces of merging satellites, albeit somewhat larger. Interestingly, KR shows no sign of an extended thin disc and surroundings with lower column densities than the other two simulations. This possibly reveals that the surrounding media is accreted much faster in KR, but a more in-depth study is needed to conclude. Also, we do not notice a significant amount of counter-rotating gas, accreting gas instead showing signs of additive accretion. It nonetheless does not lead to an extended structure. Seeing that this effect is not present at lower resolution shows how sensitive the thin extended gaseous must be to the environment.

Toomre parameter

An interesting quantity to further analyse this phenomenon is the Toomre stability criterion (or Safronov–Toomre criterion). This parameter describes the disc stability and is more adapted to differentially rotating galaxies than the Jeans stability

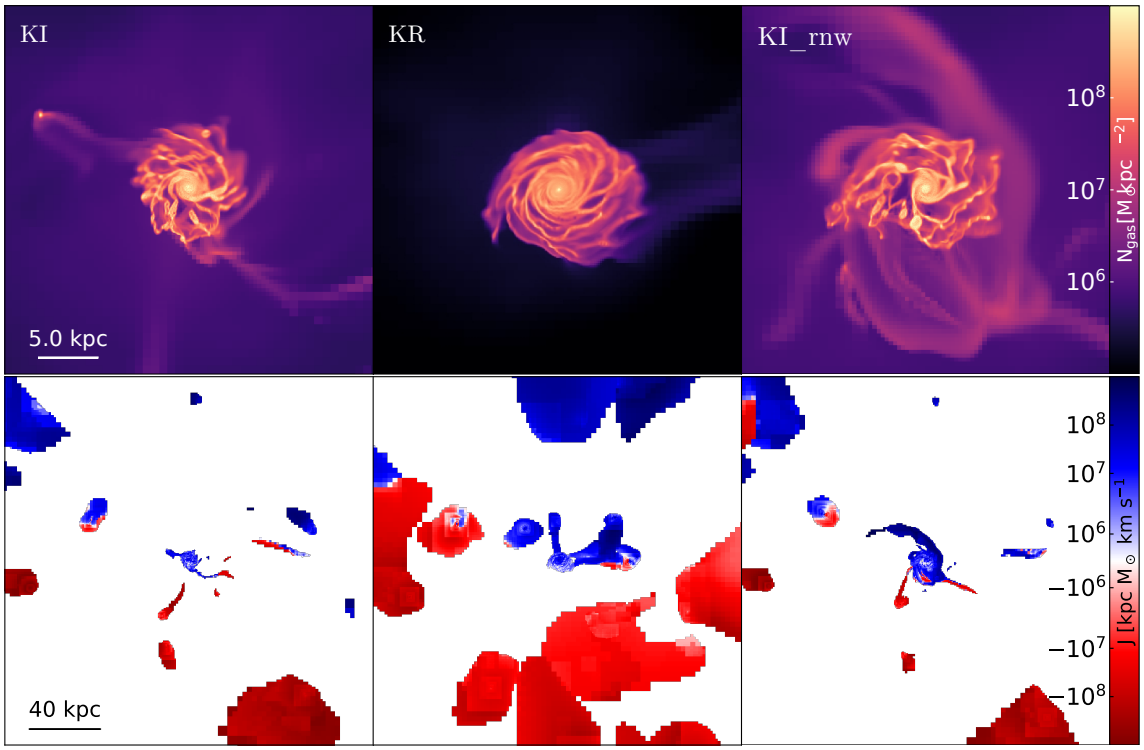

Figure 6.9 – Face-on column density maps of hydrogen (upper panels) and angular momentum of cold gas (lower panels) in simulations with a resolution of 40.3 pc at redshift $z = 1$. From left to right, we show KI, KR, and KI_rnw. We see in these figures that the morphology of the galaxies is now very similar to the three models, looking like KI or KI_rnw at a higher resolution but slightly more extended. All angular momentum maps show signs of additive accretion.

criterion since it also evaluates how the shear force can increase the disc stability (Jeans' criterion only considers internal pressure and gravity). For a disc, the Toomre stability criterion is given by (Toomre, 1964)

$$Q = \frac{\kappa c_s}{\pi G \Sigma}, \tag{6.2}$$

with Σ the surface density of the disk and κ the epicyclic frequency. The disc is stable if $Q > 1$, and this criterion could help us understand why this morphological difference arises.

6.3 Time evolution of the metal content

When first computing covering fractions, we ran different tests to assess which parameters impacted our measures and found that the covering fractions of O VI decreased with time. We first detail in this section the ionisation fractions of oxygen in the CGM of our simulations. We then show how the simulated covering fractions evolve with time and what we can learn from them.

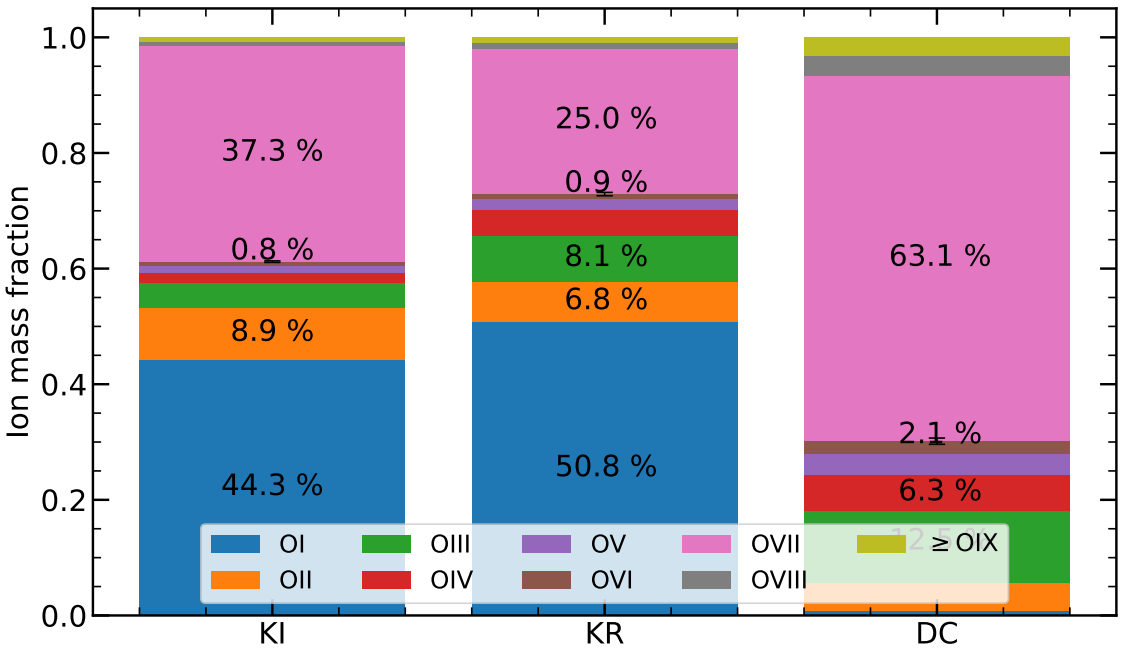

Figure 6.10 – Ionisation fractions of oxygen for KI, KR, and DC, averaged over 1 Gyr at a regular interval of 10 Myr. The values are taken between 0.3 R_{200} and R_{200}. Each colour represents an ionisation state, and O VI is shown in brown.

6.3.1 The fraction of O VI in the CGM

Before investigating the ionisation state of the CGM against impact parameter, through column densities or covering fractions, we considered the ionisation state of the CGM as a whole for oxygen, following the approach made in (Oppenheimer et al., 2016). We show in Fig. 6.10 the fraction of each oxygen ionisation state.

The first striking result is that O VI represents a tiny fraction of the oxygen content in all simulations, while there is a significant amount of O VII. Thus, as argued in Sec. 5.3, if the hotter part of the CGM was at a slightly lower temperature, the simulated column densities could provide a much better match to observations.

Also, we have seen in chapter 5 that the metal content in DC is higher than in KI and KR, but the fraction of O VI is also twice higher. This is thus also one of the causes of the higher column densities we find for DC. Interestingly, the ionisation states of oxygen in DC are remarkably distinct from that of KI and KR. While KI and KR both have $45 - 50\%$ of oxygen in the ground state, there is almost none in DC. Conversely, while there is 63.1% of gas in O VII in DC, there is only $25 - 37\%$ in KI and KR. This shows how, in DC, the gas in the CGM is in a much hotter state than in KI and KR. The significantly higher fraction of cold gas in KI and KR however raises new questions, as we could expect to also find significantly higher column densities in KI and KR with cold gas tracers. An interesting follow-up of these results would thus be to make the same computations for hydrogen, magnesium, and carbon.

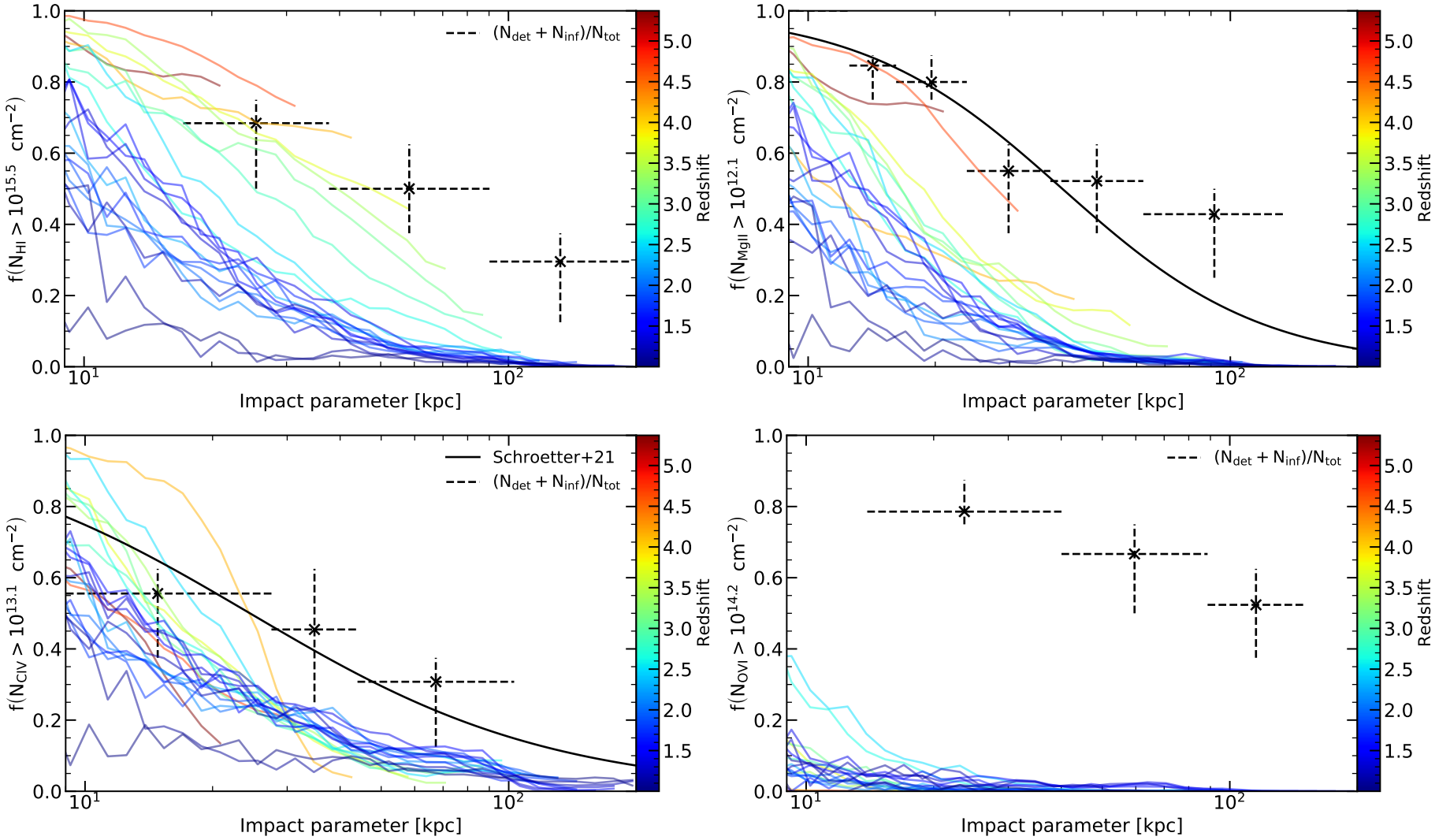

Figure 6.11 – Evolution of the covering fraction as a function of impact parameter through time in KI. We show the covering fraction of H I (top left), Mg II (top right), C IV (bottom left) and O VI (bottom right). Each line corresponds to a single timestep and the colour code depends on the corresponding time. We use a time incrementation of $z \sim 0.1$ from $z = 1$ up to $z \sim .1$ between each line. At higher redshift, the timesteps are more irregularly spaced as we have fewer simulation snapshots.

6.3.2 The decrease of the covering fractions

We now show in Fig. 6.11 the covering fraction evolution with time. This is computed in KI (the results are similar to the other models), for the same four ions as previously, but using single timesteps (they were stacked over 1 Gyr in chapter 5). We find here that for the cold and warm gas, the covering fractions are significantly higher at higher redshift, and decrease steadily with time to reach their lowest values at our lower redshift, $z = 1$. The lines at high redshift are less extended in radius than those at lower redshift because the computation domain of the sightlines extends to 2 R_{vir}, which is significantly lower at high redshift.

For H I and Mg II, this decrease is highly pronounced, with covering fractions matching with observations at redshift higher than $z = 3 - 4$, and likely at all radii (the covering fractions we show do not seem to exhibit a drop). Similarly, C IV also shows a good agreement with observations at higher redshift, but only up to $20 - 30$ kpc, and decreases sharply afterwards. This once again shows how C IV traces different phases of the gas than H I or Mg II even though a part of it traces gas at similar temperatures. Conversely, O VI shows no such evolution, being significantly low at all times.

6.3.3 A shorter timeframe

We now focus on the timeframe $z = 1.3 - 1$ as we have significantly more snapshots and show in Fig. 6.12 the same figure as previously, restricted to this timeframe. We do not show Mg II and C IV as they produce the same result as H I. The results are similar for KR and DC, and we also additionally adopt a lower column density threshold for O VI to increase the covering fractions computed and accentuate the change in covering fractions observed as a function of time. We now see that this is also the case for O VI. It was just not noticeable in the previous figure, as the covering fractions were too low.

One could interpret that this shows that there is less and less cold gas in the CGM as it is supplanted by hot gas. With time, the covering fraction of O VI can thus be expected to increase, as it traces enriched hot gas ejected from supernovae, but these plots point in the opposite direction. There is also a decrease in O VI column densities. Different processes could lead to this decrease. One of them is cosmic expansion, which dilutes the CGM content. However, the change in covering fraction is larger between redshift $z = 1.3$ and $z = 1$ than between redshift $z \sim 5$ and redshift $z = 1.3$, while the surfaces expanded respectively by a factor 1.7 and 15. Another option could be that the gas is being pushed further than the CGM by outflows. This hypothesis is not that unlikely, as we find hints in our simulations that gas is being pushed further away than the virial radius.

6.3.4 The evolution of the ionisation fractions

In Fig. 6.13, we now show the same plot as Fig. 6.10, but instead of averaging the results over time, we only show it at $z = 1.3$ and $z = 1$. We see here that this decrease in the O VI covering fraction is actually due to a change in the whole gas content of the CGM. In KI and KR, the fraction of all ionised states of oxygen is halved between $z = 1.3$ and $z = 1$, resulting in a much higher fraction of oxygen in

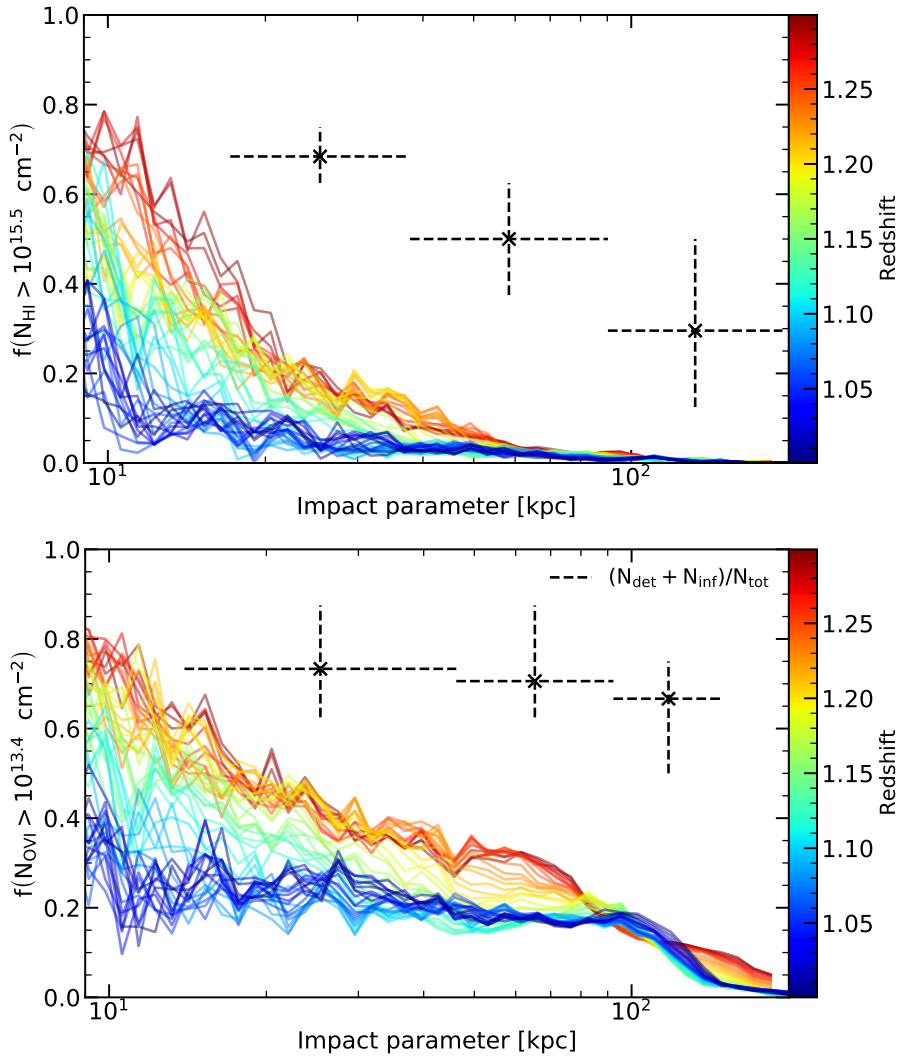

Figure 6.12 – Evolution of the covering fraction as a function of impact parameter through time in KI. We show the covering fraction of H I (top panel) and O VI (lower panel). Each line corresponds to a single timestep and the colour code depends on the corresponding time, sampling uniformly $z = 1.3 - 1$. We also use a lower column density threshold of $N_{\mathrm{O\,VI}} = 2.24 \times 10^{13}$ cm^{-2} for O VI in order to make evolution with time more visible.

the ground state. This means that either the hot gas has been cooled down without being replaced or that cold inflows recently brought more gas than hot outflows in the CGM. The behaviour of DC is different from that of KI and KR as the fraction increasing is not the ground state, but O VII. Indeed, most of O VIII and O IX decrease, but the CGM remains hot enough to keep most of the oxygen in O VII. The oxygen states strictly below O VI also decrease, going from 30% of the oxygen mass to 20%. This thus favours the hypothesis of a CGM that slightly cooled down, but due to cooling and not mixing with cold inflows, as the cold content does not increase at all.

An important point that Fig. 6.13 raises is that, as we can see in Fig. 6.1, the star formation rate of all simulations is very steady after redshift $z = 1.5$. Thus,

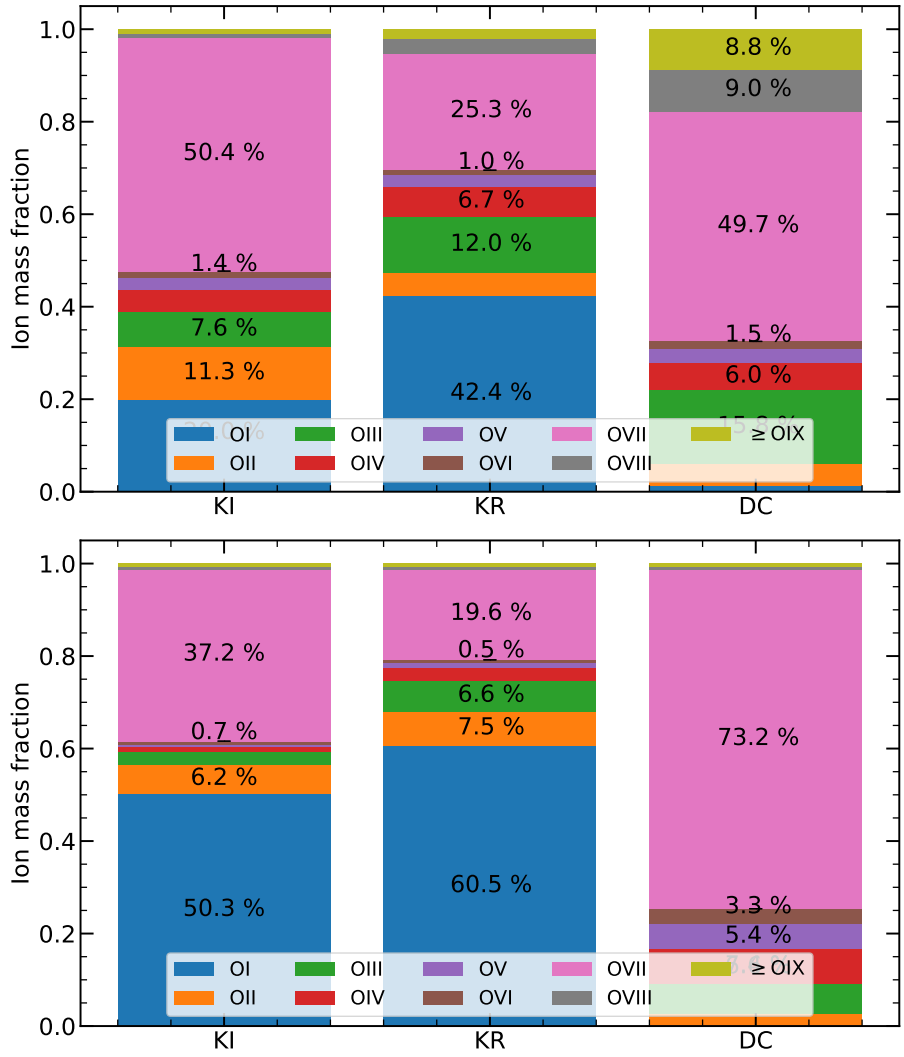

Figure 6.13 – Ionisation fractions of oxygen for KI, KR, and DC at $z = 1.3$ and $z = 1$. The values are taken between 0.3 R_{200} and R_{200}. Each colour represents an ionisation state, and O VI is shown in brown.

this decline could show that with the star formation being low, there are not enough supernovae to sustain the hot gas content of the CGM, and this leads to decreasing ionisation fractions of the ionised states of oxygen with time. As galaxy formation simulations often form too many stars compared to the semi-empirical stellar mass to halo mass relation, these preliminary results might highlight that these models form too many stars *at early times*. To continue such an investigation, it would be very interesting to compute column densities and covering fractions at higher redshift (we only have a few snapshots of the simulations at these times) and find how these measures correlate with star formation.

However, note that these results are preliminary and have not been investigated in much depth yet. For example, if we consider the O VI covering fraction of DC with the lower column density threshold (we remind that this results in covering fractions at unity up until $\sim$ 70 kpc), we see an increase in covering fraction with time further than $\sim$ 70 kpc, going from 0.7 to 0.95. This increase is increasingly

high with radius, as the covering fraction is initially lower at a higher radius (it is almost constantly at unity up to ~ 70 kpc for DC with a changed density threshold). This could show that hot gas is ejected out of the galaxy, increasing the covering fractions at large radii but lowering them at lower radii.

6.3.5 Comparison to observations

These preliminary results match with what is found in observations from Schroetter et al. (2021) (they only select strong absorbers), in the sense that we also find that Mg II decrease with redshift. However, unlike our results, these authors find no redshift evolution in C IV. We also remind that most of the observations we picked are at $z \lesssim 0.4$, while the lower redshift of our simulations is at $z = 1$. It would be interesting to run these simulations to lower redshift to find if the covering fractions keep on decreasing with time and if it matches with what is found in observations. It would also be interesting to compare the redshift evolution of our different simulations, as the differences we find between KI or KR and DC could also be reflected in their evolution in time. This finding is very interesting and could help to shed light on the processes driving the CGM content by tracing what drives this redshift evolution. We sadly did not have enough time to pursue the investigation of this process.

Chapter 7

Conclusions and perspectives

In science, observations and theory always go hand in hand. In astrophysics, observations are generally made through telescopes observing relatively distant objects, while theory largely relies on numerical simulations. With the power of supercomputers, it is now possible to model complex processes involving non-linear equations described over a wide range of scales and by various physical phenomena. During the last three years, I have been given the opportunity to work on the fascinating topic of numerical simulations of galaxy formation, focusing on the comparison of star formation and stellar feedback subgrid models. In order to find a new way to raise the degeneracy that exists between models, I specifically simulated the measure of column densities in the CGM and compared them to observations. In this last chapter, I summarise the work I have done on this topic and the results that ensued. I finally conclude by presenting several ways in which this work could be extended.

7.1 Short summary

7.1.1 Numerical simulations of galaxy formation

In this thesis, we first introduce in chapter 1 our current understanding of galaxy formation. We also present one of the challenges of this description, which is to understand what regulates the baryon fraction in galaxy formation. After detailing how numerical simulations are crucial to increase our knowledge of such complex physics, we describe how they work in chapter 2. We then detail what idealised, and cosmological simulations are, and how we produce their initial conditions. We then present their content (dark matter and stellar particles, gas), their structures, and the equations which dictate their evolution. In chapter 3, we focus on the subgrid models necessary in numerical simulations of galaxy formation, specifically subgrid models for star formation and feedback modelling and define the models AG, KI, KI_rnww, KR, and DC that we use for our simulations.

In chapter 4, we first study idealised simulations. We begin by testing the parameters of the different subgrid models and how they impact the galaxy formed. Mainly, these changes impact the first burst of star formation, the strength of the outflows and the morphology of the galaxies. All of these changes could result in widely different galaxies, so we calibrate them in stellar mass while keeping the parameters as close to possible from their original implementation. In chapter 5, we first test a few parameters with an isolated galaxy (as it is faster to run) and test the convergence of the stellar mass of the galaxy with our different models. Due to the peculiar environment of this galaxy, the stellar mass did not converge, and we chose to simulate a second less isolated galaxy. With this more massive galaxy, the AG model which we used up to this point took too long to run. We thus removed it from the analysis and use instead the DC model. We then compared the simulations KI, KR, and DC by simulating the observations of column densities in their CGM as well as their covering fractions.

7.1.2 Main results

In section 5.3 we find that these models produce different observables and that they can indeed be used to break the degeneracy of subgrid models, hence answering the original question of my thesis. Additionally, we find that the column density profiles are well-defined by an exponential profile combined with a plateau. This profile includes a drop in column density near the disc edge which is larger, the lower the ionisation energy is. We also find that the simulated column densities are far below expectations from observations for all simulations and almost all the ions probed. After analysing the limits of our simulations and observations, we investigate the causes of this discrepancy and find two main sources. First, the metal content of the CGM is not the same in all simulations, which shows how certain models are less efficient in ejecting enriched gas in the CGM, either not pushing it far enough or pushing it too far. While the simulations with the larger discrepancy compared to observations have either a lot of gas at low metallicity (KI) or little gas content with very high metallicity (KR) and math each other, the third simulation (DC) exhibits a lot of gas with a high metallicity. Second, the ionisation fractions also differ from

one simulation to another, but in all simulations, there is a consequent reservoir of ions available at higher temperatures for all ions. While on average the O VI fraction is $1-2\%$ between $z=1.3$ and $z=1$, the O VII fraction is $25-63\%$ (this is similar for the other ions). This very low ionisation fraction in O VI might indicate how all simulations distribute gas in the wrong gas phase, being slightly too hot. Indeed, if the gas is too hot, it will excite atoms to higher ionisation states, and worsen the match between simulations and observations. This incorrect temperature could stem from a lack of resolution in the CGM, which leads to unphysical thermal mixing between unresolved cold gas clouds and hot gas, or simply incorrect modelling of the outflows.

We then explore other close topics such as the convergence of the simulations with resolution or the effect of the inclusion of runaway stars. While an increased resolution slightly increases the stellar mass in all simulations and leads to a higher fraction of hot gas in KR, including runaway stars has little effect.

In chapter 6, we extend our work and first study which processes lead to star formation. While the star formation model from KR is mainly driven by supersonic turbulence, star formation in KI is driven by both supersonic turbulence and gravitational instabilities. We also look at the gaseous morphology of the galaxy and find that with KR, the galaxy formed an extended disc, while with KI, the galaxy formed is more compact. Kretschmer et al. (2020) found that extended discs were caused by additive accretion from cosmic filaments, but we see no such correlation, and even find that an extended disc is formed with counter-rotating accretion. Surprisingly, neither the counter-rotating accretion nor the counter-rotating disc is found at higher resolution. Finally, we study how covering fractions evolve in time and how, by looking at the ionisation fractions of different elements in the CGM, we can learn about the processes driving the discrepancy between observed and simulated covering fractions. By doing so, we find that the covering fractions of all ions are decreasing with time and that it is likely due to the relatively calm late-time SFR of the galaxies as do not form enough stars to keep the CGM in a hot phase.

7.2 Perspectives

By confirming the power of quasar absorption lines to constrain numerical simulations, my work brings to light how the simulation of column densities in the CGM of galaxies is a new key step to calibrate simulations. It can be used to test subgrid models in the scope of galaxy formation simulations but also extends to the implementation of any supplementary physics which could affect the thermal state of the simulated galaxies. Resulting of this, there are many topics of research that are interesting to explore using column densities.

7.2.1 The origin of the column densities

The first topic which I would like to pursue is to determine precisely what causes the discrepancy between observed and simulated column densities by continuing the work presented here. I found that there are disparities between the metal content of the different galaxies simulated. As I found disparities both in the mass of gas in the CGM and its metal metallicity, this can presently be explained by either a differing

strength in the outflows expelling the disparate amount of gas, in a different metal enrichment or both. Investigating this in more depth could lead us to understand fully what drives the low column density of our simulations, and what could be improved in the modelling to produce galaxies closer to observations.

It would also be interesting to run simulations of galaxies with different stellar masses to quantify how much it impacts the observed column densities. Indeed, in the observations selected, we only performed a broad selection in galaxy mass as the samples are large, and it is unclear how much the observed column densities depend on the stellar mass of galaxies. While observations are few and limited by low statistics, a set of simulations of different masses could shed light on this dependency, and the processes leading to a given CGM thermal state.

7.2.2 An enhanced resolution

I found in my research that there is a bimodality in the simulated column densities. A fraction of the simulated sightlines matches observations, while most others plateau at lower values, an effect which is more notable for tracers of cold gas. This bimodality might explain the mismatch between observations and simulations, and I believe that the origin of this bimodality might lie in a lack of resolution in the CGM. Indeed, cold gas in the CGM is expected to be in the form of small clouds $\lesssim 100\,\mathrm{pc}$. As they are unresolved in our simulations, they evaporate through thermal mixing when going to lower resolution regions, and end up at higher temperatures. I would thus like to run an additional simulation of the same galaxy while resolving the CGM. By using an additional resolution criterion depending on the cooling length instead of only relying on density, the CGM could preserve the structure of cold gas further away from the galaxy and increase its proportion compared to unresolved simulations. Simulations with an improved resolution in the CGM point in the direction of increased cold content at higher resolution (Peeples et al., 2019; Hummels et al., 2019; van de Voort et al., 2019).

7.2.3 Complementary physics

Conversely, a second explanation for the mismatch might lie in gas not being expelled from the galaxy efficiently enough, as suggested by DC. This model showed a better match with observations thanks to a CGM richer in metals. Another project would thus be to include AGN feedback in my simulations, as they could increase $\mathrm{N_{O\,VI}}$ by 1.5 dex (Sanchez et al., 2019) and allow for a better agreement with observations while also regulating star formation. Indeed, AGN feedback can heat the galaxy gas to the temperature of the ionisation fraction peak of O VI ($10^{5.5-5.8}\,\mathrm{K}$) (Suresh et al., 2017) while enriching the CGM in metals (Nelson et al., 2018). Their flicker could also photoionise the CGM and increase $N_{\mathrm{O\,VI}}$.

Cosmic rays could also be very interesting as they would complement the role of AGN. Since AGN heat the galaxy, the realistic cold gas content of the simulated CGM can be expected to decrease. As cosmic rays can push colder gas in the outer parts of the galaxy (Salem et al., 2016), they could compensate for the expected effect of AGN feedback on cold gas and effectively lead to a population of cold clouds in the CGM.

7.2.4 A supplementary constraint from column densities

Finally, I would like to mention that another particularly interesting topic is to test the biconality of outflows in simulations through column densities. Observations show several hints of biconical outflows in galaxies such as the cigar galaxy NGC 3034 (or M82) or through Mg II column densities Zabl et al. (2019); Schroetter et al. (2019). If it is found, for example, that Mg II is preferentially located along the minor axis of the galaxies. Comparisons with simulation could consider that by studying absorption lines depending on their azimuthal angle. Such a comparison could help to determine potential observational biases. We show in Fig 7.1 an example with the fractions of cells with a column density above a given threshold, depending on their azimuthal angle. In this plot, we see that Mg II is preferentially along the minor and major axis, which can be interpreted as a trace of biconical outflows and/or preferential accretion of gas along the minor and major axis.

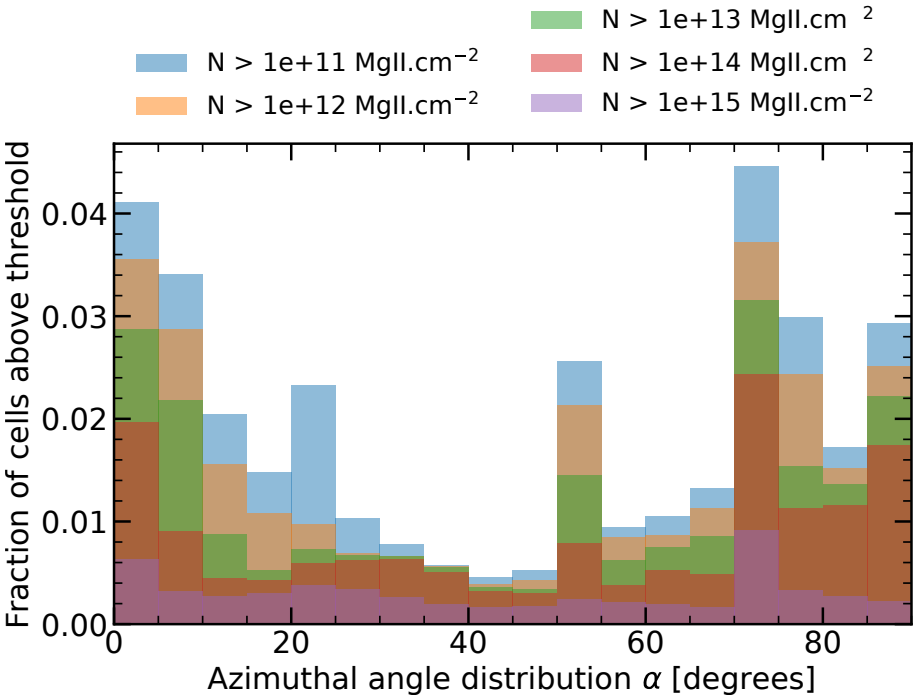

Figure 7.1 – Fraction of cells above a given threshold, depending on the azimuthal angle of the cell at redshift $z = 1$. We use five different thresholds, ranging from 10^{11} cm^{-2} to 10^{15} cm^{-2}. This effectively shows how cold gas is in this case preferentially along the minor and major axis.

Acknowledgments

These last years in Lyon were truly breathtaking, as I got hit by a car, broke two other fingers (making it five
o/), spent a year and a half working on my oh-so-destroyed couch, only seeing other humans through screens, almost died after falling from 15 m and stopping the ensuing roll right before a cliff, tore the ligaments of my left ankle (still climbed a 7a, walked in the woods for thirty-six hours and animated a climbing event), did an unplanned flip on a bike, and finally tore the ligaments of my other ankle a week before submitting this work. I also reached new heights and new depths as I won climbing competitions, reached the eighth degree in climbing, became an autonomous diver, was a scientific mediator, participated in an astrophysical symphony, learned to skate, shred, Kotegashi, and most of all, met plenty of amazing people who led me to what I am today, and I am extremely grateful to them.

First, I would like to thank Jérémy, who did not initially plan to but offered to supervise me for a PhD on the amazing topic of numerical simulations of galaxy formation. You have been the best supervisor I could have hoped for (*when available*). You helped me to have faith in myself and impressed me by understanding and answering my questions even before I could finish them. You helped me immensely on a professional side, but also personally. During the pandemic, you were one of the two persons I talked to the most (we reached 5 meetings per week !). The second person with whom I shared a lot of messages during this period is Marion. I thank you from the bottom of my heart for all the time we shared, mainly in your office, discussing amazing topics ranging from cookies to cosmic rays (of course !). You always greeted me with a smile (sometimes food !), and this PhD would surely have not been the same without you.

I express my gratitude to Joki for doing his best to answer all my extremely specific questions about RAMSES (we use the isothermal sound speed in the Jeans criterion for star formation, but do we in the Jeans refinement ?), Léo for saving me from weeks of headache (I still don't really know why the heck Anaconda let me import minirats.utils.py but not minirats.utils.py.f90utils). All this would have not been possible without Jeff, who is responsible for the most amazing master there is and showed me the most interesting research field I ever came across. I also want to express my thanks to Valentin for his help with KROME, Alex for the biscuits and for being responsible for me while I am writing this sitting in front of the copy machine and everyone else in the lab, Manu, Isabelle, the Switzerland team, and all the other incredible people I have met, who made me feel at home at the observatory.

Working surrounded by brilliant people makes for a thriving environment, and the isolated lab on the hill is without a doubt one of the best workplaces there can be (ignoring the thermal efficiency of the building during heat waves). Special mention to Christian, who let me work until unreasonable hours. Dany and Sylvie from the doctoral school are also formidable, being always available and quick to answer in times of need, and making the part of administration they are responsible for much easier. I am grateful to Taysun for giving me the opportunity to continue doing what I love in a place I have never been to and which, I am sure, will prove to be an amazing experience.

I also thank wholeheartedly all the people who settled more or less strongly in my life in these past three years, with a special mention, of course, to members of Kayoo. The formidable Maddie, Migou (who produced many drawings in this work !) and Nono who provided me with so much kindness, but also Flou, Cloclo, Lu, Robin, Mag, Fred, and all the others ! You are awesome, and I am incredibly thankful for meeting you.

Even though you think I might be done, I also want to thank in general all the Metals bands producing amazing music and giving rhythm to my life, authors who provided me with means to escape to fantastic worlds and arts for keeping me company. Special mention to the penguin galaxy as well as all the animals from the obs. for trying to keep me from working, namely squeaky the squirrel, the spiders Jacques and Géraldine (RIP Georges), B&W cat who came through my window, brown cat, woody the European green woodpecker, and the other birds whose name I don't know.

TL;DR: You're all grand.

Sometimes, Me think "What is a Friend ?", and then Me say
"Friend is someone to share the last cookie with".

– Cookie Monster

Bibliography

Abbott B. P., et al., 2016, *Observation of Gravitational Waves from a Binary Black Hole Merger*, Phys. Rev. Lett., 116, 061102

Adams F. C., Graves G. J. M., Laughlin G., 2004, in Garcia-Segura G., Tenorio-Tagle G., Franco J., Yorke H. W., eds, Revista Mexicana de Astronomia y Astrofisica Conference Series Vol. 22, Revista Mexicana de Astronomia y Astrofisica Conference Series. pp 46–49

Agertz O., et al., 2007, *Fundamental differences between SPH and grid methods*, MNRAS, 380, 963

Agertz O., Teyssier R., Moore B., 2011, *The formation of disc galaxies in a ΛCDM universe*, MNRAS, 410, 1391

Agertz O., Kravtsov A. V., Leitner S. N., Gnedin N. Y., 2013, *Toward a Complete Accounting of Energy and Momentum from Stellar Feedback in Galaxy Formation Simulations*, apJ, 770, 25

Agertz O., et al., 2020, *EDGE: the mass-metallicity relation as a critical test of galaxy formation physics*, MNRAS, 491, 1656

Andersson E. P., Agertz O., Renaud F., 2020, *How runaway stars boost galactic outflows*, MNRAS, 494, 3328

Asplund M., Grevesse N., Sauval A. J., Scott P., 2009, *The Chemical Composition of the Sun*, ARA&A, 47, 481

Aubert D., Teyssier R., 2008, *A radiative transfer scheme for cosmological reionization based on a local Eddington tensor*, MNRAS, 387, 295

Behroozi P. S., Conroy C., Wechsler R. H., 2010, *A Comprehensive Analysis of Uncertainties Affecting the Stellar Mass-Halo Mass Relation for $0 < z < 4$*, apJ, 717, 379

Behroozi P. S., Wechsler R. H., Conroy C., 2013, *The Average Star Formation Histories of Galaxies in Dark Matter Halos from $z = 0$-8*, apJ, 770, 57

Behroozi P., Wechsler R. H., Hearin A. P., Conroy C., 2019, *UNIVERSEMACHINE: The correlation between galaxy growth and dark matter halo assembly from $z = 0$-10*, MNRAS, 488, 3143

Benson A. J., Bower R. G., Frenk C. S., Lacey C. G., Baugh C. M., Cole S., 2003, *What Shapes the Luminosity Function of Galaxies?*, apJ, 599, 38

Blaauw A., 1956, *Luminosities, Ages, Kinematics, and Duplicity of the Early-Type Stars*, PASP, 68, 495

Blaauw A., 1961, *On the origin of the O- and B-type stars with high velocities (the "run-away" stars), and some related problems*, Bull. Astron. Inst. Netherlands, 15, 265

Blaauw A., Morgan W. W., 1954, *The Space Motions of AE Aurigae and μ Columbae with Respect to the Orion Nebula.*, apJ, 119, 625

Blondin J. M., Wright E. B., Borkowski K. J., Reynolds S. P., 1998, *Transition to the Radiative Phase in Supernova Remnants*, apJ, 500, 342

Blumenthal G. R., Pagels H., Primack J. R., 1982, *Galaxy formation by dissipationless particles heavier than neutrinos*, Nature, 299, 37

Bonazzola S., Heyvaerts J., Falgarone E., Perault M., Puget J. L., 1987, *Jeans collapse in a turbulent medium*, A&A, 172, 293

Bond J. R., Szalay A. S., Turner M. S., 1982, *Formation of Galaxies in a Gravitino-Dominated Universe*, Phys. Rev. Lett., 48, 1636

Boulares A., Cox D. P., 1990, *Galactic Hydrostatic Equilibrium with Magnetic Tension and Cosmic-Ray Diffusion*, apJ, 365, 544

Bryan G. L., et al., 2014, *ENZO: An Adaptive Mesh Refinement Code for Astrophysics*, ApJS, 211, 19

Castelvecchi D., Witze A., 2016, *Einstein's gravitational waves found at last*, Nature

Ceverino D., Klypin A., 2009, *The Role of Stellar Feedback in the Formation of Galaxies*, apJ, 695, 292

Chabrier G., 2003, *Galactic Stellar and Substellar Initial Mass Function*, PASP, 115, 763

Chaikin E., Schaye J., Schaller M., Bahé Y. M., Nobels F. S. J., Ploeckinger S., 2022, *The importance of the way in which supernova energy is distributed around young stellar populations in simulations of galaxies*, MNRAS, 514, 249

Chandrasekhar S., 1951, *The Gravitational Instability of an Infinite Homogeneous Turbulent Medium*, Proceedings of the Royal Society of London Series A, 210, 26

Cho H., Kang H., 2008, *Feedback from multiple supernova explosions inside a wind-blown bubble*, New A, 13, 163

Cioffi D. F., McKee C. F., Bertschinger E., 1988, *Dynamics of Radiative Supernova Remnants*, apJ, 334, 252

Colella P., 1990, *Multidimensional upwind methods for hyperbolic conservation laws*, Journal of Computational Physics, 87, 171

Commerçon B., Hennebelle P., Audit E., Chabrier G., Teyssier R., 2008, *Protostellar collapse: a comparison between smoothed particle hydrodynamics and adaptative mesh refinement calculations*, A&A, 482, 371

Commerçon B., Teyssier R., Audit E., Hennebelle P., Chabrier G., 2011, *Radiation hydrodynamics with adaptive mesh refinement and application to prestellar core collapse. I. Methods*, A&A, 529, A35

Dahlen T., et al., 2004, *High-Redshift Supernova Rates*, apJ, 613, 189

Dale J. E., Ngoumou J., Ercolano B., Bonnell I. A., 2014, *Before the first supernova: combined effects of H II regions and winds on molecular clouds*, MNRAS, 442, 694

Dekel A., Silk J., 1986, *The Origin of Dwarf Galaxies, Cold Dark Matter, and Biased Galaxy Formation*, apJ, 303, 39

Dubois Y., Commerçon B., 2016, *An implicit scheme for solving the anisotropic diffusion of heat and cosmic rays in the RAMSES code*, A&A, 585, A138

Dubois Y., Teyssier R., 2008a, in Knapen J. H., Mahoney T. J., Vazdekis A., eds, Astronomical Society of the Pacific Conference Series Vol. 390, Pathways Through an Eclectic Universe. p. 388

Dubois Y., Teyssier R., 2008b, *On the onset of galactic winds in quiescent star forming galaxies*, A&A, 477, 79

Dubois Y., Devriendt J., Slyz A., Teyssier R., 2010, *Jet-regulated cooling catastrophe*, MNRAS, 409, 985

Ellison D. C., Decourchelle A., Ballet J., 2004, *Hydrodynamic simulation of supernova remnants including efficient particle acceleration*, A&A, 413, 189

Elmegreen B. G., Scalo J., 2004, *Interstellar Turbulence I: Observations and Processes*, ARA&A, 42, 211

Faucher-Giguère C.-A., Lidz A., Zaldarriaga M., Hernquist L., 2009, *A New Calculation of the Ionizing Background Spectrum and the Effects of He II Reionization*, apJ, 703, 1416

Federrath C., Klessen R. S., 2012, *The Star Formation Rate of Turbulent Magnetized Clouds: Comparing Theory, Simulations, and Observations*, apJ, 761, 156

Federrath C., Klessen R. S., Schmidt W., 2008, *The Density Probability Distribution in Compressible Isothermal Turbulence: Solenoidal versus Compressive Forcing*, ApJ, 688, L79

Federrath C., Roman-Duval J., Klessen R. S., Schmidt W., Mac Low M. M., 2010, *Comparing the statistics of interstellar turbulence in simulations and observations. Solenoidal versus compressive turbulence forcing*, A&A, 512, A81

Ferland G. J., Korista K. T., Verner D. A., Ferguson J. W., Kingdon J. B., Verner E. M., 1998, *CLOUDY 90: Numerical Simulation of Plasmas and Their Spectra*, PASP, 110, 761

Ferrand G., Marcowith A., 2010, *On the shape of the spectrum of cosmic rays accelerated inside superbubbles*, A&A, 510, A101

Few C. G., Courty S., Gibson B. K., Kawata D., Calura F., Teyssier R., 2012, *RAMSES-CH: a new chemodynamical code for cosmological simulations*, MNRAS, 424, L11

Few C. G., Courty S., Gibson B. K., Michel-Dansac L., Calura F., 2014, *Chemodynamics of a simulated disc galaxy: initial mass functions and Type Ia supernova progenitors*, MNRAS, 444, 3845

Fromang S., Hennebelle P., Teyssier R., 2006, *A high order Godunov scheme with constrained transport and adaptive mesh refinement for astrophysical magnetohydrodynamics*, A&A, 457, 371

Fryxell B., et al., 2000, *FLASH: An Adaptive Mesh Hydrodynamics Code for Modeling Astrophysical Thermonuclear Flashes*, ApJS, 131, 273

Geen S., Rosdahl J., Blaizot J., Devriendt J., Slyz A., 2015, *A detailed study of feedback from a massive star*, MNRAS, 448, 3248

Genel S., et al., 2019, *A Quantification of the Butterfly Effect in Cosmological Simulations and Implications for Galaxy Scaling Relations*, apJ, 871, 21

Gerritsen J. P. E., de Blok W. J. G., 1999, *Star formation and the interstellar medium in low surface brightness galaxies. III. Why they are blue, thin and poor in molecular gas*, A&A, 342, 655

Gingold R. A., Monaghan J. J., 1977, *Smoothed particle hydrodynamics: theory and application to non-spherical stars.*, MNRAS, 181, 375

Girichidis P., et al., 2020, *Physical Processes in Star Formation*, Space Sci. Rev., 216, 68

Gnedin N. Y., Abel T., 2001, *Multi-dimensional cosmological radiative transfer with a Variable Eddington Tensor formalism*, New A, 6, 437

Gnedin N. Y., Kravtsov A. V., 2011, *Environmental Dependence of the Kennicutt-Schmidt Relation in Galaxies*, apJ, 728, 88

Governato F., et al., 2010, *Bulgeless dwarf galaxies and dark matter cores from supernova-driven outflows*, Nature, 463, 203

Grassi T., Bovino S., Schleicher D. R. G., Prieto J., Seifried D., Simoncini E., Gianturco F. A., 2014, *KROME - a package to embed chemistry in astrophysical simulations*, MNRAS, 439, 2386

Greggio L., Renzini A., 1983, *The binary model for type I supernovae - Theoretical rates*, A&A, 118, 217

Grevesse N., Asplund M., Sauval A. J., Scott P., 2010, *The chemical composition of the Sun*, Ap&SS, 328, 179

Grisdale K., Agertz O., Renaud F., Romeo A. B., Devriendt J., Slyz A., 2019, *On the observed diversity of star formation efficiencies in Giant Molecular Clouds*, MNRAS, 486, 5482

Haardt F., Madau P., 1996, *Radiative Transfer in a Clumpy Universe. II. The Ultraviolet Extragalactic Background*, apJ, 461, 20

Hahn O., Abel T., 2011, *Multi-scale initial conditions for cosmological simulations*, MNRAS, 415, 2101

Heger A., Fryer C. L., Woosley S. E., Langer N., Hartmann D. H., 2003, *How Massive Single Stars End Their Life*, apJ, 591, 288

Hennebelle P., Chabrier G., 2011, *Analytical Star Formation Rate from Gravoturbulent Fragmentation*, ApJ, 743, L29

Hennebelle P., Commerçon B., Chabrier G., Marchand P., 2016, *Magnetically Self-regulated Formation of Early Protoplanetary Disks*, ApJ, 830, L8

Hennebelle P., Commerçon B., Lee Y.-N., Charnoz S., 2020, *What determines the formation and characteristics of protoplanetary discs?*, A&A, 635, A67

Hopkins P. F., 2015, *A new class of accurate, mesh-free hydrodynamic simulation methods*, MNRAS, 450, 53

Hopkins P. F., Narayanan D., Murray N., 2013, *The meaning and consequences of star formation criteria in galaxy models with resolved stellar feedback*, MNRAS, 432, 2647

Hopkins P. F., Kereš D., Oñorbe J., Faucher-Giguère C.-A., Quataert E., Murray N., Bullock J. S., 2014, *Galaxies on FIRE (Feedback In Realistic Environments): stellar feedback explains cosmologically inefficient star formation*, MNRAS, 445, 581

Hopkins P. F., et al., 2018, *How to model supernovae in simulations of star and galaxy formation*, MNRAS, 477, 1578

Hummels C. B., et al., 2019, *The Impact of Enhanced Halo Resolution on the Simulated Circumgalactic Medium*, apJ, 882, 156

Kalirai J. S., Hansen B. M. S., Kelson D. D., Reitzel D. B., Rich R. M., Richer H. B., 2008, *The Initial-Final Mass Relation: Direct Constraints at the Low-Mass End*, apJ, 676, 594

Kasen D., Woosley S. E., 2009, *Type II Supernovae: Model Light Curves and Standard Candle Relationships*, apJ, 703, 2205

Katz N., 1992, *Dissipational Galaxy Formation. II. Effects of Star Formation*, apJ, 391, 502

Katz H., 2022, *RAMSES-RTZ: non-equilibrium metal chemistry and cooling coupled to on-the-fly radiation hydrodynamics*, MNRAS, 512, 348

Keller B. W., Kruijssen J. M. D., 2020, *Below the subgrid: uncertainties in supernova input rates drive qualitative differences in simulations of galaxy evolution*, arXiv e-prints, p. arXiv:2004.03608

Keller B. W., Wadsley J. W., Wang L., Kruijssen J. M. D., 2019, *Chaos and variance in galaxy formation*, MNRAS, 482, 2244

Keller B. W., Kruijssen J. M. D., Wadsley J. W., 2020, *Entropy-driven winds: Outflows and fountains lifted gently by buoyancy*, MNRAS, 493, 2149

Kelvin W. T., 1904, *Baltimore lectures on molecular dynamics and the wave theory of light*. C.J. Clay and Sons; Publication agency of the Johns Hopkins University, London, Baltimore, http://hdl.handle.net/2027/ien.35556038198842

Kelvin L. S., et al., 2014, *Galaxy And Mass Assembly (GAMA): stellar mass functions by Hubble type*, MNRAS, 444, 1647

Kennicutt Robert C. J., 1998, *The Global Schmidt Law in Star-forming Galaxies*, apJ, 498, 541

Kennicutt R. C., Evans N. J., 2012, *Star Formation in the Milky Way and Nearby Galaxies*, ARA&A, 50, 531

Khokhlov A., 1998, *Fully Threaded Tree Algorithms for Adaptive Refinement Fluid Dynamics Simulations*, Journal of Computational Physics, 143, 519

Kim C.-G., Ostriker E. C., 2015, *Momentum Injection by Supernovae in the Interstellar Medium*, apJ, 802, 99

Kim C.-G., Ostriker E. C., 2017, *Three-phase Interstellar Medium in Galaxies Resolving Evolution with Star Formation and Supernova Feedback (TIGRESS): Algorithms, Fiducial Model, and Convergence*, apJ, 846, 133

Kim J.-h., et al., 2014, *The AGORA High-resolution Galaxy Simulations Comparison Project*, ApJS, 210, 14

Kimm T., Cen R., 2014, *Escape Fraction of Ionizing Photons during Reionization: Effects due to Supernova Feedback and Runaway OB Stars*, apJ, 788, 121

Kimm T., Cen R., Devriendt J., Dubois Y., Slyz A., 2015, *Towards simulating star formation in turbulent high-z galaxies with mechanical supernova feedback*, MNRAS, 451, 2900

Kimm T., Katz H., Haehnelt M., Rosdahl J., Devriendt J., Slyz A., 2017, *Feedback-regulated star formation and escape of LyC photons from mini-haloes during reionization*, MNRAS, 466, 4826

Kimm T., Bieri R., Geen S., Rosdahl J., Blaizot J., Michel-Dansac L., Garel T., 2022, *A Systematic Study of the Escape of LyC and Lyα Photons from Star-forming, Magnetized Turbulent Clouds*, ApJS, 259, 21

Klessen R. S., Glover S. C. O., 2016, *Physical Processes in the Interstellar Medium*, Saas-Fee Advanced Course, 43, 85

Kravtsov A. V., Klypin A. A., Khokhlov A. M., 1997, *Adaptive Refinement Tree: A New High-Resolution N-Body Code for Cosmological Simulations*, ApJS, 111, 73

Kretschmer M., Teyssier R., 2020, *Forming early-type galaxies without AGN feedback: a combination of merger-driven outflows and inefficient star formation*, MNRAS, 492, 1385

Kretschmer M., Agertz O., Teyssier R., 2020, *Rapid filamentary accretion as the origin of extended thin discs*, MNRAS, 497, 4346

Kroupa P., 2001, *On the variation of the initial mass function*, MNRAS, 322, 231

Krumholz M. R., Matzner C. D., 2009, *The Dynamics of Radiation-pressure-dominated H II Regions*, apJ, 703, 1352

Krumholz M. R., McKee C. F., 2005, *A General Theory of Turbulence-regulated Star Formation, from Spirals to Ultraluminous Infrared Galaxies*, apJ, 630, 250

Krumholz M. R., et al., 2014, in Beuther H., Klessen R. S., Dullemond C. P., Henning T., eds, Protostars and Planets VI. p. 243 (`arXiv:1401.2473`), doi:10.2458/azu_uapress_9780816531240-ch011

Larson R. B., 1981, *Turbulence and star formation in molecular clouds.*, MNRAS, 194, 809

Lee J., et al., 2021, *The Horizon Run 5 Cosmological Hydrodynamical Simulation: Probing Galaxy Formation from Kilo- to Gigaparsec Scales*, apJ, 908, 11

Leitherer C., et al., 1999, *Starburst99: Synthesis Models for Galaxies with Active Star Formation*, ApJS, 123, 3

Lemaître G., 1927, *Un Univers homogène de masse constante et de rayon croissant rendant compte de la vitesse radiale des nébuleuses extra-galactiques*, Annales de la Société Scientifique de Bruxelles, 47, 49

Lemaître G., 1931, *Expansion of the universe, A homogeneous universe of constant mass and increasing radius accounting for the radial velocity of extra-galactic nebulae*, MNRAS, 91, 483

Lemons S. M., Reines A. E., Plotkin R. M., Gallo E., Greene J. E., 2015, *An X-Ray Selected Sample of Candidate Black Holes in Dwarf Galaxies*, apJ, 805, 12

Lieb E. H., Yau H.-T., 1987, *A Rigorous Examination of the Chandrasekhar Theory of Stellar Collapse*, apJ, 323, 140

Lucas W. E., Bonnell I. A., Dale J. E., 2020, *Supernova feedback and the energy deposition in molecular clouds*, MNRAS, 493, 4700

Lucy L. B., 1977, *A numerical approach to the testing of the fission hypothesis.*, AJ, 82, 1013

Mac Low M.-M., Klessen R. S., 2004, *Control of star formation by supersonic turbulence*, Reviews of Modern Physics, 76, 125

Maíz Apellániz J., Pantaleoni González M., Barbá R. H., Simón-Díaz S., Negueruela I., Lennon D. J., Sota A., Trigueros Páez E., 2018, *Search for Galactic runaway stars using Gaia Data Release 1 and HIPPARCOS proper motions*, A&A, 616, A149

Maoz D., 2008, *On the fraction of intermediate-mass close binaries that explode as Type Ia supernovae*, MNRAS, 384, 267

Martizzi D., Faucher-Giguère C.-A., Quataert E., 2015, *Supernova feedback in an inhomogeneous interstellar medium*, MNRAS, 450, 504

Matzner C. D., 2002, *On the Role of Massive Stars in the Support and Destruction of Giant Molecular Clouds*, apJ, 566, 302

Mauerhofer V., Verhamme A., Blaizot J., Garel T., Kimm T., Michel-Dansac L., Rosdahl J., 2021, *UV absorption lines and their potential for tracing the Lyman continuum escape fraction*, A&A, 646, A80

McKee C. F., Ostriker J. P., 1977, *A theory of the interstellar medium: three components regulated by supernova explosions in an inhomogeneous substrate.*, apJ, 218, 148

Merritt D., 2013, *Dynamics and Evolution of Galactic Nuclei*. Princeton University Press

Mezcua M., Civano F., Fabbiano G., Miyaji T., Marchesi S., 2016, *A Population of Intermediate-mass Black Holes in Dwarf Starburst Galaxies Up to Redshift=1.5*, apJ, 817, 20

Micelotta E. R., Matsuura M., Sarangi A., 2018, *Dust in Supernovae and Supernova Remnants II: Processing and Survival*, Space Sci. Rev., 214, 53

Michel-Dansac L., Blaizot J., Garel T., Verhamme A., Kimm T., Trebitsch M., 2020a, *RASCAS: Resonant line transfer in AMR simulations* (ascl:2002.002)

Michel-Dansac L., Blaizot J., Garel T., Verhamme A., Kimm T., Trebitsch M., 2020b, *RASCAS: RAdiation SCattering in Astrophysical Simulations*, A&A, 635, A154

Milgrom M., 1983, *A modification of the Newtonian dynamics as a possible alternative to the hidden mass hypothesis.*, apJ, 270, 365

Miller B. P., Gallo E., Greene J. E., Kelly B. C., Treu T., Woo J.-H., Baldassare V., 2015, *X-Ray Constraints on the Local Supermassive Black Hole Occupation Fraction*, apJ, 799, 98

Mitchell P. D., Schaye J., 2022, *How gas flows shape the stellar-halo mass relation in the EAGLE simulation*, MNRAS, 511, 2948

Mitchell P. D., Blaizot J., Devriendt J., Kimm T., Michel-Dansac L., Rosdahl J., Slyz A., 2018, *Gas flows in the circumgalactic medium around simulated high-redshift galaxies*, MNRAS, 474, 4279

Mo H. J., Mao S., White S. D. M., 1998, *The formation of galactic discs*, MNRAS, 295, 319

Moster B. P., Naab T., White S. D. M., 2013, *Galactic star formation and accretion histories from matching galaxies to dark matter haloes*, MNRAS, 428, 3121

Moster B. P., Naab T., Lindström M., O'Leary J. A., 2021, *GalaxyNet: connecting galaxies and dark matter haloes with deep neural networks and reinforcement learning in large volumes*, MNRAS, 507, 2115

Murray N., 2011, *Star Formation Efficiencies and Lifetimes of Giant Molecular Clouds in the Milky Way*, apJ, 729, 133

Murray N., Quataert E., Thompson T. A., 2005, *On the Maximum Luminosity of Galaxies and Their Central Black Holes: Feedback from Momentum-driven Winds*, apJ, 618, 569

Naab T., Ostriker J. P., 2017, *Theoretical Challenges in Galaxy Formation*, ARA&A, 55, 59

Navarro J. F., White S. D. M., 1993, *Simulations of Dissipative Galaxy Formation in Hierarchically Clustering Universes - Part One - Tests of the Code*, MNRAS, 265, 271

Navarro J. F., Frenk C. S., White S. D. M., 1997, *A Universal Density Profile from Hierarchical Clustering*, apJ, 490, 493

Nelson D., et al., 2018, *The abundance, distribution, and physical nature of highly ionized oxygen O VI, O VII, and O VIII in IllustrisTNG*, MNRAS, 477, 450

Offner S. S. R., Clark P. C., Hennebelle P., Bastian N., Bate M. R., Hopkins P. F., Moraux E., Whitworth A. P., 2014, in Beuther H., Klessen R. S., Dullemond C. P., Henning T., eds, Protostars and Planets VI. p. 53 (`arXiv:1312.5326`), doi:10.2458/azu_uapress_9780816531240-ch003

Okamoto I., 2006, *Electromagnetic Extraction of Energy from Kerr Black Holes*, PASJ, 58, 1047

Oppenheimer B. D., Davé R., 2006, *Cosmological simulations of intergalactic medium enrichment from galactic outflows*, MNRAS, 373, 1265

Oppenheimer B. D., et al., 2016, *Bimodality of low-redshift circumgalactic O VI in non-equilibrium EAGLE zoom simulations*, MNRAS, 460, 2157

Padoan P., Nordlund Å., 2011, *The Star Formation Rate of Supersonic Magnetohydrodynamic Turbulence*, apJ, 730, 40

Padoan P., Haugbølle T., Nordlund Å., 2012, *A Simple Law of Star Formation*, ApJ, 759, L27

Paduroiu S., 2022, *Warm Dark Matter in Simulations*, Universe, 8, 76

Peebles P. J. E., 1980, *The large-scale structure of the universe*. Princeton University Press

Peebles P. J. E., 1982, *Large-scale background temperature and mass fluctuations due to scale-invariant primeval perturbations*, ApJ, 263, L1

Peeples M. S., et al., 2019, *Figuring Out Gas & Galaxies in Enzo (FOGGIE). I. Resolving Simulated Circumgalactic Absorption at $2 \leq z \leq 2.5$*, apJ, 873, 129

Pejcha O., Prieto J. L., 2015, *On the Intrinsic Diversity of Type II-Plateau Supernovae*, apJ, 806, 225

Penrose R., 2002, *"Golden Oldie": Gravitational Collapse: The Role of General Relativity*, General Relativity and Gravitation, 7, 1141

Planck Collaboration et al., 2016, *Planck 2015 results. XIII. Cosmological parameters*, A&A, 594, A13

Planck Collaboration et al., 2020, *Planck 2018 results. VI. Cosmological parameters*, A&A, 641, A6

Posti L., Helmi A., 2019, *Mass and shape of the Milky Way's dark matter halo with globular clusters from Gaia and Hubble*, A&A, 621, A56

Prialnik D., 2000, *An introduction to the theory of stellar structure and evolution*. Cambridge University Press, Cambridge, England

Raiteri C. M., Villata M., Navarro J. F., 1996, *Simulations of Galactic chemical evolution. I. O and Fe abundances in a simple collapse model.*, A&A, 315, 105

Ratra B., Peebles P. J. E., 1988, *Cosmological consequences of a rolling homogeneous scalar field*, Phys. Rev. D, 37, 3406

Rey M. P., Pontzen A., Agertz O., Orkney M. D. A., Read J. I., Rosdahl J., 2020, *EDGE: from quiescent to gas-rich to star-forming low-mass dwarf galaxies*, MNRAS, 497, 1508

Rey M. P., Pontzen A., Agertz O., Orkney M. D. A., Read J. I., Saintonge A., Kim S. Y., Das P., 2022, *EDGE: What shapes the relationship between H I and stellar observables in faint dwarf galaxies?*, MNRAS, 511, 5672

Reynolds S. P., 2008, *Supernova Remnants at High Energy*, Annual Review of Astronomy and Astrophysics, 46, 89

Rieder M., Teyssier R., 2016, *A small-scale dynamo in feedback-dominated galaxies as the origin of cosmic magnetic fields - I. The kinematic phase*, MNRAS, 457, 1722

Rosdahl K. J., 2012, PhD thesis, Université Claude Bernard Lyon 1

Rosdahl J., Teyssier R., 2015, *A scheme for radiation pressure and photon diffusion with the M1 closure in RAMSES-RT*, MNRAS, 449, 4380

Rosdahl J., Blaizot J., Aubert D., Stranex T., Teyssier R., 2013, *RAMSES-RT: radiation hydrodynamics in the cosmological context*, MNRAS, 436, 2188

Rosdahl J., Schaye J., Teyssier R., Agertz O., 2015, *Galaxies that shine: radiation-hydrodynamical simulations of disc galaxies*, MNRAS, 451, 34

Rosdahl J., Schaye J., Dubois Y., Kimm T., Teyssier R., 2017, *Snap, crackle, pop: sub-grid supernova feedback in AMR simulations of disc galaxies*, MNRAS, 466, 11

Rosdahl J., et al., 2018, *The SPHINX cosmological simulations of the first billion years: the impact of binary stars on reionization*, MNRAS, 479, 994

Rosen A., Bregman J. N., 1995, *Global Models of the Interstellar Medium in Disk Galaxies*, apJ, 440, 634

Salem M., Bryan G. L., Corlies L., 2016, *Role of cosmic rays in the circumgalactic medium*, MNRAS, 456, 582

Saltzman J., 1994, *An Unsplit 3D Upwind Method for Hyperbolic Conservation Laws*, Journal of Computational Physics, 115, 153

Sanchez N. N., Werk J. K., Tremmel M., Pontzen A., Christensen C., Quinn T., Cruz A., 2019, *Not So Heavy Metals: Black Hole Feedback Enriches the Circumgalactic Medium*, apJ, 882, 8

Scalo J., Elmegreen B. G., 2004, *Interstellar Turbulence II: Implications and Effects*, ARA&A, 42, 275

Scannapieco E., Bildsten L., 2005, *The Type Ia Supernova Rate*, ApJ, 629, L85

Schmidt M., 1959, *The Rate of Star Formation.*, apJ, 129, 243

Schmidt W., 2014, *Numerical Modelling of Astrophysical Turbulence*. Springer

Schmidt W., Niemeyer J. C., Hillebrandt W., 2006, *A localised subgrid scale model for fluid dynamical simulations in astrophysics. I. Theory and numerical tests*, A&A, 450, 265

Schoettler C., Parker R. J., de Bruijne J., 2022, *Constraining the initial conditions of NGC 2264 using ejected stars found in Gaia DR2*, MNRAS, 510, 3178

Schroetter I., et al., 2019, *MusE GAs FLOw and Wind (MEGAFLOW) - III. Galactic wind properties using background quasars*, MNRAS, 490, 4368

Schroetter I., et al., 2021, *MusE GAs FLOw and Wind (MEGAFLOW) VI. A study of C IV and Mg II absorbing gas surrounding [O II] emitting galaxies*, MNRAS, 506, 1355

Sedov L. I., 1959, *Similarity and Dimensional Methods in Mechanics*. Academic Press, New York

Semenov V. A., Kravtsov A. V., Gnedin N. Y., 2016, *Nonuniversal Star Formation Efficiency in Turbulent ISM*, apJ, 826, 200

Shandarin S. F., Zeldovich Y. B., 1989, *The large-scale structure of the universe: Turbulence, intermittency, structures in a self-gravitating medium*, Reviews of Modern Physics, 61, 185

Silk J., 2000, *Big Bang 3ed*, 3 edn. St Martin's Press, New York, NY

Silk J., Rees M. J., 1998, *Quasars and galaxy formation*, A&A, 331, L1

Silverberg J. L., Bierbaum M., Sethna J. P., Cohen I., 2013, *Collective motion of humans in mosh and circle pits at heavy metal concerts*, Phys. Rev. Lett., 110, 228701

Smith M. C., 2021, *The sensitivity of stellar feedback to IMF averaging versus IMF sampling in galaxy formation simulations*, MNRAS, 502, 5417

Springel V., 2010a, *Smoothed Particle Hydrodynamics in Astrophysics*, ARA&A, 48, 391

Springel V., 2010b, *E pur si muove: Galilean-invariant cosmological hydrodynamical simulations on a moving mesh*, MNRAS, 401, 791

Springel V., Hernquist L., 2003, *Cosmological smoothed particle hydrodynamics simulations: a hybrid multiphase model for star formation*, MNRAS, 339, 289

Springel V., Di Matteo T., Hernquist L., 2005, *Modelling feedback from stars and black holes in galaxy mergers*, MNRAS, 361, 776

Springel V., Pakmor R., Zier O., Reinecke M., 2021, *Simulating cosmic structure formation with the GADGET-4 code*, MNRAS, 506, 2871

Springel V., Pakmor R., Zier O., Reinecke M., 2022, *GADGET-4: Parallel cosmological N-body and SPH code*, Astrophysics Source Code Library, record ascl:2204.014 (ascl:2204.014)

Stanway E. R., Eldridge J. J., 2018, *Re-evaluating old stellar populations*, MNRAS, 479, 75

Stinson G., Seth A., Katz N., Wadsley J., Governato F., Quinn T., 2006, *Star formation and feedback in smoothed particle hydrodynamic simulations - I. Isolated galaxies*, MNRAS, 373, 1074

Stone J. M., Gardiner T. A., Teuben P., Hawley J. F., Simon J. B., 2008, *Athena: A New Code for Astrophysical MHD*, ApJS, 178, 137

Strömgren B., 1939, *The Physical State of Interstellar Hydrogen.*, apJ, 89, 526

Sullivan M., et al., 2006, *Rates and Properties of Type Ia Supernovae as a Function of Mass and Star Formation in Their Host Galaxies*, apJ, 648, 868

Suresh J., Rubin K. H. R., Kannan R., Werk J. K., Hernquist L., Vogelsberger M., 2017, *On the OVI abundance in the circumgalactic medium of low-redshift galaxies*, MNRAS, 465, 2966

Taylor G., 1950, *The Formation of a Blast Wave by a Very Intense Explosion. I. Theoretical Discussion*, Proceedings of the Royal Society of London Series A, 201, 159

Teyssier R., 2002, *Cosmological hydrodynamics with adaptive mesh refinement. A new high resolution code called RAMSES*, A&A, 385, 337

Teyssier R., Pontzen A., Dubois Y., Read J. I., 2013, *Cusp-core transformations in dwarf galaxies: observational predictions*, MNRAS, 429, 3068

Thielemann F. K., Nomoto K., Yokoi K., 1986, *Explosive nucleosynthesis in carbon deflagration models of Type I supernovae*, A&A, 158, 17

Thornton K., Gaudlitz M., Janka H. T., Steinmetz M., 1998, *Energy Input and Mass Redistribution by Supernovae in the Interstellar Medium*, apJ, 500, 95

Tollet É., Cattaneo A., Macciò A. V., Dutton A. A., Kang X., 2019, *NIHAO XIX: how supernova feedback shapes the galaxy baryon cycle*, MNRAS, 485, 2511

Toomre A., 1964, *On the gravitational stability of a disk of stars.*, apJ, 139, 1217

Toro E. F., 1999, *Riemann Solvers and Numerical Methods for Fluid Dynamics*. Springer Berlin Heidelberg, doi:10.1007/978-3-662-03915-1, `https://doi.org/10.1007%2F978-3-662-03915-1`

Truelove J. K., Klein R. I., McKee C. F., Holliman John H. I., Howell L. H., Greenough J. A., 1997, *The Jeans Condition: A New Constraint on Spatial Resolution in Simulations of Isothermal Self-gravitational Hydrodynamics*, ApJ, 489, L179

Tumlinson J., Peeples M. S., Werk J. K., 2017, *The Circumgalactic Medium*, ARA&A, 55, 389

Veilleux S., Shopbell P. L., Miller S. T., 2001, *The Biconical Outflow in the Seyfert Galaxy NGC 2992*, AJ, 121, 198

Wadsley J. W., Keller B. W., Quinn T. R., 2017, *Gasoline2: a modern smoothed particle hydrodynamics code*, MNRAS, 471, 2357

Walch S. K., Whitworth A. P., Bisbas T., Wünsch R., Hubber D., 2012, *Dispersal of molecular clouds by ionizing radiation*, MNRAS, 427, 625

Wetterich C., 1988, *Cosmology and the fate of dilatation symmetry*, Nuclear Physics B, 302, 668

Wiersma R. P. C., Schaye J., Theuns T., Dalla Vecchia C., Tornatore L., 2009, *Chemical enrichment in cosmological, smoothed particle hydrodynamics simulations*, MNRAS, 399, 574

Williams J. P., McKee C. F., 1997, *The Galactic Distribution of OB Associations in Molecular Clouds*, apJ, 476, 166

Woosley S. E., Heger A., 2007, *Nucleosynthesis and remnants in massive stars of solar metallicity*, Phys. Rep., 442, 269

Woosley S. E., Weaver T. A., 1995, *The Evolution and Explosion of Massive Stars. II. Explosive Hydrodynamics and Nucleosynthesis*, ApJS, 101, 181

Zabl J., et al., 2019, *MusE GAs FLOw and Wind (MEGAFLOW) II. A study of gas accretion around $z \approx 1$ star-forming galaxies with background quasars*, MNRAS, 485, 1961

Zhukovska S., Dobbs C., Jenkins E. B., Klessen R. S., 2016, *Modeling Dust Evolution in Galaxies with a Multiphase, Inhomogeneous ISM*, apJ, 831, 147

de Plaa J., Werner N., Bleeker J. A. M., Vink J., Kaastra J. S., Méndez M., 2007, *Constraining supernova models using the hot gas in clusters of galaxies*, A&A, 465, 345

van de Voort F., Springel V., Mandelker N., van den Bosch F. C., Pakmor R., 2019, *Cosmological simulations of the circumgalactic medium with 1 kpc resolution: enhanced H I column densities*, MNRAS, 482, L85

van den Bergh S., McClure R. D., 1994, *Rediscussion of Extragalactic Supernova Rates Derived from Evans's 1980–1988 Observations*, apJ, 425, 205